SUPRASTARS OF CHEMISTRY

EDITED BY: Tony D. James, Ronald K. Castellano, Victor Borovkov, Tangxin Xiao and Chao Deng

PUBLISHED IN: Frontiers in Chemistry

frontiers Research Topics

frontiers

ISSN 1664-8714
ISBN 978-2-88976-456-3
DOI 10.3389/978-2-88976-456-3

About Frontiers

Frontiers is more than just an open-access publisher of scholarly articles: it is a pioneering approach to the world of academia, radically improving the way scholarly research is managed. The grand vision of Frontiers is a world where all people have an equal opportunity to seek, share and generate knowledge. Frontiers provides immediate and permanent online open access to all its publications, but this alone is not enough to realize our grand goals.

Frontiers Journal Series

The Frontiers Journal Series is a multi-tier and interdisciplinary set of open-access, online journals, promising a paradigm shift from the current review, selection and dissemination processes in academic publishing. All Frontiers journals are driven by researchers for researchers; therefore, they constitute a service to the scholarly community. At the same time, the Frontiers Journal Series operates on a revolutionary invention, the tiered publishing system, initially addressing specific communities of scholars, and gradually climbing up to broader public understanding, thus serving the interests of the lay society, too.

Dedication to Quality

Each Frontiers article is a landmark of the highest quality, thanks to genuinely collaborative interactions between authors and review editors, who include some of the world's best academicians. Research must be certified by peers before entering a stream of knowledge that may eventually reach the public - and shape society; therefore, Frontiers only applies the most rigorous and unbiased reviews.
Frontiers revolutionizes research publishing by freely delivering the most outstanding research, evaluated with no bias from both the academic and social point of view. By applying the most advanced information technologies, Frontiers is catapulting scholarly publishing into a new generation.

What are Frontiers Research Topics?

Frontiers Research Topics are very popular trademarks of the Frontiers Journals Series: they are collections of at least ten articles, all centered on a particular subject. With their unique mix of varied contributions from Original Research to Review Articles, Frontiers Research Topics unify the most influential researchers, the latest key findings and historical advances in a hot research area! Find out more on how to host your own Frontiers Research Topic or contribute to one as an author by contacting the Frontiers Editorial Office: frontiersin.org/about/contact

SUPRASTARS OF CHEMISTRY

Topic Editors:
Tony D. James, University of Bath, United Kingdom
Ronald K. Castellano, University of Florida, United States
Victor Borovkov, Tallinn University of Technology, Estonia
Tangxin Xiao, Changzhou University, China
Chao Deng, Soochow University, China

Citation: James, T. D., Castellano, R. K., Borovkov, V., Xiao, T., Deng, C., eds. (2022). Suprastars of Chemistry. Lausanne: Frontiers Media SA.
doi: 10.3389/978-2-88976-456-3

Table of Contents

frontiers | Frontiers in Chemistry

EDITORIAL
published: 06 June 2022
doi: 10.3389/fchem.2022.932508

Editorial: Suprastars of Chemistry

Tangxin Xiao[1], Tony D. James[2,3]*, Victor Borovkov[4]*, Ronald K. Castellano[5]* and Chao Deng[6]**

[1]School of Petrochemical Engineering, Changzhou University, Changzhou, China, [2]Department of Chemistry, University of Bath, Bath, United Kingdom, [3]School of Chemistry and Chemical Engineering, Henan Normal University, Xinxiang, China, [4]Department of Chemistry and Biotechnology, School of Science, Tallinn University of Technology, Tallinn, Estonia, [5]Department of Chemistry, University of Florida, Gainesville, FL, United States, [6]College of Chemistry, Chemical Engineering, and Materials Science, Soochow University, Suzhou, China

Keywords: supramolecular chemistry, self-assembly, host-guest systems, metal coordination, macrocycle

Editorial on the Research Topic

Suprastars of Chemistry

OPEN ACCESS

Edited by:
Andreas Hennig,
Osnabrück University, Germany

Reviewed by:
Khaleel Assaf,
Al-Balqa Applied University, Jordan
Andrea Fin,
University of Turin, Italy

****Correspondence:***
Tangxin Xiao
xiaotangxin@cczu.edu.cn
Tony D. James
t.d.james@bath.ac.uk
Victor Borovkov
victor.borovkov@taltech.ee
Ronald K. Castellano
castellano@chem.ufl.edu
Chao Deng
cdeng@suda.edu.cn

Specialty section:
This article was submitted to Supramolecular Chemistry, a section of the journal Frontiers in Chemistry

Received: *29 April 2022*
Accepted: *24 May 2022*
Published: *06 June 2022*

Citation:
Xiao T, James TD, Borovkov V, Castellano RK and Deng C (2022) Editorial: Suprastars of Chemistry. Front. Chem. 10:932508. doi: 10.3389/fchem.2022.932508

The field of Supramolecular Chemistry has rapidly evolved over the last decades to the point where it now influences a diverse range of research areas, drives technological breakthroughs, and often results in breathtaking feats of ingenuity along the way. None of these advancements would be possible without the creativity and talent of supramolecular chemists throughout the world, and this Research Topic aims to celebrate those scientists as leading experts in the field—the "Suprastars."

In this collection, excellent works cover fundamental research on self-assembly behavior, structure-property relationships, and chirality control, as well as attractive applications such as bioimaging, sensing, photodynamic therapy, and other related areas. The self-assemblies and supramolecular systems are facilitated by various kinds of dynamic non-covalent interactions, such as π-π interaction, (Hunter and Sanders, 1990; Shao et al., 2013; Fagnani et al., 2017; Xiao et al., 2019a; Mahl et al., 2022) macrocyclic host-guest interaction, (Yu et al., 2015; Xiao et al., 2019b; Roy et al., 2020; Xiao et al.; Fang et al., 2022) metal-coordination, (Sun et al., 2010; McConnell et al., 2015; Datta et al., 2018) and hydrophobic interactions (Chang et al., 2019; Xiao et al., 2019c) etc., which endow the corresponding materials with outstanding and highly desirable properties including reversibility, tunability, and stimuli-responsiveness.

In particular, macrocyclic host-guest chemistry is a hot topic in supramolecular chemistry on account of the continuous development of supramolecular macrocycles, such as crown ethers, (Pedersen, 1967; Price and Gibson, 2018; Xiao et al., 2021) cyclodextrins, (Szejtli, 1998; Harada et al., 2014) cucurbiturils, (Lagona et al., 2005; Masson et al., 2012; Ni et al., 2014; Barrow et al., 2015; Murray et al., 2017; Chen et al., 2022; Huang et al., 2022) calixarenes, (Böhmer, 1995; Guo and Liu, 2014), and pillararenes (Xue et al., 2012; Strutt et al., 2014; Ogoshi et al., 2018; Xiao et al., 2018; Xiao et al., 2019d; Wan et al., 2022). Fullerenes remain important compounds with promising applications in biomedical research but their hydrophobicity limits deployment in the body. Zhang et al. developed a water-soluble supramolecular nanoformulation based on a deep cavitand calixarene system (SAC4A), which is able to host fullerene *via* a simple grinding approach. The system enables efficient activation of reactive oxygen species and can be used as a potential photodynamic agent. Duan et al. developed a pillararene-indicator displacement system. The water-soluble pillar [6]arene macrocycle can greatly enhance the fluorescence of safranine T (ST) due to host-guest induced twisted intramolecular charge-transfer. The system can be used as a turn-off sensor for caffeine in water due to guest exchange.

As another important property, manipulating molecular chirality has been attracting significant attention. Liu et al. synthesized several new chiral pillar [4]arene [1]quinone derivatives, which showed unique chiroptical properties. Notably, the benzene sidearm attached pillar [4]arene [1] quinone derivative exhibited solvent- and complexation-driven chirality switching.

Hemicucurbiturils are chiral macrocyclic hosts similar to the cucurbituril macrocycles and their monomeric units are connected by one row of methylene bridges. Ustrnul et al. systematically studied the complexation between cyclohexanohemicucurbit [n]urils and eighteen polar organic guests.

Metal-coordination is another important non-covalent interaction that is usually employed by supramolecular chemists to construct discrete entities including metallacycles (Chakrabarty et al., 2011) and metallacages, (Mal et al., 2009; Sun et al., 2010) as well as infinite architectures such as supramolecular polymers (Winter et al., 2016) (Winter and Schubert, 2016) and metal-organic frameworks (MOF) (Stock et al., 2012), (Stock and Biswas, 2012) etc. One particularly interesting application of supramolecular analytical methods is in the assessment of food freshness. As such, Lyu et al. developed a self-assembled colorimetric chemosensor array for the qualitative and quantitative detection of sulfur-containing amino acids. It is noteworthy that the sensor is based on the reversible coordination between off-the-shelf catechol dyes and Zn^{2+}, which offered obvious color changes in the presence of the analytes.

Helicates are another class of interesting metallo-supramolecular architecture that may have potential biological applications. Lisboa et al. and Lisboa et al. synthesized two new di (2,2′-bipyridine) ligands, which can self-assemble into specific metallo-supramolecular $[Fe_2(\mathbf{L})_3](BF_4)_4$ cylinders. Moreover, *in vitro* cytotoxicity assays showed that these helicates were active against several cancer cell lines.

Metal-organic cages (MOCs) also belong to metallo-supramolecular architectures and their cavities are capable of binding guest molecules. In a mini review, Diaz and Lewis focused on the structural flexibility in MOCs and summarized typical examples of MOCs reported in recent years.

Supramolecular polymers based on coordination interactions are polymeric arrays in which the building blocks are brought together *via* metal coordination. Mackenzie et al. synthesized a 1D coordination polymer consisting of silver(I) ions bound to a [2.2] paracyclophane scaffold. The coordination polymer was fully characterized by single crystal X-ray analysis and shows strong blue fluorescence.

MOFs provide an effective template for polymerization of polymers with precisely controlled structures within the nanochannels. Wonanke et al. explored the interaction of styrene and 3,4-ethylenedioxythiophene (EDOT) at the surface and in the nanopore of a Zn-MOF. They discovered that the monomer-MOF interaction is strongest inside the nanochannels and increases with the number of monomers.

Given the π-π interaction between large polycyclic aromatic hydrocarbon (PAH) molecules and fullerene, Gover et al. developed a new combined TEM and MALDI-TOF mass spectroscopic approach to detect different nano-architectures.

Hydrophobic interactions predictably drive amphiphiles to form nano-assemblies in water. Ranathunge et al. linked a hydrophobic dye TRPZ to a hydrophilic dendron *via* azide-alkyne Huisgen cycloaddition to prepare an amphiphilic system TRPZ-bisMPA, which can further form nanoparticles in aqueous media. The authors reported that TRPZ-bisMPA nanoparticles are of low cytotoxicity, hence being suitable for bioimaging.

In another work, Magna et al. developed a facile and rapid method to achieve chiral porphyrin films on a glass support. They systematically studied the solvent effect and glass substrate on the film formation.

In summary, this Research Topic has highlighted the most advanced and cutting-edge developments in supramolecular chemistry led by "Suprastars" from all over the world. By taking the advantage of dynamic supramolecular interactions, a series of functional self-assembled nano-architectures have successfully been constructed and been fully evaluated. More interestingly, the intersection of supramolecular chemistry and other disciplines has yielded new characterization methods and novel functional materials. We believe that more and more "Suprastars" in the field of supramolecular chemistry will emerge and as a result more and more impact rich research continue to evolve.

AUTHOR CONTRIBUTIONS

All authors listed have made a substantial, direct, and intellectual contribution to the work, and approved it for publication.

ACKNOWLEDGMENTS

We acknowledge financial support by the National Natural Science Foundation of China (No. 21702020, for TX), European Union's H2020-FETOPEN grant 828779 (INITIO) and Estonian Research Council grant PRG399 (for VB), the U.S. National Science Foundation (No. CHE-1904534, for RC). TJ wishes to thank the Royal Society for a Wolfson Research Merit Award and the Open Research Fund of the School of Chemistry and Chemical Engineering, Henan Normal University for support (No. 2020ZD01).

REFERENCES

Barrow, S. J., Kasera, S., Rowland, M. J., del Barrio, J., and Scherman, O. A. (2015). Cucurbituril-Based Molecular Recognition. *Chem. Rev.* 115, 12320–12406. doi:10.1021/acs.chemrev.5b00341

Böhmer, V. (1995). Calixarenes, Macrocycles with(Almost) Unlimited Possibilities. *Angew. Chem. Int. Ed. Engl.* 34, 713–745. doi:10.1002/anie.199507131

Chakrabarty, R., Mukherjee, P. S., and Stang, P. J. (2011). Supramolecular Coordination: Self-Assembly of Finite Two- and Three-Dimensional Ensembles. *Chem. Rev.* 111, 6810–6918. doi:10.1021/cr200077m

Chang, Y., Jiao, Y., Symons, H. E., Xu, J.-F., Faul, C. F. J., and Zhang, X. (2019). Molecular Engineering of Polymeric Supra-amphiphiles. *Chem. Soc. Rev.* 48, 989–1003. doi:10.1039/c8cs00806j

Chen, X., Huang, Z., Sala, R. L., McLean, A. M., Wu, G., Sokołowski, K., et al. (2022). On-Resin Recognition of Aromatic Oligopeptides and Proteins through

Host-Enhanced Heterodimerization. *J. Am. Chem. Soc.* 144, 8474–8479. doi:10.1021/jacs.2c02287

Datta, S., Saha, M. L., and Stang, P. J. (2018). Hierarchical Assemblies of Supramolecular Coordination Complexes. *Acc. Chem. Res.* 51, 2047–2063. doi:10.1021/acs.accounts.8b00233

Fagnani, D. E., Sotuyo, A., and Castellano, R. K. (2017). "π-π Interactions," in *Comprehensive Supramolecular Chemistry II*. Editor J. L. Atwood (Oxford: Elsevier), 121–148. doi:10.1016/b978-0-12-409547-2.12485-0

Fang, G., Yang, X., Chen, S., Wang, Q., Zhang, A., and Tang, B. (2022). Cyclodextrin-based Host-Guest Supramolecular Hydrogels for Local Drug Delivery. *Coord. Chem. Rev.* 454, 214352. doi:10.1016/j.ccr.2021.214352

Guo, D.-S., and Liu, Y. (2014). Supramolecular Chemistry of P-Sulfonatocalix[n]arenes and its Biological Applications. *Acc. Chem. Res.* 47, 1925–1934. doi:10.1021/ar500009g

Harada, A., Takashima, Y., and Nakahata, M. (2014). Supramolecular Polymeric Materials via Cyclodextrin-Guest Interactions. *Acc. Chem. Res.* 47, 2128–2140. doi:10.1021/ar500109h

Huang, Z., Chen, X., O'Neill, S. J. K., Wu, G., Whitaker, D. J., Li, J., et al. (2022). Highly Compressible Glass-like Supramolecular Polymer Networks. *Nat. Mat.* 21, 103–109. doi:10.1038/s41563-021-01124-x

Hunter, C. A., and Sanders, J. K. M. (1990). The Nature of .pi.-.Pi. Interactions. *J. Am. Chem. Soc.* 112, 5525–5534. doi:10.1021/ja00170a016

Lagona, J., Mukhopadhyay, P., Chakrabarti, S., and Isaacs, L. (2005). The Cucurbit[n]uril Family. *Angew. Chem. Int. Ed.* 44, 4844–4870. doi:10.1002/anie.200460675

Mahl, M., Niyas, M. A., Shoyama, K., and Würthner, F. (2022). Multilayer Stacks of Polycyclic Aromatic Hydrocarbons. *Nat. Chem.* 14, 457–462. doi:10.1038/s41557-021-00861-5

Mal, P., Breiner, B., Rissanen, K., and Nitschke, J. R. (2009). White Phosphorus Is Air-Stable within a Self-Assembled Tetrahedral Capsule. *Science* 324, 1697–1699. doi:10.1126/science.1175313

Masson, E., Ling, X., Joseph, R., Kyeremeh-Mensah, L., and Lu, X. (2012). Cucurbituril Chemistry: a Tale of Supramolecular Success. *RSC Adv.* 2, 1213–1247. doi:10.1039/C1RA00768H

McConnell, A. J., Wood, C. S., Neelakandan, P. P., and Nitschke, J. R. (2015). Stimuli-Responsive Metal-Ligand Assemblies. *Chem. Rev.* 115, 7729–7793. doi:10.1021/cr500632f

Murray, J., Kim, K., Ogoshi, T., Yao, W., and Gibb, B. C. (2017). The Aqueous Supramolecular Chemistry of Cucurbit[n]urils, Pillar[n]arenes and Deep-Cavity Cavitands. *Chem. Soc. Rev.* 46, 2479–2496. doi:10.1039/c7cs00095b

Ni, X.-L., Xiao, X., Cong, H., Zhu, Q.-J., Xue, S.-F., and Tao, Z. (2014). Self-Assemblies Based on the "Outer-Surface Interactions" of Cucurbit[n]urils: New Opportunities for Supramolecular Architectures and Materials. *Acc. Chem. Res.* 47, 1386–1395. doi:10.1021/ar5000133

Ogoshi, T., Kakuta, T., and Yamagishi, T. A. (2018). Applications of Pillar[N]arene-Based Supramolecular Assemblies. *Angew. Chem. Int. Ed.* 58, 2197–2206. doi:10.1002/anie.201805884

Pedersen, C. J. (1967). Cyclic Polyethers and Their Complexes with Metal Salts. *J. Am. Chem. Soc.* 89, 7017–7036. doi:10.1021/ja01002a035

Price, T. L., Jr., and Gibson, H. W. (2018). Supramolecular Pseudorotaxane Polymers from Biscryptands and Bisparaquats. *J. Am. Chem. Soc.* 140, 4455–4465. doi:10.1021/jacs.8b01480

Roy, I., Garci, A., Beldjoudi, Y., Young, R. M., Pe, D. J., Nguyen, M. T., et al. (2020). Host-Guest Complexation-Mediated Supramolecular Photon Upconversion. *J. Am. Chem. Soc.* 142, 16600–16609. doi:10.1021/jacs.0c05445

Shao, C., Stolte, M., and Würthner, F. (2013). Quadruple π Stack of Two Perylene Bisimide Tweezers: A Bimolecular Complex with Kinetic Stability. *Angew. Chem. Int. Ed.* 52, 7482–7486. doi:10.1002/anie.201302479

Stock, N., and Biswas, S. (2012). Synthesis of Metal-Organic Frameworks (MOFs): Routes to Various MOF Topologies, Morphologies, and Composites. *Chem. Rev.* 112, 933–969. doi:10.1021/cr200304e

Strutt, N. L., Zhang, H., Schneebeli, S. T., and Stoddart, J. F. (2014). Functionalizing Pillar[n]arenes. *Acc. Chem. Res.* 47, 2631–2642. doi:10.1021/ar500177d

Sun, Q.-F., Iwasa, J., Ogawa, D., Ishido, Y., Sato, S., Ozeki, T., et al. (2010). Self-Assembled M 24 L 48 Polyhedra and Their Sharp Structural Switch upon Subtle Ligand Variation. *Science* 328, 1144–1147. doi:10.1126/science.1188605

Szejtli, J. (1998). Introduction and General Overview of Cyclodextrin Chemistry. *Chem. Rev.* 98, 1743–1754. doi:10.1021/cr970022c

Wan, X., Li, S., Tian, Y., Xu, J., Shen, L.-C., Zuilhof, H., et al. (2022). Twisted Pentagonal Prisms: AgnL2 Metal-Organic Pillars. *Chem*. doi:10.1016/j.chempr.2022.04.001

Winter, A., and Schubert, U. S. (2016). Synthesis and Characterization of Metallo-Supramolecular Polymers. *Chem. Soc. Rev.* 45, 5311–5357. doi:10.1039/C6CS00182C

Xiao, T., Qi, L., Zhong, W., Lin, C., Wang, R., and Wang, L. (2019). Stimuli-responsive Nanocarriers Constructed from Pillar[n]arene-Based Supra-amphiphiles. *Mat. Chem. Front.* 3, 1973–1993. doi:10.1039/c9qm00428a

Xiao, T., Wang, J., Shen, Y., Bao, C., Li, Z.-Y., Sun, X.-Q., et al. (2021). Preparation of a Fixed-Tetraphenylethylene Motif Bridged Ditopic Benzo-21-Crown-7 and its Application for Constructing AIE Supramolecular Polymers. *Chin. Chem. Lett.* 32, 1377–1380. doi:10.1016/j.cclet.2020.10.0371001-8417

Xiao, T., Xu, L., Wang, J., Li, Z.-Y., Sun, X.-Q., and Wang, L. (2019). Biomimetic Folding of Small Organic Molecules Driven by Multiple Non-covalent Interactions. *Org. Chem. Front.* 6, 936–941. doi:10.1039/c9qo00089e

Xiao, T., Xu, L., Zhong, W., Zhou, L., Sun, X.-Q., Hu, X.-Y., et al. (2018). Advanced Functional Materials Constructed from Pillar[n]arenes. *Isr. J. Chem.* 58, 1183–1193. doi:10.1002/ijch.201800026

Xiao, T., Xu, L., Zhou, L., Sun, X.-Q., Lin, C., and Wang, L. (2019). Dynamic Hydrogels Mediated by Macrocyclic Host-Guest Interactions. *J. Mat. Chem. B* 7, 1526–1540. doi:10.1039/C8TB02339E

Xiao, T., Zhou, L., Xu, L., Zhong, W., Zhao, W., Sun, X.-Q., et al. (2019). Dynamic Materials Fabricated from Water Soluble Pillar[n]arenes Bearing Triethylene Oxide Groups. *Chin. Chem. Lett.* 30, 271–276. doi:10.1016/j.cclet.2018.05.039

Xue, M., Yang, Y., Chi, X., Zhang, Z., and Huang, F. (2012). Pillararenes, A New Class of Macrocycles for Supramolecular Chemistry. *Acc. Chem. Res.* 45, 1294–1308. doi:10.1021/ar2003418

Yu, G., Jie, K., and Huang, F. (2015). Supramolecular Amphiphiles Based on Host-Guest Molecular Recognition Motifs. *Chem. Rev.* 115, 7240–7303. doi:10.1021/cr5005315

Conflict of Interest: The authors declare that the research was conducted in the absence of any commercial or financial relationships that could be construed as a potential conflict of interest.

Publisher's Note: All claims expressed in this article are solely those of the authors and do not necessarily represent those of their affiliated organizations, or those of the publisher, the editors and the reviewers. Any product that may be evaluated in this article, or claim that may be made by its manufacturer, is not guaranteed or endorsed by the publisher.

frontiers in Chemistry

ORIGINAL RESEARCH
published: 14 June 2021
doi: 10.3389/fchem.2021.700562

Piecing Together Large Polycyclic Aromatic Hydrocarbons and Fullerenes: A Combined ChemTEM Imaging and MALDI-ToF Mass Spectrometry Approach

R. K. E. Gover[1], *T. W. Chamberlain*[1,2]*, *P. J. Sarre*[1]* and *A. N. Khlobystov*[1]*

[1]School of Chemistry, The University of Nottingham, Nottingham, United Kingdom, [2]Institute of Process Research and Development, School of Chemistry, University of Leeds, Leeds, United Kingdom

OPEN ACCESS

Edited by:
Tangxin Xiao,
Changzhou University, China

Reviewed by:
Zehuan Huang,
University of Cambridge,
United Kingdom
Subhamay Pramanik,
University of Kansas, United States

***Correspondence:**
T. W. Chamberlain
t.w.chamberlain@leeds.ac.uk
P. J. Sarre
peter.sarre1@nottingham.ac.uk
A. N. Khlobystov,
andrei.khlobystov@nottingham.ac.uk

Specialty section:
This article was submitted to Supramolecular Chemistry, a section of the journal Frontiers in Chemistry

Received: 26 April 2021
Accepted: 26 May 2021
Published: 14 June 2021

Citation:
Gover RKE, Chamberlain TW, Sarre PJ and Khlobystov AN (2021) Piecing Together Large Polycyclic Aromatic Hydrocarbons and Fullerenes: A Combined ChemTEM Imaging and MALDI-ToF Mass Spectrometry Approach. Front. Chem. 9:700562. doi: 10.3389/fchem.2021.700562

Motivated by their importance in chemistry, physics, astronomy and materials science, we investigate routes to the formation of large polycyclic aromatic hydrocarbon (PAH) molecules and the fullerene C_{60} from specific smaller PAH building blocks. The behaviour of selected PAH molecules under electron (using transmission electron microscopy, TEM) and laser irradiation is examined, where four specific PAHs—anthracene, pyrene, perylene and coronene—are assembling into larger structures and fullerenes. This contrasts with earlier TEM studies in which large graphene flakes were shown to transform into fullerenes *via* a top-down route. A new combined approach is presented in which spectrometric and microscopic experimental techniques exploit the stabilisation of adsorbed molecules through supramolecular interactions with a graphene substrate and enable the molecules to be characterised and irradiated sequentially. Thereby allowing initiation of transformation and characterisation of the resultant species by both mass spectrometry and direct-space imaging. We investigate the types of large PAH molecule that can form from smaller PAHs, and discuss the potential of a "bottom-up" followed by "top-down" mechanism for forming C_{60}.

Keywords: PAH, fullerene, chemTEM, self-assembly, bottom-up

INTRODUCTION

There is widespread interest in planar aromatic and fullerenic carbon macromolecules, and in transformations between these molecular forms. The significance of these structures extends across organic, environmental, combustion, biomedical and materials chemistry, and, particularly in the context of this paper, carbon quantum dots (Tian et al., 2018; Yan et al., 2019; Semeniuk et al., 2019), and the chemistry and physics of these molecules in astronomy (Tielens, 2013). Polycyclic aromatic hydrocarbon (PAH) molecules were first suggested to be of importance in an astronomical context by Donn (1968) and are now known to be present in numerous astrophysical environments (Tielens, 2008; Tielens, 2013). The C_{60} molecule, discovered serendipitously in experiments motivated by astronomical questions (Kroto et al., 1985), has been found in a wide range of astronomical sources from planetary nebulae to young stellar objects and the interstellar medium (see references in Roberts et al., 2012; Berné et al., 2015a; Berné et al., 2015b; Maier and Campbell, 2016; Linnartz et al., 2020).

In this paper we report electron- and photon-promoted self-assembly experiments in which small planar aromatic molecules ranging in size from anthracene ($C_{14}H_{10}$) to coronene ($C_{24}H_{12}$), adsorbed on a graphitic surface, are exposed to an electron beam or laser radiation, in which chemical evolution to form larger PAHs and C_{60} is probed by transmission electron microscopy and mass spectrometry. We first briefly review "top-down" and "bottom-up" supramolecular pathways to carbon macromolecule formation.

In respect of "top-down" formation, high-resolution TEM has revealed that nm-sized flakes of graphene can transform into C_{60} as a result of high energy electron beam (e-beam) irradiation (Chuvilin et al., 2010). This occurs through loss of carbon atoms from the graphene edge, resulting in the formation of pentagons which is considered to be an essential step in folding the planar structure to form a fullerene cage. The mechanism proposed included calculated energies of the required intermediates and revealed stability of the fullerene structure to be the overall driving force in the formation process (Chuvilin et al., 2010). Comparison between the TEM results and conditions in the interstellar medium led to a proposed "top-down" C_{60} formation mechanism involving UV photo-processing of large PAH molecules, which are known to be ubiquitous in space (Berné and Tielens, 2012; Tielens, 2008). The "top-down" mechanism in this case involves UV-photolysis-initiated dehydrogenation of PAHs containing approximately 70 carbon atoms to form small graphene flakes (Goroff, 1996), loss of a carbon atom, followed by pentagon formation within the structure. This has been explored theoretically in a study carried out to calculate IR spectra of intermediates in the fullerene formation process to make comparison with IR interstellar emission features (Galué, 2014). This top-down model is supported by laboratory studies that have revealed photofragmentation patterns of large PAHs (>60C atoms) which are consistent with the formation of C_{60} (Zhen et al., 2014). Recent modelling of the conversion of circumovalene ($C_{66}H_{20}$) to C_{60} suggests that only PAH molecules with between 60 and 66 carbon atoms may be of practical significance for the formation of C_{60} in the NGC 7023 nebula due to the extended timescale required for loss of C_2 units in the shrinking of larger structures (Berné et al., 2015a).

The "bottom-up" formation of large PAHs/quantum dots and C_{60} from smaller molecular precursors has received increasing attention recently from both terrestrial and astronomical perspectives through both gas and surface reactions. For generation of large PAHs on non-metallic surfaces, approaches include thermal fusion of coronene (Talyzin et al., 2011) and pentacene (Ishii et al., 2011), soft X-ray irradiation of pentacene (Heya et al., 2020), and oligomerization of dehydrogenated PAHs deposited as cations from the gas phase (Weippert et al., 2020). In respect of fullerene formation, this route is supported by experimental observation of C_{60} formation during the pyrolysis of PAHs (Taylor et al., 1993; Osterodt et al., 1996), laser pyrolysis of hydrocarbons (Ehbrecht et al., 1993; Armand et al., 1997) and laser desorption ionisation (LDI) of triphenylene in an experiment that combines LDI with ion-mobility mass spectrometry (Han et al., 2016). Gas-phase formation of large PAHs includes conversion of ionic pyrene clusters under laser irradiation (Zhen et al., 2018), and pyrene-dicoronylene and hexabenzocoronene-anthracene equivalents (Zhen 2019; Zhen et al., 2019). Separately, isolable quantities of C_{60} have been synthesized in 12 steps from commercially available starting materials, finally proceeding via a molecular polycyclic aromatic chlorine substituents at key positions which forms C_{60} when subjected to flash vacuum pyrolysis at 1,100°C (Scott et al., 2002).

In this work we investigate the fate of small PAHs under experimental laboratory conditions in which C-H bonds are broken photochemically or by electron impact; ionisation of the samples may also occur. Our approach builds on the previously reported ChemTEM methodology of encapsulating molecules in nanosized carbon test tubes and simultaneously initiating and interrogating molecular reactions using a beam of electrons as a local-probe/local-stimulus simultaneously (Skowron et al., 2017). Herein, we explore a low-dimensional material, graphene sheets, as a nano-sized petri dish, to connect PAH molecules with the macroworld, i.e., hold them in place on the TEM grid (Markevich et al., 2015; Mirzayev et al., 2017), and utilise both local (e-beam) and macro-probes (a beam of photons) to investigate the chemistry of PAHs. PAHs have affinity for graphene (Björk et al., 2010; Dappe et al., 2015) and readily form stable supramolecular complexes (e.g., PAHs adsorbed on graphene by π - π interactions), which allows us to study the molecules both by TEM and by matrix-assisted laser desorption/ionisation time-of-flight mass spectrometry (MALDI-TOF MS). This combined approach enables the correlation of data from the local-probe and bulk-probe analysis methods for the first time, and reveals important aspects of the molecular polycondensation process, including intermediate species, and determine mechanistic details linking specific molecular precursors with formation of large PAHs and C_{60}. In addition, our new methodology was designed and implemented to utilise both of the aforementioned experimental techniques to enable characterisation of species and initiation of reactions within an identical location of a sample, so that transformation processes and molecular speciation could be carried out at each step of the experiment.

RESULTS AND DISCUSSION

Electron-Beam Irradiation of PAHs

TEM is a useful tool for probing transformations of carbon species with a vacuum chamber pressure of approx. 10^{-12} mbar and high-energy electrons to initiate transformations. It has been shown by Chuvilin et al. that under these conditions graphene flakes can undergo transformations that result in the formation of fullerene molecules (Chuvilin et al., 2010). However, in our study irradiation by the electron beam of TEM was carried out on discrete PAH molecules, rather than non-uniform flakes of graphene, in order to initiate and monitor transformations of these molecules, and hence to elucidate the processes, including fullerene formation, that occur. In these experiments, the

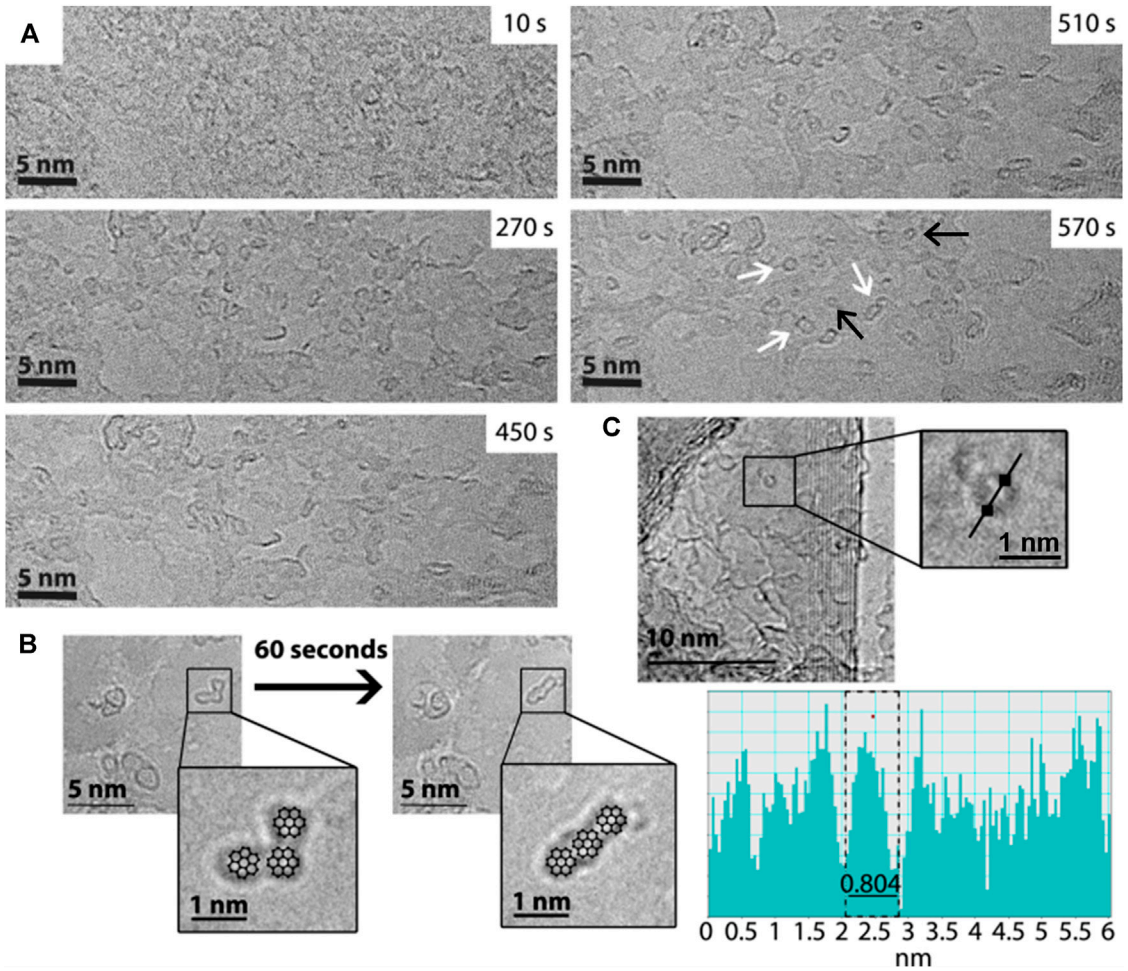

FIGURE 1 | (A) HRTEM time series of images showing the transformation from a spatially undefined starting sample of perylene (at 10 s) to well-defined "islands" or oligomers (570 s) and fullerene structures adsorbed on surface of graphite support. White arrows indicate examples of newly formed, stable oligomers and black arrows show fullerene structures. **(B)** HRTEM images showing the evolution of PAH oligomers, resulting from the irradiation of coronene over a time period of ~60 s. As a guide; coronene structures are overlaid the micrographs in the zoomed-in inserts. **(C)** HRTEM showing an example of fullerene structure (see zoomed-in region), formed as a result of prolonged irradiation of coronene, alongside a line profile plot showing the structure to have a diameter comparable to C_{60} (0.8 ± 0.1 nm).

electrons can transfer sufficient energy to remove hydrogen atoms from PAHs (Chamberlain et al., 2015) and promote rearrangement of carbon atoms, while imaging these induced transformations as they are occurring.

A full description of all experimental procedures and materials is provided in the **Supplementary Material**. TEM was carried out on the PAH molecules anthracene, pyrene, perylene and coronene. These molecules were supported on few-layers graphene—to dissipate any ionisation and heating effects caused by the e-beam—and then irradiated by the e-beam in TEM for approximately 30 min, with images taken periodically at intervals of 1.5 min (on average). Under these conditions, chemical transformations are driven by the momentum of the fast electrons which is transferred directly to the atoms within the molecules (**Supplementary Material**). All experiments were performed using a 100 keV e-beam and a dose rate of approximately 10^9 $e^- nm^{-2} s^{-1}$, under which conditions the knock-on damage experienced by the PAH molecules leads predominantly to ejection of their hydrogen atoms (Chamberlain et al., 2015). The PAH molecules are left with very reactive carbon radical sites at their edges; these react quickly via dimerisation or cross-coupling reactions, to create new C-C bonds, culminating in the formation of PAH "oligomers." These can be thought of either as larger PAH molecules, or as small graphene-like flakes (sp^2 islands). The formation of oligomeric species is seen to occur for all four PAH samples (see **Supplementary Material** for a complete set of time series images for each PAH, and videos), with the example of perylene being given in **Figure 1A**. In this figure, the initial frame of the time series shows no defined structures, whereas in the final frame well-defined shapes with dark, high-contrast edges can be seen, indicating the formation of discrete new molecular species on the carbon surface. These species increase in size over the duration of the experiment (**Supplementary Table S1**),

suggesting addition to, rather than fragmentation of, the original molecule; hence, this supports the idea of growth and formation of PAH aggregates and "oligomers." The influence of the e-beam on the molecules and oligomers is seen due to the changes in the shapes of the structures that are observed. This is demonstrated in **Figure 1B**, which shows the example of coronene under the e-beam, and the change in shape of one of these structures over time. For illustrative purposes the structures of a number of coronene molecules are depicted over the TEM micrograph; in this way shapes seen in the micrograph can more easily be visualised as individual molecules or oligomers. After prolonged e-beam irradiation examples are seen in which the more circular PAH oligomers appear to have "rolled" up to form fullerene-type structures, in a manner similar to the process described by Chuvilin et al. (2010). We propose that under the conditions of our experiments the structure of the PAH oligomer is crucial as to whether it can be transformed into C_{60} over time, for example conversion of the collinear coronene species shown in **Figure 1B** to C_{60} would involve a large number of C-C bond breaking events and thus is unlikely to occur (see **Supplementary Section S6** for full details). **Figure 1C** shows an example of a fullerene structure formed during the e-beam exposure of coronene. This has a measured diameter of ~0.8 nm, which is comparable to the diameter of C_{60} (c.f. the crystallographic diameter of C_{60} = 0.71 nm, see Liu et al., 1991). Similar fullerene structures are also observed for perylene, as highlighted in **Figure 1A**, **Supplementary Figure S3**. It is important to note that irradiation of control samples in which blank graphite substrates were present showed no evidence of the formation of PAH oligomers or C_{60} (see **Supplementary Material** for details).

The PAH oligomers formed as a result of these transformations are found to be stable, as demonstrated by their long lifetime under the e-beam. There are a number of published examples in which PAH molecules are seen to polymerize in this way under the electron beam in TEM experiments (Talyzin et al., 2011; Fujihara et al., 2012; Botka et al., 2014). For example, the commonly seen transformation of coronene to dicoronylene can happen on the coming together of two coronene molecules, having ejected one or more hydrogen atoms, with the driving force being the formation of a new stable, six-membered ring between the two, and the overall conservation of planarity and aromaticity in the final molecule. In this way, it can be seen how bottom-up construction of larger PAHs, or PAH oligomers, can be a facile process under these irradiation conditions.

UV Irradiation of PAHs

Many of the transformations likely to occur in the ISM are initiated by the irradiation of molecules with UV photons or high-energy cosmic rays. Hence, the photo-processing of PAHs, with a focus on fullerene formation, was investigated using a source of UV photons. MALDI-TOF MS is traditionally used to characterize molecules and identify molecular structures and causes little damage to the sample as it uses low UV laser fluence to vaporize and ionise the molecular species. However,

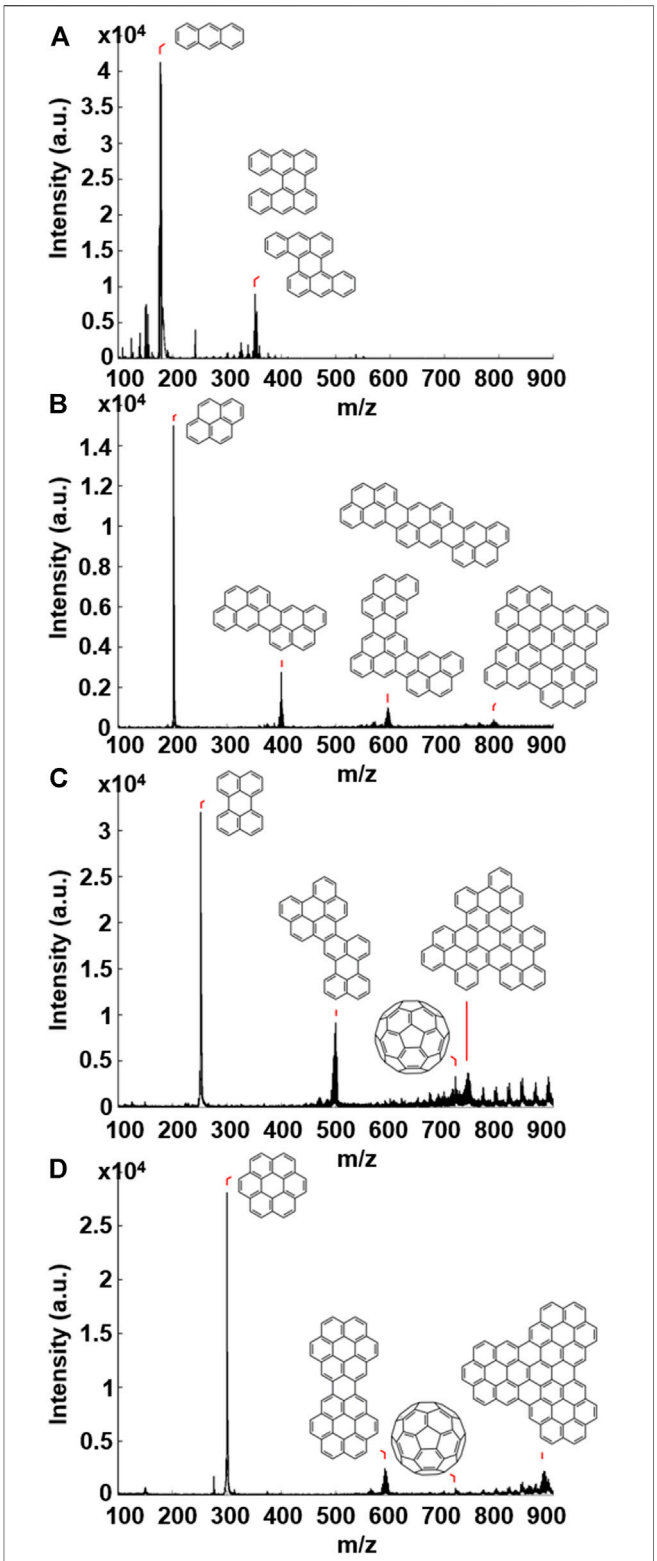

FIGURE 2 | Mass spectra resulting from UV laser irradiation at high laser fluence (~2,600 mW cm^{-2}) of; **(A)** anthracene, **(B)** pyrene, **(C)** perylene and **(D)** coronene. Proposed structures of the species present are illustrated above the corresponding m/z peaks.

if the fluence of the UV laser is increased, it can be used as a source of UV photons which are capable of initiating transformations within a sample. UV irradiation of pyrene was carried out for a range of values of laser fluence; at low laser fluence the mass peak for pyrene (m/z = 202) dominates, whereas at higher fluence heavier molecules form and are detected (for mass spectra see **Supplementary Figure S5**).

A thin layer of each of the four PAH samples was drop-cast onto a stainless steel sample holder, inserted into the vacuum chamber (10^{-7} mbar) and irradiated using the Nd:YAG laser (355 nm, 5 ns) of the MALDI-TOF mass spectrometer. The laser fluence was varied between ~2,000 and ~2,600 mW cm^{-2}, which equates to a "dose rate" (comparable to that of the e-beam in TEM) of ~34,000–~44,000 hν nm^{-2} s^{-1} (see **Supplementary Material** for full details). In each case, experiments carried out at low laser fluence showed the presence of the corresponding molecular ion peaks only, indicating simply that the PAH molecules were being vaporised and ionised, as in the example of pyrene described above. At higher laser fluence the resultant mass spectra revealed the formation of larger structures; major peaks are seen at two or three times the mass of the individual PAH, minus a number of mass units. These are assigned to PAH oligomer structures formed through C-C bond formation following the loss of hydrogen atoms; this hydrogen atom loss accounts for the unit mass deficit that is observed. Similar irradiation-induced formation of PAH oligomers, specifically from coronene to form larger coronene oligomers, has been reported (Joblin et al., 1997). **Figure 2** shows the resultant mass spectra following high laser fluence (~2,600 mW cm^{-2}) irradiation of **(A)** anthracene, **(B)** pyrene, **(C)** perylene and **(D)** coronene, and includes proposed structures of the oligomers formed above their corresponding mass peaks. Descriptions and m/z values of the PAH molecules and oligomers are given in **Supplementary Table S2**. The formation of oligomeric PAH structures under these conditions is expected to occur due to the loss of hydrogen atoms on the periphery of the PAH. This is similar to the process when the sample is irradiated under the e-beam of TEM; the loss of a hydrogen atom results in the formation of a reactive carbon radical, which can react with a neighbouring molecule to form a new C-C bond. It is important to note that a MALDI-TOF experiment with a blank graphite substrate showed no evidence of the formation of PAH oligomers or C_{60} (**Supplementary Material** for details).

In addition to the formation of PAH oligomers, irradiation of coronene and perylene also resulted in a distinctive signal at 720 m/z (**Figure 2**), corresponding to the fullerene C_{60}. The formation of C_{60} from the irradiation of PAHs is important in relation to the question of C_{60} formation in astrophysical environments, since, while not altogether surprising considering the experimental conditions under which the molecule was discovered, this is a clear transformation solely from PAH precursors of defined initial structure. The results of this paper show, as demonstrated by mass spectrometric measurements and direct-space imaging, that fullerenes are able to form from PAHs under both UV and e-beam irradiation.

Fullerene Formation

As the PAHs investigated here have fewer than sixty carbon atoms, and considering the facile formation of PAH oligomers, it is probable that C_{60} formation occurs as a result of shrinking, via the ejection of C_2 units and hydrogen atoms, of PAH oligomers that contain at least sixty carbon atoms. An astrophysical "bottom-up" followed by "top-down" mechanism can therefore be envisaged, involving the aggregation of the initial PAH molecules to form oligomers, followed by ejection of a number of atoms and rearrangement of bonds to produce the stable fullerene structure. With this in mind, the mass spectrum peaks corresponding to ≥60 C atom oligomers of perylene and coronene were examined more closely in order to determine the precise masses and probable structures of these molecules, and to elucidate the products of intermediate mechanistic steps.

Figure 3 shows the mass spectrum resulting from the MALDI-TOF MS irradiation of perylene, in addition to proposed mechanistic steps involved in the formation of C_{60}. A corresponding figure, and discussion, involving coronene is given in the (**Supplementary Figure S14**). The mass spectrum of **Figure 3** shows a distribution of peaks that are separated by two mass units, of which the largest peak falls at m/z = 744. This peak is assigned to the perylene trimer, labelled **1** in **Figure 3**. N.B. Less compact, "linear" trimer species were also considered as candidates but no conceivable structure matched the molecular masses observed in the MS. Proposed structures responsible for additional peaks in the distribution (m/z = 742, 740, and 738) are labelled **2**, **3** and **4** respectively. These structures result from the loss of two hydrogen atoms, at so-called "fjord" positions in the oligomers, followed by the formation of a new C-C bond, driven by the instability of the carbon radicals that result from the initial hydrogen loss. This process provides a route for the formation of a pentagon at that position, which is a significant step as it introduces curvature into the previously planar molecule; this has been discussed by Mackie et al. (Mackie et al., 2015) for dehydrogenated PAHs in an astrophysical context.

The final mechanistic steps in **Figure 3** show examples of the H atom loss, C-C bond formation, and rearrangement processes that lead to the fullerene molecule. Molecule **4** has no remaining "fjord" positions in the structure; however, if H atom loss occurred at the "bay" positions indicated in the figure, subsequent C-C bond formation would result in the creation of a strained four-membered ring. To stabilise this, a C-C bond has been highlighted that could undergo a Stone-Wales rearrangement (Stone and Wales, 1986) resulting in the formation of the structure labelled **5**. From there, there are two additional positions at which this H-loss, C-C bond formation and Stone-Wales rearrangement sequence can occur. The result of completing these steps at both positions is structure **6**. Between **6** and **7**, three potential Stone-Wales rearrangements are highlighted, the results of which would yield a structure that contains only five- and six-membered rings and with a curved shape which can then "zip-up" to form a fullerene molecule (**8**).

The mechanistic steps proposed here may not be exact, nor can the precise order of steps be determined, especially within the suggested H-loss, C-C bond formation and Stone-Wales

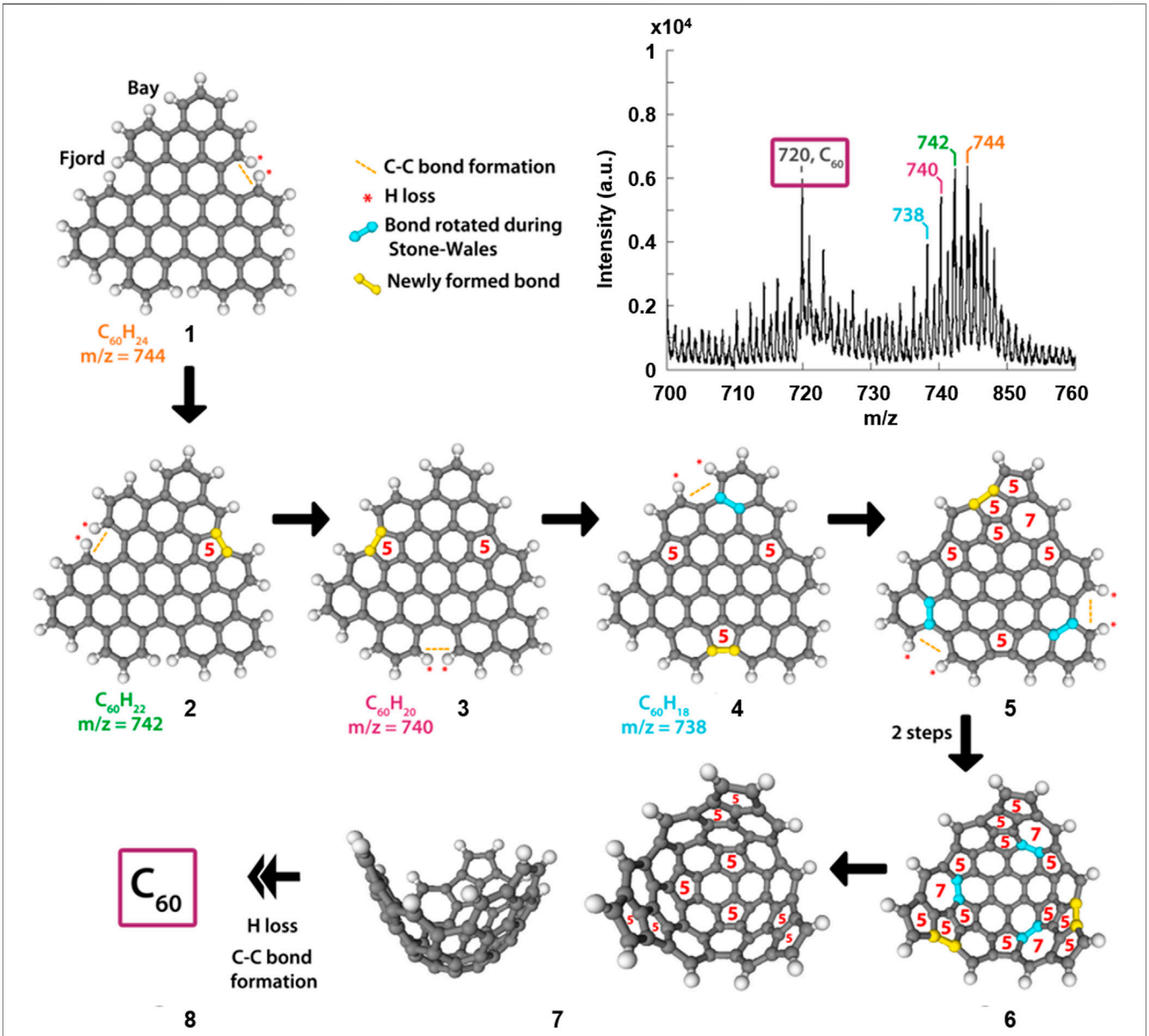

FIGURE 3 | Section of the mass spectrum (**Figure 2C**) resulting from UV irradiation of perylene (top) and our proposed mechanistic steps based on the MALDI-TOF data and chemical intuition, showing the transformation from the perylene trimer to C_{60}. The ring sizes of key parts in the structures are shown in red, and the rotated bonds and newly formed bonds are highlighted in blue and yellow respectively.

rearrangement sequence that occurs a number of times. However, support for steps of this nature is given through the evidence seen in the detection of species by mass spectrometry. It is certainly the case that C_{60} is an extremely stable molecule, due to its lack of edges, and as such it is feasible that the loss of one or more hydrogen atoms from the edge of a PAH oligomer, and the subsequent bond formations and rearrangements, would initiate a thermodynamically driven process of which the end result is the most stable molecule, under the irradiation conditions, i.e., a fullerene.

The fact that C_{60} forms only in the case of coronene and perylene is noteworthy, and suggests a dependence on the structure of the initial PAH, or of the oligomers that are formed. An analogous result was obtained for triphenylene by Han et al. (2016) though their mechanistic interpretation differs and is focused on the "zipper" mechanism involving the rapid, concerted formation of 12 pentagon rings in one step between two overlying PAHs as advanced by Homann and co-authors. The "zipper" mechanism is based principally on topological considerations and mass spectrometric observations of hydrocarbon rich, sooting flames (Baum et al., 1992; Ahrens et al., 1994). However, such a mechanism does not explain our MS observations which reveal intermediate, discrete PAH oligomers which sequentially lose pairs of H atoms in individual steps. This could potentially be due to the

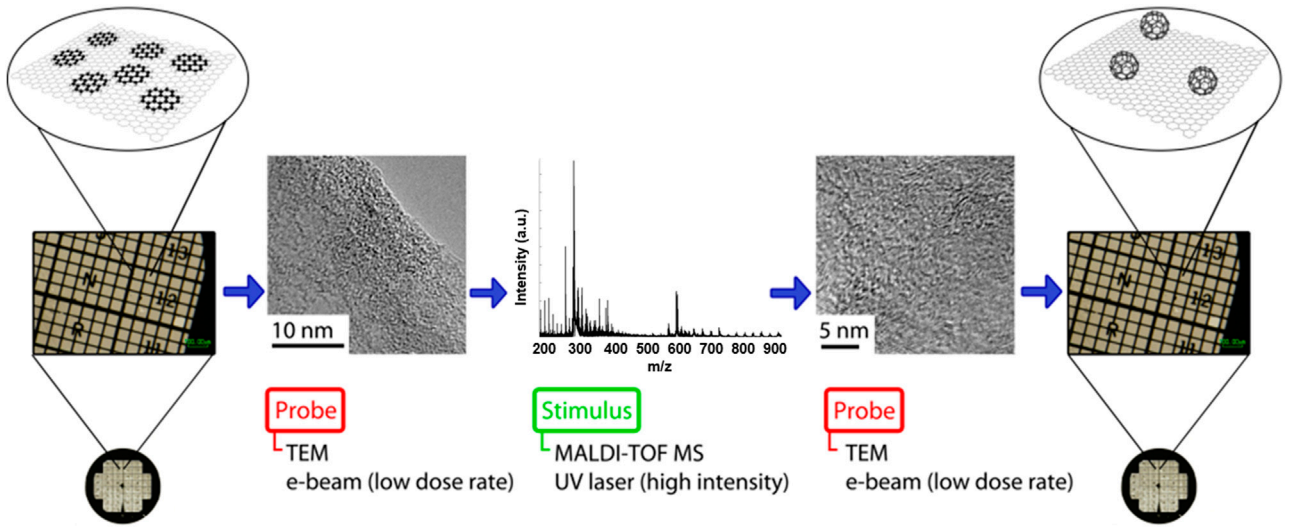

FIGURE 4 | Schematic illustration of the "probe-stimulus-probe" format in which an area of coronene deposited on a TEM grid is characterized using low-dose TEM, and then irradiated using the UV laser of MALDI-TOF MS to initiate transformations within the sample. Finally, the irradiated area is characterized again, using the locators on a TEM finder grid, to view the results of the induced transformations and determine the nature of any products formed.

nature of the energy source in our experiments, with the use of electrons or UV photons resulting in a much more stepwise mechanism compared to a thermally driven processes.

In both mechanisms the ability to form pentagons appears to be a key aspect in the propensity of a PAH to form C_{60}. However, pentagon formation could also in principle occur for oligomers of anthracene and pyrene, and not only for coronene and perylene. In the case of anthracene, the highest mass oligomer that is detected following irradiation corresponds to $C_{28}H_{16}$, and if no oligomers with more than sixty carbon atoms are formed, then they cannot "shrink" to form the fullerene molecule. Pyrene, however, forms an oligomer that is detected in MS and is assigned to $C_{64}H_{22}$ (m/z = 790), so it appears that another structural aspect is important. The lack of C_{60} formation could be due to the "compactness" of the PAH oligomer following the "bottom-up" stage of the process, or it could be related to the symmetry of the oligomer; both perylene and coronene trimers have a C_3 axis of rotation perpendicular to the plane of the molecule, whereas the pyrene tetramer has a C_2 axis of rotation in this position. Interestingly, experiments in which an equimolar mixture of pyrene and coronene are irradiated reveal the formation of both discrete PAH oligomers consisting of fragments of both species and C_{60} implying the structure of the PAHs is important, see **Supplementary Material** for full details.

Combined Transmission Electron Microscopy and MALDI-TOF MS Experiments

An experimental methodology was designed to initiate and characterize PAH transformations sequentially in order to

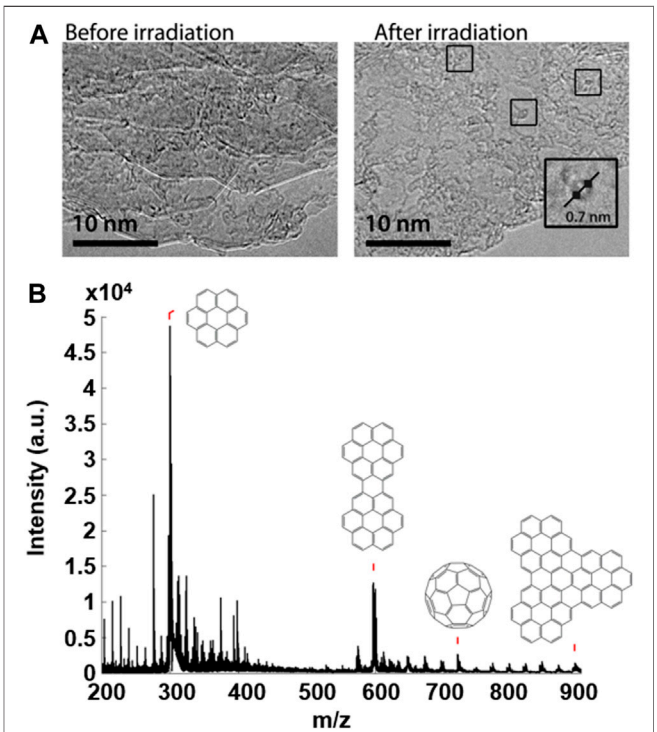

FIGURE 5 | TEM micrographs **(A)** of a sample of coronene before and after laser irradiation using MALDI-TOF MS. Boxes highlight fullerene structures seen following laser irradiation along with a magnified example illustrating the diameter of the structure (0.7 ± 0.1 nm). The mass spectrum resulting from the UV irradiation of the sample **(B)** shows the oligomer structures assigned to major peaks, along with the detection of C_{60}.

confirm the resultant products using both microscopy and mass spectrometry. **Figure 4** shows a schematic illustration detailing the steps involved in this "probe-stimulus-probe" arrangement.

A sample of coronene was supported on a graphite flake, deposited on a TEM finder grid and imaged by TEM using a low dose (~10^6 e^- nm^{-2} s^{-1}) of electrons and minimal exposure time to avoid transformations induced by the e-beam. The PAH sample on the grid was then irradiated with the UV laser in MALDI-TOF MS at high laser fluence (~2,600 mW cm^{-2}); the resultant mass spectrum showed coronene oligomers and C_{60}. Finally, the irradiated area of the sample was reanalysed using low dose TEM to assess the effect of the UV laser irradiation. TEM micrographs obtained within the UV irradiated area of the sample reveal the formation of a number of fullerene structures not observed prior to UV irradiation. **Figure 5** shows the results of this experiment, and includes the TEM micrographs obtained before and after the high laser fluence irradiation of the coronene sample, along with the mass spectrum acquired as a result of the MALDI-TOF MS (middle) part of the experiment. In addition, the sample showed far greater stability under the e-beam following UV irradiation, with structures appearing relatively static and less susceptible to e-beam-induced transformations. This indicates that the fullerene structures seen in the "after" image are in fact fullerene cages, and not remaining PAH molecules of the same diameter; if this were the case then the same sequence of peripheral hydrogen loss leading to formation of higher mass oligomers would be seen.

This experimental format can in principle be reversed, so that low laser fluence MALDI-TOF MS is used as the initial "probe," to characterize the sample before and after irradiation, and high dose TEM is used to initiate transformations within the sample. Experiments of this type are not presented here, however, due to difficulties regarding the difference in the size of the irradiated area in TEM and MALDI-TOF MS.

CONCLUSION

The existence of PAHs and fullerenes in the ISM is well established, but transformation mechanisms linking these molecules are not well understood. In this study we have demonstrated that under harsh laboratory conditions (UV laser or e-beam irradiation), medium-sized PAHs do not disintegrate, but assemble into larger carbon structures via the loss of hydrogen atoms and the condensation of reactive radical species into larger aromatic molecules with ≥60 C atoms. These undergo transformations, forming closed carbon cages — fullerenes — which are thermodynamically the most stable form of carbon at the nanoscale.

Detailed study of the molecular species in MS has shed light on mechanisms of PAH conversion to C_{60}. Mechanistic steps are proposed in which the initial irradiation-induced loss of hydrogen atoms leads, via carbon radical-containing species which react with neighbouring molecules, to the formation of large planar oligomers. A second "top-down" step involves H atom loss, C-C bond formation, and rearrangements such as Stone-Wales within the planar oligomers which promote the formation of pentagonal rings, and the subsequent rolling up of the structure to form fullerene cages. Notably, for the cases considered here, high-energy ejection of a carbon atom is not required to form a pentagonal ring as is the case for zig-zag-edged graphene (Chuvilin et al., 2010).

An experimental strategy developed in this study enabled the use of MALDI-TOF MS and TEM as triggers of PAH transformations at high dose rates of UV laser or e-beam, or as analytical tools—monitoring molecular weights in MS or molecular size in TEM imagery, respectively. The cross correlation of microscopy and mass spectrometry measurements, performed here for the first time, reveals that PAHs grown from coronene and perylene undergo major transformations leading to the formation of C_{60} fullerenes while pyrene and anthracene under the same conditions form large oligomers but no fullerenes.

Our laboratory observations indicate that high-energy radiation (UV or fast electrons) triggers chemical transformations in PAHs similar to those proposed under interstellar conditions, and therefore this work provides significant support for the hypothesis that PAH molecules can be precursors to fullerene formation in the ISM. Detailed, step-by-step mechanisms have been proposed that reveal the nature of key intermediate steps within the fullerene formation process from large PAH molecules, and these reflect examples of the mechanistic steps that may be expected in the formation of C_{60} in interstellar environments.

DATA AVAILABILITY STATEMENT

The raw data supporting the conclusion of this article will be made available by the authors, without undue reservation.

AUTHOR CONTRIBUTIONS

All authors were responsible for writing the manuscript. TC, AK, and PS conceived and developed the idea, RG performed the experiments and wrote the first draft of the paper. AK performed the TEM. TC and AK helped interpret the data. PS helped relate the observed behaviour to observations in the ISM.

ACKNOWLEDGMENTS

RG thanks EPSRC and The University of Nottingham for financial support and PS thanks the Leverhulme Trust for award of a Leverhulme Emeritus Fellowship. AK thanks ERC for a Consolidator Grant. We thank the Nanoscale and Microscale Research Centre (nmRC) University of Nottingham for the use of TEM.

SUPPLEMENTARY MATERIAL

The Supplementary Material for this article can be found online at: https://www.frontiersin.org/articles/10.3389/fchem.2021.700562/full#supplementary-material

REFERENCES

Ahrens, J., Bachmann, M., Baum, T., Griesheimer, J., Kovacs, R., Weilmünster, P., et al. (1994). Fullerenes and Their Ions in Hydrocarbon Flames. *Int. J. Mass Spectrom. Ion Process.* 138, 133–148. doi:10.1016/0168-1176(94)04036-2

Armand, X., Herlin, N., Voicu, I., and Cauchetier, M. (1997). Fullerene Synthesis by Laser Pyrolysis of Hydrocarbons. *J. Phys. Chem. Sol.* 58, 1853–1859. doi:10.1016/S0022-3697(97)00092-9

Baum, T., Löffler, S., Löffler, P., Weilmünster, P., and Homann, K.-H. (1992). Fullerene Ions and Their Relation to PAH and Soot in Low-Pressure Hydrocarbon Flames. *Berichte der Bunsengesellschaft für physikalische Chem.* 96, 841–857. doi:10.1002/bbpc.19920960702

Berné, O., Montillaud, J., and Joblin, C. (2015a). Top-down Formation of Fullerenes in the Interstellar Medium. *A&A* 577, A133–A141. doi:10.1051/0004-6361/201425338

Berné, O., Montillaud, J., Mulas, G., and Joblin, C. (2015b). "30 Years of Cosmic Fullerenes," in Proceedings of the Annual Meeting of the French Society of Astronomy and Astrophysics (SF2A 2015), Toulouse, June 2–5, 2015. Editors Boissier, V. Buat, L. Cambrésy, F. Martins, and P. Petit, 65–70. arXiv:1510.01642.

Berné, O., and Tielens, A. G. G. M. (2012). Formation of Buckminsterfullerene (C60) in Interstellar Space. *Proc. Natl. Acad. Sci.* 109, 401–406. doi:10.1073/pnas.1114207108

Björk, J., Hanke, F., Palma, C.-A., Samori, P., Cecchini, M., and Persson, M. (2010). Adsorption of Aromatic and Anti-aromatic Systems on Graphene through π−π Stacking. *J. Phys. Chem. Lett.* 1 (23), 3407–3412. doi:10.1021/jz101360k

Botka, B., Füstös, M. E., Tóháti, H. M., Németh, K., Klupp, G., Szekrényes, Z., et al. (2014). Interactions and Chemical Transformations of Coronene inside and outside Carbon Nanotubes. *Small* 10, 1369–1378. doi:10.1002/smll.201302613

Chamberlain, T. W., Biskupek, J., Skowron, S. T., Bayliss, P. A., Bichoutskaia, E., Kaiser, U., et al. (2015). Isotope Substitution Extends the Lifetime of Organic Molecules in Transmission Electron Microscopy. *Small* 11, 622–629. doi:10.1002/smll.201402081

Chuvilin, A., Kaiser, U., Bichoutskaia, E., Besley, N. A., and Khlobystov, A. N. (2010). Direct Transformation of Graphene to Fullerene. *Nat. Chem* 2, 450–453. doi:10.1038/nchem.644

Dappe, Y. J., Andersen, M., Balog, R., Hornekær, L., and Bouju, X. (2015). Adsorption and STM Imaging of Polycyclic Aromatic Hydrocarbons on Graphene. *Phys. Rev. B* 91, 045427. doi:10.1103/physrevb.91.045427

Donn, B. (1968). Polycyclic Hydrocarbons, Platt Particles, and Interstellar Extinction. *ApJ* 152, L129–L133. doi:10.1086/180196

Ehbrecht, M., Faerber, M., Rohmund, F., Smirnov, V. V., Stelmakh, O., and Huisken, F. (1993). CO2-laser-driven Production of Carbon Clusters and Fullerenes from the Gas Phase. *Chem. Phys. Lett.* 214, 34–38. doi:10.1016/0009-2614(93)85451-S

Fujihara, M., Miyata, Y., Kitaura, R., Nishimura, Y., Camacho, C., Irle, S., et al. (2012). Dimerization-Initiated Preferential Formation of Coronene-Based Graphene Nanoribbons in Carbon Nanotubes. *J. Phys. Chem. C* 116, 15141–15145. doi:10.1021/jp3037268

Galué, H. Á. (2014). Decoding the Infrared Signatures of Pyramidal Carbons in Graphenic Molecular Nanostructures of Interstellar Origin. *Chem. Sci.* 5, 2667–2676. doi:10.1039/c4sc00890a

Goroff, N. S. (1996). Mechanism of Fullerene Formation. *Acc. Chem. Res.* 29, 77–83. doi:10.1021/ar950162d

Han, J. Y., Choi, T. S., Kim, S., Lee, J. W., Ha, Y., Jeong, K. S., et al. (2016). Probing Distinct Fullerene Formation Processes from Carbon Precursors of Different Sizes and Structures. *Anal. Chem.* 88, 8232–8238. doi:10.1021/acs.analchem.6b02076

Heya, A., Oonuki, T., Utimi, R., Kanda, K., Yamasaki, R., and Sumitomo, K. (2020). Graphene Synthesis from Pentacene by Soft X-ray Irradiation. *Thin Solid Films* 713, 138365–138410. doi:10.1016/j.tsf.2020.138365

Ishii, Y., Sakashita, T., Kawasaki, S., Kato, H., and Takatori, M. (2011). Fusing Treatment of Pentacenes: toward Giant Graphene-like Molecule. *Mat Express* 1, 36–42. doi:10.1166/mex.2011.1005

Joblin, C., Masselon, C., Boissel, P., de Parseval, P., Martinovic, S., and Muller, J.-F. (1997). Simulation of Interstellar Aromatic Hydrocarbons Using Ion Cyclotron Resonance. Preliminary Results. *Rapid Commun. Mass. Spectrom.* 11, 1619–1623. doi:10.1002/(sici)1097-0231(199709)11:14<1619::aid-rcm995>3.0.co;2-p

Kroto, H. W., Heath, J. R., O'Brien, S. C., Curl, R. F., and Smalley, R. E. (1985). C60: Buckminsterfullerene. *Nature* 318, 162–163. doi:10.1038/318162a0

Linnartz, H., Cami, J., Cordiner, M., Cox, N. L. J., Ehrenfreund, P., Foing, B., et al. (2020). C60+ as a Diffuse Interstellar Band Carrier; a Spectroscopic story in 6 Acts. *J. Mol. Spectrosc.* 367 (8), 111243. doi:10.1016/j.jms.2019.111243-0022-2852

Liu, S., Lu, Y.-J., Kappes, M. M., and Ibers, J. A. (1991). The Structure of the C60 Molecule: X-Ray Crystal Structure Determination of a Twin at 110 K. *Science* 254 (5030), 408–410. doi:10.1126/science.254.5030.408

Mackie, C. J., Peeters, E., Bauschlicher Jr., C. W., and Cami, J. (2015). Characterizing the Infrared Spectra of Small, Neutral, Fully Dehydrogenated Polycyclic Aromatic Hydrocarbons. *ApJ* 799, 131–141. doi:10.1088/0004-637X/799/2/131

Maier, J. P., and Campbell, E. K. (2016). Pathway to the Identification of C 60 + in Diffuse Interstellar Clouds. *Phil. Trans. R. Soc. A.* 374 (12), 20150316. doi:10.1098/rsta.2015.0316

Markevich, A., Kurasch, S., Lehtinen, O., Reimer, O., Feng, X., Müllen, K., et al. (2015). Electron Beam Controlled Covalent Attachment of Small Organic Molecules to Graphene. *Nanoscale* 8, 2711. doi:10.1039/c5nr07539d

Mirzayev, R., Mustonen, K., Monazam, M. R. A., Mittelberger, A., Pennycook, T. J., Mangler, C., et al. (2017). Buckyball Sandwiches. *Sci. Adv.* 3 (6)), e1700176. doi:10.1126/sciadv.1700176

Osterodt, J., Zett, A., and Vögtle, F. (1996). Fullerenes by Pyrolysis of Hydrocarbons and Synthesis of Isomeric Methanofullerenes. *Tetrahedron* 52, 4949–4962. doi:10.1016/0040-4020(96)00103-2

Roberts, K. R. G., Smith, K. T., and Sarre, P. J. (2012). Detection of C60 in Embedded Young Stellar Objects, a Herbig Ae/Be star and an Unusual post-asymptotic Giant branch star. *Monthly Notices R. Astronomical Soc.* 421, þ3277–3328. doi:10.1111/j.1365-2966.2012.20552.x

Scott, L. T., Boorum, M. M., McMahon, B. J., Hagen, S., Mack, J., Blank, J., et al. (2002). A Rational Chemical Synthesis of C60. *Science* 295, 1500–1503. doi:10.1126/science.1068427

Semeniuk, M., Yi, Z., Poursorkhabi, V., Tjong, J., Jaffer, S., Lu, Z.-H., et al. (2019). Future Perspectives and Review on Organic Carbon Dots in Electronic Applications. *ACS Nano* 13, 6224–6255. doi:10.1021/acsnano.9b00688

Skowron, S. T., Chamberlain, T. W., Biskupek, J., Kaiser, U., Besley, E., and Khlobystov, A. N. (2017). Chemical Reactions of Molecules Promoted and Simultaneously Imaged by the Electron Beam in Transmission Electron Microscopy. *Acc. Chem. Res.* 50 (8), 1797–1807. doi:10.1021/acs.accounts.7b00078

Stone, A. J., and Wales, D. J. (1986). Theoretical Studies of Icosahedral C60 and Some Related Species. *Chem. Phys. Lett.* 128, 501–503. doi:10.1016/0009-2614(86)80661-3

Talyzin, A. V., Anoshkin, I. V., Krasheninnikov, A. V., Nieminen, R. M., Nasibulin, A. G., Jiang, H., et al. (2011). Synthesis of Graphene Nanoribbons Encapsulated in Single-Walled Carbon Nanotubes. *Nano Lett.* 11, 4352–4356. doi:10.1021/nl2024678

Talyzin, A. V., Luzan, S. M., Leifer, K., Akhtar, S., Fetzer, J., Cataldo, F., et al. (2011). Coronene Fusion by Heat Treatment: Road to Nanographenes. *J. Phys. Chem. C* 115, 13207–13214. doi:10.1021/jp2028627

Taylor, R., Langley, G. J., Kroto, H. W., and Walton, D. R. M. (1993). Formation of C60 by Pyrolysis of Naphthalene. *Nature* 366, 728–731. doi:10.1038/366728a0

Tian, P., Tang, L., Teng, K. S., and Lau, S. P. (2018). Graphene Quantum Dots from Chemistry to Applications. *Mater. Today Chem.* 10, 221–258. doi:10.1016/j.mtchem.2018.09.007

Tielens, A. G. G. M. (2008). Interstellar Polycyclic Aromatic Hydrocarbon Molecules. *Annu. Rev. Astron. Astrophys.* 46, 289–337. doi:10.1146/annurev.astro.46.060407.145211

Tielens, A. G. G. M. (2013). The Molecular Universe. *Rev. Mod. Phys.* 85, 1021–1081. doi:10.1103/revmodphys.85.1021

Weippert, J., Hauns, J., Bachmann, J., Greisch, J.-F., Narita, A., Müllen, K., et al. (2020). Oligomerization of Dehydrogenated Polycyclic Aromatic Hydrocarbons on Highly Oriented Pyrolytic Graphite. *J. Phys. Chem. C* 124, 8236–8246. doi:10.1021/acs.jpcc.0c00883

Yan, Y., Gong, J., Chen, J., Zeng, Z., Huang, W., Pu, K., et al. (2019). Recent Advances on Graphene Quantum Dots: from Chemistry and Physics to Applications. *Adv. Mater.* 31 (22pp), 1808283. doi:10.1002/adma.201808283

Zhen, J., Castellanos, P., Paardekooper, D. M., Linnartz, H., and Tielens, A. G. G. M. (2014). Laboratory Formation of Fullerenes from PAHs: Top-Down Interstellar Chemistry. *ApJ* 797, L30–L34. doi:10.1088/2041-8205/797/2/l30

Zhen, J., Chen, T., and Tielens, A. G. G. M. (2018). Laboratory Photochemistry of Pyrene Clusters: an Efficient Way to Form Large PAHs. *ApJ* 863 (6pp), 128. doi:10.3847/1538-4357/aad240

Zhen, J. (2019). Laboratory Formation of Large Molecules in the Gas Phase. *A&A* 623 (5pp), A102. doi:10.1051/0004-6361/201834847

Zhen, J., Zhang, W., Yang, Y., Zhu, Q., and Zhu, Q. F. (2019). Laboratory Formation and Photo-Chemistry of Ionic HBC/anthracene Clusters in the Gas Phase. *Monthly Notices R. Astronomical Soc.* 486, 3259–3265. doi:10.1093/mnras/stz1095

Conflict of Interest: The authors declare that the research was conducted in the absence of any commercial or financial relationships that could be construed as a potential conflict of interest.

frontiers in Chemistry

MINI REVIEW
published: 17 June 2021
doi: 10.3389/fchem.2021.706462

Structural Flexibility in Metal-Organic Cages

*Andrés E. Martín Díaz and James E. M. Lewis**

Department of Chemistry, Imperial College London, Molecular Sciences Research Hub, London, United Kingdom

Metal-organic cages (MOCs) have emerged as a diverse class of molecular hosts with potential utility across a vast spectrum of applications. With advances in single-crystal X-ray diffraction and economic methods of computational structure optimisation, cavity sizes can be readily determined. In combination with a chemist's intuition, educated guesses about the likelihood of particular guests being bound within these porous structures can be made. Whilst practically very useful, simple rules-of-thumb, such as Rebek's 55% rule, fail to take into account structural flexibility inherent to MOCs that can allow hosts to significantly adapt their internal cavity. An often unappreciated facet of MOC structures is that, even though relatively rigid building blocks may be employed, conformational freedom can enable large structural changes. If it could be exploited, this flexibility might lead to behavior analogous to the induced-fit of substrates within the active sites of enzymes. To this end, in-roads have already been made to prepare MOCs incorporating ligands with large degrees of conformational freedom. Whilst this may make the constitution of MOCs harder to predict, it has the potential to lead to highly sophisticated and functional synthetic hosts.

Keywords: self-assembly, cages, flexibility, host-guest, metallosupramolecular

OPEN ACCESS

Edited by:
Chao Deng,
Soochow University, China

Reviewed by:
Narayanan Selvapalam,
Kalasalingam University, India
Richard J. Hooley,
University of California, Riverside, United States

****Correspondence:***
James E. M. Lewis
james.lewis@imperial.ac.uk

Specialty section:
This article was submitted to Supramolecular Chemistry, a section of the journal Frontiers in Chemistry

Received: *07 May 2021*
Accepted: *02 June 2021*
Published: *17 June 2021*

Citation:
Martín Díaz AE and Lewis JEM (2021) Structural Flexibility in Metal-Organic Cages. Front. Chem. 9:706462. doi: 10.3389/fchem.2021.706462

INTRODUCTION

Metal-organic cages (MOCs) are self-assembled structures derived from carefully selected combinations of metal ions and ligands (Cook and Stang, 2015; Debata et al., 2019; Pilgrim and Champness, 2020). Porous MOCs of myriad shape and size are capable of binding guest molecules in their cavities (Rizzuto et al., 2019), leading to applications in catalysis (Yoshizawa et al., 2009; Sinha and Mukherjee, 2018), storage of reactive species (Galan and Ballester, 2016), molecular separations (Zhang et al., 2021), and drug delivery (Casini et al., 2017) amongst others. Guest-binding is a complex process involving contributions from enthalpic and entropic factors for both the encapsulation of the guest(s) and the liberation of solvent molecules (or displacement of extant guest molecules) (Metherell et al., 2018). The 55% rule originally established by Rebek (Mecozzi and Rebek, 1998) has been a good guiding principle when predicting molecular binding based on the packing coefficient of the guest inside the host's cavity. This volume-based approach, however, assumes the cavity to be static and therefore does not take into consideration host flexibility, which can greatly affect cavity size and shape and is a relatively underexplored consideration. The ability to harness this structural flexibility could lead to enzyme-like conformational adaptability (Boehr et al., 2009; Feixas et al., 2014). Characterising host flexibility is therefore crucial to understanding its effects on any potential applications.

In this mini review we highlight examples from the literature that demonstrate the inherent structural flexibility of *rigid* metal-organic hosts, both in solution and the solid-state, and examine the limited number of examples wherein units with high degrees of conformational freedom have

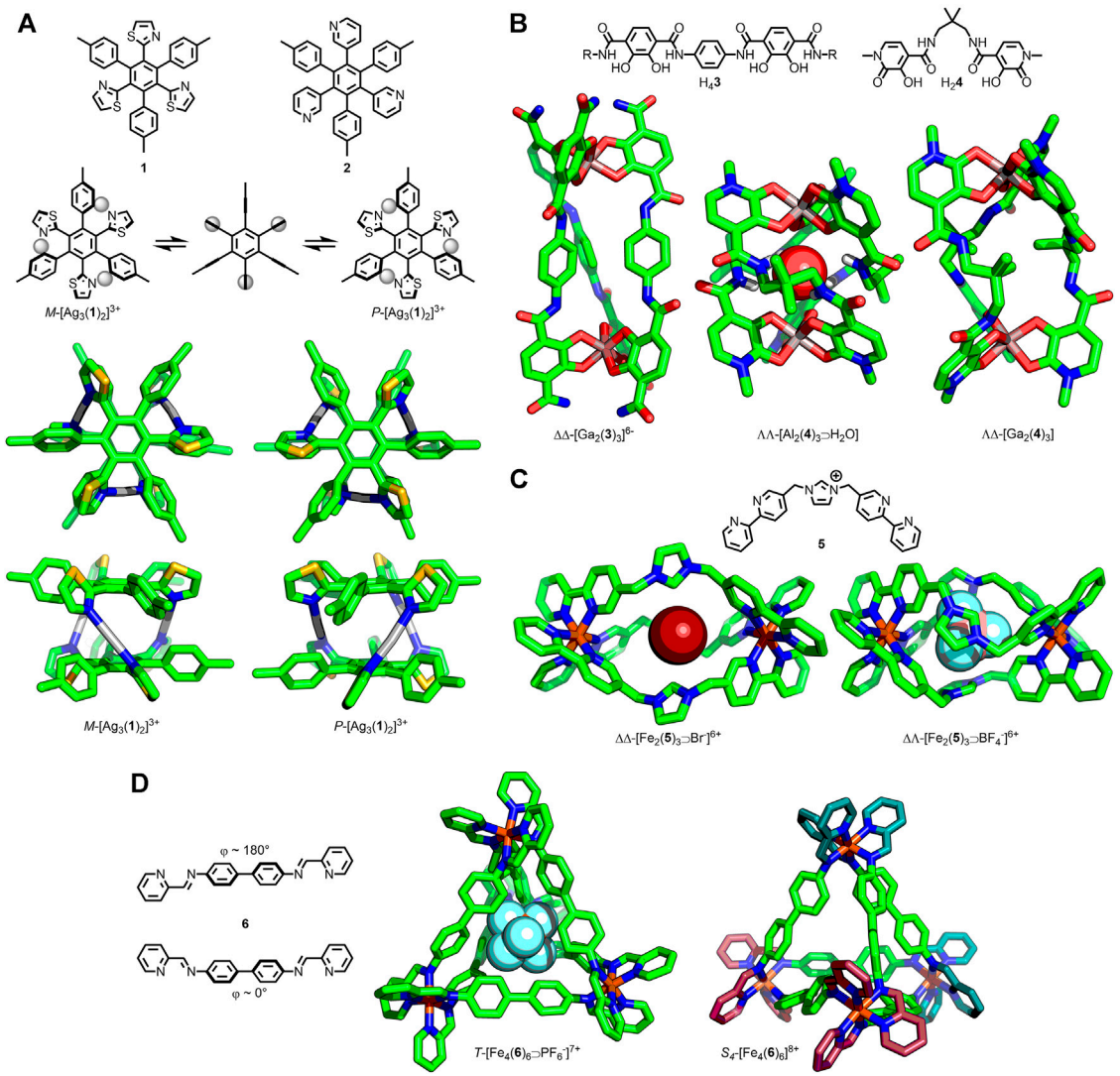

FIGURE 1 | (A) Shionoya's trinuclear *P*/*M*-$[Ag_3(\mathbf{1}/\mathbf{2})_2]^{3+}$ helicates capable of undergoing stereochemical inversion *via* an achiral intermediate. **(B)** Raymond's $[Ga_2(\mathbf{3})_3]$ helicate able to undergo helical inversion *via* a Bailar twist mechanism; SCXRD structures of $[Al_2(\mathbf{4})_3 \ni H_2O]$ helicate and $[Ga_2(\mathbf{4})_3]$ mesocate. **(C)** Wu's triply-stranded $[Fe_2(\mathbf{5})_3 \ni X^-]^{6+}$ assemblies with encapsulated anion-dependent formation of helicate (X^- = Br^-) or mesocate (X^- = BF_4^-) structures. **(D)** Nitschke's $[Fe_4(\mathbf{6})_6]^{8+}$ tetrahedra, with encapsulation of a PF_6^- anion favouring the *T*-symmetric assembly, whilst the *empty* cage preferentially crystallised as the S_4 structure with Δ (cyan) and Λ (magenta) Fe(II) centers.

been purposefully incorporated into ligand frameworks. A focus is placed on assemblies that undergo conformational, rather than configurational, changes without requiring dissociation and rearrangement of components. Full-scale compositional changes will not be covered, although it is noted than for some examples the involvement of bond dissociation in the mechanism of observed adaptability cannot be absolutely excluded. Neither will assemblies with stimuli-responsive, switchable units be included (Han et al., 2013; Oldknow et al., 2018), which have been covered elsewhere (McConnell et al., 2015). This review is not intended to be comprehensive—selected examples from the literature have been chosen to demonstrate key principles.

OBSERVATION OF STRUCTURAL FLEXIBILITY IN SOLUTION

Various 1D and 2D NMR techniques are commonly used to characterise MOCs and to probe their guest-binding properties. Flexibility arising from conformational freedom, however, is likely to occur rapidly on the NMR timescale, resulting in a time-averaged structure. This makes it difficult to gain accurate information regarding the extent of conformational plasticity. Despite this, observations made during particular experiments can allow inference of structural flexibility, often aided by use in conjunction with SCXRD data.

In 2003 Shionoya and co-workers reported the synthesis of the helical sandwich-shaped assembly $[Ag_3(\mathbf{1})_2]^{3+}$ as a racemic

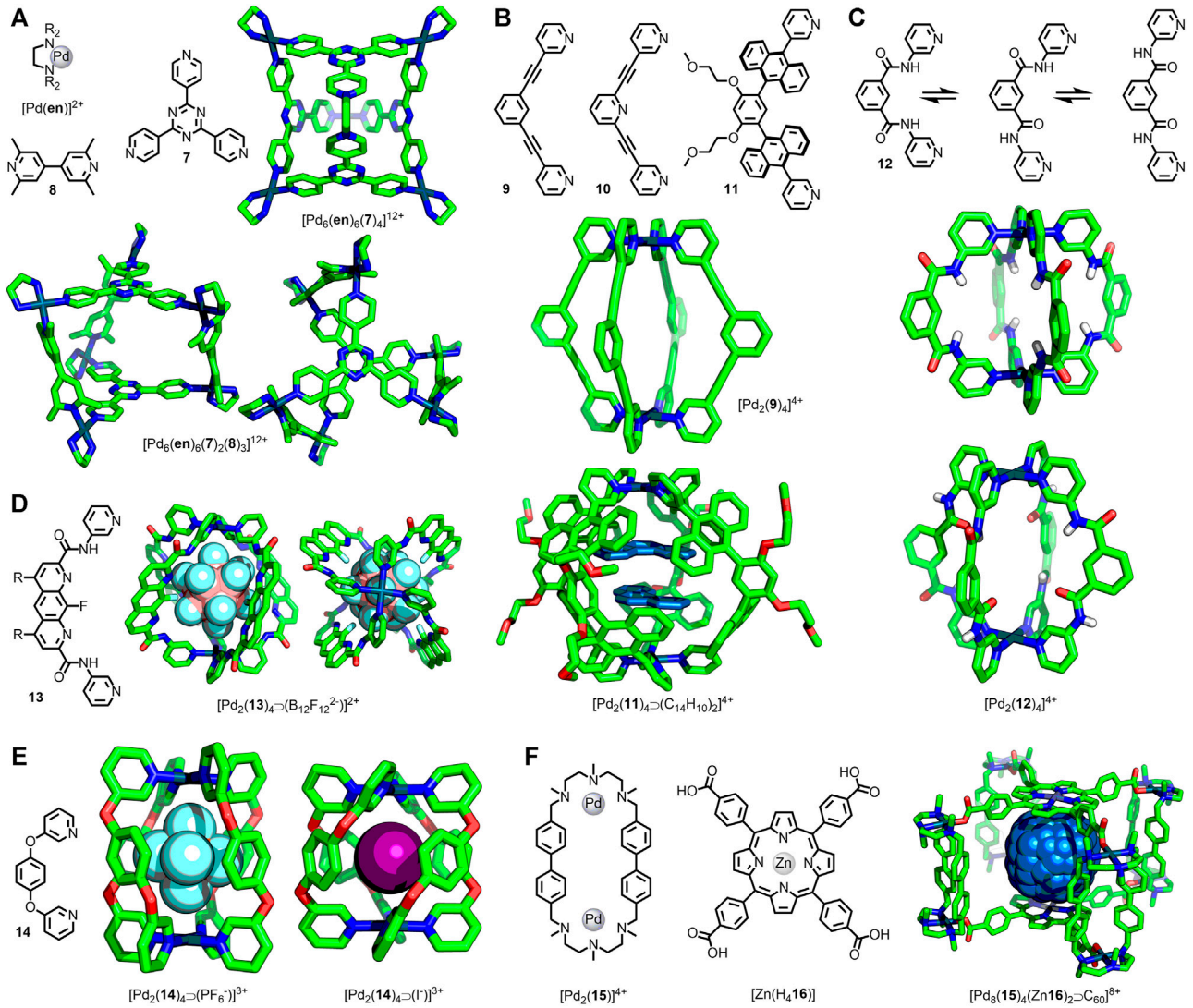

FIGURE 2 | (A) Fujita's octahedral cage, $[Pd_6(\mathbf{en})_6(\mathbf{7})_4]^{12+}$, and trigonal prismatic assembly $[Pd_6(\mathbf{en})_6(\mathbf{8})_3(\mathbf{7})_2]^{12+}$ shown from the side and above. **(B)** Ditopic ligands **9**, **10** and **11** used in the assembly of Pd_2L_4 cages. SCXRD structures of $[Pd_2(\mathbf{9})_4]^{4+}$ and $[Pd_2(\mathbf{11})_4 \ni (C_{14}H_{10})_2]^{4+}$. **(C)** Puddephatt's ditopic ligand **12** with three possible conformations accessed through rotation about the amide bonds; SCXRD structures of $[Pd_2(\mathbf{12})_4]^{4+}$ with **12** exhibiting two different ligand conformations. **(D)** Gan's $[Pd_2(\mathbf{13})_4 \ni (B_{12}F_{12}{}^{2-})]^{2+}$ cage viewed from the side **(left)** and above **(right)**. **(E)** McMorran and Steel's $[Pd_2(\mathbf{14})_4]^{4+}$ helicates with PF_6^- **(left)** and I^- **(right)** anions bound. **(F)** Ribas' porphyrin-based cage, $[Pd_8(\mathbf{15})_4(Zn\mathbf{16})_2]^{8+}$, with encapsulated C_{60} guest.

mixture of the *M* and *P* isomers (**Figure 1A**), demonstrated in solution through the formation of the Δ-TRISPHAT salt (Hiraoka et al., 2003). At 253 K (in 2:1 d_6-acetone/$CDCl_3$) two sets of equal intensity signals were observed for the two enantiomers, suggesting a lack of chiral induction from the anion. Upon increasing the temperature to 303 K coalescence to a single set of signals was observed, the result of rapid interconversion between the *P* and *M* enantiomers on the NMR timescale. In order to switch between the two enantiomers, the cage likely transitions through a high energy, achiral conformer with an increased distance between the core phenyl units of the ligands (< 1 Å). In an analogous complex, $[Ag_3(\mathbf{2})_2]^{3+}$, interconversion between isomers occurred rapidly only at elevated temperatures, indicating a larger energy barrier to helical inversion.

Raymond and co-workers investigated the stereochemical inversion of triply-stranded dinuclear helicates assembled from bis-catecholate ligands (**3**) and Ga(III) ions (**Figure 1B**) (Kerstin et al., 1996). From a comprehensive NMR study the authors were able to ascertain that the isomers were interconverting through an intramolecular helical inversion process (ΔΔ⇋ΛΛ), with independent chiral inversion occurring at each metal centre through a non-dissociative Bailar twist mechanism, *via* a mesocate intermediate. Subsequent work with related $[M_2(\mathbf{4})_3]$ [M = Al(III) or Ga(III)] assemblies (**Figue 1B**) demonstrated an ability to controllably switch between the chiral helicate (M···M

7.13 Å) and larger, achiral mesocate (M···M 9.74 Å) using host-guest interactions (Xu et al., 1999). Despite crystallising as the mesocate, $[Ga_2(\mathbf{4})_3]$ existed in solution as an equilibrium between the helicate and mesocate forms. The helicate was shown to be stabilised by an encapsulated solvent molecule (water or DMSO); increasing the water concentration served to shift the equilibrium further towards the helicate.

More recently Wu and co-workers (Cui et al., 2012) observed a similar change in the structure of a triply-stranded, dinuclear structure, assembled from bis-bidentate ligand **5** and Fe(II), with different anions bound in its cavity (**Figure 1C**). With Br^- or NO_3^- encapsulated a helicate assembly was formed. In contrast, the tetrahedral anions BF_4^-, ClO_4^-, and SO_4^{2-} resulted in mesocates, with the helicates being significantly longer (Fe···Fe ~11.7 Å vs ~10.6 Å). This switch between helicate and mesocate was reasoned to arise from conformational changes of the ligand in order to maximize favourable interactions with the encapsulated anion. In the case of the mesocate the ligands adopt a C-shaped conformation, whilst an S-conformer led to the helicate assembly.

A related concept has been studied by Nitschke and co-workers, wherein the relative stereochemistry of octahedral metal centres within a tetrahedral MOC could be affected by encapsulation of different anions, impacting the overall symmetry of the assembly (Clegg et al., 2013). Subcomponent self-assembly of 4,4′-diaminobiphenyl, 2-formylpyridine and Fe(II) with large triflimide counteranions resulted in a tetrahedral cage structure, $[Fe_4(\mathbf{6})_6]^{8+}$ (**Figure 1D**). In the solid state, SCXRD data demonstrated that the cage possessed two metal centres of one stereochemistry and two of the opposite (i.e., ΔΔΛΛ), giving the tetrahedron an overall S_4 symmetry [with two ligands adopting an S-shaped conformation ($\varphi \approx 180^\circ$), the remaining four a C-shape ($\varphi \approx 0^\circ$)]. In solution, however, a mixture of S_4-, *T*-, and C_3-symmetric assemblies were observed in an approximately 5:3:2 ratio at equilibrium. Smaller anions were capable of binding within the cavity of the cage, and altering the equilibrium position of this diasteroeomeric mixture, with ClO_4^- and PF_6^- shifting the equilibrium in favor of the *T*-symmetric isomer (ΔΔΔΔ/ΛΛΛΛ; all ligands S-conformation). Remarkably NO_3^-, BF_4^-, Cl^-, Br^-, and I^- encapsulation all resulted in quantitative conversion to the *T* diasteroisomer, as determined by solution-phase NMR analysis. In addition, SCXRD data demonstrated that the MOC framework was able to conformationally adapt to encapsulate the various anions; the cavity volume was found to expand from 69 $Å^3$ with BF_4^- to 87 $Å^3$ with PF_6^-.

In these studies solution phase data were able to demonstrate structural changes in the MOCs arising from alterations to the assembly's symmetry. More subtle changes from, e.g., flexing and conformational adjustment of ligands, are not so readily detected in this manner. SCXRD, however, provides more precise structural information and was used effectively in combination with the solution-phase data in the previous examples to add quantitative spatial information. It is important to note that the solid-state data merely provides a *snap-shot* image of the assemblies, which can be affected by various packing interactions. Multiple sets of SCXRD data, however, can show differences in structural parameters, allowing inference of the extent of MOC flexibility.

SOLID-STATE SCXRD EVIDENCE FOR STRUCTURAL FLEXIBILITY

Arguably one of the most studied MOCs in the literature is the hexanuclear octahedron ($[Pd_6(\mathbf{en})_6(\mathbf{7})_4]^{12+}$; **Figure 2A**) originally reported by the Fujita group (Fujita et al., 1995). For this assembly multiple sets of SCXRD data are available with different guests encapsulated within the host, allowing quantitative comparison of structural parameters in the solid state (Tashira et al., 2005; Nishioka et al., 2007; Kohyama et al., 2014; Takezawa et al., 2014; Cullen et al., 2019; Takezawa et al., 2020). These demonstrate that the M···M distance varies by less than 1% across numerous solid-state structures. Clearly, in this instance, significant distortion of the cage structure through host-guest interactions and crystal packing effects is not in evidence. For other MOCs, however, such effects have been observed.

The heteroleptic trigonal prismatic cage $[Pd_6(\mathbf{en})_6(\mathbf{7})_2(\mathbf{8})_3]^{12+}$ (**Figure 2A**), also reported by Fujita and co-workers (Yoshizawa et al., 2005a), was assembled from **7** and 2,2′-6,6′-tetramethyl-4,4′-bipyridine (**8**) with *cis*-Pd^{II}(**en**) metal nodes (**Figure 1A**). Due to the manner in which the ligands are arranged in this assembly, **7** and **8** are orthogonal in the most symmetric form. In this conformer the two **7** ligands would eclipse one another and the torsion angle between them would be 0°. As this angle increases, the **7** ligands will become more offset, and the angle between **7** and **8** will diverge from orthogonality. With extensive investigation of this cage's host-guest properties having been undertaken, it was possible to examine multiple SCXRD structures of the assembly to analyse changes in structural parameters. From this it was seen that the average torsion angle varied between ~19 and ~39°, and the distance between triazines ranged from 9.9–10.6 Å (Yoshizawa et al., 2005a; Yoshizawa et al., 2005b; Ono et al., 2007; Ono et al., 2009; Yamauchi et al., 2010; Schmidt et al., 2016).

Torsional twisting of trigonal prismatic cages, leading to a dramatic change in cavity size, has been reported by others. Severin and co-workers prepared a hexanuclear cage from ligand **7** and diruthenium(II) clips. Upon binding two molecules of coronene in the cavity the torsion angle between the two **7** ligands decreased from ~75–~3°, increasing the distance between them from 3.4–11.1 Å, thereby expanding the cavity size from effectively zero to > 500 $Å^3$ (Mirtschin et al., 2010). Likewise, Han and Jin have reported a trigonal prism assembled from **7** and diiridium(III) clips that collapsed (**7**···**7** distance reduced from 6.9–3.3 Å) through increased torsion between the **7** ligands (~16–~30°) upon removal of a coronene guest molecule (Han and Jin, 2011).

Ditopic *banana-shaped* ligands (Han et al., 2014) are commonly combined with Pd(II) ions to form dinuclear, lantern-shaped architectures. These are often designed with the ligand framework fully conjugated; however, rotation about certain bonds is still feasible, potentially introducing some dynamic character to the resultant assemblies. In 2010

Hooley and co-workers reported the cage $[Pd_2(\mathbf{9})_4]^{4+}$ (**Figure 2B**) and its SCXRD structure with an encapsulated OTf^- anion (Liao et al., 2010). More recently, Lusby and co-workers have examined this cage for its catalytic potential (Spicer et al., 2020) and were able to obtain SCXRD data of the PF_6^- salt with pentacenedione bound in the cavity (August et al., 2016). Although relatively minor, there was a difference of 0.36 Å in the Pd···Pd distance between the cage SCXRD structures (11.85 and 12.21 Å), and the torsion angle between the core phenyl and terminal pyridyl rings were greater for the longer cage (12.5° on average compared to 5.1°).

The related $[Pd_2(\mathbf{10})_4]^{4+}$ architecture, in which the central phenyl unit of the ligand is replaced with a pyridine, has been reported by Crowley and co-workers. They were able to obtain SCXRD structures of various salts of the cage (Lewis and Crowley, 2014), as well as a host-guest adduct with two cisplatin molecules (Lewis et al., 2012). Again, some variation in the Pd···Pd distance was observed (11.5–12.2 Å) with torsion angles between the core and coordinating pyridine rings ranging from 2.5–19.0°.

In a similar Pd_2L_4 system (**Figure 2B**) reported by Yoshizawa and co-workers (Kishi et al., 2011), with anthracene units linking the core phenyl ring and coordinating pyridines instead of alkynes (ligand **11**), even more dramatic differences were observed with various host-guest adducts. For instance, in the 1:1 adduct formed between the cage and [2.2]-paracyclophane the Pd···Pd distance was found to be 13.8 Å. In contrast, with two molecules of corranulene encapsulated this was found to shrink to 12.4 Å, a reduction of 10% (Kishi et al., 2013).

Puddephatt and co-workers prepared ligand **12** with 3-pyridyl units attached to a *meta*-phenyl core through amide bonds. Rotation about these amide bonds ostensibly permitted three conformations of the ligand (**Figure 2C**). When combined with Pd(II) ions the expected $[Pd_2(\mathbf{12})_4]^{4+}$ assembly was obtained, wherein adoption of different ligand conformations could alter the character of the cavity depending on whether the amide carbonyl or N-H units were directed internally. SCXRD structures of the cage (**Figure 2C**) with both $F_3CSO_3^-$ and $F_3CCO_2^-$ anions were obtained. In the case of the former both N-H units of each ligand were directed endohedrally, allowing the formation of hydrogen-bonds to partially encapsulated $F_3CSO_3^-$ anions. Conversely the $F_3CCO_2^-$ salt resulted in adoption of ligand conformations with one carbonyl directed exohedrally, the other endohedrally acting as a hydrogen-bond acceptor to encapsulated water molecules. This change from a higher to lower symmetry assembly was coincident with a lengthening of the Pd···Pd distance from 9.5–11.2 Å (Yue et al., 2003). Despite its lower symmetry in the solid state, the observation of a single set of signals for the pyridyl units by NMR demonstrated rapid conformational interconversion on the NMR timescale (Yue et al., 2004).

Likewise, Gan and co-workers were able to observe significant changes in structural parameters in a similarly designed system (Lin et al., 2018). $[Pd_2(\mathbf{13})_4]^{4+}$ (**Figure 2D**) was assembled from ligand **13** and an appropriate Pd(II) source. SCXRD structures for this architecture were obtained with BF_4^-, NO_3^- (two polymorphs were reported), and $B_{12}F_{12}^{2-}$ anions encapsulated within the internal cavity, with changes in the ligand conformation demonstrated through significant variation in the Pd···Pd distance (12.1–13.4 Å).

Unsurprisingly the introduction of saturated units within the ligand framework offers the potential for greater degrees of flexibility within assemblies. In 1998 McMorran and Steel reported the first example of a dipalladium(II) helical cage assembled from a ditopic ligand, namely 1,4-bis(3-pyridyloxy) benzene (**14**) (McMorran and Steel, 1998). In contrast to the previous examples, the ether linkage between the core and coordinating units engendered the ligands with more significant degrees of freedom. This work was recently extended to include a thorough examination of the anion-binding properties of this cage, including an extensive study in the solid state from SCXRD data (Steel and McMorran, 2019). This revealed a significant 16% reduction in the Pd···Pd distance upon exchanging a bound PF_6^- anion (8.84 Å) for an I^- guest (7.44 Å) (**Figure 2E**), the result of a drastic change in the Pd-N···N-Pd torsion angle (average 41.5° for PF_6^- and 80.9° for I^-). The associated reduced helical pitch (77–37 Å) reduced the effective cavity size from 92–41 $Å^3$.

MOLECULAR DYNAMICS SIMULATIONS OF METAL-ORGANIC CAGE FLEXIBILITY

Computational modelling of supramolecular systems has become cheaper and more readily available in recent years, allowing combinations of experimental and theoretical data to be used to gain in-depth understanding of these artificial mimics of biological assemblies (Frederix et al., 2018). Given the previously mentioned constraints placed on information related to conformation dynamics that can be gleaned from solution and solid-state data, computational analysis offers a potential route to quantitatively examine flexibility of metal-organic assemblies. Perhaps most interestingly these techniques could be effectively used to aid in the design of such systems for specific applications (Young et al., 2020a).

Recently Lusby, Duarte and co-workers utilised molecular dynamics (MD) simulations to explore the conformational flexibility of the two dipalladium(II) cages assembled from **9** and **10** to explain observations related to their catalytic activity (Young et al., 2020b). In these simulations the Pd···Pd distance in the cages was found to vary between 11.3 and 12.9 Å for ligand **9**, and 10.9 and 12.5 Å for ligand **10**, with the torsion angle between the core ring and terminal pyridines ranging from 0–60°. Interestingly, for the $[Pd_2(\mathbf{10})_4]^{4+}$ cage, conformations with significant twisting of the ligands were found to be of similar energy to the highly symmetric structure (conformer with $\Phi = 41°$ was only 2.6 kcal mol^{-1} higher in energy than the symmetric $\Phi = 0°$ conformer).

Ribas and co-workers reported the synthesis of a nanocage assembled from four dinuclear macrocycle Pd(II) complexes ($[Pd_2(\mathbf{15})]^{4+}$) and two tetracarboxylate Zn(II)-porphyrins ($[Zn(H_4\mathbf{16})]$) (García-Simón et al., 2014). These cages were observed to bind fullerene guests, and the SCXRD structures of the "empty" cage and C60 and C70 adducts were obtained (**Figure 2F**). For the empty cage the distance between Zn(II) ions

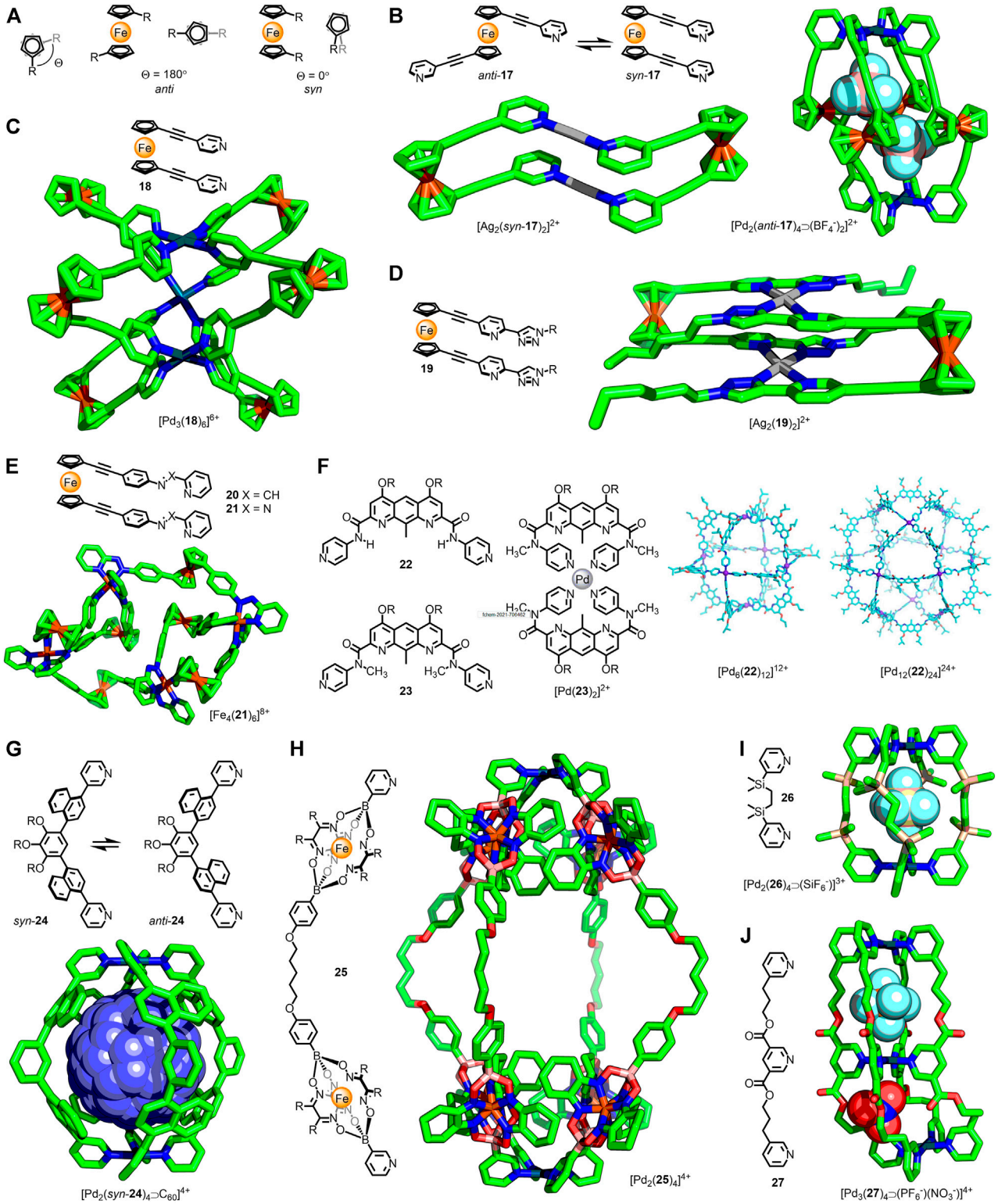

FIGURE 3 | (A) The cyclopentadiene rings of ferrocene are able to undergo 360° rotation. The two extremes of conformation are the *anti* ($\Theta = 180°$) and *syn* ($\Theta = 0°$) conformers. **(B)** In the dinuclear metallacycle $[Ag_2(\mathbf{17})_2]^{2+}$ ligand **17** is observed to adopt a *syn* conformation; in the quadruple-stranded $[Pd_2(\mathbf{17})_4]^{4+}$ cage the *anti* conformer is observed. **(C)** Crowley's trigonal prismatic $[Pd_3(\mathbf{18})_6]^{6+}$ assembly with ligands in *syn* arrangements ($\Theta = 25–42°$). **(D)** A dinuclear metallacycle, $[Ag_2(syn\text{-}\mathbf{18})_2]^{2+}$ reported by Crowley. **(E)** Nitschke's twisted parallelogram assembly, with ligand **21** in both *syn* and *anti* conformations. **(F)** Non-covalent interactions affect favoured ligand conformations: self-assembly with Pd(II) led to a $Pd_{12}L_{24}$ cuboctahedron with **22** (*via* a kinetic Pd_6L_{12} cube; calculated structures shown), whilst ligand **23** gives the mononuclear

(*Continued*)

FIGURE 3 | $[Pd(\mathbf{23})_2]^{2+}$ complex. Adapted with permission from Liu et al. (2020). Copyright © 2020 Wiley-VCH GmbH. **(G)** Yoshizawa's atropisomeric ditopic ligand that formed $[Pd_2(\mathbf{24})_4]^{4+}$ assemblies; guest encapsulation biased the distribution of cage atropisomers. **(H)** Severin's alkyl-linked metallo-ligand that formed the large (Pd···Pd ~ 3 nm) $[Pd_2(\mathbf{25})_4]^{4+}$ cage. **(I)** Alkyl-linked ligand **26** formed Pd_2L_4 cages capable of anion-encapsulation. **(J)** Jung's trinuclear, double-cavity cage bound anions in each cavity, which adapt their shape to best match the encapsulated guest.

was 14.1 Å, with a contraction seen for the C70 (13.8 Å) and C60 (13.1 Å) host-guest adducts. This was concomitant with a small decrease in the Pd···Pd distance within the macrocycles from 11.25–11.17 Å. Subsequent molecular dynamics simulations (2.5 μs) showed flexing of the cage to give Zn···Zn distances ranging between 11.3 and 15.8 Å. Binding of fullerene guests induced a compression of this distance, consistent with the SCXRD structures. To enable fullerene guests to enter the cage cavity a transient expansion of both the portal size, from ~50 $Å^2$ up to ~90 $Å^2$, and the Zn···Zn distance (~15 Å) was observed, demonstrating a significant dynamic range for this host assembly (García-Simón et al., 2020).

METAL-ORGANIC ASSEMBLIES DERIVED FROM LIGANDS WITH LARGE AMPLITUDE CONFORMATIONAL FLEXIBILITY

The previous sections have sought to demonstrate that even MOCs assembled from what would normally be considered rigid ligands–including those with fully conjugated systems–can display a reasonable amount of flexibility. There is a paucity of examples in the literature, however, of purposeful introduction of units that display large-amplitude conformational freedom into metal-organic systems. A key facet of metallo-supramolecular self-assembly is predicting products of self-assembly based on constituent metal ion geometry and ligand conformation. The importance of ligand conformation has been amply demonstrated by the work of the Fujita group on Pd_nL_{2n} cages assembled from ditopic ligands, in which the ligand angle determines the thermodynamically favoured value of n (Harris et al., 2013). When multiple ligand conformers are accessible, predicting/controlling self-assembly outcomes becomes more difficult. Adaptability, however, is a hallmark of natural self-assembled systems, and could offer an increased level of stimuli-responsiveness if incorporated into artificial systems seeking to mimic Nature's success.

Ferrocene, first synthesised 70 years ago (Kealy and Pauson, 1951), is the most well-known of the organometallic sandwich complexes. The ability of the two cyclopentadiene ligands to rotate relative to each other has led to significant interest in ferrocene's use as a "ball-bearing" component in molecular machines (Scottwell and Crowley, 2016). The ability of the ligands to undergo a full 360° rotation means that the dihedral angle between substituents of 1,1′-disubstituted ferrocenes can vary from 0 (*syn*)–180° (*anti*) (**Figure 3A**).

In 2003 Lindner and co-workers reported the self-assembly of 1,1′-bis(pyridin-3-ylethynyl)ferrocene (**17**) with Ag(I) and *trans*-Pd(II)Cl_2 metal nodes (Lindner et al., 2003). In both instances dinuclear metallacycles were obtained (**Figure 3B**), with the ligands adopting a stacked conformation (Θ = 7°). Crowley and co-workers subsequently examined the self-assembly of this ligand with Pd(II) ions (Vasdev et al., 2019), observing formation of $[Pd_2L_4]^{4+}$ cages (**Figure 3B**) with the ligands in *anti* conformations (Θ = 105–134°). SCXRD structures of the cage revealed that the Pd···Pd distance was affected by changes in the dihedral angle between the pyridyl arms (13.1 Å for one crystallographically independent molecule of $[Pd_2(\mathbf{17})_4 \supset (BF_4^-)_2]^{2+}$ and Θ_{ave} = 109°; 13.4 Å for $[Pd_2(\mathbf{17})_4 \supset (SbF_6^-)]^{3+}$ and Θ_{ave} = 126°), demonstrating an ability for the cage to adapt its shape based on the ligand conformation.

Self-assembly of the isomeric 1,1′-bis(pyridin-4-ylethynyl) ferrocene ligand (**18**) with Pd(II) ions resulted in formation of a trigonal prismatic structure (Vasdev et al., 2021). SCXRD data of the BF_4^- salt revealed an eclipsed conformation adopted by the ferrocene units (**Figure 3C**), with a small variation in the dihedral angle between independent ligands (25–42°).

The self-assembly of twin-armed ferrocene ligands with bidentate coordinating groups has also been investigated. The formation and solid-state structures of dinuclear metallacycles (**Figure 3D**) assembled from bis(2-pyridyl-1,2,3-triazole) ligand **19** were reported by Crowley and co-workers (Findlay et al., 2018). For both the Ag(I) and Pd(II) metallacycles the ligands were eclipsed, with a slight difference in the dihedral angles observed between the two assemblies (0.9 and 16.2°, respectively). Nitschke and co-workers synthesised isostructural $[Fe(II)_4L_6]^{8+}$ twisted parallelogram assemblies from imine and azo ligands **20**/**21** (Plajer et al., 2020). The SCXRD structure of one of these intriguing architectures (**Figure 3E**) revealed the co-existence of both *syn* (55–67°) and *anti* (118–121°) ligand conformations, demonstrating the ability of chemically identical ligands to occupy inequivalent environments through accessing different conformers. Attempts to oxidise the ferrocene units led to dis-assembly of the parallelogram, and formation of mononuclear $[Fe(II)L]^{3+}$ complexes.

Singleton and co-workers synthesised dipyridyl ligands **22** and **23** (**Figure 3F**) capable of bond rotation about the amide units (Liu et al., 2020). For **22** the range of favourable conformations was restricted by intramolecular hydrogen bonds between the amide proton and diazaanthracene core. Initially self-assembly of this ligand with Pd(II) resulted in an M_6L_{12} cube, with an average angle of 97° between the coordinating pyridyl groups in the calculated structure. This species was, however, revealed to be a kinetically trapped intermediate; prolonged heating of the sample led to rearrangement to form a larger $M_{12}L_{24}$ cuboctahedron, with the calculated average ligand angle increasing to 120°. In contrast, ligand **23**, with methylated amide units preventing hydrogen bonds across the ligand framework, yielded a simple mononuclear ML_2 complex (**Figure 3F**) as a result of increased conformational flexibility.

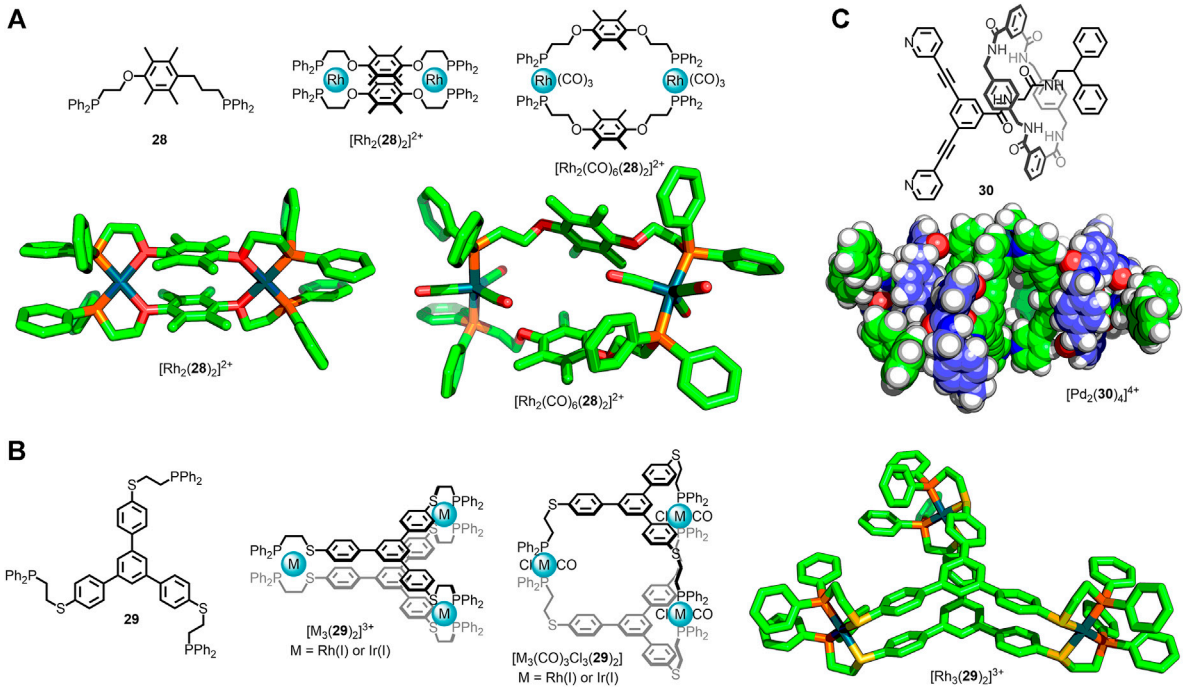

FIGURE 4 | (A) Mirkin's Weak-Link Approach in which a rigid metallacycle precursor, $[Rh_2(\mathbf{28})_2]^{2+}$, is first formed under thermodynamic control. Subsequent displacement of the ether oxygen donors gave the flexible metallacycle $[Rh_2(CO)_6(\mathbf{28})_2]^{2+}$, with ligand **28** coordinated in a bis-monodentate fashion. **(B)** This principle has been applied to MOCs, with flexible cage $[M_3(CO)_3Cl_3(\mathbf{29})_2]$ accessed *via* thermodynamic intermediate $[M_3(\mathbf{29})_2]^{3+}$ [M = Rh(I) or Ir(I)]. **(C)** Lewis' [2]rotaxane ligand, **30**, that self-assembled with Pd(II) ions to form a Pd_2L_4 cage (molecular model) with dynamic interlocked macrocycle components (shown in blue).

Recently Yoshizawa and co-workers investigated the dynamics of a Pd_2L_4 cage assembled from ditopic ligands with 1,4-naphthylene linkers (**24**) (Tsutsui et al., 2020). Hindered rotation of these units resulted in atropisomeric forms of the ligand. Although this did not inherently affect the relative orientations of the coordinating pyridyl groups, it did lead to an interconverting mixture of 42 virtually isoenergetic cage isomers. Guest encapsulation was found to bias the mixture towards individual isomers, with C_{60} inducing quantitative conversion to the all-*syn* assembly, as shown by SCXRD (**Figure 3G**). As such, the cage was able to undergo subtle structural modification in response to guest molecules in order to provide a favourable fit.

Alkyl spacers are inherently flexible and are therefore not usually used in MOC ligand design. Their conformational freedom, however, could allow for large amplitude adaptability through interactions with guest molecules. Severin and co-workers successfully synthesised Pd_2L_4 cages (**Figure 3H**) up to 3 nm in length using ditopic metallo-ligands with akyl spacer units (**25**), demonstrating the potential for the controlled incorporation of highly flexible alkyl units into metallo-assemblies (Jansze et al., 2016). Jung, Lee and co-workers obtained SCXRD structures for $[Pd_2L_4 \ni (X^-)]^{3+}$ cages (**Figure 3I**), assembled from a dipyridyl ligand with a flexible disilylethane core (**26**), with a range of encapsulated anions (Lee et al., 2020). The flexibility of the alkyl linker enabled expansion of the capsule to suit the encapsulated anion (Pd···Pd = 8.49 and 9.58 Å for $X^- = BF_4^-$ and SiF_6^-, respectively). This concept was exploited in the double-cavity $[Pd_3(\mathbf{27})_4 \ni (X^-)_2]^{4+}$ architecture, with both homo and hetero-anion adducts formed (Sarada et al., 2020). In this instance each cavity was able to independently adopt an *extended* or *crumpled* shape, dependent on the anion encapsulated (**Figure 3J**).

An alternative method to introduce flexible, saturated units into MOCs is to use the Weak-Link Approach (WLA), developed by the Mirkin group (Giannesci et al., 2005). In this methodology kinetically stable metal-organic architectures assembled from flexible ligands are formed *via* ligand exchange from a rigid, thermodynamically-favourable precursor species. This enables access to flexible structures that may not be thermodynamic products and cannot be directly accessed from a combination of ligand and metal nodes. This was first demonstrated with ligand **28** which formed the metallacycle $[Rh_2(\mathbf{28})_2]^{2+}$, with chelation to the metal centres between the phosphine and ether oxygen (Farrell et al., 1998). The hemilabile oxygen donors could be displaced through addition of competing ligands, such as CO, giving the *expanded* structure $[Rh_2(CO)_6(\mathbf{28})_2]^{2+}$ (**Figure 4A**). The Weak-Link Approach has since been shown to be suitable for the preparation of flexible MOCs (Ovchinnikov et al., 2002). The condensed cage $[M_3(\mathbf{29})_2]^{3+}$ [M = Rh(I) or Ir(I)] could be *opened* through addition of CO and Cl^- ligands, leading to the expanded structure, $[M_3(CO)_3Cl_3(\mathbf{29})_2]$ (**Figure 4B**).

Mechanically interlocked molecules have been widely investigated for their use as molecular machines due to the

high degree of co-conformational freedom between their components afforded by the lack of covalent bonds (Heard and Goldup, 2020). Consequently there has been considerable interest in the development of mechanically interlocked ligands (Lewis et al., 2017) and the use of metal ions/nodes to periodically arrange them (Hoyas Pérez and Lewis, 2020; Wilson and Loeb, 2020). Lewis and co-workers recently reported the synthesis of [2]rotaxane ligand **30** (**Figure 4C**), wherein one of the stopper units preventing escape of the macrocycle component was based on dipyridyl ligand **9** (Wong et al., 2020). Self-assembly with Pd(II) ions led to the quadruple-stranded cage $[Pd_2(\mathbf{30})_4]^{4+}$. NMR analysis of this structure revealed a single set of signals for the macrocycle, indicating rapid pirouetting on the NMR timescale. As such the large degree of co-conformational freedom inherent to rotaxane **30** was maintained in the metal-organic assembly, demonstrating the potential for mechanical bonds to be employed as flexible components within MOCs.

CONCLUSION AND FUTURE OUTLOOKS

The complexity of MOCs that are routinely reported has increased dramatically since preliminary studies in the field over thirty years ago (Pullen et al., 2021). Heteroleptic (Bloch and Clever, 2017), mixed-metal (Li et al., 2015) and low symmetry (Lewis and Crowley, 2020) assemblies towards the development of more sophisticated host systems are becoming more commonplace. Coincident with this, easier access to and improvements within SCXRD and the advancement of computational power for theoretical investigations allow researchers to gain rapid and in-depth analysis of these systems. This has led to some remarkable applications for MOCs, particularly in the area of catalysis. Appreciation of the structural flexibility these systems are capable of, however, is largely overlooked, despite the parallels that are often drawn between MOCs and enzymes. Herein we have taken a brief look at some of the solution-phase, solid-state and computational data available to highlight how significant variations in the structural parameters of MOCs can be. If this flexibility could be harnessed it could open up the doors for developing more sophisticated artificial systems to mimic biological machinery. Steps towards this lofty goal have already been undertaken, with a handful of examples reported of MOCs derived from ligands containing moieties with significant conformational freedom. With continuing investigations into flexible metal-organic assemblies, elucidation of methodologies for their controlled self-assembly and manipulation will lead to increasingly sophisticated systems capable of displaying adaptive behaviour and allow their use in new and exciting applications.

AUTHOR CONTRIBUTIONS

JL designed and supervised the writing of the review. Both authors contributed to writing and approved the final manuscript.

FUNDING

This work was supported by an Imperial College Research Fellowship (JL).

ACKNOWLEDGMENTS

Professor Matthew Fuchter is thanked for useful discussions and access to resources.

REFERENCES

August, D. P., Nichol, G. S., and Lusby, P. J. (2016). Maximizing Coordination Capsule-Guest Polar Interactions in Apolar Solvents Reveals Significant Binding. *Angew. Chem. Int. Ed.* 55, 15022–15026. doi:10.1002/anie.201608229

Bloch, W. M., and Clever, G. H. (2017). Integrative Self-Sorting of Coordination Cages Based on Naked Metal Ions. *Chem. Commun.* 53, 8506–8516. doi:10.1039/C7CC03379F

Boehr, D. D., Nussinov, R., and Wright, P. E. (2009). The Role of Dynamic Conformational Ensembles in Biomolecular Recognition. *Nat. Chem. Biol.* 5, 789–796. doi:10.1038/nchembio.232

Casini, A., Woods, B., and Wenzel, M. (2017). The Promise of Self-Assembled 3D Supramolecular Coordination Complexes for Biomedical Applications. *Inorg. Chem.* 56, 14715–14729. doi:10.1021/acs.inorgchem.7b02599

Clegg, J. K., Cremers, J., Hogben, A. J., Breiner, B., Smulders, M. M. J., Thoburn, J. D., et al. (2013). A Stimuli Responsive System of Self-Assembled Anion-Binding Fe4L68+cages. *Chem. Sci.* 4, 68–76. doi:10.1039/c2sc21486e

Cook, T. R., and Stang, P. J. (2015). Recent Developments in the Preparation and Chemistry of Metallacycles and Metallacages *via* Coordination. *Chem. Rev.* 115, 7001–7045. doi:10.1021/cr5005666

Cui, F., Li, S., Jia, C., Mathieson, J. S., Cronin, L., Yang, X.-J., et al. (2012). Anion-Dependent Formation of Helicates versus Mesocates of Triple-Stranded M2L3 (M = Fe2+, Cu2+) Complexes. *Inorg. Chem.* 51, 179–187. doi:10.1021/ic201417y

Cullen, W., Takezawa, H., and Fujita, M. (2019). Demethylenation of Cyclopropanes *via* Photoinduced Guest-to-Host Electron Transfer in an M6L4 Cage. *Angew. Chem. Int. Ed.* 58, 9171–9173. doi:10.1002/anie.201904752

Debata, N. B., Tripathy, D., and Sahoo, H. S. (2019). Development of Coordination Driven Self-Assembled Discrete Spherical Ensembles. *Coord. Chem. Rev.* 387, 273–298. doi:10.1016/j.ccr.2019.02.016

Farrell, J. R., Mirkin, C. A., Guzei, I. A., Liable-Sands, L. M., and Rheingold, A. L. (1998). The Weak-Link Approach to the Synthesis of Inorganic Macrocycles. *Angew. Chem. Int. Ed.* 37, 465–467. doi:10.1002/(sici)1521-3773(19980302)37:4<465::aid-anie465>3.0.co;2-a

Feixas, F., Lindert, S., Sinko, W., and McCammon, J. A. (2014). Exploring the Role of Receptor Flexibility in Structure-Based Drug Discovery. *Biophy. Chem.* 186, 31–45. doi:10.1016/j.bpc.2013.10.007

Findlay, J. A., McAdam, C. J., Sutton, J. J., Preston, D., Gordon, K. C., and Crowley, J. D. (2018). Metallosupramolecular Architectures Formed with Ferrocene-Linked Bis-Bidentate Ligands: Synthesis, Structures, and Electrochemical Studies. *Inorg. Chem.* 57, 3602–3614. doi:10.1021/acs.inorgchem.7b02503

Frederix, P. W. J. M., Patmanidis, I., and Marrink, S. J. (2018). Molecular Simulations of Self-Assembling Bio-Inspired Supramolecular Systems and Their Connection to Experiments. *Chem. Soc. Rev.* 47, 3470–3489. doi:10.1039/c8cs00040a

Fujita, M., Oguro, D., Miyazawa, M., Oka, H., Yamaguchi, K., and Ogura, K. (1995). Self-assembly of Ten Molecules Into Nanometre-Sized Organic Host Frameworks. *Nature* 378, 469–471. doi:10.1038/378469a0

Galan, A., and Ballester, P. (2016). Stabilization of Reactive Species by Supramolecular Encapsulation. *Chem. Soc. Rev.* 45, 1720–1737. doi:10.1039/C5CS00861A

García-Simón, C., Colomban, C., Çetin, Y. A., Gimeno, A., Pujals, M., Ubasart, E., et al. (2020). Complete Dynamic Reconstruction of C60, C70, and (C59N)2 Encapsulation into an Adaptable Supramolecular Nanocapsule. *J. Am. Chem. Soc.* 142, 16051–16063. doi:10.1021/jacs.0c07591

García-Simón, C., Garcia-Borràs, M., Gómez, L., Parella, T., Osuna, S., Juanhuix, J., et al. (2014). Sponge-like Molecular Cage for Purification of Fullerenes. *Nat. Commun.* 5, 5557. doi:10.1038/ncomms6557

Giannesci, N. C., Masar, M. S., III, and Mirkin, C. A. (2005). Development of a Coordination Chemistry-Based Approach for Functional Supramolecular Structures. *Acc. Chem. Res.* 38, 825–837. doi:10.1021/ar980101q

Han, M., Engelhard, D. M., and Clever, G. H. (2014). Self-Assembled Coordination Cages Based on Banana-Shaped Ligands. *Chem. Soc. Rev.* 43, 1848–1860. doi:10.1039/C3CS60473J

Han, M., Michel, R., He, B., Chen, Y.-S., Stalke, D., John, M., et al. (2013). Light-Triggered Guest Uptake and Release by a Photochromic Coordination Cage. *Angew. Chem. Int. Ed.* 52, 1319–1323. doi:10.1002/anie.201207373

Han, Y.-F., and Jin, G.-X. (2011). Flexible Organometallic Cages: Efficient Formation by C–H Activation-Directed Muticomponent Assembly, Isomerization, and Host-Guest Properties. *Chem. Asian J.* 6, 1348–1352. doi:10.1002/asia.201100080

Harris, K., Fujita, D., and Fujita, M. (2013). Giant Hollow MnL2n Spherical Complexes: Structure, Functionalisation and Applications. *Chem. Commun.* 49, 6703–6712. doi:10.1039/C3CC43191F

Heard, A. W., and Goldup, S. M. (2020). Simplicity in the Design, Operation, and Applications of Mechanically Interlocked Molecular Machines. *ACS Cent. Sci.* 6, 117–128. doi:10.1021/acscentsci.9b01185

Hiraoka, S., Harano, K., Tanaka, T., Shiro, M., and Shionoya, M. (2003). Quantitative Formation of Sandwich-Shaped Trinuclear Silver(I) Complexes and Dynamic Nature of Their P⇌M Flip Motion in Solution. *Angew. Chem. Int. Ed.* 42, 5182–5185. doi:10.1002/anie.200351068

Hoyas Pérez, N., and Lewis, J. E. M. (2020). Synthetic Strategies towards Mechanically Interlocked Oligomers and Polymers. *Org. Biomol. Chem.* 18, 6757–6780. doi:10.1039/d0ob01583k

Jansze, S. M., Wise, M. D., Vologzhanina, A. V., Scopelliti, R., and Severin, K. (2016). PdII2L4-type Coordination Cages up to Three Nanometers in Size. *Chem. Sci.* 8, 1901–1908. doi:10.1039/c6sc04732g

Kealy, T. J., and Pauson, P. L. (1951). A New Type of Organo-Iron Compound. *Nature* 168, 1039–1040. doi:10.1038/1681039b0

Kerstin, B., Meyer, M., Powers, R. E., and Raymond, K. N. (1996). Dinuclear Catecholate Helicates: Their Inversion Mechanism. *J. Am. Chem. Soc.* 118, 7221–7222. doi:10.1021/ja9613522

Kishi, N., Li, Z., Sei, Y., Akita, M., Yoza, K., Siegel, J. S., et al. (2013). Wide-Ranging Host Capability of a PdII-Linked M2L4 Molecular Capsule With an Anthracene Shell. *Chem. Eur. J.* 19, 6313–6320. doi:10.1002/chem.201204010

Kishi, N., Li, Z., Yoza, K., Akita, M., and Yoshizawa, M. (2011). An M2L4 Molecular Capsule With an Anthracene Shell: Encapsulation of Large Guests up to 1 nm. *J. Am. Chem. Soc.* 133, 11438–11441. doi:10.1021/ja2037029

Kohyama, Y., Murase, T., and Fujita, M. (2014). Metal-Organic Proximity in a Synthetic Pocket. *J. Am. Chem. Soc.* 136, 2966–2969. doi:10.1021/ja412582k

Lee, J., Lim, S., Kim, D., Jung, O.-S., and Lee, Y.-A. (2020). Flexibility and Anion Exchange of [(X)@Pd2L4] Cages for Recognition of Size and Charge of Polyatomic Anions. *Dalton Trans.* 49, 15002–15008. doi:10.1039/d0dt03005h

Lewis, J. E. M., and Crowley, J. D. (2014). Exo- and Endo-Hedral Interactions of Counteranions with Tetracationic Pd2L4 Metallosupramolecular Architectures. *Supramolecular Chem.* 26, 173–181. doi:10.1080/10610278.2013.842644

Lewis, J. E. M., and Crowley, J. D. (2020). Metallo-Supramolecular Self-Assembly with Reduced-Symmetry Ligands. *ChemPlusChem* 85, 815–827. doi:10.1002/cplu.202000153

Lewis, J. E. M., Galli, M., and Goldup, S. M. (2017). Properties and Emerging Applications of Mechanically Interlocked Ligands. *Chem. Commun.* 53, 298–312. doi:10.1039/C6CC07377H

Lewis, J. E. M., Gavey, E. L., Cameron, S. A., and Crowley, J. D. (2012). Stimuli-Responsive Pd2L4 metallosupramolecular Cages: Towards Targeted Cisplatin Drug Delivery. *Chem. Sci.* 3, 778–784. doi:10.1039/C2SC00899H

Li, H., Yao, Z.-J., Liu, D., and Jin, G.-X. (2015). Multi-component Coordination-Driven Self-Assembly toward Heterometallic Macrocycles and Cages. *Coord. Chem. Rev.* 293-294, 139–157. doi:10.1016/j.ccr.2014.08.014

Liao, P., Langloss, B. W., Johnson, A. M., Knudsen, E. R., Tham, F. S., Julian, R. R., et al. (2010). Two-component Control of Guest Binding in a Self-Assembled Cage Molecule. *Chem. Commun.* 46, 4932–4934. doi:10.1039/C0CC00234H

Lin, Q., Gao, L., Kauffmann, B., Zhang, J., Ma, C., Luo, D., et al. (2018). Helicity Adaptation Within a Quadruply Stranded Helicate by Encapsulation. *Chem. Commun.* 54, 13447–13450. doi:10.1039/c8cc07932c

Lindner, E., Zong, R., Eichele, K., Weisser, U., and Ströbele, M. (2003). Synthesis and Structure of Redox-Active Heterotetranuclear Molecular Polygons by Self-Assembly of Two Ferrocene-Bridged Bis(pyridines) With Two Transition Metals. *Eur. J. Inorg. Chem.* 2003, 705–712. doi:10.1002/ejic.200390097

Liu, C. L., Bobylev, E. O., Fu, Y., Poole, D. A., III, Robeyns, K., Fustin, C. A., et al. (2020). Balancing Ligand Flexibility versus Rigidity for the Stepwise Self-Assembly of M12L24 *via* M6L12 Metal-Organic Cages. *Chem. Eur. J.* 26, 11960–11965. doi:10.110/chem.20200139910.1002/chem.202001399

McConnell, A. J., Wood, C. S., Neelakandan, P. P., and Nitschke, J. R. (2015). Stimuli-Responsive Metal-Ligand Assemblies. *Chem. Rev.* 115, 7729–7793. doi:10.1021/cr500632f

McMorran, D. A., and Steel, P. J. (1998). The First Coordinatively Saturated, Quadruply Stranded Helicate and its Encapsulation of a Hexafluorophosphate Anion, *Angew. Chem. Int. Ed. Engl.* 37. 3295–3297. doi:10.1002/(SICI)1521-3773(19981217)37:23<3295::AID-ANIE3295>3.0.CO;2-5

Mecozzi, S., and Rebek, J., Jr. (1998). The 55% Solution: A Formula for Molecular Recognition in the Liquid State. *Chem. Eur. J.* 4, 1016–1022. doi:10.1002/(SICI)1521-3765(19980615)4:6<1016::AID-CHEM1016>3.0.CO;2-B

Metherell, A. J., Cullen, W., Williams, N. H., and Ward, M. D. (2018). Binding of Hydrophobic Guests in a Coordination Cage Cavity Is Driven by Liberation of "High-Energy" Water. *Chem. Eur. J.* 24, 1554–1560. doi:10.1002/cem.201704163

Mirtschin, S., Slabon-Turski, A., Scopelliti, R., Velders, A. H., and Severin, K. (2010). A Coordination Cage with an Adaptable Cavity Size. *J. Am. Chem. Soc.* 132, 14004–14005. doi:10.1021/ja1063789

Nishioka, Y., Yamaguchi, T., Yoshizawa, M., and Fujita, M. (2007). Unusual [2+4] and [2+2] Cycloadditions of Arenes in the Confined Cavity of Self-Assembled Cages. *J. Am. Chem. Soc.* 129, 7000–7001. doi:10.1021/ja071591x

Oldknow, S., Martir, D. R., Pritchard, V. E., Blitz, M. A., Fishwick, C. W. G., Zysman-Colman, E., et al. (2018). Structure-Switching M3L2 Ir(iii) Coordination Cages With Photo-Isomerising Azo-Aromatic Linkers. *Chem. Sci.* 9, 8150–8159. doi:10.1039/C8SC03499K

Ono, K., Yoshizawa, M., Akita, M., Kato, T., Tsunobuchi, Y., Ohkoshi, S.-i., et al. (2009). Spin Crossover by Encapsulation. *J. Am. Chem. Soc.* 131, 2782–2783. doi:10.1021/ja8089894

Ono, K., Yoshizawa, M., Kato, T., Watanabe, K., and Fujita, M. (2007). Porphine Dimeric Assemblies in Organic-Pillared Coordination Cages. *Angew. Chem. Int. Ed.* 46, 1803–1806. doi:10.1002/anie.200604790

Ovchinnikov, M. V., Holliday, B. J., Mirkin, C. A., Zakharov, L. N., and Rheingold, A. L. (2002). Threefold Symmetric Trimetallic Macrocycles Formed *via* the Weak-Link Approach. *Proc. Natl. Acad. Sci.* 99, 4927–4931. doi:10.1073/pnas.072690599

Pilgrim, B. S., and Champness, N. R. (2020). Metal-Organic Frameworks and Metal-Organic Cages - A Perspective. *ChemPlusChem* 85, 1842–1856. doi:10.1002/cplu.202000408

Plajer, A. J., Rizzuto, F. J., von Krbek, L. K. S., Gisbert, Y., Martínez-Agramunt, V., and Nitschke, J. R. (2020). Oxidation Triggers Guest Dissociation During Reorganization of an FeII4L6 Twisted Parallelogram. *Chem. Sci.* 11, 10399–10404. doi:10.1039/d0sc04352d

Pullen, S., Tessarolo, J., and Clever, G. H. (2021). Increasing Structural and Functional Complexity in Self-Assembled Coordination Cages. *Chem. Sci.* 12, 7269–7293. doi:10.1039/D1SC01226F

Rizzuto, F. J., von Krbek, L. K. S., and Nitschke, J. R. (2019). Strategies for Binding Multiple Guests in Metal-Organic Cages. *Nat. Rev. Chem.* 3, 204–222. doi:10.1038/s41570-019-0085-3

Sarada, G., Kim, A., Kim, D., and Jung, O.-S. (2020). Diverse Anion Exchange of Pliable [X2@Pd3L4]4+ Double Cages: a Molecular Ruler for Recognition of Polyatomic Anions. *Dalton Trans.* 49, 6183–6190. doi:10.1039/d0dt01027h

Schmidt, B. M., Osuga, T., Sawada, T., Hoshino, M., and Fujita, M. (2016). Compressed Corannulene in a Molecular Cage. *Angew. Chem. Int. Ed.* 55, 1561–1564. doi:10.1002/anie201509963

Scottwell, S. Ø., and Crowley, J. D. (2016). Ferrocene-containing Non-interlocked Molecular Machines. *Chem. Commun.* 52, 2451–2464. doi:10.1039/c5cc09569g

Sinha, I., and Mukherjee, P. S. (2018). Chemical Transformations in Confined Space of Coordination Architectures. *Inorg. Chem.* 57, 4205–4221. doi:10.1021/acs.inorgchem.7b03067

Spicer, R. L., Stergiou, A. D., Young, T. A., Duarte, F., Symes, M. D., and Lusby, P. J. (2020). Host-Guest-Induced Electron Transfer Triggers Radical-Cation Catalysis. *J. Am. Chem. Soc.* 142, 2134–2139. doi:10.1021/jacs.9b11273

Steel, P. J., and McMorran, D. A. (2019). Selective Anion Recognition by a Dynamic Quadruple Helicate. *Chem. Asian J.* 14, 1098–1101. doi:10.1002/asia.201801262

Takezawa, H., Murase, T., Resnati, G., Metrangolo, P., and Fujita, M. (2014). Recognition of Polyfluorinated Compounds Through Self-Aggregation in a Cavity. *J. Am. Chem. Soc.* 136, 1786–1788. doi:10.1021/ja412893c

Takezawa, H., Tabuchi, R., Sunohara, H., and Fujita, M. (2020). Confinement of Water-Soluble Cationic Substrates in a Cationic Molecular Cage by Capping the Portals with Tripodal Anions. *J. Am. Chem. Soc.* 142, 17919–17922. doi:10.1021/jacs.0c08835

Tashiro, S., Tominaga, M., Kawano, M., Therrien, B., Ozeki, T., and Fujita, M. (2005). Sequence-Selective Recognition of Peptides within the Single Binding Pocket of a Self-Assembled Coordination Cage. *J. Am. Chem. Soc.* 127, 4546–4547. doi:10.1021/ja044782y

Tsutsui, T., Catti, L., Yoza, K., and Yoshizawa, M. (2020). An Atropisomeric M2L4 Cage Mixture Displaying Guest-Induced Convergence and Strong Guest Emission in Water. *Chem. Sci.* 11, 8145–8150. doi:10.1039/d0sc03223a

Vasdev, R. A. S., Findlay, J. A., Garden, A. L., and Crowley, J. D. (2019). Redox Active [Pd2L4]4+ Cages Constructed From Rotationally Flexible 1,1′-disubstituted Ferrocene Ligands. *Chem. Commun.* 55, 7506–7509. doi:10.1039/c9cc03321a

Vasdev, R. A. S., Findlay, J. A., Turner, D. R., and Crowley, J. D. (2021). Self-Assembly of a Redox Active, Metallosupramolecular [Pd3L6]6+ Complex Using a Rotationally Flexible Ferrocene Ligand. *Chem. Asian J.* 16, 39–43. doi:10.1002/asia.202001277

Wilson, B. H., and Loeb, S. J. (2020). Integrating the Mechanical Bond Into Metal-Organic Frameworks. *Chem* 6, 1604–1612. doi:10.1016/j.chempr.2020.06.016

Wong, K. K. G., Hoyas Pérez, N., White, A. J. P., and Lewis, J. E. M. (2020). Self-assembly of a Porous Metallo-[5]rotaxane. *Chem. Commun.* 56, 10453–10456. doi:10.1039/D0CC04780E

Xu, J., Parac, T. N., and Raymond, K. N. (1999). Meso Myths: What Drives Assembly of Helical versus meso-[M2L3] Clusters? *Angew. Chem. Int. Ed.* 38:2, 2878–2882. doi:10.1002/(SICI)1521-3773(19991004)38:19<2878::aid-anie2878>3.0.co;2-w

Yamauchi, Y., Yoshizawa, M., Akita, M., and Fujita, M. (2010). Engineering Double to Quintuple Stacks of a Polarized Aromatic in Confined Cavities. *J. Am. Chem. Soc.* 132, 960–966. doi:10.1021/ja904063r

Yoshizawa, M., Klosterman, J. K., and Fujita, M. (2009). Functional Molecular Flasks: New Properties and Reactions within Discrete, Self-Assembled Hosts. *Angew. Chem. Int. Ed.* 48, 3418–3438. doi:10.1002/anie.200805340

Yoshizawa, M., Nakagawa, J., Kumazawa, K., Nagao, M., Kawano, M., Ozeki, T., et al. (2005a). Discrete Stacking of Large Aromatic Molecules within Organic-Pillared Coordination Cages. *Angew. Chem. Int. Ed.* 44, 1810–1813. doi:10.1002/anie.200462171

Yoshizawa, M., Ono, K., Kumazawa, K., Kato, T., and Fujita, M. (2005b). Metal–Metal d–d Interaction through the Discrete Stacking of Mononuclear M(II) Complexes (M = Pt, Pd, and Cu) Within an Organic-Pillared Coordination Cage. *J. Am. Chem. Soc.* 127, 10800–10801. doi:10.1021/ja053009f

Young, T. A., Gheorghe, R., and Duarte, F. (2020a). Cgbind: A Python Module and Web App for Automated Metallocage Construction and Host-Guest Characterization. *J. Chem. Inf. Model.* 60, 3546–3557. doi:10.1021/acs.jcim.0c00519

Young, T. A., Martí-Centelles, V., Wang, J., Lusby, P. J., and Duarte, F. (2020b). Rationalizing the Activity of an "Artificial Diels-Alderase": Establishing Efficient and Accurate Protocols for Calculating Supramolecular Catalysis. *J. Am. Chem. Soc.* 142, 1300–1310. doi:10.1021/jacs.9b10302

Yue, N. L. S., Eisler, D. J., Jennings, M. C., and Puddephatt, R. J. (2004). Macrocyclic and Lantern Complexes of Palladium(II) With Bis(amidopyridine) Ligands: Synthesis, Structure, and Host–Guest Chemistry. *Inorg. Chem.* 43, 7671–7681. doi:10.1021/ic048893+

Yue, N., Qin, Z., Jennings, M. C., Eisler, D. J., and Puddephatt, R. J. (2003). Host Complexes that Adapt to Their Guests: Amphitopic Receptors. *Inorg. Chem. Commun.* 6, 1269–1271. doi:10.1016/S1387-7003(03)00246-6

Zhang, D., Ronson, T. K., Zou, Y.-Q., and Nitschke, J. R. (2021). Metal-Organic Cages for Molecular Separations. *Nat. Rev. Chem.* 5, 168–182. doi:10.1038/s41570-020-00246-1

Conflict of Interest: The authors declare that the research was conducted in the absence of any commercial or financial relationships that could be construed as a potential conflict of interest.

frontiers in Chemistry

ORIGINAL RESEARCH
published: 17 June 2021
doi: 10.3389/fchem.2021.685783

Toward Food Freshness Monitoring: Coordination Binding–Based Colorimetric Sensor Array for Sulfur-Containing Amino Acids

*Xiaojun Lyu[1], Wei Tang[1], Yui Sasaki[1], Jie Zhao[2], Tingting Zheng[2], Yang Tian[2] and Tsuyoshi Minami[1]**

[1]Institute of Industrial Science, The University of Tokyo, Tokyo, Japan, [2]Key Laboratory of Green Chemistry and Chemical Processes, Department of Chemistry, School of Chemistry and Molecular Engineering, East China Normal University, Shanghai, China

Herein, a self-assembled colorimetric chemosensor array composed of off-the-shelf catechol dyes and a metal ion (i.e., Zn^{2+}) has been used for the sulfur-containing amino acids (SCAAs; i.e., glutathione, glutathione disulfide, L–cysteine, DL–homocysteine, and L–cystine). The coordination binding–based chemosensor array (CBSA) fabricated by a competitive assay among SCAAs, Zn^{2+} ions, and catechol dyes [i.e., pyrocatechol violet (PV), bromopyrogallol red (BPR), pyrogallol red (PR), and alizarin red S (ARS)] yielded fingerprint-like colorimetric changes. We succeeded in the qualification of SCAAs based on pattern recognition [i.e., a linear discrimination analysis (LDA)] with 100% correct classification accuracy. The semiquantification of reduced/oxidized forms of SCAAs was also performed based on LDA. Furthermore, we carried out a spike test of glutathione in food samples using the proposed chemosensor array with regression analysis. It is worth mentioning that we achieved a 91–110% recovery rate in real sample tests, which confirmed the accuracy of the constructed model. Thus, this study represents a step forward in assessing food freshness based on supramolecular analytical methods.

Keywords: glutathione, cysteine, chemosensor array, food analysis, regression analysis, colorimetric sensing

OPEN ACCESS

Edited by:
Tony D. James,
University of Bath, United Kingdom

Reviewed by:
Robert Elmes,
Maynooth University, Ireland
Xin Wu,
The University of Sydney, Australia

****Correspondence:***
Tsuyoshi Minami
tminami@iis.u-tokyo.ac.jp

Specialty section:
This article was submitted to Supramolecular Chemistry, a section of the journal Frontiers in Chemistry

Received: *25 March 2021*
Accepted: *31 May 2021*
Published: *17 June 2021*

Citation:
Lyu X, Tang W, Sasaki Y, Zhao J, Zheng T, Tian Y and Minami T (2021) Toward Food Freshness Monitoring: Coordination Binding–Based Colorimetric Sensor Array for Sulfur-Containing Amino Acids. Front. Chem. 9:685783. doi: 10.3389/fchem.2021.685783

INTRODUCTION

To date, there is an increasing demand from consumers to evaluate the safety of food products. Freshness is the main standard for food quality assessment, including the physical form (Luo et al., 2021), the number of microorganisms (Jacxsens et al., 2003), and biochemical components (Lonchamp et al., 2009). Among the common biochemical components, sulfur-containing amino acids (SCAAs) including L–cysteine (Cys) (Cebi et al., 2017; Garcia et al., 2015), L–cystine (CySS) (Chen and Li, 2019), DL–homocysteine (HCys) (Hoey et al., 2007), glutathione reduced form (GSH) (Xu et al., 2015), and glutathione oxidized form (GSSG) (Moreira et al., 2011) have been used as analyte markers in food samples, including wine (Valero et al., 2003), wheat flour (Reinbold et al., 2008), and fruit juice (Fracassetti et al., 2011), to evaluate food quality. The reduced form of SCAAs acts as antioxidants in food (Nikolantonaki et al., 2018), which is oxidized by air over time. Thus, by quantifying the reduced form and the oxidized form of SCAAs, the freshness of food samples can be assessed.

SCAAs are currently quantified by instrumental methods (i.e., high-performance liquid chromatography (HPLC) (Zhu et al., 2020) and mass spectrometry (MS) (Kuster et al., 2008), or

enzyme-linked immunosorbent assay (ELISA) (Kurose et al., 1997) because of their high reliability and accuracy. However, the requirement of expensive instruments, complex sensing procedures, and trained personnel limits their application for rapid and straightforward analysis. To simplify the sensing procedures, chemosensors have become a promising option, which can exhibit optical property changes based on molecular recognition (Hyman and Franz, 2012; Lee et al., 2015; Wu et al., 2015; Yan et al., 2017; Khorasani et al., 2019; Roy, 2021). In this regard, several optical chemosensors have been developed for natural amino acids (Buryak and Severin, 2005; Ma et al., 2013; Yin et al., 2013; Sener et al., 2014; Ghasemi et al., 2015; Meng et al., 2015; Chao and Zhang, 2017; Gholami et al., 2019; Liu et al., 2019; Xu et al., 2020). However, these chemosensors require complicated synthetic processes (Yang et al., 2011; Song et al., 2016; Yang et al., 2018), which limit their practical usage in real-world scenarios. Chemosensor arrays by supramolecular interactions with pattern recognition can avoid the synthetic processes and simultaneously quantify multiple analytes (Cao et al., 2020; Sasaki et al., 2021a; Sasaki et al., 2021b; Lyu et al., 2021). To the best of our knowledge, the development of a colorimetric sensor array using only a combination of off-the-shelf reagents for simultaneous SCAA detection has not yet been reported.

Herein, we report a simple, rapid, and accurate coordination binding–based chemosensor array (CBSA) for the high-throughput colorimetric detection of SCAAs (GSH, GSSG, Cys, hCys, and CySS). Four catechol dyes [i.e., pyrocatechol violet (PV), bromopyrogallol red (BPR), pyrogallol red (PR), and alizarin red S (ARS)] were employed as colorimetric indicators (Sasaki et al., 2019), and Zn^{2+} ions were used as the color and binding manipulator (Kaushik et al., 2015). The catechol dyes produce the dye–Zn^{2+} coordination complex upon the addition of Zn^{2+} ions, which exhibit colorimetric changes (Hamedpour et al., 2019). Subsequently, colorimetric changes can be observed by the addition of SCAAs because of the generation of coordination complexes of Zn^{2+} and SCAAs, which dissociate the dye–Zn^{2+} complex with a colorimetric recovery (**Figure 1**). The use of commercially available reagents avoids complex synthesis, which is a major advantage for the simple establishment of a sensor array (Sasaki et al., 2021c). In this study, various cross-reactive colorimetric responses demonstrated by the CBSA were analyzed using chemometric methods, including a linear discrimination analysis (LDA) (Anzenbacher et al., 2010) and regression analysis (SVM) (Hamel, 2009; Minami et al., 2012). The LDA is a mathematical method used in statistics to establish a linear combination to characterize two or more groups of objects, which could be used for qualitative and semiquantitative analyses of the targets. The SVM is a supervised learning model for data classification and regression analysis. To predict the unknown concentrations of the target samples, we established the SVM model with the calibration dataset using standard solutions. Notably, we quantified the pseudo-oxidation processes of SCAAs in aqueous media and predicted the GSH concentration in tomato and grapefruit juice (Minich and Brown, 2019). These results indicate that our simple preparation and user-friendly sensing system could achieve high-throughput analysis for SCAAs, which would be a step forward for assessing food freshness based on supramolecular analytical methods.

MATERIALS AND METHODS

Materials

SCAAs (Cys, CySS, GSH, and HCys), 1,4-benzoquinone (pBQ), 3-mercaptopropionic acid (3-MPA), PR, BPR, PV, and other

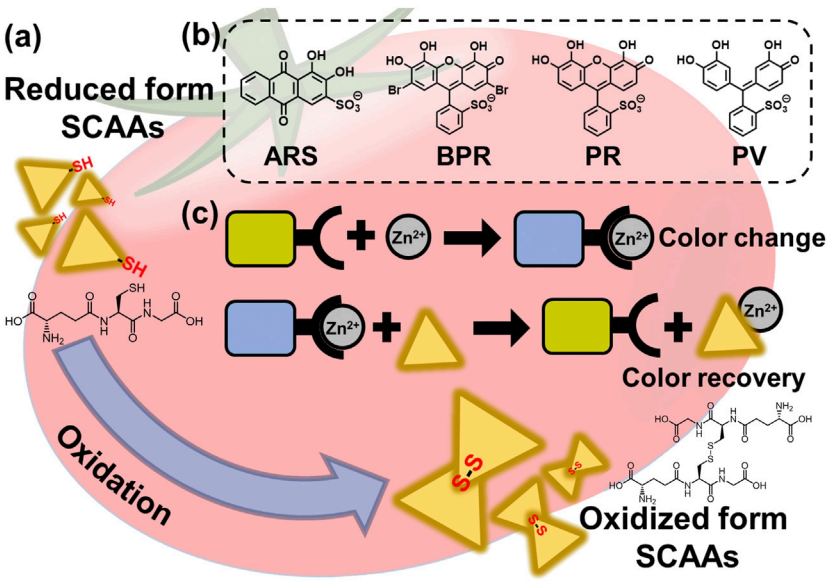

FIGURE 1 | (A) Schematic illustration of the SCAA oxidation (e.g., glutathione). **(B)** Chemical structure of catechol dyes (PV, BPR, PR, and ARS). **(C)** Illustrated detection mechanism of SCAAs.

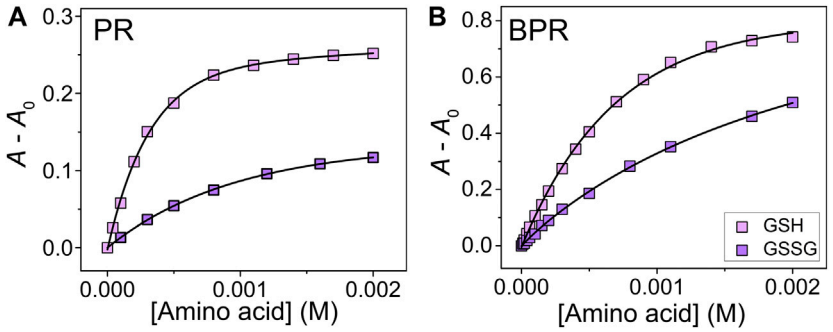

FIGURE 2 | UV-Vis titration isotherm of **(A)** PR–Zn^{2+} and **(B)** BPR–Zn^{2+} to GSH and GSSG (0–2.0 mM) at 25°C. The concentrations of dye and Zn^{2+} were 40 μM.

amino acids [L–alanine (Ala), L–arginine (Arg), L–aspartic acid (Asp), L–glutamine (Gln), L–glutamic acid (Gln), glycine (Gly), L–histidine (His), L–isoleucine (Ile), L–leucine (Leu), L–lysine (Lys), L–methionine (Met), L–phenylalanine (Phe), L–proline (Pro), L–serine (Ser), L–threonine (Thr), L–tryptophan (Trp), L–tyrosine (Tyr), and L–valine (Val)] were purchased from Tokyo Chemical Industries Co. Inc. (Tokyo, Japan). Additionally, ARS, sodium chloride, methanol, and zinc nitrate hexahydrate were purchased from FUJIFILM Wako Pure Chemical Co. Inc. (Osaka, Japan). *N*-(2-hydroxyethyl)-1-piperazineethanesulfonic acid (HEPES) was purchased from Dojindo Laboratories (Kumamoto, Japan). All chemicals were used without further purification. All aqueous samples were prepared with Milli-Q water (18.2 MΩcm) (Millipore, Bedford, MA, United States).

Measurements

The UV-Vis spectra were measured within the wavelength range of 350–800 nm at a scan rate of 240 nm/min using a Shimadzu UV-2600 UV-Vis spectrophotometer. The dye (40 μM) was mixed with Zn^{2+} solutions at various concentrations and incubated at room temperature (25°C) for 10–60 min (i.e., ARS, BPR, and PR for 60 min, and PV for 10 min) in HEPES buffer (50 mM) with 10 mM NaCl at pH 7.4. Titration isotherms were prepared from the variations with maximum absorption at 615 nm for PV, 557 nm for BPR, 543 nm for PR, and 515 nm for ARS, respectively.

Qualitative and quantitative analyses were carried out by array experiments in 384-well microplates using a microplate reader (SYNERGY H1, Biotek, Winooski, United States). For the array experiments, the dye–Zn^{2+} complex solution (90 μL) was first added to each well. Subsequently, the analyte and buffer solutions (10 μL) were mixed with the sensor solution. The microplate was then shaken for 3 min for incubation. Furthermore, a spike test using food samples was performed to evaluate the accuracy of the chemosensor array for real-world applications. A commercial tomato juice (Ito En tomato juice) was centrifuged at 14,000 rpm for 30 min to remove any insoluble matter. The supernatant fluid was diluted 40-fold and applied to a 384-well microplate without any further treatment. A series of standard GSH samples was calibrated with a concentration of 0–2 mM.

LDA was applied for qualitative analysis based on the raw dataset without any further treatment using SYSTAT 13. Moreover, a semiquantitative assay of the mixture of GSH/GSSG and Cys/CySS was also carried out using LDA. Student's *t*-test was used to eliminate outlier data points. The quantitative analyses and real sample tests were conducted by a regression analysis based on a supporting vector machine (SVM) with Solo 7.5.2. Two parameters [root-mean-square errors for calibration (RMSEC) and prediction (RMSEP)] were applied to confirm the accuracy of the constructed models.

DISCUSSIONS

The complexation of catechol dyes and Zn^{2+} ions in a HEPES buffer (50 mM) with NaCl (10 mM) at pH 7.4 and at 25°C was evaluated according to a previous study (Hamedpour et al., 2019). To maintain the ionic strength, sodium chloride (10 mM) was added. Each dye complex showed specific colorimetric changes upon the addition of SCAAs (GSH, GSSG, Cys, and hCys) (see **Supplementary Material**). The spectral shift accompanying the color recovery was observed by the ascension of the concentration, indicating the decomposition of the Zn^{2}–catechol dye complex. Because of the low solubility of CySS in the buffer solution, we could not apply UV-Vis titration for CySS in this study. Association constants (K_{assoc}) for the SCAAs with Zn^{2+} ions were calculated by titration isotherms according to a nonlinear regression fitting method (see supporting material) (Hargrove et al., 2010). The K_{assoc} for GSH were determined as follows: PV: $(4.7 \pm 0.3) \times 10^3\ M^{-1}$; BPR: $(2.8 \pm 0.8) \times 10^4\ M^{-1}$; PR: $(1.5 \pm 0.3) \times 10^5\ M^{-1}$; and ARS: $(6.5 \pm 0.6) \times 10^5\ M^{-1}$. In the case of GSSG, the K_{assoc} were calculated as $(1.6 \pm 0.1) \times 10^4\ M^{-1}$, $(9.6 \pm 1.8) \times 10^3\ M^{-1}$, $(2.4 \pm 0.6) \times 10^4\ M^{-1}$, and $(9.2 \pm 1.7) \times 10^6\ M^{-1}$ PV for, BPR, PR, and ARS, respectively. With the various binding affinities for the targets, our proposed chemosensor array could be applied for simultaneous qualitative and quantitative SCAA detection. Interestingly, the reduced/oxidized form of glutathione showed different isotherms toward the dye–Zn^{2+} complex (**Figure 2**), which indicates that we could monitor the oxidizing process of SCAAs based on colorimetric changes.

Subsequently, we applied natural amino acids to our proposed chemosensor array for the selectivity test. Most of the natural

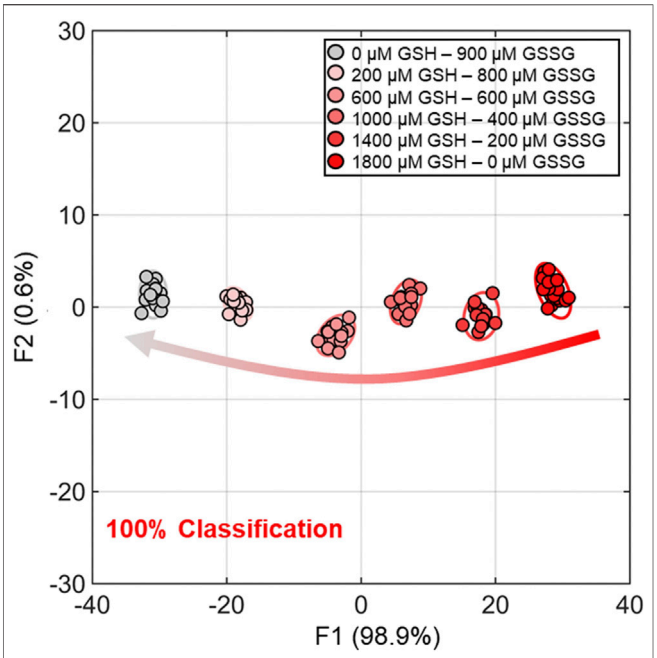

FIGURE 3 | Semiquantitative LDA result for dynamic molar ratios of GSH and GSSG. The measurements were performed with eighteen repetitions for each concentration group for 100% classification accuracy. The confidence ellipses indicate 95% confidence rate.

amino acids [i.e., valine (Val), tyrosine (Tyr), tryptophan (Trp), threonine (Thr), serine (Ser), proline (Pro), phenylalanine (Phe), methionine (Met), lysine (Lys), leucine (Leu), isoleucine (Ile), glycine (Gly), glutamic acid (Glu), glutamine (Gln), aspartic acid (Asp), asparagine (Asn), arginine (Arg), and alanine (Ala)] showed slight or almost no response, whereas histidine (His) caused significant absorbance changes with the peak wavelength shifts. This response was due to the high association constant of Zn^{2+} ions and His compared to the aforementioned natural amino acids (Krężel and Maret, 2016). In addition, the selectivity test indicated that the sulfur group contributes to the sensing mechanism based on CBSA (see **Supplementary Material**) (Namuswe and Berg, 2012). Thus, we attempted to apply a high-throughput assay to the aforementioned five analytes (i.e., GSH, GSSG, hCys, Cys, and His). We selected LDA among the pattern recognition methods because it can reduce the dimensionality and evaluate classification accuracy based on a leave-one-out cross-validation protocol (i.e., the jackknife method). The classification of the six cluster groups (one control group and five analyte groups) achieved 100% accuracy (**Supplementary Figure S24**). Thus, we can conclude that the proposed chemosensor array can discriminate between similar structural amino acids and reduced/oxidized forms of SCAAs.

In addition, semiquantitative LDA was carried out using the proposed chemosensor array for the mixture of oxidized/reduced SCAAs (i.e., glutathione and cysteine). For example, GSH–GSSG was selected as the representative analyte pair at various concentration ratios (**Figure 3**). The dynamic concentration changing rate of GSH and GSSG was selected as 2:1 to mimic the natural oxidizing process of glutathione (**Supplementary Table S5**). It is worth mentioning that the semiquantitative LDA of the mixture of oxidized/reduced SCAAs achieved a 100% correct classification rate. Furthermore, quantitative analyses were employed without sample preprocessing to investigate their capability for practical applications. Quantitative analyses were performed in a mixture containing GSH–GSSG or Cys–CySS in different molar ratios. An SVM-based regression analysis was carried out to establish a rapid and accurate assay (**Figure 4**). The SVM process includes two steps: the first step for the calibration of the measured data set and the second step for feature prediction of the unknown samples. More importantly, the limits of detection (LoDs) based on the 3σ method (Miller and Miller, 2018) were calculated as follows: 2.4 ppm for Cys, 2.0 ppm for hCys, 0.4 ppm for GSH, and 2.6 ppm for GSSG. As aforementioned, the constructed SVM model demonstrated the prediction of unknown concentrations of SCAAs with high accuracy, which indicates our array system could be applied to real sample analyses.

Finally, we performed a spike test with GSH using concentrated tomato juice, grapefruit juice, and fresh tomato samples (Minich and Brown, 2019). Different concentrations of GSH were mixed

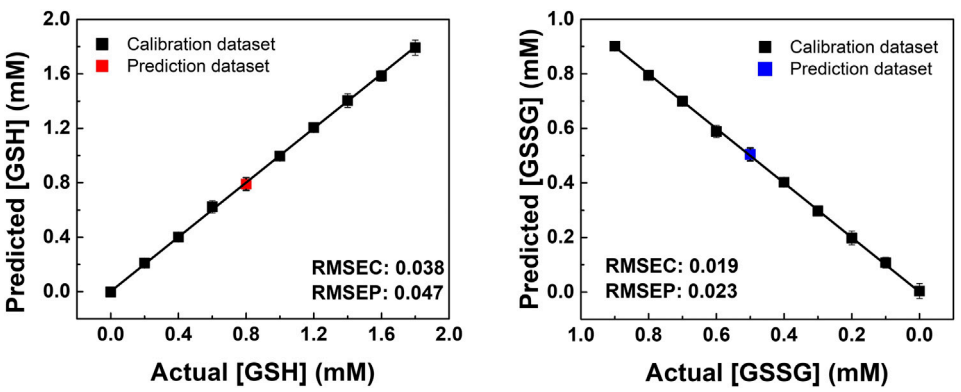

FIGURE 4 | SVM regression analysis for quantitative analysis of the GSH and GSSG mixtures in various concentration ratios. The RMSEC and RMSEP values (shown as insets) represent the accuracy of the constructed model and the prediction.

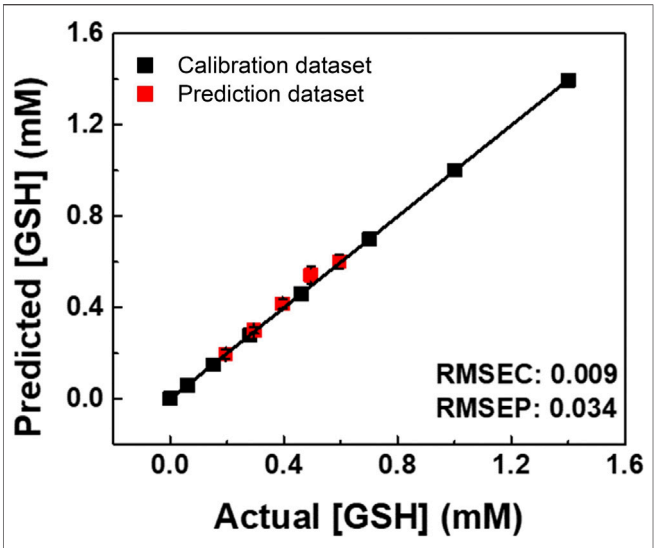

FIGURE 5 | SVM regression for real sample analysis of GSH in a juice (Ito En tomato juice). The RMSEC and RMSEP values (shown as insets) represent the accuracy of the constructed model and the prediction.

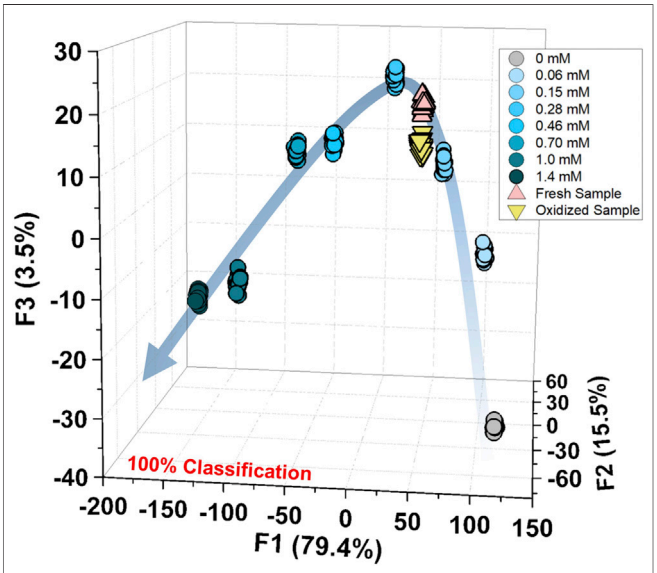

FIGURE 6 | Semiquantitative analysis for the fresh and oxidized tomato samples with the calibration of GSH (0–1.4 mM). The measurements were repeated twenty times, resulting in 100% accurate classification.

with the diluted tomato juice and chemosensors, which were estimated by the previously calibrated SVM model (**Figure 5**). As shown in the **Supplementary Table S6**, the prediction of the GSH concentration in the real sample was successfully performed with a recovery rate of 91–110%. Moreover, the semiquantitative analysis offered 100% accurate classification of the fresh and oxidized tomato samples (**Figure 6**). The decrease in GSH concentration in the oxidized tomato sample was confirmed by HPLC–electrospray ionization MS (ESI-MS, see **Supplementary Figures S32, S33**). The LDA results indicated that the oxidized tomato sample demonstrated a closer distance to the low GSH concentration group, rather than the fresh sample (**Figure 6**). The result of the semiquantitative analysis and the spike test indicated that the chemosensor array combined with pattern recognition could be applied for quantifying unknown GSH concentrations, which suggests that the proposed method would become a rapid and promising method for the detection of SCAAs in food samples.

CONCLUSION

In summary, we proposed a self-assembled colorimetric chemosensor array system for the qualitative and quantitative detection of SCAAs. The proposed array system was fabricated by CBSA utilizing off-the-shelf reagents, which avoided complicated synthetic processes. The reversible coordination binding of dye–Zn^{2+} complexes offered significant color changes upon the addition of the analytes. The LDA results reflected a clear classification of six groups (i.e., control, non-SCAAs, and reduced/oxidized SCAAs) with 100% classification accuracy. Moreover, quantitative analyses with high accuracy were achieved by the SVM, which allowed for the prediction of reduced/oxidized SCAAs in the mixtures. Most importantly, the spike test of GSH was performed in juice samples with high recovery rates. This study would lead to the application of supramolecular chemosensors for food freshness monitoring in the general society.

DATA AVAILABILITY STATEMENT

The original contributions presented in the study are included in the article/**Supplementary Material**, further inquiries can be directed to the corresponding author.

AUTHOR CONTRIBUTIONS

XL and YS performed the spectroscopic and high-throughput array experiments and wrote the manuscript. WT and XL performed the HPLC/ESI-MS analyses. JZ performed the spectroscopic experiments. TZ and YT wrote the manuscript. TM conceived the entire project.

FUNDING

TM acknowledges the financial support from JST CREST (Grant No. JPMJCR 2011) and JSPS KAKENHI (Grant Numbers JP21H01780 and JP20K21204). YS thanks JSPS KAKENHI (Grant No. JP18J21190). TM and YT also acknowledge the Japan–China Joint Research Cooperative Program (Joint Project).

SUPPLEMENTARY MATERIAL

The Supplementary Material for this article can be found online at: https://www.frontiersin.org/articles/10.3389/fchem.2021.685783/full#supplementary-material

REFERENCES

Anzenbacher, P., Lubal, P., Buček, P., Palacios, M. A., and Kozelkova, M. E. (2010). A Practical Approach to Optical Cross-Reactive Sensor Arrays. *Chem. Soc. Rev.* 39, 3954–3979. doi:10.1039/B926220M

Buryak, A., and Severin, K. (2005). A Chemosensor Array for the Colorimetric Identification of 20 Natural Amino Acids. *J. Am. Chem. Soc.* 127, 3700–3701. doi:10.1021/ja042363v

Cao, Z., Cao, Y., Kubota, R., Sasaki, Y., Asano, K., Lyu, X., et al. (2020). Fluorescence Anion Chemosensor Array Based on Pyrenylboronic Acid. *Front. Chem.* 8, 414. doi:10.3389/fchem.2020.00414

Cebi, N., Dogan, C. E., Develioglu, A., Yayla, M. E. A., and Sagdic, O. (2017). Detection of L-Cysteine in Wheat Flour by Raman Microspectroscopy Combined Chemometrics of HCA and PCA. *Food Chem.* 228, 116–124. doi:10.1016/j.foodchem.2017.01.132

Chao, D., and Zhang, Y. (2017). Aggregation Enhanced Luminescent Detection of Homocysteine in Water with Terpyridine-Based Cu^{2+} Complexes. *Sens. Actuators, B* 245, 146–155. doi:10.1016/j.snb.2017.01.176

Chen, S.-H., and Li, C.-W. (2019). Detection and Characterization of Catechol Quinone-Derived Protein Adducts Using Biomolecular Mass Spectrometry. *Front. Chem.* 7, 571. doi:10.3389/fchem.2019.00571

Fracassetti, D., Lawrence, N., Tredoux, A. G. J., Tirelli, A., Nieuwoudt, H. H., and Du Toit, W. J. (2011). Quantification of Glutathione, Catechin and Caffeic Acid in Grape Juice and Wine by a Novel Ultra-performance Liquid Chromatography Method. *Food Chem.* 128, 1136–1142. doi:10.1016/j.foodchem.2011.04.001

Garcia, I., Romero, L. C., and Gotor, C. (2015). "Cysteine Homeostasis," in *Amino Acids in Higher Plants*. Editor J. P. F. D'Mello (Wallingford: CABI), 219–233.

Ghasemi, F., Hormozi-Nezhad, M. R., and Mahmoudi, M. (2015). A Colorimetric Sensor Array for Detection and Discrimination of Biothiols Based on Aggregation of Gold Nanoparticles. *Anal. Chim. Acta* 882, 58–67. doi:10.1016/j.aca.2015.04.011

Gholami, M. D., Manzhos, S., Sonar, P., Ayoko, G. A., and Izake, E. L. (2019). Dual Chemosensor for the Rapid Detection of Mercury(II) Pollution and Biothiols. *Analyst* 144, 4908–4916. doi:10.1039/c9an01055f

Hamedpour, V., Sasaki, Y., Zhang, Z., Kubota, R., and Minami, T. (2019). Simple Colorimetric Chemosensor Array for Oxyanions: Quantitative Assay for Herbicide Glyphosate. *Anal. Chem.* 91, 13627–13632. doi:10.1021/acs.analchem.9b02822

Hamel, L. H. (2009). *Knowledge Discovery with Support Vector Machines*. (Hoboken, NJ: Wiley).

Hargrove, A. E., Zhong, Z., Sessler, J. L., and Anslyn, E. V. (2010). Algorithms for the Determination of Binding Constants and Enantiomeric Excess in Complex Host : Guest Equilibria Using Optical Measurements. *New J. Chem.* 34, 348–354. doi:10.1039/B9NJ00498J

Hoey, L., Mcnulty, H., Askin, N., Dunne, A., Ward, M., Pentieva, K., et al. (2007). Effect of a Voluntary Food Fortification Policy on Folate, Related B Vitamin Status, and Homocysteine in Healthy Adults. *Am. J. Clin. Nutr.* 86, 1405–1413. doi:10.1093/ajcn/86.5.1405

Hyman, L. M., and Franz, K. J. (2012). Probing Oxidative Stress: Small Molecule Fluorescent Sensors of Metal Ions, Reactive Oxygen Species, and Thiols. *Coord. Chem. Rev.* 256, 2333–2356. doi:10.1016/j.ccr.2012.03.009

Jacxsens, L., Devlieghere, F., Ragaert, P., Vanneste, E., and Debevere, J. (2003). Relation between Microbiological Quality, Metabolite Production and Sensory Quality of Equilibrium Modified Atmosphere Packaged Fresh-Cut Produce. *Int. J. Food Microbiol.* 83, 263–280. doi:10.1016/s0168-1605(02)00376-8

Kaushik, R., Kumar, P., Ghosh, A., Gupta, N., Kaur, D., Arora, S., et al. (2015). Alizarin Red S-Zinc(II) Fluorescent Ensemble for Selective Detection of Hydrogen Sulphide and Assay with an H_2S Donor. *RSC Adv.* 5, 79309–79316. doi:10.1039/C5RA11901D

Khorasani, M. Y., Langari, H., Sany, S. B. T., Rezayi, M., and Sahebkar, A. (2019). The Role of Curcumin and its Derivatives in Sensory Applications. *Mater. Sci. Eng. C* 103, 109792. doi:10.1016/j.msec.2019.109792

Krężel, A., and Maret, W. (2016). The Biological Inorganic Chemistry of Zinc Ions. *Arch. Biochem. Biophys.* 611, 3–19. doi:10.1016/j.abb.2016.04.010

Kurose, I., Higuchi, H., Miura, S., Saito, H., Watanabe, N., Hokari, R., et al. (1997). Oxidative Stress-Mediated Apoptosis of Hepatocytes Exposed to Acute Ethanol Intoxication. *Hepatology* 25, 368–378. doi:10.1002/hep.510250219

Küster, A., Tea, I., Sweeten, S., Rozé, J.-C., Robins, R. J., and Darmaun, D. (2008). Simultaneous Determination of Glutathione and Cysteine Concentrations and ^2H Enrichments in Microvolumes of Neonatal Blood Using Gas Chromatography-Mass Spectrometry. *Anal. Bioanal. Chem.* 390, 1403–1412. doi:10.1007/s00216-007-1799-5

Lee, M. H., Kim, J. S., and Sessler, J. L. (2015). Small Molecule-Based Ratiometric Fluorescence Probes for Cations, Anions, and Biomolecules. *Chem. Soc. Rev.* 44, 4185–4191. doi:10.1039/C4CS00280F

Liu, L., Zhang, Q., Wang, J., Zhao, L., Liu, L., and Lu, Y. (2019). A Specific Fluorescent Probe for Fast Detection and Cellular Imaging of Cysteine Based on a Water-Soluble Conjugated Polymer Combined with Copper(II). *Talanta* 198, 128–136. doi:10.1016/j.talanta.2019.02.003

Lonchamp, J., Barry-Ryan, C., and Devereux, M. (2009). Identification of Volatile Quality Markers of Ready-To-Use Lettuce and Cabbage. *Food Res. Int.* 42, 1077–1086. doi:10.1016/j.foodres.2009.05.002

Luo, X., Masuda, T., Matsubara, K., Wada, Y., and Ikehata, A. (2021). The Relationship between Perceived Freshness and Water Content of Cabbage Leaves: A Near Infrared Imaging Survey of Substance Distribution Underlying Product Appearance. *Lwt* 139, 110523. doi:10.1016/j.lwt.2020.110523

Lyu, X., Hamedpour, V., Sasaki, Y., Zhang, Z., and Minami, T. (2021). 96-Well Microtiter Plate Made of Paper: A Printed Chemosensor Array for Quantitative Detection of Saccharides. *Anal. Chem.* 93, 1179–1184. doi:10.1021/acs.analchem.0c04291

Ma, Y., Zheng, B., Zhao, Y., Yuan, H., Cai, Y., Du, J., et al. (2013). A Sensitive and Selective Chemosensor for GSSG Detection Based on the Recovered Fluorescence of NDPA-Fe_3O_4@SiO_2-Cu(II) Nanomaterial. *Biosens. Bioelectron.* 48, 138–144. doi:10.1016/j.bios.2013.04.006

Meng, Q., Jia, H., Succar, P., Zhao, L., Zhang, R., Duan, C., et al. (2015). A Highly Selective and Sensitive ON-OFF-ON Fluorescence Chemosensor for Cysteine Detection in Endoplasmic Reticulum. *Biosens. Bioelectron.* 74, 461–468. doi:10.1016/j.bios.2015.06.077

Miller, J., and Miller, J. C. (2018). *Statistics and Chemometrics for Analytical Chemistry*. (Upper Saddle River: Pearson education).

Minami, T., Esipenko, N. A., Zhang, B., Kozelkova, M. E., Isaacs, L., Nishiyabu, R., et al. (2012). Supramolecular Sensor for Cancer-Associated Nitrosamines. *J. Am. Chem. Soc.* 134, 20021–20024. doi:10.1021/ja3102192

Minich, D. M., and Brown, B. I. (2019). A Review of Dietary (Phyto)Nutrients for Glutathione Support. *Nutrients* 11, 2073. doi:10.3390/nu11092073

Moreira, A. R. S., Benedi, J., Gonzalez-Torres, L., Olivero-David, R., Bastida, S., Sanchez-Reus, M. I., et al. (2011). Effects of Diet Enriched with Restructured Meats, Containing Himanthalia Elongata, on Hypercholesterolaemic Induction, CYP7A1 Expression and Antioxidant Enzyme Activity and Expression in Growing Rats. *Food Chem.* 129, 1623–1630. doi:10.1016/j.foodchem.2011.06.019

Namuswe, F., and Berg, J. M. (2012). Secondary Interactions Involving Zinc-Bound Ligands: Roles in Structural Stabilization and Macromolecular Interactions. *J. Inorg. Biochem.* 111, 146–149. doi:10.1016/j.jinorgbio.2011.10.018

Nikolantonaki, M., Julien, P., Coelho, C., Roullier-Gall, C., Ballester, J., Schmitt-Kopplin, P., et al. (2018). Impact of Glutathione on Wines Oxidative Stability: A Combined Sensory and Metabolomic Study. *Front. Chem.* 6, 182. doi:10.3389/fchem.2018.00182

Reinbold, J., Rychlik, M., Asam, S., Wieser, H., and Koehler, P. (2008). Concentrations of Total Glutathione and Cysteine in Wheat Flour as Affected by Sulfur Deficiency and Correlation to Quality Parameters. *J. Agric. Food Chem.* 56, 6844–6850. doi:10.1021/jf800880n

Roy, P. (2021). Fluorescent Chemosensors Based on 4-Methyl-2,6-Diformylphenol. *Coord. Chem. Rev.* 427, 213562. doi:10.1016/j.ccr.2020.213562

Sasaki, Y., Kubota, R., and Minami, T. (2021a). Molecular Self-Assembled Chemosensors and Their Arrays. *Coord. Chem. Rev.* 429, 213607. doi:10.1016/j.ccr.2020.213607

Sasaki, Y., Lyu, X., Kubota, R., Takizawa, S.-Y., and Minami, T. (2021b). Easy-to-Prepare Mini-Chemosensor Array for Simultaneous Detection of Cysteine and Glutathione Derivatives. *ACS Appl. Bio Mater.* 4, 2113–2119. doi:10.1021/acsabm.0c01275

Sasaki, Y., Lyu, X., Zhou, Q., and Minami, T. (2021c). Indicator Displacement Assay-Based Chemosensor Arrays for Saccharides Using Off-The-Shelf Materials toward Simultaneous On-Site Detection on Paper. *Chem. Lett.* 50, 987–995. doi:10.1246/cl.200962

Sasaki, Y., Zhang, Z., and Minami, T. (2019). A Saccharide Chemosensor Array Developed Based on an Indicator Displacement Assay Using a Combination of Commercially Available Reagents. *Front. Chem.* 7, 49. doi:10.3389/fchem.2019.00049

Sener, G., Uzun, L., and Denizli, A. (2014). Colorimetric Sensor Array Based on Gold Nanoparticles and Amino Acids for Identification of Toxic Metal Ions in Water. *ACS Appl. Mater. Inter.* 6, 18395–18400. doi:10.1021/am5071283

Song, K., Kai, R., Lu, C., Gao, L., Wang, G., and Guo, L. (2016). Towards Two Up-Conversion Optical Sensing Systems for Cysteine Detection: Synthesis, Characterization and Sensing Performance. *Sens. Actuators, B* 236, 249–256. doi:10.1016/j.snb.2016.06.005

Valero, E., Millán, C., Ortega, J. M., and Mauricio, J. C. (2003). Concentration of Amino Acids in Wine after the End of Fermentation by Saccharomyces Cerevisiae strains. *J. Sci. Food Agric.* 83, 830–835. doi:10.1002/jsfa.1417

Wu, J., Kwon, B., Liu, W., Anslyn, E. V., Wang, P., and Kim, J. S. (2015). Chromogenic/Fluorogenic Ensemble Chemosensing Systems. *Chem. Rev.* 115, 7893–7943. doi:10.1021/cr500553d

Xu, W., Feng, H., Zhao, W., Huang, C., Redshaw, C., Tao, Z., et al. (2020). Amino Acid Recognition by a Fluorescent Chemosensor Based on Cucurbit[8]uril and Acridine Hydrochloride. *Anal. Chim. Acta* 1135, 142–149. doi:10.1016/j.aca.2020.09.028

Xu, Y., Niu, X., Zhang, H., Xu, L., Zhao, S., Chen, H., et al. (2015). Switch-on Fluorescence Sensing of Glutathione in Food Samples Based on a Graphitic Carbon Nitride Quantum Dot (g-CNQD)-Hg^{2+} Chemosensor. *J. Agric. Food Chem.* 63, 1747–1755. doi:10.1021/jf505759z

Yan, F., Fan, K., Bai, Z., Zhang, R., Zu, F., Xu, J., et al. (2017). Fluorescein Applications as Fluorescent Probes for the Detection of Analytes. *Trends Analyt. Chem.* 97, 15–35. doi:10.1016/j.trac.2017.08.013

Yang, X., Guo, Y., and Strongin, R. M. (2011). Conjugate Addition/Cyclization Sequence Enables Selective and Simultaneous Fluorescence Detection of Cysteine and Homocysteine. *Angew. Chem. Int. Ed.* 50, 10690–10693. doi:10.1002/anie.201103759

Yang, Z., Wang, X., Wu, Y., Li, X., and Chen, M. (2018). Two Emission Turn-On Optical Chemosensors for Cysteine Detection Using Up-Conversion Nanocrystals as Excitation Host: Synthesis, Characterization and Performance. *Sens. Actuators, B* 255, 1587–1594. doi:10.1016/j.snb.2017.08.182

Yin, C., Huo, F., Zhang, J., Martínez-Máñez, R., Yang, Y., Lv, H., et al. (2013). Thiol-addition Reactions and Their Applications in Thiol Recognition. *Chem. Soc. Rev.* 42, 6032–6059. doi:10.1039/c3cs60055f

Zhu, B., Li, L., Wei, H., Zhou, W., Zhou, W., Li, F., et al. (2020). A Simultaneously Quantitative Profiling Method for 40 Endogenous Amino Acids and Derivatives in Cell Lines Using Hydrophilic Interaction Liquid Chromatography Coupled with Tandem Mass Spectrometry. *Talanta* 207, 120256. doi:10.1016/j.talanta.2019.120256

Conflict of Interest: The authors declare that the research was conducted in the absence of any commercial or financial relationships that could be construed as a potential conflict of interest.

frontiers in Chemistry

ORIGINAL RESEARCH
published: 28 June 2021
doi: 10.3389/fchem.2021.701028

Binding Between Cyclohexanohemicucurbit[*n*]urils and Polar Organic Guests

Lukas Ustrnul[1], Tatsiana Burankova[2], Mario Öeren[3], Kristina Juhhimenko[1], Jenni Ilmarinen[1], Kristjan Siilak[1], Kamini A. Mishra[1] and Riina Aav[1]**

[1]Department of Chemistry and Biotechnology, School of Science, Tallinn University of Technology, Tallinn, Estonia, [2]Process Analytics, Hamilton Bonaduz AG, Bonaduz, Switzerland, [3]Optibrium Limited, Cambridge, United Kingdom

Inherently chiral, barrel-shaped, macrocyclic hosts such as cyclohexanohemicucurbit[*n*]urils (cycHC[*n*]) bind zinc porphyrins and trifluoroacetic acid externally in halogenated solvents. In the current study, we tested a set of eighteen organic guests with various functional groups and polarity, namely, thiophenols, phenols, and carboxylic and sulfonic acids, to identify a preference toward hydrogen bond–donating molecules for homologous cycHC[6] and cycHC[8]. Guests were characterized by Hirshfeld partial charges on acidic hydrogens and their binding by ^{1}H and ^{19}F NMR titrations. Evaluation of association constants revealed the complexity of the system and indirectly proved an external binding with stoichiometry over 2:1 for both homologs. It was found that overall binding strength is influenced by the stoichiometry of the formed complexes, the partial atomic charge on the hydrogen atom of the hydrogen bond donor, and the bulkiness of the guest. Additionally, a study on the formation of complexes with halogen anions (Cl^- and Br^-) in methanol and chloroform, analyzed by ^{1}H NMR, did not confirm complexation. The current study widens the scope of potential applications for host molecules by demonstrating the formation of hydrogen-bonded complexes with multisite hydrogen bond acceptors such as cycHC[6] and cycHC[8].

Keywords: supramolecular chemistry, binding evaluation, hemicucurbit[n]uril, hydrogen bond, complex stoichiometry, NMR, partial charge, organic acid

OPEN ACCESS

Edited by:
Tony D. James,
University of Bath, United Kingdom

Reviewed by:
Xin Wu,
The University of Sydney, Australia
Evgeny Kataev,
University of Erlangen Nuremberg, Germany

****Correspondence:***
Lukas Ustrnul
lukas.ustrnul@taltech.ee
Riina Aav
riina.aav@taltech.ee

Specialty section:
This article was submitted to Supramolecular Chemistry, a section of the journal Frontiers in Chemistry

Received: *27 April 2021*
Accepted: *07 June 2021*
Published: *28 June 2021*

Citation:
Ustrnul L, Burankova T, Öeren M, Juhhimenko K, Ilmarinen J, Siilak K, Mishra KA and Aav R (2021) Binding Between Cyclohexanohemicucurbit[n]urils and Polar Organic Guests. Front. Chem. 9:701028. doi: 10.3389/fchem.2021.701028

INTRODUCTION

Cucurbiturils and hemicucurbiturils are a large family of urea-based macrocycles (Lagona et al., 2005; Assaf and Nau, 2014; Andersen et al., 2018) that went through a rapid expansion during the last three decades—from the research of reaction conditions for selective synthesis of cucurbiturils of a specific size (Kim et al., 2000; Day et al., 2001) to a variety of uses in supramolecular catalysis, material chemistry, drug delivery, chemical sensors, or ion transport, to name a few (Walker et al., 2011; Barrow et al., 2015; Ji et al., 2019; Davis et al., 2020; Tang et al., 2020). Hemicucurbiturils have monomeric units connected by one row of methylene bridges and are mainly known for their ability to bind anions strongly in various solvents, which can be utilized for anion recognition and transport (Kaabel and Aav, 2017; Andersen et al., 2018; Lizal and Sindelar, 2018; Reany et al., 2018). In Aav's group, the first enantiomerically pure, inherently chiral member of the family—specifically cyclohexanohemicucurbit[6]uril (cycHC[6]) (Aav et al., 2013)—was prepared. Later, its larger homologs, cycHC[8] (Prigorchenko et al., 2015) and cycHC[12] (Mishra et al., 2020), were also made.

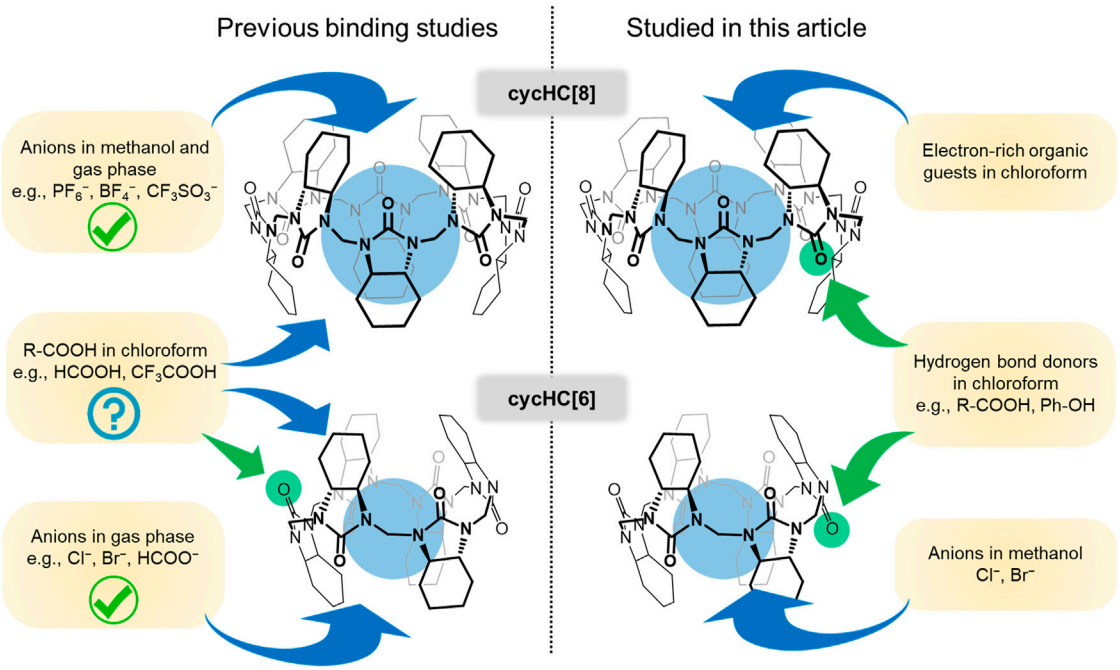

FIGURE 1 | Depiction of previously described binding of various guests to cycHC[*n*] **(left)** and supramolecular interactions studied in this article **(right)**.

First studies of cycHC[6] evaluated the binding of various carboxylic acids in chloroform using the 1:1 binding model based on DOSY NMR and ^{13}C NMR data (Aav et al., 2013). In this first study of cycHC[6]s and its binding, dependence on the size and shape of the guest was observed; therefore, the formation of inclusion complexes was proposed (**Figure 1**). The same approach was used to study complexes of cycHC[8], and the obtained association constants were analogous to results obtained for cycHC[6], which has a cavity volume that is roughly three times smaller (Prigorchenko et al., 2015). Such a result did not support the theory of inclusion complex formation as it should show a significant difference between cycHC[6] and cycHC[8] for the binding of the same guest. Hence, it was concluded that the complex formation depended on the acidity of the guest. Moreover, a computation and ion-mobility–mass spectrometry (IM-MS) study for cycHC[6] concluded that the macrocycle prefers to interact with the non-dissociated acids through their electron-poor hydrogen without forming an inclusion complex (Öeren et al., 2014). It should be noted that the study did confirm the formation of inclusion complexes with Cl^-, Br^-, and $HCOO^-$, and these theoretical studies were validated with gas-phase IM-MS.

CycHC[*n*] macrocycles were obtained from a template (anion)-driven synthesis in polar media; therefore, the binding of inorganic anions in methanol was described in detail for cycHC[8] (Kaabel et al., 2017). A discovered preference for encapsulation of large symmetrical anions (e.g., SbF_6^-, PF_6^- > BF_4^-, $CF_3SO_3^-$, and AcO^-) was later beneficial in the development of the solid-state synthesis of cycHC[*n*]s (Kaabel et al., 2019).

In 2019, it was demonstrated that cycHC[*n*] exhibits binding to zinc(II) porphyrins in chlorinated solvents *via* coordination with carbonyl oxygen on their outer surface (Ustrnul et al., 2019). At the same time, a study of *inverted*-cycHC[6] confirmed that strong organic acids are also bound from outside (**Figure 1**) with stoichiometry assumed to be 2:1 (acid:cycHC[6]) (Prigorchenko et al., 2019). These studies have shown the dependence of association constants on the geometry and size of the host. Notably, the significantly larger binding strength of guests with cycHC[6] (K_1 = 10^2–10^3 M^{-1}; K_2 = 10^2 M^{-1}) than the binding strength of the same guests with monomeric urea (*N,N'*-dimethylcyclohexadiylurea) (K_1 = 10^1 M^{-1}) was observed, which highlights the superiority of these multifunctional macrocycles compared to their monofunctional counterparts. The results on the binding of acids have motivated us to look deeper into and revise previous conclusions about binding and broaden the scope of guest molecules tested in chlorinated solvents.

Herein, we report several experiments increasing the knowledge about cycHC[*n*]-binding properties and bringing clarity on the binding of carboxylic acids in chlorinated solvents. A set of guests bearing electron-rich functional groups and their interaction with chiral cycHC[8] were tested. The binding of polar hydrogen bond (HB)-donating guests was studied mainly with cycHC[6], and we discuss difficulties related to stepwise association constant evaluation for systems with multiple binding sites. Additionally, we have examined the incorporation of small anions into the cycHC[6] cavity in methanol and chloroform solutions.

MATERIALS AND METHODS

Materials, Instrumentation, and Sample Preparation

All reagents and solvents were purchased from commercial suppliers. Macrocyclic host compounds were used only as (*R*,*R*)-cycHC[*n*] enantiomers and were synthesized in our laboratory from (*R*,*R*)-cyclohexanourea according to procedures described in the literature (Aav et al., 2013; Prigorchenko et al., 2015; Kaabel et al., 2019).

^{1}H NMR (400 MHz) and ^{19}F NMR (376.5 MHz) spectra were recorded on a Bruker Avance III spectrometer, using a Bruker BBO probe equipped with a z-gradient coil. Chemical shifts were referenced to the residual proton solvent peak ($\delta(^1H)$ = 3.34 ppm in CD_3OD-d_4 and $\delta(^1H)$ = 7.26 ppm in $CDCl_3$) or to TMS (0.00 ppm) as an internal standard. All chemical shifts are reported in ppm units. The data were analyzed using the program MNova (Mestrelab).

All the solutions were prepared using Hamilton® Gastight syringes; these syringes were also used for all additions during titrations. In the case of precise measurements of higher volumes (over 1 ml), the mass and density of the solvent were used instead of volumetric glassware. Samples were weighed on a microbalance with an accuracy of 6 μg (Radwag® MYA 11.4Y, Poland).

Anion Binding With CycHC[6]

The binding of anions to cycHC[6] was tested in CD_3OD-d_4 (0.8 mM cycHC[6]) and $CDCl_3$ (1.2 mM cycHC[6]) by the addition of salt excess to the macrocycle solution. Tetrabutylammonium (TBA) chloride and bromide have been added as a solid compound. The specific excess of salt was determined from the integration of NMR signals against the known concentration of macrocycle. ^{1}H NMR was measured shortly before and after salt addition and then after 18 h. The dissolution of weakly soluble cycHC[6] in methanol was achieved by heating the sample repeatedly and employing sonification.

Screening of Potential Guests, Titrations, and Job's Plot in $CDCl_3$

In the first screening of guests, chemical shift changes of cycHC[8] (ca 2.5 mM) proton signals induced by the addition of 0.5, 5, and 40 equivalents (equiv) of guests (**1–9**) were investigated by ^{1}H NMR in $CDCl_3$. Guests were added in solutions of known concentration (typically 300–400 mM).

All NMR titrations were performed at a constant concentration of guest (2 mM for qualitative comparison titrations, guests **6, 9–18**) in a sample throughout the whole experiment, which was achieved by the dissolution of titrant (cycHC[*n*]) in the solution of the guest. ^{1}H or ^{19}F NMR was used according to the guest's structure; ^{19}F NMR was preferred as it usually revealed more significant changes in the chemical shift.

The continuous variation method (Job's plot) was conducted for trifluoroacetic acid (guest **16**) with cycHC[8] (10 mM) and for **16** with cycHC[6] (20 mM).

Binding Strength Evaluation and Partial Charge Calculation

Stepwise association constants were evaluated and simulated using online tools at supramolecular.org (Thordarson, 2011; Hibbert and Thordarson, 2016) and our 3:1 binding model, which was introduced in our previous publication (Ustrnul et al., 2019). The script for the 3:1 binding model uses the NumPy (1.10.2) and SciPy (0.18.1) libraries of Python 3. The script was adapted to the studied system of HB donors and macrocycles using the following constraints: 1) $K_{1obs} > K_{2obs} > K_{3obs}$ and 2) $\delta_{HG1}, \delta_{HG2}, \delta_{HG3} \geq \delta_{EXPmax} - 5\ (\delta_{EXPmax} - \delta_{EXPmin})$; these constraints prevent the chemical shift δ of the complexed guest (HG_x) from diverging extremely from experimentally observed values.

The atomic charges presented in the study are calculated using the modified Hirshfeld charge analysis. The wave function for the population analysis was obtained using the density functional theory (DFT) (Lu and Chen, 2012; Aprà et al., 2020).

RESULTS AND DISCUSSION

Test of Anion Binding Inside CycHC[6] in Methanol Solutions

Precisely described anion binding inside the cycHC[8] cavity in methanol solutions (Kaabel et al., 2017) and previously calculated and experimentally confirmed (in gas phase) complexes of Cl^-, Br^-, and $HCOO^-$ with cycHC[6] (Öeren et al., 2014) would imply a possible interaction between a 6-membered macrocycle and small anions in methanol (**Figure 1**). The cycHC[6] is poorly soluble in protonic media; nevertheless, stable solutions with concentrations suitable for ^{1}H NMR measurements (ca 1 mM) can be reached by heating the sample combined with sonification. Hence, we prepared samples of cycHC[6] in MeOD-d_4 (0.8 mM) and added an excess of Cl^- and Br^- salts. ^{1}H NMR spectra were measured shortly before and after the addition of salts and then 18 h later to rule out a possible slow kinetics of binding (**Supplementary Figure S1**). Surprisingly, there was no change in the cycHC[6] spectra. Later, we conducted the same experiment in chloroform with the chloride anion, and there was also no visible interaction in this solvent (**Supplementary Figure S2**). Therefore, we can conclude that in chloroform and even in methanol solutions, the binding of anions ($Cl^-$and Br^-) inside the cycHC[6] cavity is too weak to be observed at the conditions used due to the competition of anion solvation.

Screening of Various Guests for CycHC[8]

Our knowledge of the binding properties of cycHC[*n*]s in aprotic solvents was limited mainly to carboxylic acid derivatives; therefore, several small compounds **1–9** (**Figure 2**) bearing various functional groups were used to test the interaction with cycHC[8] in chloroform to learn more about the possibility of external and inclusion complex formation. The binding site can be detected by changes in either the spectra of protons positioned inside the cavity or external ones (see the numeration in **Figure 2**). It was previously shown in methanol

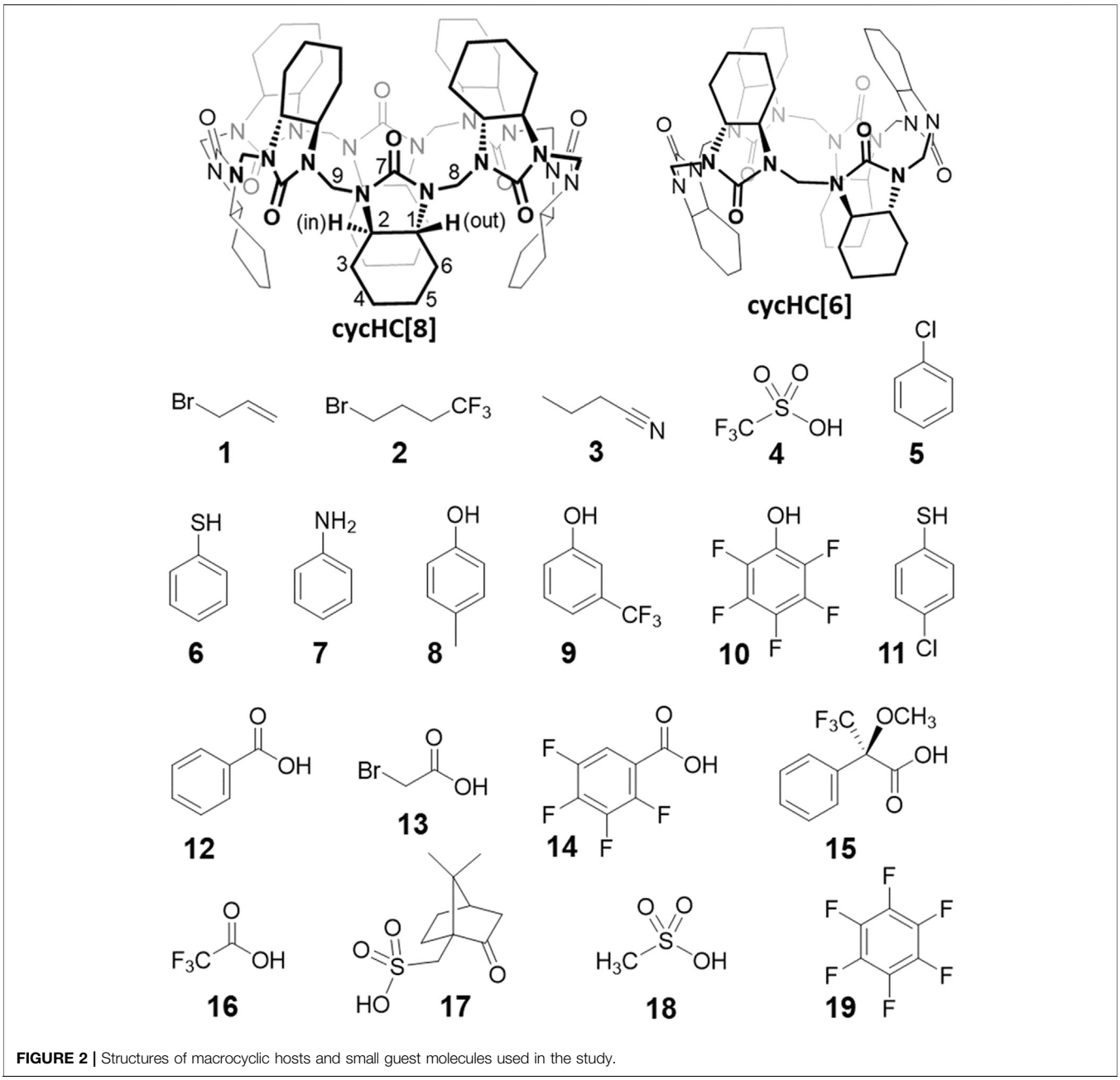

FIGURE 2 | Structures of macrocyclic hosts and small guest molecules used in the study.

that changes of cycHC[8] chemical shifts (δ) in ^{1}H NMR are most pronounced for the protons H2*ax* and H6*ax* directing inside the cavity and indicating the position of the complexed anion (Kaabel et al., 2017). Similarly, for a complex between cycHC[6] and externally bound trifluoroacetic acid in chloroform, the only slightly shifted signal is H1*ax* directing outside the cavity (Prigorchenko et al., 2019). Interestingly, the binding of porphyrins in dichloromethane has induced a noticeable upfield shift of all macrocycle signals (cycHC[6] or cycHC[8]) as a consequence of the proximity of the large porphyrin's aromatic system (Ustrnul et al., 2019).

Based on the previous results, we followed ^{1}H NMR signals of cycHC[8] (2.5 mM) in the presence of 0, 0.5, 5, and 40 equiv of guests **1–9** in $CDCl_3$. Aliphatic guests **1–3** bearing electron-rich groups have not induced any shift of cycHC[8] signals, clearly showing they are not forming any type of complexes (**Supplementary Figure S3**). The presence of trifluoromethanesulfonic superacid **4** (Howells and Mc Cown, 1977) was expected to provide a hydrogen bond (HB) from its strongly polarized O-H group or cause protonation of the macrocycle. Also, it is known that some superacids are capable of inducing the formation of HCl and chloronium cations from chlorinated solvents (Stoyanov and Stoyanova, 2018). However, the chemical shifts of the macrocycle were not influenced, and we can only speculate that acid four preferred to interact with itself and be passive toward the macrocycle in this solvent.

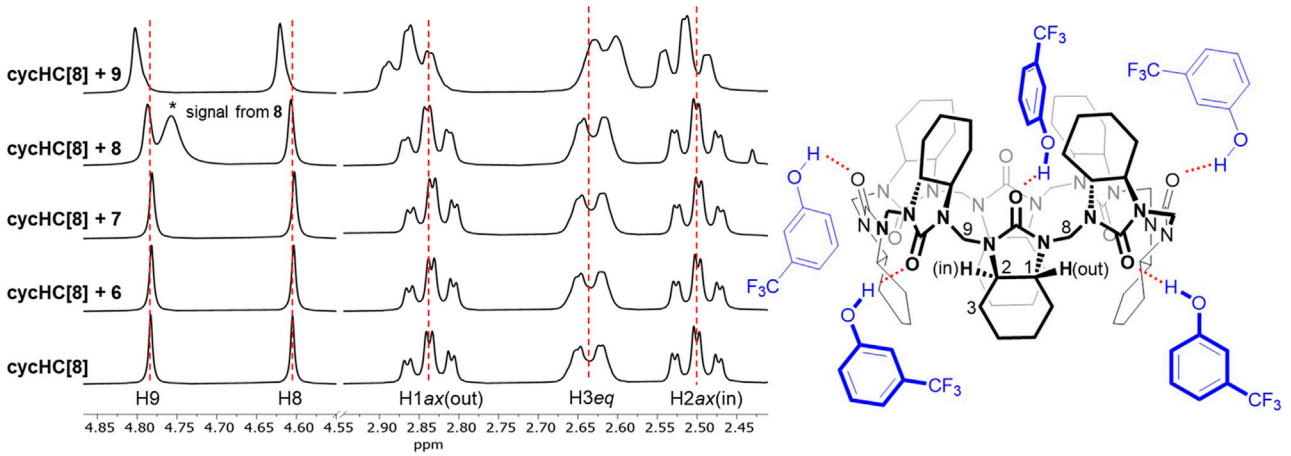

FIGURE 3 | ^{1}H NMR spectra of free cycHC[8] (2 mM) and in the presence of 40 equiv of guests **6–9 (left)** and visualization of probable interactions (red, dashed) between **9** and cycHC[8] **(right)**. Guest orientations and binding stoichiometry are illustrative.

Benzene derivatives **5–9** are small enough to possibly fit inside the cycHC[8] cavity (Prigorchenko et al., 2015), so we presumed an inclusion complex for the electron-rich chlorobenzene **5**; nevertheless, no signal shift occurred. The addition of 40 equiv of thiophenol **6** and aniline **7** provided a barely noticeable change in the macrocycle's proton spectra (**Figure 3**); hence, we could not deduce the binding site, and we concluded that the compounds were bound very weakly or did not bound at all. Finally, phenol derivatives 4-methylphenol **8** and 3-(trifluoromethyl)phenol **9** induced a change in cycHC[8] chemical shifts (**Figure 3**). The less polarized **8** caused almost negligible changes, and the more polarized electron-withdrawing group (-CF_3)-bearing **9** generated a clear shift of multiple signals. A similar change in the chemical shift of cycHC[8]'s inner H2*ax* and outer H1*ax* and methylene bridges H8 and H9 is inconsistent with inclusion complex formation. Alternatively, it can be related to the creation of an external hydrogen bond between the phenol O–H and the carbonyl groups of the macrocycle or to the protonation of the macrocycle formation of an ion pair. The more pronounced change of chemical shifts of signals of guest **9** (more-polarized) compared with guest **8** (less-polarized) support both options. Evidence supporting the hydrogen bond formation was noticed while comparing the chemical shifts of cycHC[8] in the presence of phenol **8** and thiophenol **6**, as, in general, phenols are less acidic than thiophenols (pKa = 18 and pKa = 10, respectively, in DMSO) (Bordwell, 1988). If the protonation of the macrocycle were the main cause of the signal shift, then the thiophenol **6** should induce a larger chemical shift due to the more pronounced protonation. However, this was not the case (**Figure 3**). Direct evidence for HB formation was obtained by the addition of cycHC[8] to the solution of **10**, which induced a typical strong downfield shift (Hibbert et al., 1990) of the acidic proton in ^{1}H NMR of **10** (see **Supplementary Figure S4**).

In conclusion, guests **1–8** have no or a very weak interaction with cycHC[8], and only the polarized, HB-donating guest **9** induced evident changes in the ^{1}H NMR spectra of the macrocycle in chloroform. We assume that a test of binding to cycHC[6] would provide similar results as there was no sign of inclusion complex formation with cycHC[8].

NMR Titration Studies

Based on the previous screening, hydrogen bonds are the dominant interaction of cycHC[*n*] in chlorinated solvents—the macrocycle's carbonyl groups act as an acceptor and the guest as an HB donor. It could be deduced that cycHC[6] and cycHC[8] have six and eight available binding sites, respectively. Therefore, a complete description of such a complex system would require a determination of six or eight stepwise association constants. Considering that the necessary amount of reliable experimental data and the subsequent data evaluation would be disproportionately demanding for such a study, we decided to compare the affinity of guests **6** and **9–18** toward cycHC[*n*] by a qualitative approach as described further. Nevertheless, we first needed to scrutinize the general binding properties of the suggested host–guest systems and their cooperativity (Ercolani, 2003; Hunter and Anderson, 2009; Thordarson, 2011).

The macrocycle is relatively rigid at a normal temperature, so we can assume there is no positive or negative cooperativity in stepwise binding caused by its conformational changes (**Figure 3**). Next, the formation of an HB will cause a local decrease of electron density on the bound carbonyl group, which can induce a small decrease in electron density on the neighboring carbonyl groups, leading to their smaller affinity toward a guest and, therefore, negative cooperativity. Further, we need to consider the role of the guests. All of them bear only one apparent group capable of providing an HB. Hence, we can assume the mechanism of binding to the macrocycle has to be similar. Additional guest-specific effects that influence the binding strength could be 1) guest self-aggregation through the hydrogen bond (e.g., dimerization of carboxylic acids) (Fujii et al., 1988; Colominas et al., 1998) as a competitive interaction to complexation with cycHC[*n*] and 2) steric hindrance between a bulky guest and cycHC[*n*] (see **Figure 3**) or between guests bound at adjacent carbonyl groups of cycHC[*n*] (significant in saturated

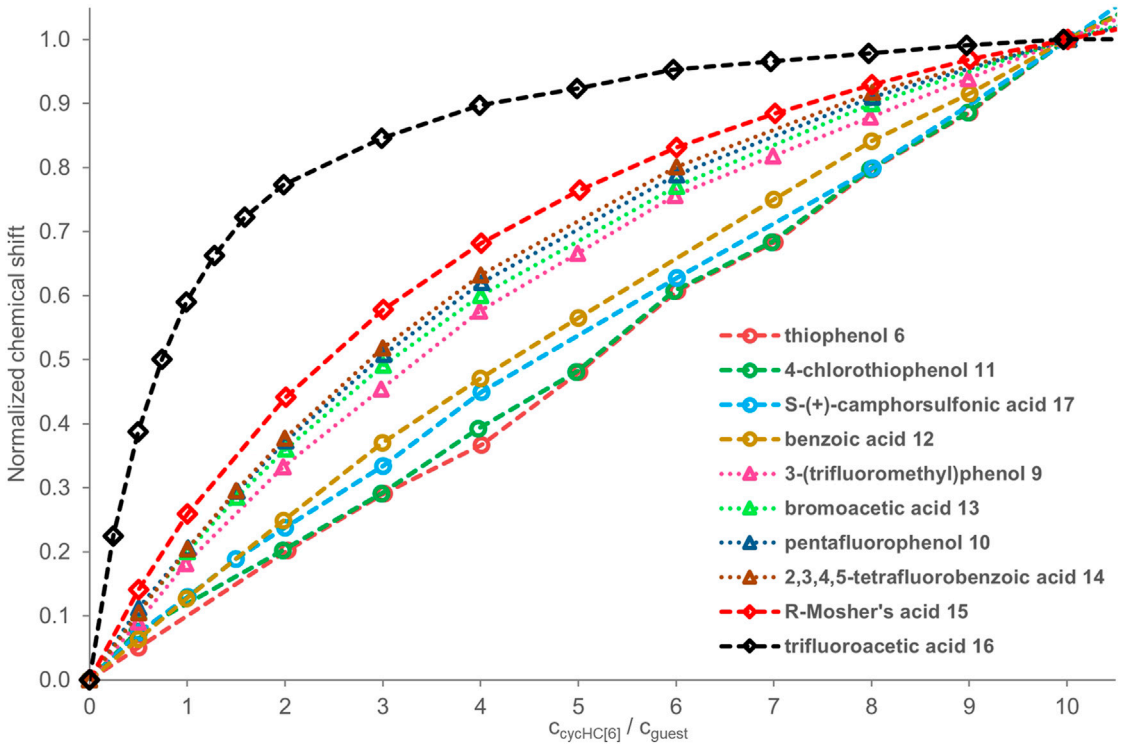

FIGURE 4 | ^{1}H and ^{19}F NMR titration data for guests **6** and **9–17** (2 mM) in the presence of a growing concentration of cycHC[6]; values of guest's chemical shift δ normalized at 10 equiv of cycHC[6]. The legend of the graph follows the order of binding from the weakest **(top)** to strongest **(bottom)**. Experimental data points are assigned with geometrical shapes; the dotted lines are shown to guide the eye. The invalid points were excluded for some guests, specifically for guests **6, 11** (at 1 equiv), and **12** (at 6 equiv). As an internal reference for the fluorine signal position in ^{19}F NMR, we added hexafluorobenzene **19**; however, it appeared that the presence of reference inside the samples was not necessary, as we did not observe fluctuations in reference δ between individual spectra.

complexes). Based on the given reasoning, we can expect no cooperativity or negative cooperativity in the external binding of cycHC[*n*] with single HB donors in a nonpolar solvent. Therefore, every stepwise association constant K_i has to be stronger than the following stepwise K_{i+1} (for more details, see supporting information on page S9).

All NMR titrations (^{1}H and ^{19}F) for a qualitative comparison of binding strength were carried out in the same constant concentration of a guest (2 mM) with additions of specific equivalents of cycHC[6] (**Figure 4**). The reasons for such experimental setup were as follows: 1) in the previous screening, the ^{1}H signals of cycHC[*n*] were relatively insensitive upon interaction with a guest, so we wanted to track the guest's signal instead; 2) polar and acidic guests could exhibit changes in NMR spectra related to a change of their concentration in chloroform (e.g., dimerization of carboxylic acids); therefore, it is desired to keep their concentration invariable throughout the titration; 3) titration will lead to the excess of cycHC[6], and the formation of a saturated 1:1 complex; and 4) the smaller cycHC[*n*] derivative was chosen for those experiments to prevent any theoretical influence of incorporation of guests into the macrocycle cavity. In this setup, the observed changes in the chemical shift of guests can be associated exclusively with cycHC[6]. Stepwise association constants for the binding of second, third, and further guests will influence the shape of the titration curve only at the very beginning as it is the only condition where an excess of guest over the cycHC[6] is present. When the mechanism of complexation is the same for all the guests, then the more pronounced titration curve of a particular guest (reaching a plateau at lower equivalents of cycHC[6]) must correspond with its stronger K_1 compared to a guest with a flatter titration curve (reaching a plateau in higher equivalents of cycHC[6]) (**Figure 4**). Moreover, the strength of K_1 should be representative in this case and sufficient to compare the overall binding affinity of different guests as we cannot determine cumulative association constant β ($\beta = K_1 \cdot K_2 \cdot \ldots \cdot K_m$, where m corresponds to the stoichiometry of complex), due to the limitations of acquiring reliable data for higher stoichiometry (see supporting information, page S10).

On that account and all mentioned above, we can compare the strength of binding of selected guests with each other by simply comparing the shapes of titration curves. To do that, we normalized the experimental values from NMR as the extent of chemical shift δ change varies for different guests and depends on their sensitivity to the change of their close electronic environment upon binding. Data were normalized at 10 equiv of cycHC[6] (see details in SI) as such an excess of macrocycle should be sufficient to get over 85% saturation of 1:1 complex even for moderate association constants (simulated for $K_1 = 1000\ M^{-1}$, $K_2 = 500\ M^{-1}$ with a 2:1 NMR binding model in the online tool Bindsim from supramolecular.org) (Thordarson, 2011; Hibbert and Thordarson, 2016).

We aimed to observe differences between various HB-donating functional groups and the influence of electron-withdrawing

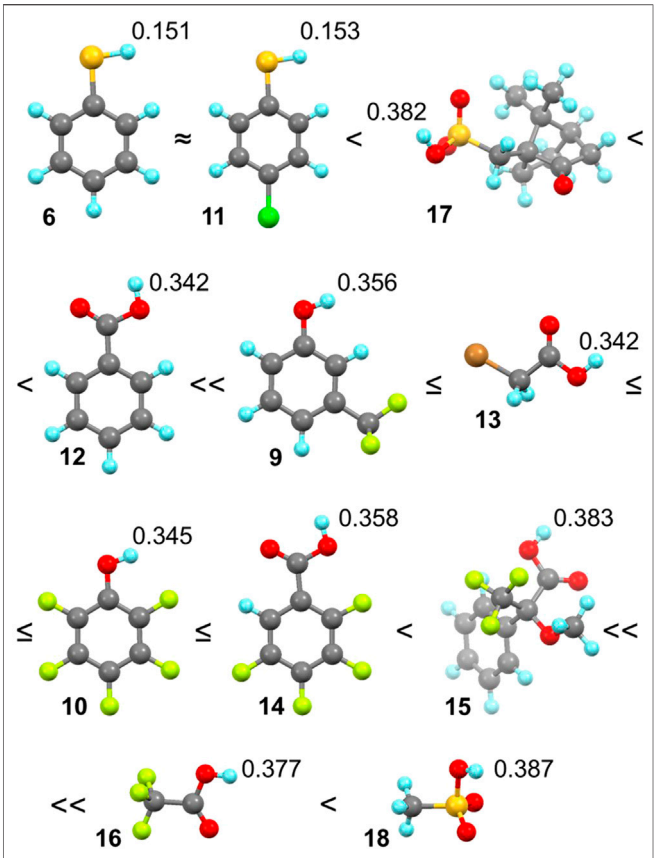

FIGURE 5 | Order of binding according to the shape of titration curves (assigned by ≈, ≤, <) and values of partial positive charge on the hydrogen atom participating in the hydrogen bond formation of guests **6** and **9–18** with cycHC[6]. Color coding: H: bright blue, C: dark gray, O: red, S: yellow, F: bright green, Cl: green, and Br: orange.

groups in the structure of guests as they should enhance the strength of the HB. The selected guests **6** and **9–18** fulfilled those aims well. We expected that the binding of HB donors with cycHC[6] should correlate with Abraham's hydrogen bond acidity (Abraham, 1993; Abraham et al., 2006), which is a measure of the compound's ability to perform as an HB donor or acceptor. However, the values are not available for all studied guests, and we could only generalize that in our set of guests, the thiophenols are bad HB donors, and phenols with carboxylic acids should be roughly equal. However, we were interested in comparing the whole set of measured guests. Therefore, we calculated Hirshfeld partial atomic charges for protons contributing to HB interaction with cycHC[6] (**Figure 5**) using the density functional theory (DFT). The higher value means a higher partial positive charge, therefore, a better ability to act as an HB donor. One should bear in mind that gas-phase calculations explain the relative polarity difference between the studied guests and cannot fully reflect the situation in the solution.

In the qualitative comparison of binding (**Figure 4**), the titrations of thiophenols **6** and **11** provided barely any signal shift, which resulted in a straight line instead of a curved titration isotherm. This observation is not surprising as sulfur has a significantly lower electronegativity, and our calculations showed a very small partial charge on a hydrogen atom compared to the other guests. Surprising results were obtained for camphorsulfonic acid **17**; its acidic proton had a larger atomic charge than that of carboxylic acids, but the titration curve of **17** was very flat, suggesting binding barely stronger than that with thiophenols **6** and **11**. Reasons for such a weak interaction can be 1) steric hindrance between the macrocycle and the bulky structure of **17**, and 2) formation of intra- or intermolecular HB between the sulfonic group and the carbonyl group of **17**.

Guest **12** provided a less pronounced titration curve than equally charged **13** and **10**, which could be related to a steric hindrance and eventually to the different behavior of different functional groups in the solution. Stronger than **12** was a group of guests with similar titration curves showing the order of binding corresponding well with atomic charges (**9** ≤ **13** ≤ **10** ≤ **14**) with small irregularity. The binding of the phenol derivative **9** is slightly weaker than that of **10**, which is in the opposite order of their partial charge on the proton. However, this could also be reasoned by the steric hindrance of the trifluoromethyl group. Like **12**, **15** has a weaker affinity in comparison with equally charged but less sterically hindered **16** and **18**. Trifluoroacetic acid **16** is a small molecule bearing an electron-withdrawing CF_3 group nearest to the HB donor, causing its high atomic charge and the strongest interaction with cycHC[6].

Methanesulfonic acid **18** exhibited results that did not correspond between parallel titrations due to difficulties in the sample preparation caused by the low solubility of **18** in chloroform. Accurate experimental concentrations of **18** in the titrations were obtained from comparing the NMR signal intensities of **18** and a compound of known concentration, which was either host cycHC[6] or, on one occasion, a standard 1,2,4,5-tetrachloro-3-nitrobenzene. Unfortunately, we could not include guest **18** in **Figure 4** because its concentrations in titrations were not comparable with other guests (titration data for all guests, including concentrations other than 2 mM, are present in **Supplementary Tables S1–S22**). At the same time, we were able to estimate that the binding of **18** with cycHC[6] is the strongest out of all the tested guests because at the concentration ca of 0.4 mM, the titration curve was as pronounced as the curve of 2 mM trifluoroacetic acid **16** (see **Supplementary Figure S8**).

Enantioselective Interaction With Chiral Guests

Previous studies showed chiral recognition of *α*-methoxyphenylacetic acid enantiomers by cycHC[6], illustrated by changes in ^{13}C NMR (Aav et al., 2013). Those studies also showed enantioselective binding by cycHC[6] and cycHC[8] based on the DOSY NMR and fitting with a 1:1 model of binding (Prigorchenko et al., 2015). Further, a low selectivity of binding for Mosher's acid (guest **15**) enantiomers by cycHC[8] was reported using the same method (DOSY NMR). However, the ability of cycHC[6] to differentiate between enantiomers of **15** was not tested, so we decided to apply our qualitative approach to this system. First, we conducted the ^{1}H NMR titration for both enantiomers of **15** (2 mM) (see **Supplementary Table S11, S12**). The change in

chemical shift was very small, and normalized titration curves (at 4 equiv) were almost overlapping (**Figure 6A**). Then we exploited ^{19}F NMR in two titrations of *R*-**15** and one titration of *S*-**15** (2 mM) and normalized the titration curves at 11 equiv (see **Supplementary Tables S8–S10**) as the latest common data point (**Figure 6B**). Surprisingly, the titration curves overlap perfectly, so it seems cycHC[6] cannot bind Mosher's acid **15** enantioselectively, or the selectivity is so low that it cannot be differentiated by the method used. Indeed, only a very low selectivity was previously reported for cycHC[8] (Prigorchenko et al., 2015).

Evaluation of Apparent Association Constants

The evaluated system should have negative or no cooperativity. Therefore, K_a values for higher stoichiometry complexes are decreasing, and the concentration of corresponding complexes becomes negligible in solution. Additionally, there is generally no meaning in fitting data with the model using higher stoichiometry if such fitting does not significantly improve the overall quality of fit (Thordarson, 2011; Hibbert and Thordarson, 2016). Therefore, we decided to apply an adapted version of our 3:1 binding model, developed to evaluate the porphyrin binding (Ustrnul et al., 2019), to quantify the binding between the HB donors and cycHC[*n*].

The fitting with the 3:1 binding model for titration data used at a qualitative comparison of binding strength has revealed that most of the studied guests had too low binding for acceptable determination of the first three apparent stepwise K_{obs}; therefore, 2:1 and 1:1 binding models had to be used. Only some of the titration data for guests **16** and **18** provided a reasonable fit for K_{1obs}–K_{3obs} (**Supplementary Table S23**). Overall, the binding between the guests and cycHC[6] cannot be compared quantitatively as the data cannot be evaluated with the same binding model (see supporting information, page S32–S33). Nevertheless, we focused on the strongest binding acids **16** and **18** to confirm the stoichiometry of the complexes higher than 2:1 and evaluated K_{obs} with a 3:1 (Python script) and a 2:1 (Bindfit) binding model.

To justify using the 3:1 binding model, we have conducted a continuous variation method known as a Job plot experiment between guest **16** and cycHC[6] and also cycHC[8] by ^{19}F NMR. Although it was previously proved that the Job plot method is not suitable for determination of precise stoichiometry, it can still provide useful and demonstrative information for suitable systems (Hibbert and Thordarson, 2016; Ulatowski et al., 2016). First, we conducted the experiment with cycHC[8] (**Figure 7A**) using a common arrangement, varying mole fractions of host and guest from 0 to 1 at a high overall concentration (10 mM). Results showed a maximum at points 0.7 and 0.8 mole fraction of guest **16** (full data in **Supplementary Table S25**); therefore, we can assume that the maximum of the curve lay around 0.75, which is a position corresponding to the formation of a complex with a stoichiometry at least 3:1 (**16**:cycHC[8]). Based on those results, we modified the experimental arrangement for measurement with cycHC[6] (**Figure 7B**) and increased the concentration (20 mM). Also, we focused on mole fractions in excess of guest **16**. The mole fraction values were chosen to correspond with specific host–guest ratios (x_i = 0.5 for 1:1, x_i = 0.66 for 2:1, x_i = 0.75 for 3:1, x_i = 0.8 for 4:1,...). Obtained data revealed a flat top between 0.66 and 0.8 with a maximum at 0.75 (full data in **Supplementary Table S26**), which reflects at least 3:1 binding (**16**:cycHC[6]) stoichiometry, the same as cycHC[8]. Hence, using the 3:1 binding model to evaluate apparent association constants between **16** and cycHC[*n*] should provide values of K_{obs} that better correspond to reality than models describing a lower stoichiometry binding.

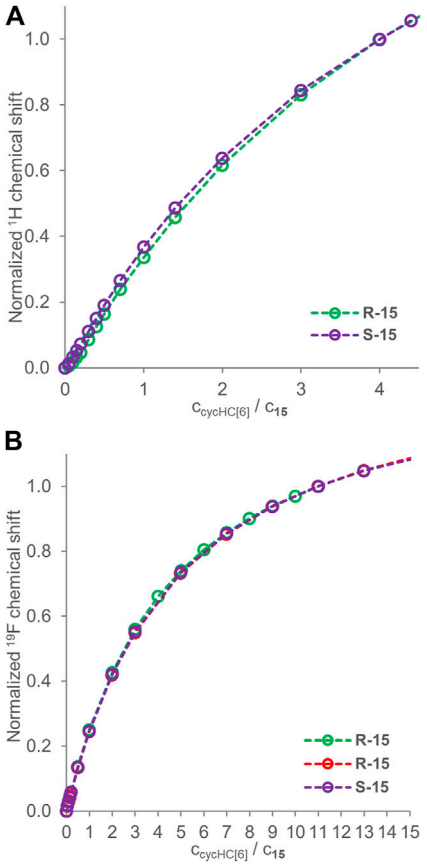

FIGURE 6 | Titration data for enantiomers of guest **15** (2 mM) in the presence of a growing concentration of cycHC[6]. Graph **(A)** shows ^{1}H NMR normalized at 4 equiv, and **(B)** shows ^{19}F NMR normalized at 11 equiv. Experimental data points are assigned with circles; the dotted lines are shown to guide the eye.

We have conducted additional ^{19}F NMR titrations to collect sufficient data to evaluate association constants between trifluoroacetic acid **16** and cycHC[*n*] macrocycles. Specifically, we have measured two titrations with cycHC[8] at the same concentration of guest **16** (2 mM) as in the titrations for a qualitative comparison. Then, we performed two titrations at a higher concentration of **16** (18 mM), one with cycHC[6] and one with cycHC[8] (full titration data in **Supplementary Tables S13–S17**), because concentration range broadening of titrations should improve the outcome quality of the following fitting procedure more than simply repeating experiments at the same concentration (Thordarson, 2011; Hibbert and Thordarson, 2016). In the end, we had data for

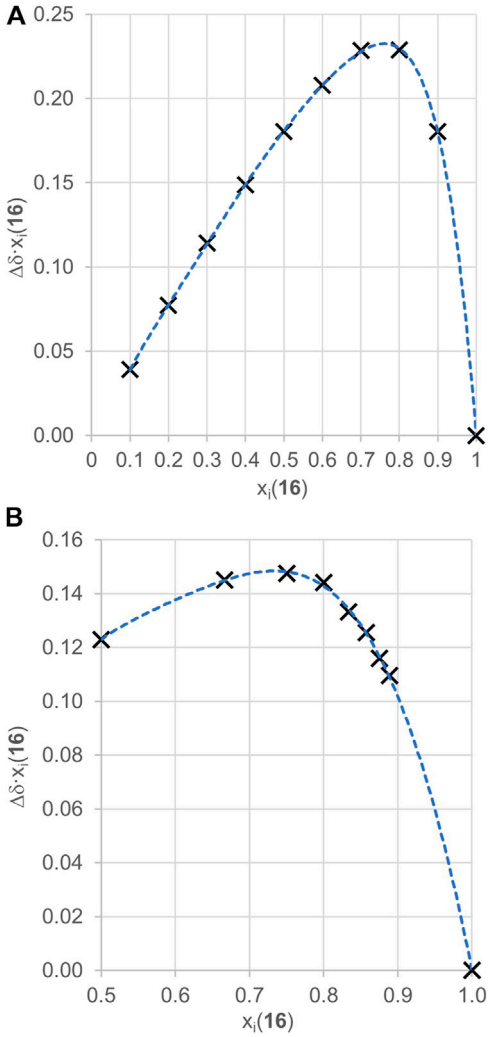

FIGURE 7 | ^{19}F NMR Job plot experiment results for a complex of **(A)** cycHC[8] with guest **16** (c_{total} = 10 mM) and **(B)** cycHC[6] with guest **16** (c_{total} = 20 mM). Black crosses are experimental points, and the blue dotted lines are shown to guide the eye.

2 mM and 18 mM solutions of guest **16** with studied cycHC[*n*]s that allowed us to compare cycHC[6] and cycHC[8] using our qualitative approach. Titration data for 18 mM guest **16** were normalized at 1.2 equiv and provided almost identical titration curves for both cycHC[*n*] (**Figure 8**). However, a slightly more pronounced curve for titrations with cycHC[8] suggests a stronger binding, probably as a result of a larger amount of available binding sites (carbonyl groups) on cycHC[8] than cycHC[6]. Data collected for 2 mM guest **16** and normalized at 5 equiv confirmed the trend observed at the higher concentration (see **Supplementary Figure S5**). Nevertheless, such comparison is only demonstrative as the binding mechanism is not known in detail and can differ due to the different size or properties of cycHC[6] and cycHC[8].

We attempted to determine K_{obs} by a 3:1 (Python script) and a 2:1 (Bindfit) binding model from all the titration data collected for both guests **16** and **18** with cycHC[*n*] (**Supplementary Table S23**). The 3:1 binding model allowed us to evaluate the data from titrations at different concentrations simultaneously; however, it was successfully realized only for two datasets for **18** titrated by cycHC[6] (**Table 1**, entry 1). The experimental data and obtained fit (**Figure 9**, the normalized version in **Supplementary Figure S9**) show a more pronounced titration curve at a higher concentration of **18** due to the increased abundance of the 1:1 complex and higher stoichiometry complexes. By combining data from various concentrations, the simultaneous fit should provide more precise K_{obs}; however, that cannot apply to systems with K_{obs} significantly dependent on experimental concentration. Therefore, we can assume that simultaneous fit in most cases failed because of the dimerization of acids in chloroform. Hence, we applied the 3:1 model on every titration dataset separately and obtained a reasonable fit between experimental and calculated values only for one experiment for every combination of acid and cycHC[*n*] (**Table 1**), giving us no opportunity to evaluate the reliability of the results. Fitting for the guest **18** with cycHC[8] (**Table 1**, entry 2) showed $K_{1obs} \approx K_{2obs}$ values corresponding to a positive cooperativity, which we ruled out earlier. Guest **16** with cycHC[6] exhibited an error of K_{3obs} same as the value itself (**Table 1**, entry 3 and **Supplementary Figure S10**). Finally, **16** with cycHC[8] showed reasonable values of all three K_{obs} (**Table 1**, entry 4).

Interestingly, we were not able to determine K_{obs} for any titration of 18 mM **16**. All these results indicate that the 3:1 binding model cannot provide reliable K_{obs} without a better understanding of the binding mechanism as it would lead to additional or improved constraints. Moreover, the binding at higher concentrations of acid could still be difficult to evaluate due to an increasing influence of complexes with stoichiometry over 3:1.

Evaluation of titration data by the 2:1 binding model provided additional evidence for the higher stoichiometry of binding. In

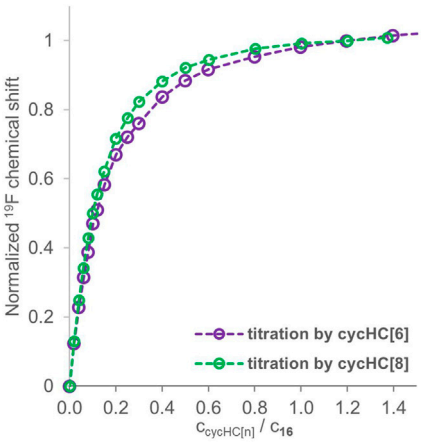

FIGURE 8 | ^{19}F NMR titration data for guest **16** (18 mM) in the presence of a growing concentration of cycHC[6] (purple) and cycHC[8] (green) normalized at 1.2 equiv. Experimental data points are assigned with circles; the dotted lines are shown to guide the eye.

TABLE 1 | Observed association constants (K_{obs}) obtained from fitting with a 3:1 binding model.

	Guest	Macrocycle	Guest concentration, mM	K_{1obs}, M^{-1}	K_{2obs}, M^{-1}	K_{3obs}, M^{-1}
1.[a]	**18**	**cycHC[6]**	0.4	1,700 ± 250	500 ± 250	400 ± 200
	18	**cycHC[6]**	2.2			
2.	**18**	**cycHC[8]**	0.8	1,211 ± 150	1,175 ± 100	470 ± 120
3.[b]	**16**	**cycHC[6]**	2.0	600 ± 100	350 ± 50	30 ± 30
4.	**16**	**cycHC[8]**	1.9	1,180 ± 20	326 ± 17	195 ± 20

[a]*Experimental data from two independent titrations were fitted simultaneously.*
[b]*Despite the large deviation of K_{3obs}, the overall fit is reliable; see the distribution of residuals in* ***Supplementary Figure S10****.*

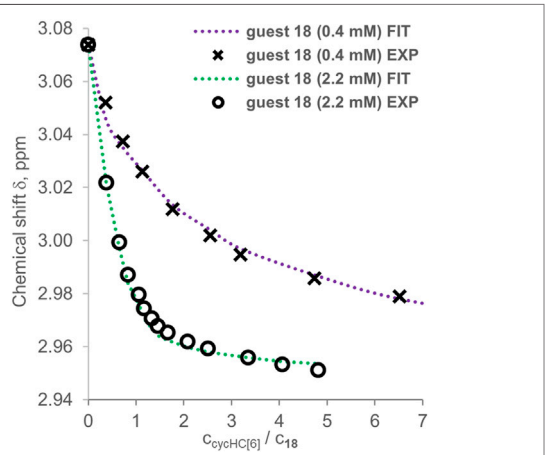

FIGURE 9 | Experimental points and binding isotherms (dotted lines) obtained from simultaneous fitting for titrations of guest **18** titrated by cycHC[6], which were performed at different concentrations.

the case of 2 mM guest **16** titrated by cycHC[6], a very good fit was obtained, as can be recognized from the random distribution of residuals (**Figure 10A**). The 2:1 binding model seems to suit the host–guest system very well, and we could falsely deduce that, indeed, one cycHC[6] binds exactly two molecules of **16**. However, the determined K_{1obs} = 928 ± 17 M^{-1} and K_{2obs} = 501 ± 38 M^{-1} indicate refuted positive cooperativity (K_{2obs}/K_{1obs} > 5/12 for 6:1 systems or K_{2obs}/K_{1obs} > 1/4 for 2:1 systems; for more details, see supporting information, page S9). In addition, both K_{obs} are significantly different from the previously published K_{1obs} = 280 ± 10 M^{-1}, K_{2obs} = 630 ± 20 M^{-1} obtained for similar guest concentration (Prigorchenko et al., 2019).

If any of these apparent K_{1obs} and K_{2obs} were real association constants, then an evaluation of titration for 18 mM guest **16** should provide similar values of binding constants or possibly lower values due to enhanced competition with the guest's dimerization. Nevertheless, the fitting of 18 mM **16** titrated by cycHC[6] provided large sinusoidal residuals, and we can speculate that the large K_{2obs} and a very steep change of experimental values of the chemical shift at low equivalents of cycHC[6] are evidence for the formation of higher stoichiometry complexes (**Figure 10B**). Comparable results were obtained from the fitting of data for the same acid (**16**) with cycHC[8] (**Supplementary Table S23**). Two titrations at 2 mM concentration gave, on average, K_{1obs} = 389 ± 59 M^{-1} and K_{2obs} = 601 ± 85 M^{-1}. An 18 mM titration exhibited large sinusoidal residuals (see **Supplementary Figures S11–S13**). In the case of acid **18**, concentrations were very similar in all titrations, but the results of fitting were inconsistent. Overall, a comparison of all titration experiments for guests **16** and **18** shows the trend of larger apparent positive cooperativity ($K_{1obs} < K_{2obs}$) for experiments at elevated concentrations of guest that can be easily explained by a higher relative amount of complexes with stoichiometry over 2:1 at the beginning of titration in such conditions. It also indicates that a 2:1 binding model is inappropriate as it does not correspond to real complex stoichiometry.

CONCLUSION

Previous studies of cycHC[*n*]-binding properties in nonpolar solvents (chloroform) have focused almost exclusively on interactions with carboxylic acids and their derivatives. The DOSY NMR was used to investigate the complex formation at the molar equivalency of the host and guest. It was not suitable for uncovering the existence of complexes of higher stoichiometry. Later, classical NMR titrations were conducted for cycHC[6] derivatives and trifluoroacetic acid. However, data evaluation with a 2:1 binding model that underestimated the stoichiometry of the guest has provided the false impression of positive cooperativity.

This article has broadened the scope of knowledge on cycHC[*n*]-binding properties in chloroform by testing interactions between a set of guests **1–9** bearing various functional groups and cycHC[8]. Only the guests capable of providing a hydrogen bond exhibited signs of complex formation through the carbonyl groups of the macrocycle. Despite a size difference, cycHC[6] is chemically analogous to cycHC[8] and, due to their similar binding properties, the external binding of guests was confirmed.

We carried out titrations for cycHC[6] and polar organic hydrogen bond donors from a group of thiophenols, phenols, carboxylic acids, and sulfonic acids (guests **6** and **9–18**). We observed a broad range of binding strengths from almost no binding (thiophenols) to moderate (acids **16** and **18**), which did not allow the quantification of association constants with the same binding model for all the collected data and their subsequent comparison. Therefore, we have made a qualitative comparison based on titration curves. The final order of binding strength from weakest to strongest was **6** ≈ **11** < **17** < **12** << **9** ≤ **13** ≤ **10** ≤ **14** < **15** << **16** and correlates with the increasing hydrogen bond donor's partial atomic charge. Methanesulfonic acid **18** exhibited strong binding, but it could

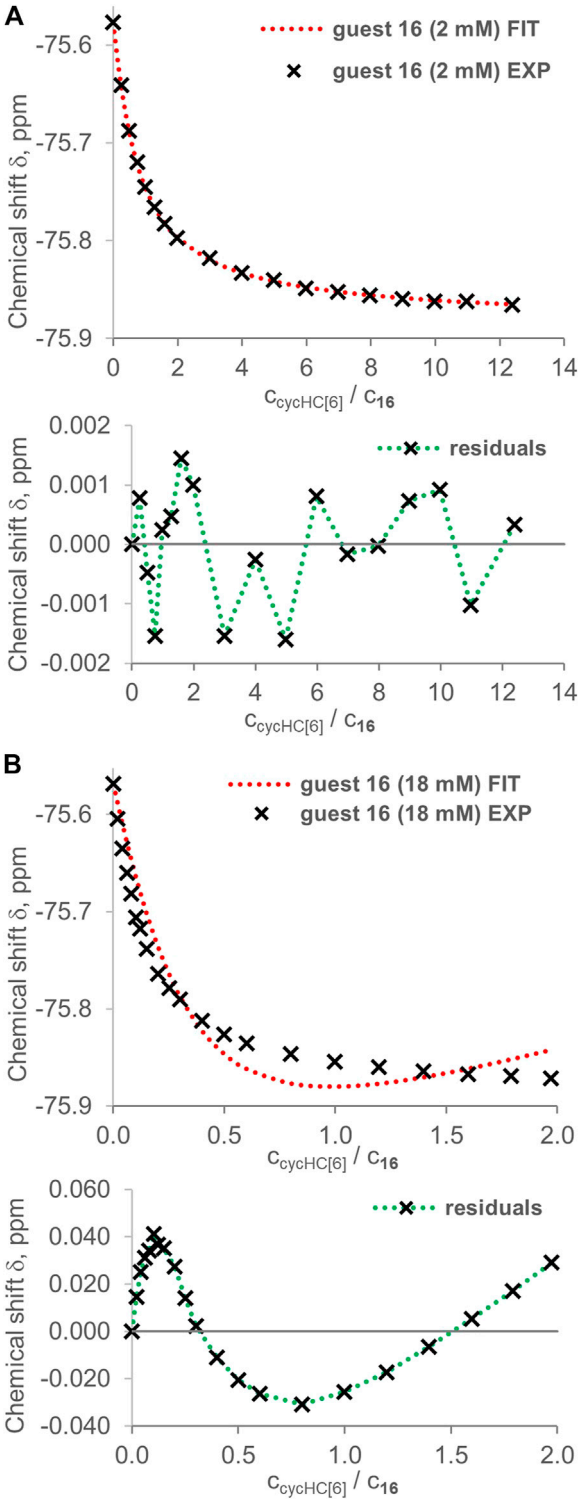

FIGURE 10 | Examples of fitting by the online tool Bindfit (supramolecular.org) using a 2:1 binding model for guest **16** titrated by cycHC[6] at different concentrations. Upper graphs show experimental points (black crosses) and fitted binding isotherm (red dashed line); lower graphs show residuals (distance between the experimental value and fitted isotherm). In the case of **(A)** 2 mM **16,** we obtained a good fit and K_{1obs} = 928 ± 17 M^{-1} and K_{2obs} = 501 ± 38 M^{-1}. However, for **(B)** 18 mM **16,** we obtained a poor fit reflecting the inappropriate binding model (K_{1obs} = 0.04 ± 0.01 M^{-1}, K_{2obs} = 228,544 ± 21,727 M^{-1}).

not be compared to other guests directly due to limited miscibility in chloroform.

We collected additional data to quantify apparent association constants for the strongest binding acids **16** and **18** with our 3:1 and the Bindfit 2:1 binding model. Surprisingly, the 3:1 binding model did not provide a fit for all of the data; however, for acid **18** with cycHC[6], we have obtained K_{1obs} = 1700 ± 250 M^{-1}, K_{2obs} = 500 ± 250 M^{-1}, and K_{3obs} = 400 ± 200 M^{-1} from simultaneous evaluation of two titrations while the 2:1 model gave inconsistent results for all titrations of **18**. None of the models provided an acceptable fit for measurements at high concentration (18 mM) for acid **16**; this could be a consequence of the formation of higher stoichiometry complexes. Nevertheless, we observed a very good fit from 3:1 and 2:1 binding models for titrations of 2 mM of **16**. In such cases, the simpler model should be preferred; therefore, we can report K_{1obs} = 928 ± 17 M^{-1} and K_{2obs} = 501 ± 38 M^{-1} with cycHC[6] and K_{1obs} = 389 ± 59 M^{-1} and K_{2obs} = 601 ± 85 M^{-1} with cycHC[8]. However, macrocycles have enough binding sites to accommodate more than two or three guests, so the determined stepwise association constants are only apparent. We can assume that they include information on higher stoichiometry K_{obs} because of our experimental arrangement. We consider the determined K_{obs} to be valid and useful for the same (ca 2 mM) or lower concentrations in chloroform, which we used in corresponding titration experiments.

Unlike other single-bridged cucurbituril family members, the current study confirmed that the binding of chloride and bromide with cycHC[6] does not occur in methanol and chloroform solutions.

This article has provided new insights into the cycHC[*n*] binding properties that will help recognize promising guests from several biologically active compounds. The binding of HB-donating guests is a dominant interaction in chlorinated solvents, and its strength can be related to the shape, size, and partial charge on the hydrogen atom (of the HB-donating functional group) of the guests. The evaluation of stepwise association constants is challenging because cycHC[*n*] can bind three or more guests at once. Hence, we have demonstrated an alternative approach of qualitative comparison of binding affinity for a set of guests. The same method can be used for any host–guest system where the same binding mechanism can be assumed for all tested guests.

DATA AVAILABILITY STATEMENT

The original contributions presented in the study are included in the article/**Supplementary Material**, and further inquiries can be directed to the corresponding authors.

AUTHOR CONTRIBUTIONS

LU has planned a study, analyzed the results and lead writing of manuscript and supporting information, and evaluated data using online tools from supramolecular.org. TB has developed and modified the 3:1 binding model and evaluated the titration data. MÖ carried out modeling and partial charges calculations

and contributed to manuscript writing. KJ and JI have conducted all NMR titrations equally. KS has conducted tests of interaction between inorganic anions and cycHC[6] in MeOD-d_4 and $CDCl_3$. KAM synthesized (*R,R*)-cycHC[*n*]s. RA has contributed by planning, analyzing, and writing of the manuscript.

FUNDING

The authors would like to acknowledge the Estonian Research Council grant nos. PRG399 and H2020-FETOPEN (828779 (INITIO)) for their financial support. UL has been supported by the Estonian Research Council grant MOBJD592.

ACKNOWLEDGMENTS

The authors thank Marina Kudrajašova for assistance with ^{19}F NMR measurements, Aet Laurik for conducting the Job plot experiment between guest **16** and cycHC[8], and Kristin Erkman for laboratory management.

SUPPLEMENTARY MATERIAL

The Supplementary Material for this article can be found online at: https://www.frontiersin.org/articles/10.3389/fchem.2021.701028/full#supplementary-material

REFERENCES

Aav, R., Shmatova, E., Reile, I., Borissova, M., Topić, F., and Rissanen, K. (2013). New Chiral Cyclohexylhemicucurbit[6]uril. *Org. Lett.* 15, 3786–3789. doi:10.1021/ol401766a

Abraham, M. H., Abraham, R. J., Byrne, J., and Griffiths, L. (2006). NMR Method for the Determination of Solute Hydrogen Bond Acidity. *J. Org. Chem.* 71, 3389–3394. doi:10.1021/jo052631n

Abraham, M. H. (1993). Scales of Solute Hydrogen-Bonding: Their Construction and Application to Physicochemical and Biochemical Processes. *Chem. Soc. Rev.* 22, 73–83. doi:10.1039/CS9932200073

Andersen, N. N., Lisbjerg, M., Eriksen, K., and Pittelkow, M. (2018). Hemicucurbit [n]urils and Their Derivatives - Synthesis and Applications. *Isr. J. Chem.* 58, 435–448. doi:10.1002/ijch.201700129

Aprà, E., Bylaska, E. J., de Jong, W. A., Govind, N., Kowalski, K., Straatsma, T. P., et al. (2020). NWChem: Past, Present, and Future. *J. Chem. Phys.* 152, 184102. doi:10.1063/5.0004997

Assaf, K. I., and Nau, W. M. (2014). Cucurbiturils: from Synthesis to High-Affinity Binding and Catalysis. *Chem. Soc. Rev.* 44, 394–418. doi:10.1039/C4CS00273C

Barrow, S. J., Kasera, S., Rowland, M. J., del Barrio, J., and Scherman, O. A. (2015). Cucurbituril-Based Molecular Recognition. *Chem. Rev.* 115, 12320–12406. doi:10.1021/acs.chemrev.5b00341

Bordwell, F. G. (1988). Equilibrium Acidities in Dimethyl Sulfoxide Solution. *Acc. Chem. Res.* 21, 456–463. doi:10.1021/ar00156a004

Colominas, C., Teixidó, J., Cemelí, J., Luque, F. J., and Orozco, M. (1998). Dimerization of Carboxylic Acids: Reliability of Theoretical Calculations and the Effect of Solvent. *J. Phys. Chem. B* 102, 2269–2276. doi:10.1021/jp973414w

Davis, J. T., Gale, P. A., and Quesada, R. (2020). Advances in Anion Transport and Supramolecular Medicinal Chemistry. *Chem. Soc. Rev.* 49, 6056–6086. doi:10.1039/C9CS00662A

Day, A., Arnold, A. P., Blanch, R. J., and Snushall, B. (2001). Controlling Factors in the Synthesis of Cucurbituril and its Homologues. *J. Org. Chem.* 66, 8094–8100. doi:10.1021/jo015897c

Ercolani, G. (2003). Assessment of Cooperativity in Self-Assembly. *J. Am. Chem. Soc.* 125, 16097–16103. doi:10.1021/ja038396c

Fujii, Y., Yamada, H., and Mizuta, M. (1988). Self-association of Acetic Acid in Some Organic Solvents. *J. Phys. Chem.* 92, 6768–6772. doi:10.1021/j100334a054

Hibbert, D. B., and Thordarson, P. (2016). The Death of the Job Plot, Transparency, Open Science and Online Tools, Uncertainty Estimation Methods and Other Developments in Supramolecular Chemistry Data Analysis. *Chem. Commun.* 52, 12792–12805. doi:10.1039/C6CC03888C

Hibbert, F., and Emsley, J. (1990). "Hydrogen Bonding and Chemical Reactivity," in *"Hydrogen Bonding and Chemical Reactivity," in* Advances In Physical Organic Chemistry. Editor D. Bethell (Academic Press), 255–379. doi:10.1016/S0065-3160(08)60047-7

Howells, R. D., and Mc Cown, J. D. (1977). Trifluoromethanesulfonic Acid and Derivatives. *Chem. Rev.* 77, 69–92. doi:10.1021/cr60305a005

Hunter, C. A., and Anderson, H. L. (2009). What Is Cooperativity? *Angew. Chem. Int. Ed.* 48, 7488–7499. doi:10.1002/anie.200902490

Ji, X., Ahmed, M., Long, L., Khashab, N. M., Huang, F., and Sessler, J. L. (2019). Adhesive Supramolecular Polymeric Materials Constructed from Macrocycle-Based Host-Guest Interactions. *Chem. Soc. Rev.* 48, 2682–2697. doi:10.1039/C8CS00955D

Kaabel, S., and Aav, R. (2017). Templating Effects in the Dynamic Chemistry of Cucurbiturils and Hemicucurbiturils. *Isr. J. Chem.* 58, 296–313. doi:10.1002/ijch.201700106

Kaabel, S., Adamson, J., Topić, F., Kiesilä, A., Kalenius, E., Öeren, M., et al. (2017). Chiral Hemicucurbit[8]uril as an Anion Receptor: Selectivity to Size, Shape and Charge Distribution. *Chem. Sci.* 8, 2184–2190. doi:10.1039/C6SC05058A

Kaabel, S., Stein, R. S., Fomitšenko, M., Järving, I., Friščić, T., and Aav, R. (2019). Size-Control by Anion Templating in Mechanochemical Synthesis of Hemicucurbiturils in the Solid State. *Angew. Chem. Int. Ed.* 58, 6230–6234. doi:10.1002/anie.201813431

Kim, J., Jung, I.-S., Kim, S.-Y., Lee, E., Kang, J.-K., Sakamoto, S., et al. (2000). New Cucurbituril Homologues: Syntheses, Isolation, Characterization, and X-ray Crystal Structures of Cucurbit[n]uril (N = 5, 7, and 8). *J. Am. Chem. Soc.* 122, 540–541. doi:10.1021/ja993376p

Lagona, J., Mukhopadhyay, P., Chakrabarti, S., and Isaacs, L. (2005). The Cucurbit [n]uril Family. *Angew. Chem. Int. Ed.* 44, 4844–4870. doi:10.1002/anie.200460675

Lizal, T., and Sindelar, V. (2018). Bambusuril Anion Receptors. *Isr. J. Chem.* 58, 326–333. doi:10.1002/ijch.201700111

Lu, T., and Chen, F. (2012). Multiwfn: A Multifunctional Wavefunction Analyzer. *J. Comput. Chem.* 33, 580–592. doi:10.1002/jcc.22885

Mishra, K. A., Adamson, J., Öeren, M., Kaabel, S., Fomitšenko, M., and Aav, R. (2020). Dynamic Chiral Cyclohexanohemicucurbit[12]uril. *Chem. Commun.* 56, 14645–14648. doi:10.1039/D0CC06817A

Öeren, M., Shmatova, E., Tamm, T., and Aav, R. (2014). Computational and Ion Mobility MS Study of (All-S)-Cyclohexylhemicucurbit[6]uril Structure and Complexes. *Phys. Chem. Chem. Phys.* 16, 19198–19205. doi:10.1039/C4CP02202E

Prigorchenko, E., Kaabel, S., Narva, T., Baškir, A., Fomitšenko, M., Adamson, J., et al. (2019). Formation and Trapping of the Thermodynamically Unfavoured Inverted-Hemicucurbit[6]uril. *Chem. Commun.* 55, 9307–9310. doi:10.1039/C9CC04990H

Prigorchenko, E., Öeren, M., Kaabel, S., Fomitšenko, M., Reile, I., Järving, I., et al. (2015). Template-controlled Synthesis of Chiral Cyclohexylhemicucurbit[8]uril. *Chem. Commun.* 51, 10921–10924. doi:10.1039/C5CC04101E

Reany, O., Mohite, A., and Keinan, E. (2018). Hetero-Bambusurils. *Isr. J. Chem.* 58, 449–460. doi:10.1002/ijch.201700138

Stoyanov, E. S., and Stoyanova, I. V. (2018). Chloronium Cations in Dichloromethane Solutions as Catalysts for the Conversion of CH2 Cl2 to CHCl3 /CCl4 and CH3 Cl/CH4. *ChemistrySelect* 3, 122–126. doi:10.1002/slct.201702738

Tang, B., Zhao, J., Xu, J. F., and Zhang, X. (2020). Cucurbit[N]urils for Supramolecular Catalysis. *Chem. Eur. J.* 26, 15446–15460. doi:10.1002/chem.202003897

Thordarson, P. (2011). Determining Association Constants from Titration Experiments in Supramolecular Chemistry. *Chem. Soc. Rev.* 40, 1305–1323. doi:10.1039/C0CS00062K

Ulatowski, F., Dąbrowa, K., Bałakier, T., and Jurczak, J. (2016). Recognizing the Limited Applicability of Job Plots in Studying Host-Guest Interactions in Supramolecular Chemistry. *J. Org. Chem.* 81, 1746–1756. doi:10.1021/acs.joc.5b02909

Ustrnul, L., Kaabel, S., Burankova, T., Martõnova, J., Adamson, J., Konrad, N., et al. (2019). Supramolecular Chirogenesis in Zinc Porphyrins by Enantiopure Hemicucurbit[n]urils (N = 6, 8). *Chem. Commun.* 55, 14434–14437. doi:10.1039/C9CC07150D

Walker, S., Oun, R., McInnes, F. J., and Wheate, N. J. (2011). The Potential of Cucurbit[n]urils in Drug Delivery. *Isr. J. Chem.* 51, 616–624. doi:10.1002/ijch.201100033

Conflict of Interest: Authors TB and MÖ were employed by the company Process Analytics, Hamilton Bonaduz AG and Optibrium Limited, respectively.

The remaining authors declare that the research was conducted in the absence of any commercial or financial relationships that could be construed as a potential conflict of interest.

frontiers in Chemistry

ORIGINAL RESEARCH
published: 29 June 2021
doi: 10.3389/fchem.2021.710808

Deep Cavitand Calixarene–Solubilized Fullerene as a Potential Photodynamic Agent

Tian-Xing Zhang[†], *Juan-Juan Li*[†], *Hua-Bin Li* * *and Dong-Sheng Guo* *

College of Chemistry, Key Laboratory of Functional Polymer Materials (Ministry of Education), State Key Laboratory of Elemento-Organic Chemistry, Tianjin Key Laboratory of Biosensing and Molecular Recognition, Nankai University, Tianjin, China

Fullerene has attracted much attention in biomedical research due to its unique physical and chemical properties. However, the hydrophobic nature of fullerene is limited to deploy in the body, given that the biofluids are mainly water. In this study, a water-soluble supramolecular nanoformulation based on a deep cavitand calixarene (SAC4A) and fullerene is developed to overcome the hydrophobicity of fullerene and is used as a potential photodynamic agent. SAC4A solubilizes fullerene very well with a simple grinding method. The significantly increased water solubility of fullerene enables efficient activation of reactive oxygen species. The host–guest strategy to solubilize fullerene can not only provide a new method to achieve water solubility but also expand the biomedical applications of fullerene.

Keywords: supramolecular chemistry, photodynamic agent, calixarene, fullerene, solubility

OPEN ACCESS

Edited by:
Tangxin Xiao,
Changzhou University, China

Reviewed by:
Yong Yao,
Nantong University, China
Yan-Long Ma,
Guangdong Pharmaceutical University, China

****Correspondence:***
Hua-Bin Li
lihuabin@nankai.edu.cn
Dong-Sheng Guo
dshguo@nankai.edu.cn

[†]These authors have contributed equally to this work and share first authorship

Specialty section:
This article was submitted to Supramolecular Chemistry, a section of the journal Frontiers in Chemistry

Received: *17 May 2021*
Accepted: *09 June 2021*
Published: *29 June 2021*

Citation:
Zhang T-X, Li J-J, Li H-B and Guo D-S (2021) Deep Cavitand Calixarene–Solubilized Fullerene as a Potential Photodynamic Agent. Front. Chem. 9:710808. doi: 10.3389/fchem.2021.710808

INTRODUCTION

Fullerene has been widely used in biomedical research, acting as an antimicrobial agent (Mashino et al., 1999; Tsao et al., 2001), a human immunodeficiency virus protease inhibitor (Friedman et al., 1993), and a photosensitizer to cleave DNA (Boutorine et al., 1995; Sharma et al., 2011). It can efficiently form long-lived triplet excited states by visible-light irradiation and generate highly reactive oxygen species (ROS) *via* an electron transfer Type I reaction, which generates superoxide anions ($O_2^{-\bullet}$) yielding hydroxyl radicals, and/or an energy transfer Type II reaction, which generates singlet oxygen molecules ($^1O_2$) (Yamakoshi et al., 2003). However, the hydrophobicity of fullerene limits its potential applications as photosensitizer in biological fluids. Much effort has been focused on increasing fullerene water solubility by grafting hydrophilic groups on fullerene (Rašović, 2016). Nevertheless, chemical modifications usually lead to the unanticipated alternation of fullerene photophysical properties (Hamano et al., 1997; Prat et al., 1999). Therefore, the solubilization of fullerene in a non-covalent approach emerges to be an alternative approach (Zhang et al., 2014). Macrocyclic hosts have been engaged in solubilizing fullerene in water [e.g., cyclodextrins (CD) and calixarenes] (Ikeda, 2013). Braun et al. investigated the solid–solid mechanochemical reaction between fullerene and γ-CD by ball-milling their mixture. The concentration of C_{60} in water was 1.5×10^{-4} M [(γ-CD) = 6.5×10^{-3} M] (Braun et al., 1994). Komatsu et al. examined that the equimolar amounts of C_{60} and sulfonatocalix[8]arene were subjected to high-speed vibration milling treatment, and the concentration of C_{60} was calculated to be 1.3×10^{-4} M (Komatsu et al., 1999). These water-soluble fullerenes solubilized by macrocycles confirm the feasibility of the host–guest strategy. Moreover, the complexation of fullerenes by macrocycles is an important way used to improve their photoactivities (Antoku et al., 2019).

In this work, we synthesized sulfonated azocalix[4]arene (SAC4A), which possesses a deep cavity that imparts strong binding to hydrophobic cargoes. Additionally, the -SO_3^- functional

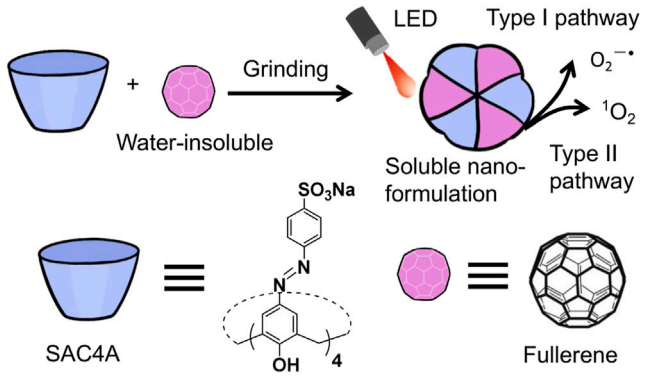

FIGURE 1 | Schematic illustration of supramolecular nanoformulation formed by the host–guest complexation between SAC4A and fullerene. The encapsulation of fullerene with SAC4A gives rise to improved solubility and efficiently activated ROS.

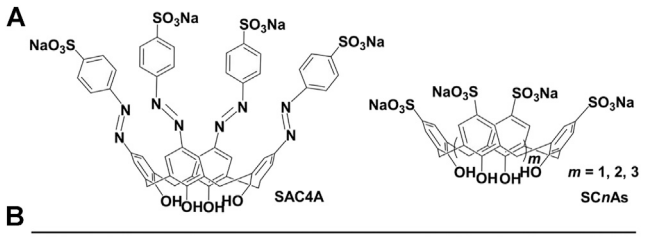

B

Host	C_{60} (μM)	C_{70} (μM)	Host	C_{60} (μM)	C_{70} (μM)
SAC4A	645 ± 8	573 ± 26	SC4A	< 1	< 1
SC5A	< 1	< 1	SC6A	< 1	< 1

FIGURE 2 | (A) Molecular structures of SAC4A and SC*n*As. **(B)** The concentrations of C_{60} and C_{70} solubilized by calixarenes (1 mM for hosts).

groups endow calixarene with water solubility and also provide anchoring points that supplement the cavity binding to guests (Guo et al., 2014; Pan et al., 2017; Pan et al., 2021; Pan et al., 2021). As expected, SAC4A solubilized fullerene under the condition of a molar ratio of 1:1 by the grinding method (**Figure 1**), which is a simpler method than ball-milling or high-speed vibration milling treatment. We further evaluated its ability to generate ROS under LED irradiation, which is significant on account of its further biomedical applications.

RESULTS AND DISCUSSION

Molecular Design of Macrocyclic Host SAC4A and SAC4A-Solubilized Fullerene

Calixarene was employed as the macrocyclic host because of its broad chemical design space (Böhmer, 1995). By making calix[4]arene to directly react with 4-sulfobenzenediazonium

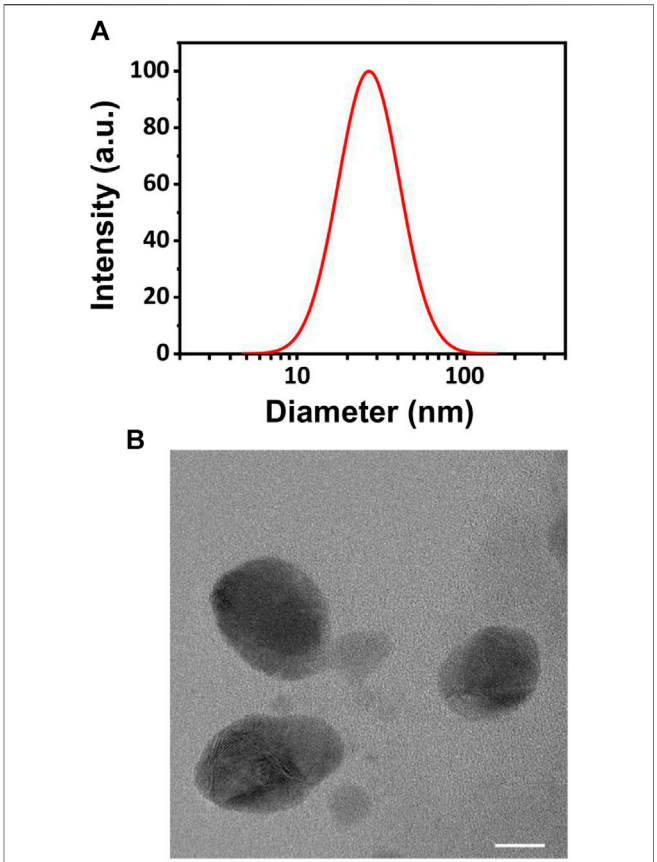

FIGURE 3 | (A) The DLS data of the C_{60}@SAC4A assembly in PBS buffer (10 mM, pH = 7.4), at 25°C. **(B)** TEM image of the C_{60}@SAC4A assembly (scale bar, 10 nm).

chloride, SAC4A was obtained with a high yield (**Figure 2A** and **Supplementary Figure S1**) (Lu et al., 2005). Sulfocalix[*n*]arenes (SC*n*As, *n* = 4, 5, and 6) without deep cavity were synthesized as controls (**Figure 2A**), referring to literatures (Shinkai et al., 1987; Steed et al., 1995). The calixarene-solubilized fullerenes (C_{60} and C_{70}) were prepared by the grinding method (for more details, see the **Supplementary Material**). The concentrations of C_{60} and C_{70} in the supernatant were determined by high-performance liquid chromatography (**Figure 2B**). The concentration of C_{60} by supramolecular complexation with SAC4A increased to 6.45×10^{-4} M. The solubilization effect of SAC4A is significantly higher than that of the control of SC*n*As. It may be observed that the cavity of SC4A is too small to accommodate fullerene. Even if adding repetitive units to expand the cavity latitudinally, the cavities of SC5A and SC6A are still too shallow to encapsulate fullerene. On the other hand, the azobenzene modification endows SAC4A with a deep cavity that is suitable to include hydrophobic guests (Zhang et al., 2020). It is suggested that calixarene is more effective in solubilizing fullerene by extending the cavity longitudinally than latitudinally.

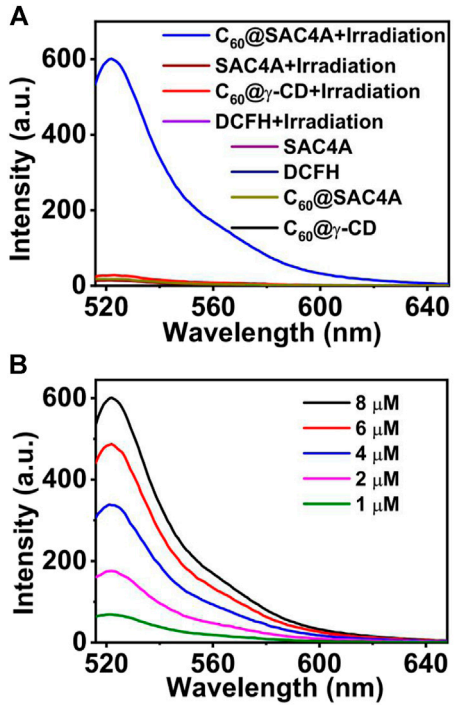

FIGURE 4 | (A) Fluorescence response of DCFH to ROS treated with C_{60}@SAC4A (8 μM for C_{60}), SAC4A (10 μM), and C_{60}@γ-CD (8 μM for C_{60}) under LED irradiation for 1 min or no irradiation. **(B)** Fluorescence response of DCFH to ROS treated with C_{60}@SAC4A of different concentrations under LED irradiation for 1 min.

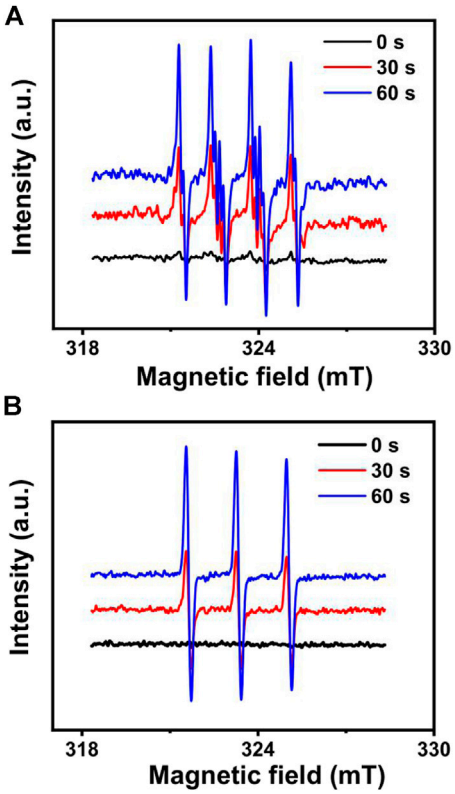

FIGURE 5 | (A) EPR signals of DMPO (for Type I ROS detection) in the presence of C_{60}@SAC4A (80 μM for C_{60}) with NADH (5 mM) irradiated for 0, 30, or 60 s. **(B)** EPR signals of TEMP (for Type II ROS detection) in the presence of C_{60}@SAC4A (80 μM for C_{60}) irradiated for 0, 30, or 60 s.

Size, Morphology, and Stability of C_{60}@SAC4A

Due to the best solubilizing effect, we selected the C_{60}@SAC4A system to representatively study its size and morphology. Dynamic light scattering (DLS) was employed to identify the size of the C_{60}@SAC4A assembly (Guo et al., 2020), giving a hydration diameter of 28 nm with a polydispersity index (PDI) of 0.135 (**Figure 3A**). The representative transmission electron microscopy (TEM) image (Li et al., 2020) revealed that the C_{60}@SAC4A assembly possessed a spherical morphology with an average size of 20 nm (**Figure 3B**), which was smaller than the DLS result due to the dehydration that occurred during the TEM sample preparation (Yang et al., 2020). C_{60}@SAC4A forms water-soluble nanoformulation rather than simple host–guest complex, implying a potential passive targeting ability through enhanced permeation and retention (EPR) effect when used *in vivo* (Gao et al., 2018; Cai et al., 2021).

The stability of assembly is a fundamental factor. A DLS test was performed to observe the particle size changes of C_{60}@SAC4A at different time points (**Supplementary Figure S2**). The C_{60}@SAC4A assembly shows no significant changes in particle size within 7 days. These results proved that the C_{60}@SAC4A assembly is stable in time. SAC4A is expected to be a supramolecular solubilizing agent to disperse fullerene in water.

ROS Generation of C_{60}@SAC4A

The identification and research of ROS are crucial for the further development of photodynamic therapy based on fullerenes as photosensitizers. In order to see if it was a potential photodynamic agent, the ROS generation capacities of C_{60}@SAC4A were investigated by a commercial indicator, 2,7-dichlorodihydrofluorescein (DCFH), that responds to general types of ROS (Zhuang et al., 2020). Upon exposure to LED irradiation, the nonemissive DCFH solution with C_{60}@SAC4A exhibits increased fluorescence intensity, accomplishing approximately 35-fold enhancement within 1 min, while those of control groups under the same conditions are barely increased (**Figure 4A**). Additionally, γ-cyclodextrin–solubilized C_{60} (C_{60}@γ-CD) was chosen as the positive control group, showing a little fluorescence increase under LED irradiation, due to the reactivity of C_{60} with O_2 decreased when it was enclosed in the γ-CD cavity (Priyadarsini et al., 1994). Another possible reason is that the amount of cyclodextrin used for solubilization is much higher than that of calixarene, resulting that the cyclodextrin limits the contact between C_{60} and O_2. **Figure 4B** showed the fluorescence response of DCFH to ROS treated with C_{60}@SAC4A of different concentrations, suggesting that the peak intensity and the concentration of C_{60}@SAC4A were increased in a concentration-dependent manner.

Electron paramagnetic resonance (EPR) spectroscopy is one powerful method to identify short-lived ROS species (Zang et al., 1998). 5,5-Dimethyl-1-pyrroline-*N*-oxide (DMPO) was used as a spin-trap agent to detect $O_2^{-\bullet}$. **Figure 5A** shows the spectra obtained for DMPO/$O_2^{-\bullet}$ adduct, indicative of the generation of $O_2^{-\bullet}$ from C_{60}@SAC4A under light and nicotinamide adenine dinucleotide (reduced, NADH, to mimic the strong reducing environment) conditions, namely, Type I ROS (Zhao et al., 2008). In the absence of either NADH or C_{60}, there were no appreciable $O_2^{-\bullet}$ signals detected (**Supplementary Figure S3A**), showing that electron transfer processes induced by reducing agents are very significant for the generation of $O_2^{-\bullet}$ in aqueous systems (Yamakoshi et al., 2003). For the detection of $^1O_2$, the EPR method with 2,2,6,6-tetramethyl-4-piperidone (TEMP) was employed. As shown in **Figure 5B**, the resultant EPR spectra displayed a typical 1:1:1 triplet signal, which is the characteristic resonance for TEMP/$^1O_2$ adduct, whereas no signal was detected in the control group containing SAC4A under the same condition (**Supplementary Figure S3B**), indicative of its good ability of Type II ROS (Yamakoshi et al., 2003). Based on the above evidence, it is consequently reasonable to draw a conclusion that C_{60}@SAC4A followed both Type I and Type II pathways to generate ROS species, indicating that C_{60}@SAC4A can be a promising candidate as a water-soluble supramolecular photosensitizer.

CONCLUSION

In summary, SAC4A was synthesized and used to improve the water solubility of fullerene by host–guest complexation. Compared with SC*n*As that are widely studied as classical water-soluble calixarene derivatives, SAC4A possesses the deeper cavity longitudinally and is more effective in solubilizing fullerene. The supramolecular nanoformulation C_{60}@SAC4A generates ROS species effectively in both Type I and Type II pathways, indicative of a potential photodynamic agent. Calixarene is highly modifiable, and thus, a lot of water-soluble derivatives could be obtained to solubilize hydrophobic substances besides fullerenes. One important lesson from this work is that vertical expansion of cavity emerges to be a more powerful way than horizontal expansion to solubilize large hydrophobic species on account of the cone shape of calixarene.

DATA AVAILABILITY STATEMENT

The original contributions presented in the study are included in the article/**Supplementary Material**; further inquiries can be directed to the corresponding authors.

AUTHOR CONTRIBUTIONS

H-BL and D-SG conceived the experiments. T-XZ and J-JL conducted the experiments. T-XZ, H-BL, and D-SG contributed to writing of the manuscript with input from the other authors.

FUNDING

Financial support was obtained from the NSFC (U20A20259 and 31961143004), the Fundamental Research Funds for the Central Universities, and NCC Fund (NCC2020FH04), which are gratefully acknowledged.

SUPPLEMENTARY MATERIAL

The Supplementary Material for this article can be found online at: https://www.frontiersin.org/articles/10.3389/fchem.2021.710808/full#supplementary-material

REFERENCES

Antoku, D., Sugikawa, K., and Ikeda, A. (2019). Photodynamic Activity of Fullerene Derivatives Solubilized in Water by Natural-Product-Based Solubilizing Agents. *Chem. Eur. J.* 25, 1854–1865. doi:10.1002/chem.201803657

Böhmer, V. (1995). Calixarenes, Macrocycles with(Almost) Unlimited Possibilities. *Angew. Chem. Int. Ed. Engl.* 34, 713–745. doi:10.1002/anie.199507131

Boutorine, A. S., Takasugi, M., Hélène, C., Tokuyama, H., Isobe, H., and Nakamura, E. (1995). Fullerene-Oligonucleotide Conjugates: Photoinduced Sequence-specific DNA Cleavage. *Angew. Chem. Int. Ed. Engl.* 33, 2462–2465. doi:10.1002/anie.199424621

Braun, T., Buvaribarcza, A., Barcza, L., Konkolythege, I., Fodor, M., and Migali, B. (1994). Mechanochemistry: a Novel Approach to the Synthesis of Fullerene Compounds. Water Soluble Buckminsterfullerene - γ-cyclodextrin Inclusion Complexes *via* a Solid-Solid Reaction. *Solid State Ionics* 74, 47–51. doi:10.1016/0167-2738(94)90435-9

Cai, Y., Zhang, Z., Ding, Y., Hu, L., Wang, J., Chen, T., et al. (2021). Recent Development of Pillar[*n*]arene-Based Amphiphiles. *Chin. Chem. Lett.* 32, 1267–1279. doi:10.1016/j.cclet.2020.10.036

Friedman, S. H., DeCamp, D. L., Sijbesma, R. P., Srdanov, G., Wudl, F., and Kenyon, G. L. (1993). Inhibition of the HIV-1 Protease by Fullerene Derivatives: Model Building Studies and Experimental Verification. *J. Am. Chem. Soc.* 115, 6506–6509. doi:10.1021/ja00068a005

Gao, J., Li, J., Geng, W.-C., Chen, F.-Y., Duan, X., Zheng, Z., et al. (2018). Biomarker Displacement Activation: a General Host-Guest Strategy for Targeted Phototheranostics *In Vivo*. *J. Am. Chem. Soc.* 140, 4945–4953. doi:10.1021/jacs.8b02331

Guo, D.-S., and Liu, Y. (2014). Supramolecular Chemistry of *P*-Sulfonatocalix[*n*]arenes and its Biological Applications. *Acc. Chem. Res.* 47, 1925–1934. doi:10.1021/ar500009g

Guo, H., Yan, X., Lu, B., Wang, J., Yuan, X., Han, Y., et al. (2020). Pillar[5]arene-based Supramolecular Assemblies with Two-step Sequential Fluorescence Enhancement for Mitochondria-Targeted Cell Imaging. *J. Mater. Chem. C* 8, 15622–15625. doi:10.1039/d0tc04343e

Hamano, T., Okuda, K., Mashino, T., Hirobe, M., Arakane, K., Ryu, A., et al. (1997). Singlet Oxygen Production from Fullerene Derivatives: Effect of Sequential Functionalization of the Fullerene Core. *Chem. Commun.*, 21–22. doi:10.1039/a606335g

Ikeda, A. (2013). Water-soluble Fullerenes Using Solubilizing Agents, and Their Applications. *J. Incl Phenom Macrocycl Chem.* 77, 49–65. doi:10.1007/s10847-013-0319-9

Komatsu, K., Fujiwara, K., Murata, Y., and Braun, T. (1999). Aqueous Solubilization of Crystalline Fullerenes by Supramolecular Complexation

with γ-cyclodextrin and Sulfocalix[8]arene under Mechanochemical High-Speed Vibration Milling. *J. Chem. Soc. Perkin Trans. 1* 1, 2963–2966. doi:10.1039/A904736K

Li, L., Tuo, W., Zhu, Q., Sepehrpour, H., Yao, Y., Yan, C., et al. (2020). Resorcinarene Induced Assembly of Carotene and Lutein into Hierarchical Superstructures. *J. Am. Chem. Soc.* 142, 20583–20587. doi:10.1021/jacs.0c10901

Lu, L., Zhu, S., Liu, X., Xie, Z., and Yan, X. (2005). Highly Selective Chromogenic Ionophores for the Recognition of Chromium(III) Based on a Water-Soluble Azocalixarene Derivative. *Analytica Chim. Acta* 535, 183–187. doi:10.1016/j.aca.2004.11.059

Mashino, T., Okuda, K., Hirota, T., Hirobe, M., Nagano, T., and Mochizuki, M. (1999). Inhibition of*E. Coli* Growth by Fullerene Derivatives and Inhibition Mechanism. *Bioorg. Med. Chem. Lett.* 9, 2959–2962. doi:10.1016/S0960-894X(99)00515-6

Pan, Y.-C., Tian, H.-W., Peng, S., Hu, X.-Y., and Guo, D.-S. (2017). Molecular Recognition of Sulfonatocalixarene with Organic Cations at the Self-Assembled Interface: a Thermodynamic Investigation. *Chin. Chem. Lett.* 28, 787–792. doi:10.1016/j.cclet.2016.12.027

Pan, Y. C., Barba-Bon, A., Tian, H. W., Ding, F., Hennig, A., Nau, W. M., et al. (2021). An Amphiphilic Sulfonatocalix[5]arene as an Activator for Membrane Transport of Lysine-rich Peptides and Proteins. *Angew. Chem. Int. Ed.* 60, 1875–1882. doi:10.1002/anie.202011185

Pan, Y. C., Hu, X. Y., and Guo, D. S. (2021). Biomedical Applications of Calixarenes: State of the Art and Perspectives. *Angew. Chem. Int. Ed.* 60, 2768–2794. doi:10.1002/anie.201916380

Prat, F., Stackow, R., Bernstein, R., Qian, W., Rubin, Y., and Foote, C. S. (1999). Triplet-state Properties and Singlet Oxygen Generation in a Homologous Series of Functionalized Fullerene Derivatives. *J. Phys. Chem. A.* 103, 7230–7235. doi:10.1021/jp991237o

Priyadarsini, K. I., Mohan, H., Tyagi, A. K., and Mittal, J. P. (1994). Inclusion Complex of .gamma.-Cyclodextrin-C60: Formation, Characterization, and Photophysical Properties in Aqueous Solutions. *J. Phys. Chem.* 98, 4756–4759. doi:10.1021/j100068a044

Rašović, I. (2016). Water-soluble Fullerenes for Medical Applications. *Mater. Sci. Techn.* 33, 777–794. doi:10.1080/02670836.2016.1198114

Sharma, S. K., Chiang, L. Y., and Hamblin, M. R. (2011). Photodynamic Therapy with Fullerenesin Vivo: Reality or a Dream? *Nanomedicine* 6, 1813–1825. doi:10.2217/NNM.11.144

Shinkai, S., Araki, K., Tsubaki, T., Arimura, T., and Manabe, O. (1987). New Syntheses of Calixarene-*P*-Sulphonates and *P*-Nitrocalixarenes. *J. Chem. Soc. Perkin Trans. 1* 1, 2297–2299. doi:10.1039/P19870002297

Steed, J. W., Johnson, C. P., Barnes, C. L., Juneja, R. K., Atwood, J. L., Reilly, S., et al. (1995). Supramolecular Chemistry of *P*-Sulfonatocalix[5]arene: a Water-Soluble, Bowl-Shaped Host with a Large Molecular Cavity. *J. Am. Chem. Soc.* 117, 11426–11433. doi:10.1021/ja00151a006

Tsao, N., Luh, T.-Y., Chou, C.-K., Wu, J.-J., Lin, Y.-S., and Lei, H.-Y. (2001). Inhibition of Group a streptococcus Infection by Carboxyfullerene. *Antimicrob. Agents Chemother.* 45, 1788–1793. doi:10.1128/aac.45.6.1788-1793.2001

Yamakoshi, Y., Umezawa, N., Ryu, A., Arakane, K., Miyata, N., Goda, Y., et al. (2003). Active Oxygen Species Generated from Photoexcited Fullerene (C60) as Potential Medicines: O2-versus1O2. *J. Am. Chem. Soc.* 125, 12803–12809. doi:10.1021/ja0355574

Yang, L., Zhang, C., Liu, J., Huang, F., Zhang, Y., Liang, X. J., et al. (2020). ICG-Conjugated and 125 I-Labeled Polymeric Micelles with High Biosafety for Multimodality Imaging-Guided Photothermal Therapy of Tumors. *Adv. Healthc. Mater.* 9, 1901616. doi:10.1002/adhm.201901616

Zang, L.-Y., Cosma, G., Gardner, H., and Vallyathan, V. (1998). Scavenging of Reactive Oxygen Species by Melatonin. *Biochim. Biophys. Acta (Bba) - Gen. Subjects* 1425, 469–477. doi:10.1016/s0304-4165(98)00099-3

Zhang, T. X., Zhang, Z. Z., Yue, Y. X., Hu, X. Y., Huang, F., Shi, L., et al. (2020). A General Hypoxia-Responsive Molecular Container for Tumor-Targeted Therapy. *Adv. Mater.* 32, 1908435. doi:10.1002/adma.201908435

Zhang, W., Gong, X., Liu, C., Piao, Y., Sun, Y., and Diao, G. (2014). Water-soluble Inclusion Complex of Fullerene with γ-cyclodextrin Polymer for Photodynamic Therapy. *J. Mater. Chem. B* 2, 5107–5115. doi:10.1039/c4tb00560k

Zhao, B., Bilski, P. J., He, Y.-Y., Feng, L., and Chignell, C. F. (2008). Photo-induced Reactive Oxygen Species Generation by Different Water-Soluble Fullerenes (C60) and Their Cytotoxicity in Human Keratinocytes. *Photochem. Photobiol.* 84, 1215–1223. doi:10.1111/j.1751-1097.2008.00333.x

Zhuang, Z., Dai, J., Yu, M., Li, J., Shen, P., Hu, R., et al. (2020). Type I Photosensitizers Based on Phosphindole Oxide for Photodynamic Therapy: Apoptosis and Autophagy Induced by Endoplasmic Reticulum Stress. *Chem. Sci.* 11, 3405–3417. doi:10.1039/d0sc00785d

Conflict of Interest: The authors declare that the research was conducted in the absence of any commercial or financial relationships that could be construed as a potential conflict of interest.

frontiers in Chemistry

ORIGINAL RESEARCH
published: 07 July 2021
doi: 10.3389/fchem.2021.697684

Cavity-Containing $[Fe_2L_3]^{4+}$ Helicates: An Examination of Host-Guest Chemistry and Cytotoxicity

Lynn S. Lisboa[1†], Mie Riisom[2,3†], Roan A. S. Vasdev[1†], Stephen M. F. Jamieson[3†], L. James Wright[2†], Christian G. Hartinger[2†] and James D. Crowley[1†]*

[1]Department of Chemistry, University of Otago, Dunedin, New Zealand, [2]School of Chemical Sciences, University of Auckland, Auckland, New Zealand, [3]Auckland Cancer Society Research Centre, University of Auckland, Auckland, New Zealand

OPEN ACCESS

Edited by:
Tony D. James,
University of Bath, United Kingdom

Reviewed by:
Guzman Gil-Ramirez,
University of Lincoln, United Kingdom
Apurba Lal Koner,
Indian Institute of Science Education and Research, Bhopal, India

***Correspondence:**
James D. Crowley
jcrowley@chemistry.otago.ac.nz

†ORCID:
James D. Crowley
orcid.org/0000-0002-3364-2267
Christian G. Hartinger
orcid.org/0000-0001-9806-0893
L. James Wright
orcid.org/0000-0003-1995-0236
Stephen M. F. Jamieson
orcid.org/0000-0002-5485-9211
Roan A. S. Vasdev
orcid.org/0000-0002-0777-3677
Mie Riisom
orcid.org/0000-0002-5669-6284
Lynn S. Lisboa
orcid.org/0000-0002-5909-9389

Specialty section:
This article was submitted to Supramolecular Chemistry, a section of the journal Frontiers in Chemistry

Received: 20 April 2021
Accepted: 16 June 2021
Published: 07 July 2021

Citation:
Lisboa LS, Riisom M, Vasdev RAS, Jamieson SMF, Wright LJ, Hartinger CG and Crowley JD (2021) Cavity-Containing $[Fe_2L_3]^{4+}$ Helicates: An Examination of Host-Guest Chemistry and Cytotoxicity. Front. Chem. 9:697684. doi: 10.3389/fchem.2021.697684

Two new di(2,2′-bipyridine) ligands, 2,6-bis([2,2′-bipyridin]-5-ylethynyl)pyridine (**L1**) and bis(4-([2,2′-bipyridin]-5-ylethynyl)phenyl)methane (**L2**) were synthesized and used to generate two metallosupramolecular $[Fe_2(\mathbf{L})_3](BF_4)_4$ cylinders. The ligands and cylinders were characterized using elemental analysis, electrospray ionization mass spectrometry, UV-vis, ^{1}H-, ^{13}C and DOSY nuclear magnetic resonance (NMR) spectroscopies. The molecular structures of the $[Fe_2(\mathbf{L})_3](BF_4)_4$ cylinders were confirmed using X-ray crystallography. Both the $[Fe_2(\mathbf{L1})_3](BF_4)_4$ and $[Fe_2(\mathbf{L2})_3](BF_4)_4$ complexes crystallized as racemic (*rac*) mixtures of the ΔΔ (P) and ΛΛ (M) helicates. However, ^{1}H NMR spectra showed that in solution the larger $[Fe_2(\mathbf{L2})_3](BF_4)_4$ was a mixture of the *rac*-ΔΔ/ΛΛ and *meso*-ΔΛ isomers. The host-guest chemistry of the helicates, which both feature a central cavity, was examined with several small drug molecules. However, none of the potential guests were found to bind within the helicates. *In vitro* cytotoxicity assays demonstrated that both helicates were active against four cancer cell lines. The smaller $[Fe_2(\mathbf{L1})_3](BF_4)_4$ system displayed low μM activity against the HCT116 ($IC_{50} = 7.1 \pm 0.5$ μM) and NCI-H460 ($IC_{50} = 4.9 \pm 0.4$ μM) cancer cells. While the antiproliferative effects against all the cell lines examined were less than the well-known anticancer drug cisplatin, their modes of action would be expected to be very different.

Keywords: iron(II), helicate, cytotoxicity, host-guest chemistry, metallosupramolecular architectures

INTRODUCTION

Metallosupramolecular architectures (MSAs) are beginning to display a wide range of applications (Yoshizawa et al., 2009; Cook and Stang, 2015; Hong et al., 2018; Saha et al., 2018; Bardhan and Chand, 2019; Gao et al., 2019; Rizzuto et al., 2019; Percastegui et al., 2020) Largely inspired by the success of small molecule metallo-drugs (Hartinger and Dyson, 2009; Mjos and Orvig, 2014; Anthony et al., 2020; Boros et al., 2020; Frei, 2020; Frei et al., 2020; Steel et al., 2021b) there is a growing interest in biological applications of MSAs (Cook et al., 2013; Therrien, 2015; Pöthig and Casini, 2019; Sepehrpour et al., 2019; Samanta and Isaacs, 2020). Systems have been studied for their anti-cancer and anti-microbial activity and their potential as drug delivery agents. Helicates (Piguet et al., 1997; Albrecht, 2001; Hannon and Childs, 2004; Howson and Scott, 2011; Boiocchi and Fabbrizzi, 2014; Paneerselvam et al., 2018; Albrecht et al., 2019; Albrecht, 2020; Tran and Yoo, 2020) are one of the earlier known and well-studied sub-classes of MSAs. Lehn and co-workers reported the first helicates; a double-stranded dinuclear and larger trinuclear system were generated from poly(2,2′-bipyridine)

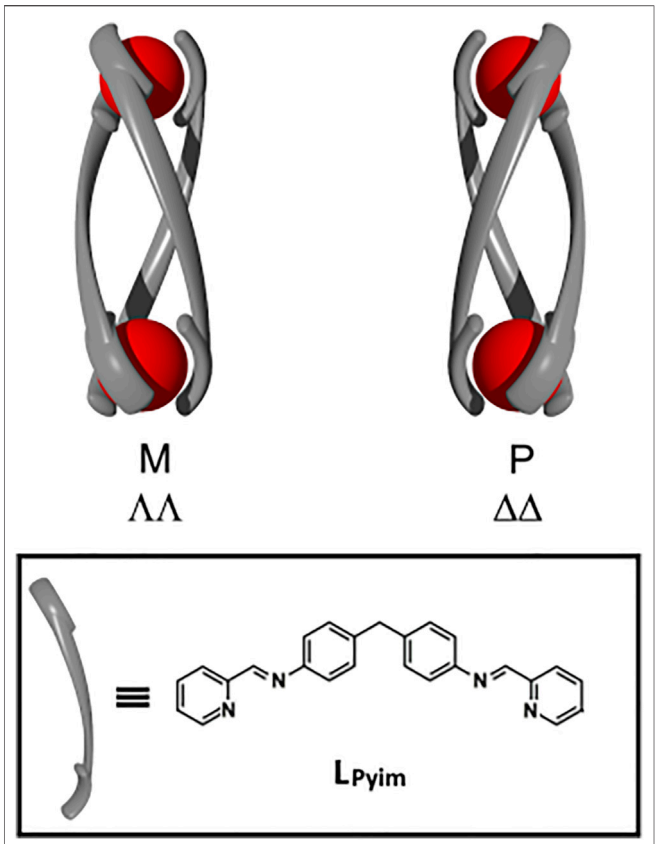

FIGURE 1 | Cartoon representations of the minus (M, ΛΛ), plus (P, ΔΔ) helicate isomers of a generic triple-stranded helicate and the chemical structure of the (1E,1′E)-N,N′-[methylenebis(4,1-phenylene)]bis[1-(pyridin-2-yl)methanimine] ligand ($\mathbf{L_{Pyim}}$) developed by Hannon and co-workers (Hannon et al., 1997).

ligands and Cu(I) ions (Lehn et al., 1987) Subsequently, single, triple, and quadruple stranded helicates have all been synthesized and these systems are chiral featuring P (plus, right-handed) and M (minus, left-handed) helices (**Figure 1**). Because of the structural relationship to helical natural materials such as DNA, α-helices and zinc fingers of proteins there has been considerable interest in the biological properties, of helicates. Early work by Lehn and co-workers showed that double-stranded helicates assembled from poly(2,2′-bipyridine) ligands and Cu(I) ions could bind to double stranded DNA (Schoentjes and Lehn, 1995). Others have examined DNA binding and nuclease activity (Childs et al., 2006), and the cytotoxicity of related double-stranded complexes (Holtze et al., 2006; Allison et al., 2018). In addition, quadruple-stranded helicates have been shown to be cytotoxic (Mcneill et al., 2015; Ahmedova et al., 2016a; Ahmedova et al., 2016b; Schmidt et al., 2016; Vasdev et al., 2018; Ahmedova et al., 2020) and in some cases the modes of action of the complexes have been studied (Mcneill et al., 2020).

While there are only a few reports on the biological properties of double- and quadruple-stranded helicates, the related triple-stranded analogues have been extensively examined. These triply-stranded supramolecular structures are assembled from an octahedral metal ion and di(bidentate) linker ligands $[M_2L_3]$; this combination of building blocks can generate three isomeric complexes the chiral M (ΛΛ) and P (ΔΔ), and the *meso* (ΛΔ). Pioneering work by Hannon and co-workers described the synthesis of the first $[Fe_2(\mathbf{L_{Pyim}})_3]^{4+}$ helicates (where $\mathbf{L_{Pyim}}$ = (1E,1′E)-N,N′-[methylenebis(4,1-phenylene)]bis[1-(pyridin-2-yl) methanimine, **Figure 1**] obtained from pyridylimine binding motifs, octahedral Fe(II) ions and a diphenylmethylene spacer unit (Hannon et al., 1997). The mechanical coupling exerted by the spacer unit meant that a racemic (*rac*) mixture of the M (ΛΛ) and P (ΔΔ) $[M_2(\mathbf{L_{Pyim}})_3]^{4+}$ helicates (where M = Fe(II) or Ni(II)) was formed and the authors went on to show that the M and P helicates could be resolved by chiral chromatography (Hannon et al., 2001a). The interaction of the M− and P−$[Fe_2(\mathbf{L_{Pyim}})_3]^{4+}$ helicates with DNA has been extensively examined. The complexes have been shown to bind in the major grove of duplex DNA (Moldrheim et al., 2002), and at the center of three-way DNA (Oleksi et al., 2006; Cerasino et al., 2007; Malina et al., 2007; Cardo et al., 2011) and RNA (Phongtongpasuk et al., 2013) junctions (3WJ). More recently, the $[Fe_2(\mathbf{L_{Pyim}})_3]^{4+}$ helicates were also shown to bind to DNA and RNA bulges (Malina et al., 2014; Malina et al., 2016). Similar observations have been made with the related $[M_2(\mathbf{L_{Pyim}})_3]^{4+}$ helicates [where M = Ru(II) or Ni(II)] (Cardo et al., 2018) and the Ni(II) and Fe(II) helicates have been demonstrated to interact with G-quadruplexes (Zhao et al., 2013; Zhao et al., 2016) and the β-amyloid polypeptide (Aβ) (Yu et al., 2012; Li et al., 2015). Furthermore, the interaction of the iron(II) helicate with duplex DNA induces intramolecular DNA coiling (Hannon et al., 2001b; Malina et al., 2008) and it has been shown to display anti-cancer (Hotze et al., 2008), anti-bacterial (Richards et al., 2009) and anti-fungal (Vellas et al., 2013) properties, but is not mutagenic or genotoxic. This remarkable range of biological properties has been obtained without investigating changes to either the metal binding (pyridylimine) or spacer units of the helicates, suggesting that the system could potentially be improved by further tuning of the molecular scaffold.

Building on the aforenoted work, Scott and co-workers developed an excellent method for the self-assembly of optically pure single diastereomer *fac*-$[Fe(\mathbf{L_{pyimR}})_3]^{2+}$ (where $\mathbf{L_{pyimR}}$ = functionalized pyridylimine ligand) complexes (Howson et al., 2009). The same group then exploited this method to synthesize enantiomerically pure Fe(II) and Zn(II) $[M_2(\mathbf{L_{pyimR}})_3]^{4+}$ helicates and flexicates which feature different spacer systems. Like the parent Hannon helicate, it has been shown that these new pyridylimine-based complexes have shown a diverse range of biological properties and some flexicates have impressive, tunable anti-microbial (Howson et al., 2012; Simpson et al., 2019) and anti-cancer (Brabec et al., 2013; Faulkner et al., 2014; Kaner and Scott, 2015; Kaner et al., 2016; Song et al., 2019; Song et al., 2020) properties. The interactions of this more diverse family of helicates with DNA/RNA (Song et al., 2021) and proteins (Li et al., 2014) have also been examined and the systems show structure-dependent binding to duplex DNA (Brabec et al., 2013; Malina et al., 2015b), G-quadruplexes (Zhao et al., 2017; Zhao et al., 2018), 3WJ and 4WJ (Brabec et al., 2013), and bulges (Malina et al., 2015a; Hrabina et al., 2020).

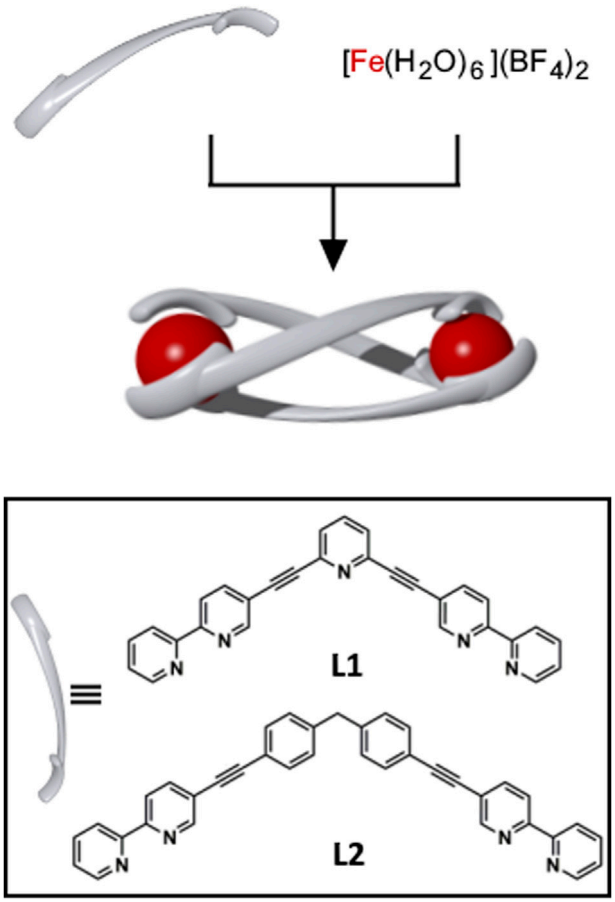

SCHEME 1 | Cartoon representation of the synthesis of the triply-stranded metallo-cylinders $[Fe_2(\mathbf{L1})_3](BF_4)_4$ and $[Fe_2(\mathbf{L2})_3](BF_4)_4$. The complexes were synthesized by combining **L1** or **L2** (3 equiv.) with $[Fe(H_2O)_6](BF_4)_2$ (2 equiv.), CH_3CN, 65°C, 16 h. Bottom: inset showing the structures of **L1** and **L2**.

The success of the pyridylimine $[M_2L_3]^{4+}$ helicates discussed above has inspired others to examine the biological properties of related $[M_2L_3]^{4+}$ triply-stranded helicates. For example, we have explored the use of small families of di(2-pyridyl-1,2,3-triazole) ligands ($\mathbf{L_{dipytri}}$) to generate Fe(II), Ru(II), and Co(III) helicates (Vellas et al., 2013; Kumar et al., 2015; Vasdev et al., 2016). The biological properties of the Fe(II) and Ru(II) systems were poor but the more robust Co(III) helicates were shown to bind to and condense DNA and in addition displayed good anticancer activity (Crlikova et al., 2020). Di(2,2′-bipyridine) ligands (Glasson et al., 2008; Glasson et al., 2011a; Glasson et al., 2011b) have also been used to generate $[M_2L_3]^{4+}$ triple-stranded helicates and recently Vázquez and co-workers have examined the DNA binding and cytotoxicity of some peptide linked $[M_2L_3]^{4+}$ helicates [where M = Fe(II) or Co(III)] (Gamba et al., 2014; Gómez-González et al., 2018; Gomez-Gonzalez et al., 2021).

Given the well demonstrated ability of $[M_2L_3]^{4+}$ helicates to bind to DNA/RNA and proteins and their potential to be used as targeted therapeutics, we herein report the synthesis of two new di(2,2′-bipyridine) ligands, 2,6-bis([2,2′-bipyridin]-5-ylethynyl)-pyridine (**L1**) and bis(4-([2,2′-bipyridin]-5-ylethynyl)phenyl)-methane (**L2**) and their use in the assembly of two new triple-stranded $[Fe_2L_3]X_4$ helicates ($X = BF_4^-$, OTf^- or Cl^-). Moreover, due the presence of a central cavity in both the $[Fe_2(\mathbf{L1})_3](BF_4)_4$ and $[Fe_2(\mathbf{L2})_3](BF_4)_4$ helicates, we also report our examination of the host-guest properties of these systems with some small molecule drugs and our studies of the anti-cancer activity of the complexes.

RESULTS AND DISCUSSION

The new di(2,2′-bipyridine) ligands, 2,6-bis([2,2′-bipyridin]-5-ylethynyl)-pyridine (**L1**) and bis(4-([2,2′-bipyridin]-5-ylethynyl)-phenyl)methane (**L2**) were synthesized from 5-ethynyl-2,2′-bipyridine (Grosshenny et al., 1997) and either 2,5-dibromopyridine or bis(4-iodophenyl)methane (Austin et al., 1981) using standard Sonogashira cross-coupling conditions (**Supplementary Material**) and were obtained in modest yields (**L1** = 51% and **L2** = 61%). The ligands were characterized using ^{1}H nuclear magnetic resonance (NMR), ^{13}C{^{1}H} NMR, electrospray ionization mass spectrometry (ESIMS) and elemental analysis (**Supplementary Figures S1–S4**).

The $[Fe_2(\mathbf{L})_3](BF_4)_4$ helicates were synthesised by combining either **L1** or **L2** (3 equiv.) with $[Fe(H_2O)_6](BF_4)_2$ (2 equiv.) in acetonitrile at 65°C (**Scheme 1** and **Supplementary Material**). The ligands were initially insoluble in the reaction mixture, however, after 5 min the ligands dissolved and deep red solutions (λ_{max} = 545 or 547 nm, respectively) were obtained. The resulting Fe(II) complexes were purified by recrystallization (vapour diffusion of diethyl ether into a nitromethane solution) and deep red crystals were isolated in good yields (89% for $[Fe_2(\mathbf{L1})_3](BF_4)_4$ and 77% for $[Fe_2(\mathbf{L2})_3](BF_4)_4$). The complexes were characterised by ^{1}H NMR, ^{13}C{^{1}H} NMR, ^{1}H DOSY NMR, UV-vis spectroscopy, ESIMS, and X-ray crystallography (**Supplementary Material**).

The ESIMS data obtained for the two complexes displayed a major peak consistent with the corresponding $[Fe_2\mathbf{L}_3]^{4+}$ cation (m/z = 354.5886 $[Fe_2(\mathbf{L1})_3]^{4+}$ and m/z = 421.3972 m/z $[Fe_2(\mathbf{L2})_3]^{4+}$, respectively) suggestive of the formation of the expected triple-stranded helicates (Figure, **Supplementary Figures S7, S10**). The ^{1}H DOSY NMR spectra (500 MHz, CD_3CN, 298 K) of $[Fe_2(\mathbf{L1})_3](BF_4)_4$ and $[Fe_2(\mathbf{L2})_3](BF_4)_4$ were collected, and all the proton resonances displayed the same diffusion coefficients ($6.51 \pm 0.03 \times 10^{-10}$ m^2 s^{-1} and $5.40 \pm 0.10 \times 10^{-10}$ m^2 s^{-1}, respectively) suggesting that a single metallosupramolecular architecture or mixtures of isomeric architectures were obtained (**Supplementary Figures S11, S12**). In addition, the observed diffusion coefficients were similar to those found for some related $[Fe_2(\mathbf{L_{dipytri}})_3]^{4+}$ metallo-cylinders (Vellas et al., 2013) providing further support for the formation of the desired triple-stranded helicates.

The ^{1}H NMR spectra (500 MHz, CD_3CN, 298 K) for the complexes of **L1** and **L2** were significantly distinct (**Figure 2**; **Supplementary Material**). The spectrum of $[Fe_2(\mathbf{L1})_3](BF_4)_4$ displayed nine sharp resonances in the

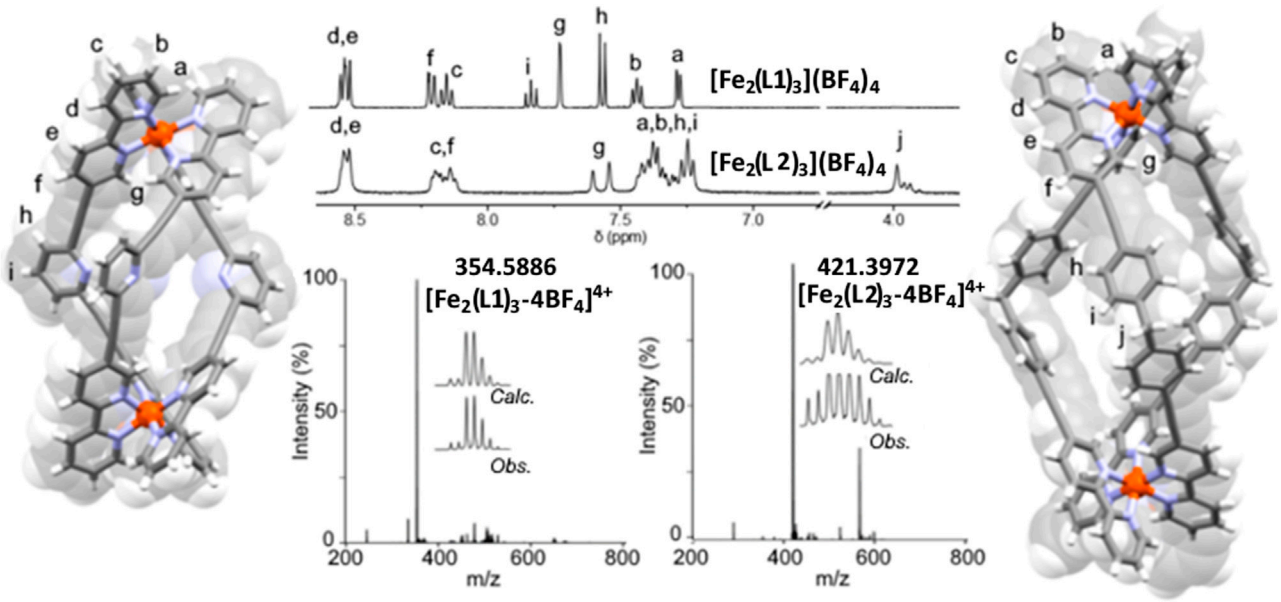

FIGURE 2 | X-ray structures showing the overlaid stick and spacefill representations of $[Fe_2(\mathbf{L1})_3](BF_4)_4$ and $[Fe_2(\mathbf{L2})_3](BF_4)_4$ with related partial ^{1}H NMR spectra (500 MHz, CD_3CN, 298 K) and associated ESI-mass spectra. Fe-Fe distances; $[Fe_2(\mathbf{L1})_3](BF_4)_4$ = 14.2 Å, $[Fe_2(\mathbf{L2})_3](BF_4)_4$ = 19.1 Å. Solvent molecules and counter anions were omitted for clarity.

aromatic region (δ = 8.5–7.0 ppm) consistent with the formation of a racemic (*rac*) mixture of the helical $[Fe_2(\mathbf{L1})_3]^{4+}$ isomers, P = ΔΔ and M = ΛΛ. Conversely, the ^{1}H NMR spectrum of $[Fe_2(\mathbf{L2})_3](BF_4)_4$ was more complex with several broad overlapping resonances in the aromatic region. However, the methylene protons of the spacer backbone (H_j, δ = 4.0–3.8 ppm) were clearly split into two distinct resonances; a singlet and an AB quartet. This suggests that in solution $[Fe_2(\mathbf{L2})_3](BF_4)_4$ forms a mixture of helicate *rac*-ΔΔ/ΛΛ and mesocate *meso*-ΔΛ isomers. Others (Goetz and Kruger, 2006; Vellas et al., 2013) have observed this behavior in solution with related $[Fe_2\mathbf{L}_3]^{4+}$ systems that feature the diphenylmethylene spacer unit. This is in contrast to observations with the pyridyl imine helicate, $[Fe_2(\mathbf{L_{Pyim}})_3]^{4+}$ of Hannon and co-workers (Hannon et al., 1997). Those helicates have the same spacer unit and are found to exclusively form *rac*-helicates in solution and the solid state. The difference appears to be related to the larger size of $[Fe_2(\mathbf{L2})_3]^{4+}$ compared to $[Fe_2(\mathbf{L_{Pyim}})_3]^{4+}$. In $[Fe_2(\mathbf{L_{Pyim}})_3]^{4+}$, the aryl rings of the spacer unit are in close contact and interdigitate, mechanically locking the complex into the helical arrangement. The larger size of **L2** lessens this steric interdigitation of the spacer aryl groups, therefore making the mesocate arrangement more energetically accessible.

The molecular structures of $[Fe_2(\mathbf{L1})_3](BF_4)_4$ and $[Fe_2(\mathbf{L2})_3](BF_4)_4$ were confirmed by X-ray crystallography with crystals grown by slow vapour diffusion of diethyl ether into nitromethane solutions (**Figure 2**, **Supplementary Figures S27, S28**). The $[Fe_2(\mathbf{L1})_3](BF_4)_4$ structure was solved in the $P\bar{1}$ space group and the asymmetric unit contains two iron ions, three **L1** ligands, four tetrafluoroborate anions and two nitromethane solvent molecules. Each iron(II) ion is coordinated to three bipy units generating a triple-stranded helicate architecture. The Fe-Fe distance of 14.2 Å confirmed that the system is elongated in comparison to the parent Hannon helicate. The compound crystallized as a racemic mixture in the solid state with both the ΔΔ (P) and ΛΛ (M) isomers (see the structural representations in **Figure 2**) present in the crystal.

The $[Fe_2(\mathbf{L2})_3](BF_4)_4$ structure was solved in the $P2_1/n$ space group and the asymmetric unit was occupied by one $[Fe_2(\mathbf{L2})_3]^{4+}$ unit, two tetrafluoroborate anions and seven co-crystallized nitromethane molecules. $[Fe_2(\mathbf{L2})_3](BF_4)_4$ was shown to crystallize as a *rac* mixture of the ΔΔ (P) and ΛΛ (M) helicates. The *meso*-form detected in solution by ^{1}H NMR spectroscopy was not observed in the solid state, presumably due to crystal packing effects (Vellas et al., 2013). The combination of the two 5-ethynyl-2,2′-bipyridine units and the diphenylmethylene spacer in **L2** led to a large Fe-Fe distance (19.1 Å) in $[Fe_2(\mathbf{L2})_3](BF_4)_4$. The metallo-architectures of both $[Fe_2(\mathbf{L1})_3](BF_4)_4$ and $[Fe_2(\mathbf{L2})_3](BF_4)_4$ displayed a clear central cavity and notable π surfaces available for potential host-guest interactions (**Figure 2**; **Supplementary Material**).

MSA cage systems have been used extensively as hosts for small molecule guests (Yoshizawa et al., 2009; Cook and Stang, 2015; Hong et al., 2018; Saha et al., 2018; Bardhan and Chand, 2019; Gao et al., 2019; Rizzuto et al., 2019; Percastegui et al., 2020). In contrast, the use of $[Fe_2\mathbf{L}_3]^{4+}$ helicate architectures as hosts is far less common, presumably because the vast majority of reported MSAs do not contain a central cavity. Recently, there have been a few reports of guest binding [anions (Goetz and Kruger, 2006; Cui et al., 2012), sugars (Yang et al., 2021) and small aromatic molecules (Fazio et al., 2018; Jiang et al., 2019)] within $[Fe_2\mathbf{L}_3]^{4+}$ helicates that feature small cavities. As the cavities of

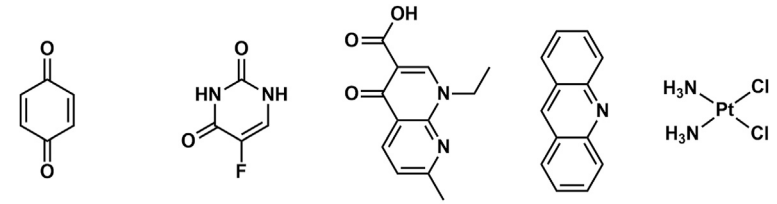

FIGURE 3 | Guest molecules examined in the host-guest study with the helicates.

the $[Fe_2(\mathbf{L1})_3]^{4+}$ and $[Fe_2(\mathbf{L2})_3]^{4+}$ helicates are both lined by functional groups that could interact with guests through either hydrogen bonding or π-interactions, we sought out some small drug molecules that could potentially interact with the helicates using those non-covalent interactions. Therefore, the guest molecules 1,4-benzoquinone, nalidixic acid, acridine (as an analogue of proflavine), cisplatin and 5-fluorouracil were selected as they are either known or analogues of known anticancer and antibacterial drugs (**Figure 3**; **Supplementary Material**). The host-guest (HG) interactions were examined using ^{1}H NMR spectroscopy and ESIMS. One of the potential guest molecules (2 equiv.) was combined with one of the helicates (1 equiv.) in CD_3CN at 298 K and the ^{1}H NMR spectrum acquired (**Supplementary Material**). ^{1}H NMR spectra of the host-guest mixtures were then compared to the ^{1}H NMR spectra of the corresponding "free" host and guest compounds (**Supplementary Figures S23, S24**). Disappointingly, no complexation induced shifts were observed for either the host or the guest resonances suggesting that none of the guests bound within the cavities of the helicates. Molecular models (SPARTAN16, MMFF, **Supplementary Figures S25, S26**) showed that there are no obvious steric interactions that would prevent host-guest formation for the majority of the examined HG pairs. Thus, the lack of guest binding in the cases examined appears to be due to the absence of the correct combination of complementary non-covalent and solvaphobic interactions. Additionally, the BF_4^- counter-anions may be competing for the cavity as has been observed in other cationic MSA systems (August et al., 2016).

Related $[Fe_2\mathbf{L}_3]^{4+}$ helicates have shown excellent anticancer activity (Song et al., 2021). Therefore, we examined the cytotoxicity of $[Fe_2(\mathbf{L1})_3]^{4+}$ and $[Fe_2(\mathbf{L2})_3]^{4+}$ against a panel of cancer cell lines. As the $[Fe_2(\mathbf{L1})_3](BF_4)_4$ and $[Fe_2(\mathbf{L2})_3](BF_4)_4$ complexes were only soluble in polar organic solvents (DMSO, CH_3CN, CH_3NO_2, and acetone) we attempted to render the helicates water soluble by exchanging the BF_4^- counter anions with Cl^- or OTf^- (**Supplementary Material**). While we were able to generate the new $[Fe_2(\mathbf{L1})_3](X)_4$ and $[Fe_2(\mathbf{L2})_3](X)_4$ (where X = Cl^-, OTf^-) salts, they proved even less soluble than the original BF_4^- salts. The OTf^- salts were soluble in CH_3CN and DMSO, however, the Cl^- salts were only soluble in DMSO with none of the systems showing any appreciable water solubility (**Supplementary Figures S18–S21**). Due to these complications, we carried out the cytotoxicity experiments with $[Fe_2(\mathbf{L1})_3](BF_4)_4$ and $[Fe_2(\mathbf{L2})_3](BF_4)_4$ dissolved in DMSO and these solutions were then diluted with biological media to the required concentrations.

Due to the modest water solubility of many drug candidates, it is common to use DMSO to solubilize compounds for cytotoxicity experiments. However, it is also well known that DMSO can displace coordinated ligands and decompose metal complexes (Patra et al., 2013; Vellas et al., 2013; Hall et al., 2014; Huang et al., 2017). Therefore, the stability of the helicates in neat DMSO and a 1:19 v/v DMSO:water mixture was examined before carrying out the cytotoxicity experiments. The stabilities of $[Fe_2(\mathbf{L1})_3](BF_4)_4$ and $[Fe_2(\mathbf{L2})_3](BF_4)_4$ in these solvents were monitored using ^{1}H NMR and UV-vis spectroscopy (**Supplementary Figures S14, S15**). Both complexes completely decomposed (*ca.* 3 h for $[Fe_2(\mathbf{L1})_3](BF_4)_4$ and 24 h for $[Fe_2(\mathbf{L2})_3](BF_4)_4$) in neat DMSO liberating the free ligands and presumably forming $[Fe(DMSO)_6]^{2+}$ (White et al., 2007).

The helicates were more long lived in 1:19 v/v DMSO:water mixtures. A 72 h UV-visible stability study of $[Fe_2(\mathbf{L1})_3](BF_4)_4$ and $[Fe_2(\mathbf{L2})_3](BF_4)_4$ in 1:19 v/v DMSO:water was conducted to replicate the timeframe of the biological testing (**Supplementary Figures S16, S17**). Interestingly, the smaller $[Fe_2(\mathbf{L1})_3](BF_4)_4$ showed no signs of decomposition (within the uncertainty of the measurement) whereas the larger $[Fe_2(\mathbf{L2})_3](BF_4)_4$ did slowly degrade, approximately 43% of the $[Fe_2(\mathbf{L2})_3](BF_4)_4$ was still present in solution after 72 h. Given the moderate to good stability of the helicates under conditions similar to those required for the cytotoxicity assay we proceeded to measure the *in vitro* antiproliferative activity of the compounds.

The ligands (**L1** and **L2**) and helicates $[Fe_2(\mathbf{L1})_3](BF_4)_4$ and $[Fe_2(\mathbf{L2})_3](BF_4)_4$ were subjected to the sulforhodamine B cytotoxicity assay in the human cancer cell lines HCT116 (colorectal carcinoma), NCI-H460 (non-small cell lung carcinoma), SiHa (cervical carcinoma), and SW480 (colon adenocarcinoma) (**Table 1**). **L1** and **L2** proved to be insoluble under the conditions of the experiments, and therefore their antiproliferative activity could not be determined (**Table 1**). The helicates $[Fe_2(\mathbf{L1})_3](BF_4)_4$ and $[Fe_2(\mathbf{L2})_3](BF_4)_4$ were both active *in vitro* against all the cancer cells tested. The smaller $[Fe_2(\mathbf{L1})_3](BF_4)_4$ was more active than $[Fe_2(\mathbf{L2})_3](BF_4)_4$ against all the cell lines examined, and displayed low μM activity against HCT116 (IC_{50} = 7.1 ± 0.5 μM) and NCI-H460 (IC_{50} = 4.9 ± 0.4 μM) cancer cells. Unfortunately, direct comparisons with the previously studied isostructural helicates $[Fe_2(\mathbf{L_{Pyim}})_3]^{4+}$ and $[Fe(\mathbf{L_{pyimR}})_3]^{2+}$ are difficult as their cytotoxicity was

TABLE 1 | IC_{50} values (μM) for **L1** and **L2** and the iron(II) cylinders against HCT116 (human colorectal carcinoma), NCI-H460 (human non-small cell lung carcinoma), SiHa (human cervical carcinoma), and SW480 (human colon adenocarcinoma) cancer cells as compared to cisplatin, expressed as mean ± standard error (n = 3, incubation period 72 h).

Compound	IC_{50}/μM			
	HCT116	NCI-H460	SiHa	SW480
L1	n.d.	n.d.	n.d.	n.d.
L2	n.d.	n.d.	n.d.	n.d.
rac-$[Fe_2(\mathbf{L1})_3](BF_4)_4$	7.1 ± 0.5	4.9 ± 0.4	39 ± 2	24 ± 4
rac/meso-$[Fe_2(\mathbf{L2})_3](BF_4)_4$	19 ± 1	46 ± 15	55 ± 15	13 ± 4
$\mathbf{L_{pyim}}$ Steel et al. (2021a)	21 ± 6	31 ± 4	42 ± 3	46 ± 5
rac-$[Fe_2(\mathbf{L_{Pyim}})_3](BF_4)_4$	9 ± 2	10 ± 3	26 ± 4	28 ± 7
$[(Rh(Cp^*)Cl)_2(\mathbf{L_{pyim}})]$ Steel et al. (2021a)	78 ± 21	>100	45 ± 4	73 ± 5
$[Fe(H_2O)_6](BF_4)_2$	>200	184 ± 11	>500	>300
Cisplatin Tremlett et al. (2019)	2.5 ± 0.3	0.80 ± 0.03	3.0 ± 0.6	8.1 ± 2.9

n.d., not determined due to the poor solubility of the compound.

determined with different cell lines. However, the low μM activity observed for $[Fe_2(\mathbf{L1})_3](BF_4)_4$ suggests that it could be more active than the $[Fe_2(\mathbf{L_{Pyim}})_3]^{4+}$ helicates (IC_{50} values ranged from 19–52 μM, despite having been determined in different cell lines) (Hotze et al., 2008). The observed activity of $[Fe_2(\mathbf{L1})_3](BF_4)_4$ is similar in magnitude to that found by Scott et al. for their family of $[Fe_2(\mathbf{L_{pyimR}})_3]^{2+}$ helicates (Song et al., 2021). However, the $[Fe_2(\mathbf{L_{pyimR}})_3]^{2+}$ systems are more effective overall with some of that family displaying nanomolar activities (Kaner et al., 2016; Song et al., 2020). We have recently studied the cytotoxicity of a small family of dimetallic organometallic (Ru, Rh, Os, and Ir) complexes (Steel et al., 2021a) of $\mathbf{L_{Pyim}}$ against the same series of cell lines enabling a more direct comparison (**Table 1**). Both helicates displayed better activity than the dimetallic complexes and $\mathbf{L_{Pyim}}$ across the range of cell lines. Presumably the higher activity of the helicates is associated with the different molecular shape and higher charge. While the *in vitro* activity of the $[Fe_2(\mathbf{L1})_3](BF_4)_4$ helicate is promising we note that the widely used anti-cancer drug cisplatin is more active in all the cell lines examined (**Table 1**). However, the mode of action of this covalent DNA binder, in comparison to supramolecular structures that are more likely to form non-covalent interactions with biological targets, will be very different, making any direct comparison difficult.

CONCLUSION

Two new di(2,2′-bipyridine) ligands, 2,6-bis([2,2′-bipyridin]-5-ylethynyl)-pyridine (**L1**) and bis(4-([2,2′-bipyridin]-5-ylethynyl)-phenyl)methane (**L2**) were synthesized and exploited to generate two triple-stranded metallo-cylinders, $[Fe_2(\mathbf{L1})_3](BF_4)_4$ and $[Fe_2(\mathbf{L2})_3](BF_4)_4$. The ligands and cylinders were characterized by elemental analysis, ESIMS and UV-vis, ^{1}H–, ^{13}C–, and DOSY-NMR spectroscopies. The molecular structures of the $[Fe_2\mathbf{L}_3](BF_4)_4$ cylinders were confirmed using X-ray crystallography. Both $[Fe_2(\mathbf{L1})_3](BF_4)_4$ and $[Fe_2(\mathbf{L2})_3](BF_4)_4$ crystallized as racemic (*rac*) mixtures of the ΔΔ (P) and ΛΛ (M) helicates. NMR spectroscopy and ESIMS confirmed the presence of the $[Fe_2\mathbf{L}_3]^{4+}$ supramolecular architectures in solution. However, ^{1}H NMR spectra showed that in solution the larger $[Fe_2(\mathbf{L2})_3](BF_4)_4$ was present as a mixture of the *rac*-ΔΔ/ΛΛ and *meso*-ΔΛ isomers. The host-guest chemistry of the helicates, which both feature an accessible central cavity, was examined with several small drug molecules, including cisplatin and 5-fluorouracil. However, none of the potential guests were found to bind within the helicates, despite molecular modelling confirming that there were no obvious steric impediments to the interaction. Cytotoxicity assays demonstrated that both helicates were active against the four cell lines examined. The smaller *rac*-$[Fe_2(\mathbf{L1})_3](BF_4)_4$ helicate was more cytotoxic than the larger *rac/meso*-$[Fe_2(\mathbf{L2})_3](BF_4)_4$ analogue and displayed promising low μM antiproliferative activity against HCT116 (IC_{50} = 7.1 ± 0.5 μM) and NCI-H460 (IC_{50} = 4.9 ± 0.4 μM) human cancer cells. Although both helicates were less active than the widely used anti-cancer drug cisplatin, these results suggest that helicates constructed from di(2,2′-bipyridine) ligands have potential as anti-cancer agents in their own right. The combination of a cytotoxic supramolecular structure with encapsulated drugs may result in synergistic activity. However, the poor aqueous solubility and modest stability in biological media of the current $[Fe_2(\mathbf{L1})_3](BF_4)_4$ helicates means that the properties of these compounds will need to be fine-tuned to overcome these shortfalls. This could potentially be achieved by using more kinetically inert metal ions such as Ru(II) (Glasson et al., 2008; Kumar et al., 2015) or Co(III) (Symmers et al., 2015; Burke et al., 2018; Crlikova et al., 2020) to assemble the helicates.

DATA AVAILABILITY STATEMENT

The original contributions presented in the study are included in the article/**Supplementary Material**, further inquiries can be directed to the corresponding author.

AUTHOR CONTRIBUTIONS

LL, JC, CH, and LW conceived the idea. JC, CH, and LW obtained the funding. LL and JC analyzed the data and wrote the manuscript. LL conducted the synthesis. RV collected and refined the X-ray data. MR conducted cytotoxicity studies and

analyzed the data. CH and SJ oversaw the cytotoxicity studies and analyzed the data. All authors provided feedback on the manuscript drafts and approved the submission.

FUNDING

We thank the Marsden Fund Council (Grant UOA1726), managed by the Royal Society Te Apārangi for funding this work. All the authors thank the University of Otago and the University of Auckland for providing additional support. JC thanks the MacDiarmid Institute for funding. LL and RV acknowledge the University of Otago for funding doctoral stipends. MR thanks Knud Højgaards Fond, Dagmar Marshalls Fond, Christian og Ottilia Brorsons Rejselegat for yngre videnskabsmænd—og kvinder, Carl og Ellen Hertz'legat til Dansk Læge—og Naturvidenskab, Viet-Jacobsen Fonden, Eva and Henry Frænkels Mindefond and Direktør Jacob Madsens og Hustru Olga Madsens Fond for financial support.

ACKNOWLEDGMENTS

All the authors thank Charlotte Dobson, Pauline Lane and Oceanbridge for their kind donations which supported this work. We are grateful to Tasha Steel for the support with the cytotoxicity assays.

SUPPLEMENTARY MATERIAL

The Supplementary Material for this article can be found online at: https://www.frontiersin.org/articles/10.3389/fchem.2021.697684/full#supplementary-material

REFERENCES

Ahmedova, A., Mihaylova, R., Momekova, D., Shestakova, P., Stoykova, S., Zaharieva, J., et al. (2016a). M_2L_4 Coordination Capsules With Tunable Anticancer Activity Upon Guest Encapsulation. *Dalton Trans.* 45, 13214–13221. doi:10.1039/c6dt01801g

Ahmedova, A., Mihaylova, R., Stoykova, S., Mihaylova, V., Paunova-Krasteva, T., Mihaylov, L., et al. (2020). Enhanced Cellular Uptake of Platinum by a Tetracationic Pt(II) Nanocapsule and its Implications to Cancer Treatment. *Eur. J. Pharm. Sci.* 155, 105545. doi:10.1016/j.ejps.2020.105545

Ahmedova, A., Momekova, D., Yamashina, M., Shestakova, P., Momekov, G., Akita, M., et al. (2016b). Anticancer Potencies of PtII - and PdII -Linked M_2L_4 Coordination Capsules With Improved Selectivity. *Chem. Asian J.* 11, 474–477. doi:10.1002/asia.201501238

Albrecht, M. (2001). "Let's Twist Again" Double-Stranded, Triple-Stranded, and Circular Helicates. *Chem. Rev.* 101, 3457–3498. doi:10.1021/cr0103672

Albrecht, M. (2020). Catecholate-Based Helicates. *Eur. J. Inorg. Chem.* 2020, 2227–2237. doi:10.1002/ejic.202000255

Albrecht, M., Chen, X., and Van Craen, D. (2019). From Hierarchical Helicates to Functional Supramolecular Devices. *Chem. Eur. J.* 25, 4265–4273. doi:10.1002/chem.201804963

Allison, S. J., Cooke, D., Davidson, F. S., Elliott, P. I. P., Faulkner, R. A., Griffiths, H. B. S., et al. (2018). Ruthenium-Containing Linear Helicates and Mesocates With Tuneable P53-Selective Cytotoxicity in Colorectal Cancer Cells. *Angew. Chem. Int. Ed.* 57, 9799–9804. doi:10.1002/anie.201805510

Anthony, E. J., Bolitho, E. M., Bridgewater, H. E., Carter, O. W. L., Donnelly, J. M., Imberti, C., et al. (2020). Metallodrugs Are Unique: Opportunities and Challenges of Discovery and Development. *Chem. Sci.* 11, 12888–12917. doi:10.1039/d0sc04082g

August, D. P., Nichol, G. S., and Lusby, P. J. (2016). Maximizing Coordination Capsule-Guest Polar Interactions in Apolar Solvents Reveals Significant Binding. *Angew. Chem. Int. Ed.* 55, 15022–15026. doi:10.1002/anie.201608229

Austin, W. B., Bilow, N., Kelleghan, W. J., and Lau, K. S. Y. (1981). Facile Synthesis of Ethynylated Benzoic Acid Derivatives and Aromatic Compounds via Ethynyltrimethylsilane. *J. Org. Chem.* 46, 2280–2286. doi:10.1021/jo00324a015

Bardhan, D., and Chand, D. K. (2019). Palladium(II)-Based Self-Assembled Heteroleptic Coordination Architectures: A Growing Family. *Chem. Eur. J.* 25, 12241–12269. doi:10.1002/chem.201900831

Boiocchi, M., and Fabbrizzi, L. (2014). Double-stranded Dimetallic Helicates: Assembling-Disassembling Driven by the Cu(I)/Cu(II) Redox Change and the Principle of Homochiral Recognition. *Chem. Soc. Rev.* 43, 1835–1847. doi:10.1039/c3cs60428d

Boros, E., Dyson, P. J., and Gasser, G. (2020). Classification of Metal-Based Drugs According to Their Mechanisms of Action. *Chem.* 6, 41–60. doi:10.1016/j.chempr.2019.10.013

Brabec, V., Howson, S. E., Kaner, R. A., Lord, R. M., Malina, J., Phillips, R. M., et al. (2013). Metallohelices with Activity Against Cisplatin-Resistant Cancer Cells; Does the Mechanism Involve DNA Binding? *Chem. Sci.* 4, 4407–4416. doi:10.1039/c3sc51731d

Burke, B. P., Grantham, W., Burke, M. J., Nichol, G. S., Roberts, D., Renard, I., et al. (2018). Visualizing Kinetically Robust $Co(III)_4L_6$ Assemblies in Vivo: SPECT Imaging of the Encapsulated [99mTc]TcO_4-Anion. *J. Am. Chem. Soc.* 140, 16877–16881. doi:10.1021/jacs.8b09582

Cardo, L., Nawroth, I., Cail, P. J., Mckeating, J. A., and Hannon, M. J. (2018). Metallo Supramolecular Cylinders Inhibit HIV-1 TARTAT Complex Formation and Viral Replication in Cellulo. *Sci. Rep.* 8, 13342. doi:10.1038/s41598-018-31513-3

Cardo, L., Sadovnikova, V., Phongtongpasuk, S., Hodges, N. J., and Hannon, M. J. (2011). Arginine Conjugates of Metallo-Supramolecular Cylinders Prescribe Helicity and Enhance DNA Junction Binding and Cellular Activity. *Chem. Commun.* 47, 6575–6577. doi:10.1039/c1cc11356a

Cerasino, L., Hannon, M. J., and Sletten, E. (2007). DNA Three-Way Junction With a Dinuclear Iron(II) Supramolecular Helicate at the Center: A NMR Structural Study. *Inorg. Chem.* 46, 6245–6251. doi:10.1021/ic062415c

Childs, L. J., Malina, J., Rolfsnes, B. E., Pascu, M., Prieto, M. J., Broome, M. J., et al. (2006). A DNA-Binding Copper(I) Metallosupramolecular cylinder that Acts as an Artificial Nuclease. *Chem. Eur. J.* 12, 4919–4927. doi:10.1002/chem.200600060

Cook, T. R., and Stang, P. J. (2015). Recent Developments in the Preparation and Chemistry of Metallacycles and Metallacages via Coordination. *Chem. Rev.* 115, 7001–7045. doi:10.1021/cr5005666

Cook, T. R., Vajpayee, V., Lee, M. H., Stang, P. J., and Chi, K.-W. (2013). Biomedical and Biochemical Applications of Self-Assembled Metallacycles and Metallacages. *Acc. Chem. Res.* 46, 2464–2474. doi:10.1021/ar400010v

Crlikova, H., Malina, J., Novohradsky, V., Kostrhunova, H., Vasdev, R. A. S., Crowley, J. D., et al. (2020). Antiproliferative Activity and Associated DNA Interactions of $[Co_2L_3]^{6+}$ Cylinders Derived From Bis(bidentate) 2-Pyridyl-1,2,3-Triazole Ligands. *Organometallics* 39, 1448–1455. doi:10.1021/acs.organomet.0c00146

Cui, F., Li, S., Jia, C., Mathieson, J. S., Cronin, L., Yang, X.-J., et al. (2012). Anion-Dependent Formation of Helicates Versus Mesocates of Triple-Stranded M_2L_3 (M = Fe^{2+}, Cu^{2+}) Complexes. *Inorg. Chem.* 51, 179–187. doi:10.1021/ic201417y

Faulkner, A. D., Kaner, R. A., Abdallah, Q. M. A., Clarkson, G., Fox, D. J., Gurnani, P., et al. (2014). Asymmetric Triplex Metallohelices With High and Selective Activity Against Cancer Cells. *Nat. Chem.* 6, 797–803. doi:10.1038/nchem.2024

Fazio, E., Haynes, C. J. E., De La Torre, G., Nitschke, J. R., and Torres, T. (2018). A Giant M_2L_3 Metallo-Organic Helicate Based on Phthalocyanines as a Host for Electroactive Molecules. *Chem. Commun.* 54, 2651–2654. doi:10.1039/c7cc09528g

Frei, A. (2020). Metal Complexes, an Untapped Source of Antibiotic Potential? *Antibiotics* 9, 90. doi:10.3390/antibiotics9020090

Frei, A., Zuegg, J., Elliott, A. G., Baker, M., Braese, S., Brown, C., et al. (2020). Metal Complexes as a Promising Source for New Antibiotics. *Chem. Sci.* 11, 2627–2639. doi:10.1039/c9sc06460e

Gamba, I., Rama, G., Ortega-Carrasco, E., Maréchal, J.-D., Martínez-Costas, J., Eugenio Vázquez, M., et al. (2014). Programmed Stereoselective Assembly of DNA-Binding Helical Metallopeptides. *Chem. Commun.* 50, 11097–11100. doi:10.1039/c4cc03606a

Gao, W.-X., Zhang, H.-N., and Jin, G.-X. (2019). Supramolecular Catalysis Based on Discrete Heterometallic Coordination-Driven Metallacycles and Metallacages. *Coord. Chem. Rev.* 386, 69–84. doi:10.1016/j.ccr.2019.01.023

Glasson, C. R. K., Meehan, G. V., Clegg, J. K., Lindoy, L. F., Smith, J. A., Keene, F. R., et al. (2008). Microwave Synthesis of a Rare $[Ru_2L_3]^{4+}$ Triple Helicate and its Interaction With DNA. *Chem. Eur. J.* 14, 10535–10538. doi:10.1002/chem.200801790

Glasson, C. R. K., Meehan, G. V., Motti, C. A., Clegg, J. K., Turner, P., Jensen, P., et al. (2011a). New Nickel(II) and Iron(II) Helicates and Tetrahedra Derived From Expanded Quaterpyridines. *Dalton Trans.* 40, 10481–10490. doi:10.1039/c1dt10667h

Glasson, C. R. K., Meehan, G. V., Motti, C. A., Clegg, J. K., Turner, P., Jensen, P., et al. (2011b). Nickel(II) and Iron(II) Triple Helicates Assembled from Expanded Quaterpyridines Incorporating Flexible Linkages. *Dalton Trans.* 40, 12153–12159. doi:10.1039/c1dt10820d

Goetz, S., and Kruger, P. E. (2006). A New Twist in Anion Binding: Metallo-Helicate Hosts for Anionic Guests. *Dalton Trans.*, 1277–1284. doi:10.1039/b514580e

Gómez-González, J., Pérez, Y., Sciortino, G., Roldan-Martín, L., Martínez-Costas, J., Maréchal, J. D., et al. (2021). Dynamic Stereoselection of Peptide Helicates and Their Selective Labeling of DNA Replication Foci in Cells*. *Angew. Chem. Int. Ed. Engl.* 60, 8859–8866. doi:10.1002/anie.202013039

Gómez-González, J., Peña, D. G., Barka, G., Sciortino, G., Maréchal, J.-D., Vázquez López, M., et al. (2018). Directed Self-Assembly of Trimeric DNA-Bindingchiral Miniprotein Helicates. *Front. Chem.* 6, 520. doi:10.3389/fchem.2018.00520

Grosshenny, V., Romero, F. M., and Ziessel, R. (1997). Construction of Preorganized Polytopic Ligands via Palladium-Promoted Cross-Coupling Reactions. *J. Org. Chem.* 62, 1491–1500. doi:10.1021/jo962068w

Hall, M. D., Telma, K. A., Chang, K.-E., Lee, T. D., Madigan, J. P., Lloyd, J. R., et al. (2014). Say No to DMSO: Dimethylsulfoxide Inactivates Cisplatin, Carboplatin, and Other Platinum Complexes. *Cancer Res.* 74, 3913–3922. doi:10.1158/0008-5472.can-14-0247

Hannon, M. J., and Childs, L. J. (2004). Helices and Helicates: Beautiful Supramolecular Motifs With Emerging Applications. *Supramolecular Chem.* 16, 7–22. doi:10.1080/10610270310001632386

Hannon, M. J., Meistermann, I., Isaac, C. J., Blomme, C., Rodger, A., and Aldrich-Wright, J. R. (2001a). Paper: a Cheap yet Effective Chiral Stationary Phase for Chromatographic Resolution of Metallo-Supramolecular Helicates. *Chem. Commun.*, 1078–1079. doi:10.1039/b101970h

Hannon, M. J., Moreno, V., Prieto, M. J., Moldrheim, E., Sletten, E., Meistermann, I., et al. (2001b). Intramolecular DNA Coiling Mediated by a Metallo-Supramolecular Cylinder. *Angew. Chem. Int. Ed.* 40, 880–884. doi:10.1002/1521-3773(20010302)40:5<879::aid-anie879>3.0.co;2-x

Hannon, M. J., Painting, C. L., Jackson, A., Hamblin, J., and Errington, W. (1997). An Inexpensive Approach to Supramolecular Architecture. *Chem. Commun.*, 1807–1808. doi:10.1039/a703713i

Hartinger, C. G., and Dyson, P. J. (2009). Bioorganometallic Chemistry-From Teaching Paradigms to Medicinal Applications. *Chem. Soc. Rev.* 38, 391–401. doi:10.1039/b707077m

Holtze, A. C. G., Kariuki, B. M., and Hannon, M. J. (2006). Dinuclear Double-Stranded Metallosupramolecular Ruthenium Complexes: Potential Anticancer Drugs. *Angew. Chem. Int. Ed.* 45, 4839–4842. doi:10.1002/anie.200601351

Hong, C. M., Bergman, R. G., Raymond, K. N., and Toste, F. D. (2018). Self-Assembled Tetrahedral Hosts as Supramolecular Catalysts. *Acc. Chem. Res.* 51, 2447–2455. doi:10.1021/acs.accounts.8b00328

Hotze, A. C. G., Hodges, N. J., Hayden, R. E., Sanchez-Cano, C., Paines, C., Male, N., et al. (2008). Supramolecular Iron Cylinder with Unprecedented DNA Binding Is a Potent Cytostatic and Apoptotic Agent without Exhibiting Genotoxicity. *Chem. Biol.* 15, 1258–1267. doi:10.1016/j.chembiol.2008.10.016

Howson, S. E., Allan, L. E. N., Chmel, N. P., Clarkson, G. J., Van Gorkum, R., and Scott, P. (2009). Self-assembling Optically Pure $Fe(A\text{-}B)_3$ Chelates. *Chem. Commun.*, 1727–1729. doi:10.1039/b821573a

Howson, S. E., Bolhuis, A., Brabec, V., Clarkson, G. J., Malina, J., Rodger, A., et al. (2012). Optically Pure, Water-Stable Metallo-Helical "flexicate" Assemblies with Antibiotic Activity. *Nat. Chem* 4, 31–36. doi:10.1038/nchem.1206

Howson, S. E., and Scott, P. (2011). Approaches to the Synthesis of Optically Pure Helicates. *Dalton Trans.* 40, 10268–10277. doi:10.1039/c1dt11423a

Hrabina, O., Malina, J., Scott, P., and Brabec, V. (2020). Cationic Fe(II) Triplex-Forming Metallohelices as DNA Bulge Binders. *Chem. Eur. J.* 26, 16554–16562. doi:10.1002/chem.202004060

Huang, H., Humbert, N., Bizet, V., Patra, M., Chao, H., Mazet, C., et al. (2017). Influence of the Dissolution Solvent on the Cytotoxicity of Octahedral Cationic Ir(III) Hydride Complexes. *J. Organomet. Chem.* 839, 15–18. doi:10.1016/j.jorganchem.2016.12.010

Jiang, P., Wu, W.-Y., Tang, T.-H., Chen, Z.-F., Fang, Y.-C., and Wan, R. (2019). ^{1}H NMR STUDY OF THE HOST-GUEST CHEMISTRY IN A SUPRAMOLECULAR HELICATE $FE(II)_2L_3$ SOLUTION. *Quim. Nova* 42, 412–417. doi:10.21577/0100-4042.20170355

Kaner, R. A., Allison, S. J., Faulkner, A. D., Phillips, R. M., Roper, D. I., Shepherd, S. L., et al. (2016). Anticancer Metallohelices: Nanomolar Potency and High Selectivity. *Chem. Sci.* 7, 951–958. doi:10.1039/c5sc03677a

Kaner, R. A., and Scott, P. (2015). Metallohelices: Potential Mimetics of α-Helical Peptides in Cancer Treatment? *Future Med. Chem.* 7, 1–4. doi:10.4155/fmc.14.150

Kumar, S. V., Lo, W. K. C., Brooks, H. J. L., and Crowley, J. D. (2015). Synthesis, Structure, Stability and Antimicrobial Activity of a Ruthenium(II) Helicate Derived from a Bis-Bidentate "click" Pyridyl-1,2,3-Triazole Ligand. *Inorg. Chim. Acta* 425, 1–6. doi:10.1016/j.ica.2014.10.011

Lehn, J. M., Rigault, A., Siegel, J., Harrowfield, J., Chevrier, B., and Moras, D. (1987). Spontaneous Assembly of Double-Stranded Helicates from Oligobipyridine Ligands and Copper(I) Cations: Structure of an Inorganic Double helix. *Proc. Natl. Acad. Sci.* 84, 2565–2569. doi:10.1073/pnas.84.9.2565

Li, M., Howson, S. E., Dong, K., Gao, N., Ren, J., Scott, P., et al. (2014). Chiral Metallohelical Complexes Enantioselectively Target Amyloid β for Treating Alzheimer's Disease. *J. Am. Chem. Soc.* 136, 11655–11663. doi:10.1021/ja502789e

Li, M., Zhao, C., Ren, J., and Qu, X. (2015). Chiral Metallo-Supramolecular Complex Directed Enantioselective Self-Assembly of β-Sheet Breaker Peptide for Amyloid Inhibition. *Small* 11, 4651–4655. doi:10.1002/smll.201501329

Malina, J., Hannon, M. J., and Brabec, V. (2008). DNA Binding of Dinuclear Iron(II) Metallosupramolecular Cylinders. DNA Unwinding and Sequence Preference. *Nucleic Acids Res.* 36, 3630–3638. doi:10.1093/nar/gkn244

Malina, J., Hannon, M. J., and Brabec, V. (2016). Iron(II) Supramolecular Helicates Interfere with the HIV-1 Tat-TAR RNA Interaction Critical for Viral Replication. *Sci. Rep.* 6, 29674. doi:10.1038/srep29674

Malina, J., Hannon, M. J., and Brabec, V. (2014). Recognition of DNA Bulges by Dinuclear Iron(II) Metallosupramolecular Helicates. *FEBS J.* 281, 987–997. doi:10.1111/febs.12696

Malina, J., Hannon, M. J., and Brabec, V. (2007). Recognition of DNA Three-Way Junctions by Metallosupramolecular Cylinders: Gel Electrophoresis Studies. *Chem. Eur. J.* 13, 3871–3877. doi:10.1002/chem.200700159

Malina, J., Scott, P., and Brabec, V. (2015a). Recognition of DNA/RNA Bulges by Antimicrobial and Antitumor Metallohelices. *Dalton Trans.* 44, 14656–14665. doi:10.1039/c5dt02018b

Malina, J., Scott, P., and Brabec, V. (2015b). Shape-selective Recognition of DNA Abasic Sites by Metallohelices: Inhibition of Human AP Endonuclease 1. *Nucleic Acids Res.* 43, 5297–5306. doi:10.1093/nar/gkv438

McNeill, S. M., Giles, N. M., Preston, D., Jones, P. P., Crowley, J. D., and Giles, G. I. (2020). Quadruply Stranded Metallo-Supramolecular Helicate $[Pd_2(hextrz)_4]^{4+}$ Acts as a Molecular Mimic of Cytolytic Peptides. *Chem. Res. Toxicol.* 33, 1822–1834. doi:10.1021/acs.chemrestox.0c00061

McNeill, S. M., Preston, D., Lewis, J. E. M., Robert, A., Knerr-Rupp, K., Graham, D. O., et al. (2015). Biologically Active $[Pd_2L_4]^{4+}$ Quadruply-Stranded Helicates: Stability and Cytotoxicity. *Dalton Trans.* 44, 11129–11136. doi:10.1039/c5dt01259g

Mjos, K. D., and Orvig, C. (2014). Metallodrugs in Medicinal Inorganic Chemistry. *Chem. Rev.* 114, 4540–4563. doi:10.1021/cr400460s

Moldrheim, E., Hannon, M. J., Meistermann, I., Rodger, A., and Sletten, E. (2002). Interaction between a DNA Oligonucleotide and a Dinuclear Iron(II) Supramolecular Cylinder; an NMR and Molecular Dynamics Study. *J. Biol. Inorg. Chem.* 7, 770–780. doi:10.1007/s00775-002-0354-2

Oleksi, A., Blanco, A. G., Boer, R., Usón, I., Aymamí, J., Rodger, A., et al. (2006). Molecular Recognition of a Three-Way DNA Junction by a Metallosupramolecular Helicate. *Angew. Chem. Int. Ed.* 45, 1227–1231. doi:10.1002/anie.200503822

Paneerselvam, A. P., Mishra, S. S., and Chand, D. K. (2018). Linear and Circular Helicates: A Brief Review. *J. Chem. Sci.* 130, 96. doi:10.1007/s12039-018-1497-1

Patra, M., Joshi, T., Pierroz, V., Ingram, K., Kaiser, M., Ferrari, S., et al. (2013). DMSO-Mediated Ligand Dissociation: Renaissance for Biological Activity of N-Heterocyclic-$[Ru(\eta^6\text{-arene})Cl_2]$ Drug Candidates. *Chem. Eur. J.* 19, 14768–14772. doi:10.1002/chem.201303341

Percástegui, E. G., Ronson, T. K., and Nitschke, J. R. (2020). Design and Applications of Water-Soluble Coordination Cages. *Chem. Rev.* 120, 13480–13544. doi:10.1021/acs.chemrev.0c00672

Phongtongpasuk, S., Paulus, S., Schnabl, J., Sigel, R. K. O., Spingler, B., Hannon, M. J., et al. (2013). Binding of a Designed Anti-cancer Drug to the Central Cavity of an RNA Three-Way Junction. *Angew. Chem. Int. Ed.* 52, 11513–11516. doi:10.1002/anie.201305079

Piguet, C., Bernardinelli, G., and Hopfgartner, G. (1997). Helicates as Versatile Supramolecular Complexes. *Chem. Rev.* 97, 2005–2062. doi:10.1021/cr960053s

Pöthig, A., and Casini, A. (2019). Recent Developments of Supramolecular Metal-Based Structures for Applications in Cancer Therapy and Imaging. *Theranostics* 9, 3150–3169. doi:10.7150/thno.31828

Richards, A. D., Rodger, A., Hannon, M. J., and Bolhuis, A. (2009). Antimicrobial Activity of an Iron Triple Helicate. *Int. J. Antimicrob. Agents* 33, 469–472. doi:10.1016/j.ijantimicag.2008.10.031

Rizzuto, F. J., Von Krbek, L. K. S., and Nitschke, J. R. (2019). Strategies for Binding Multiple Guests in Metal-Organic Cages. *Nat. Rev. Chem.* 3, 204–222. doi:10.1038/s41570-019-0085-3

Saha, S., Regeni, I., and Clever, G. H. (2018). Structure Relationships between Bis-Monodentate Ligands and Coordination Driven Self-Assemblies. *Coord. Chem. Rev.* 374, 1–14. doi:10.1016/j.ccr.2018.06.010

Samanta, S. K., and Isaacs, L. (2020). Biomedical Applications of Metal Organic Polygons and Polyhedra (MOPs). *Coord. Chem. Rev.* 410, 213181. doi:10.1016/j.ccr.2020.213181

Schmidt, A., Molano, V., Hollering, M., Pöthig, A., Casini, A., and Kühn, F. E. (2016). Evaluation of New Palladium Cages as Potential Delivery Systems for the Anticancer Drug Cisplatin. *Chem. Eur. J.* 22, 2253–2256. doi:10.1002/chem.201504930

Schoentjes, B., and Lehn, J.-M. (1995). Interaction of Double-Helical Polynuclear Copper(I) Complexes with Double-Stranded DNA. *Helv. Chim. Acta* 78, 1–12. doi:10.1002/hlca.19950780103

Sepehrpour, H., Fu, W., Sun, Y., and Stang, P. J. (2019). Biomedically Relevant Self-Assembled Metallacycles and Metallacages. *J. Am. Chem. Soc.* 141, 14005–14020. doi:10.1021/jacs.9b06222

Simpson, D. H., Hapeshi, A., Rogers, N. J., Brabec, V., Clarkson, G. J., Fox, D. J., et al. (2019). Metallohelices that Kill Gram-Negative Pathogens Using Intracellular Antimicrobial Peptide Pathways. *Chem. Sci.* 10, 9708–9720. doi:10.1039/c9sc03532j

Song, H., Postings, M., Scott, P., and Rogers, N. J. (2021). Metallohelices Emulate the Properties of Short Cationic α-helical Peptides. *Chem. Sci.* 12, 1620–1631. doi:10.1039/d0sc06412b

Song, H., Rogers, N. J., Allison, S. J., Brabec, V., Bridgewater, H., Kostrhunova, H., et al. (2019). Discovery of Selective, Antimetastatic and Anti-cancer Stem Cell Metallohelicesviapost-Assembly Modification. *Chem. Sci.* 10, 8547–8557. doi:10.1039/c9sc02651g

Song, H., Rogers, N. J., Brabec, V., Clarkson, G. J., Coverdale, J. P. C., Kostrhunova, H., et al. (2020). Triazole-based, Optically-Pure Metallosupramolecules; Highly Potent and Selective Anticancer Compounds. *Chem. Commun.* 56, 6392–6395. doi:10.1039/d0cc02429e

Steel, T. R., Tong, K. K. H., Söhnel, T., Jamieson, S. M. F., Wright, L. J., Crowley, J. D., et al. (2021a). Homodinuclear Organometallics of Ditopic N,N-chelates: Synthesis, Reactivity and *In Vitro* Anticancer Activity. *Inorg. Chim. Acta* 518, 120220. doi:10.1016/j.ica.2020.120220

Steel, T. R., Walsh, F., Wieczorek-Błauż, A., Hanif, M., and Hartinger, C. G. (2021b). Monodentately-coordinated Bioactive Moieties in Multimodal Half-sandwich Organoruthenium Anticancer Agents. *Coord. Chem. Rev.* 439, 213890. doi:10.1016/j.ccr.2021.213890

Symmers, P. R., Burke, M. J., August, D. P., Thomson, P. I. T., Nichol, G. S., Warren, M. R., et al. (2015). Non-equilibrium Cobalt(iii) "click" Capsules. *Chem. Sci.* 6, 756–760. doi:10.1039/c4sc03036b

Therrien, B. (2015). Biologically Relevant Arene Ruthenium Metalla-Assemblies. *CrystEngComm* 17, 484–491. doi:10.1039/c4ce02146k

Tran, N. M., and Yoo, H. (2020). Recent Advances in Heteroleptic Multiple-Stranded Metallosupramolecules. *Dalton Trans.* 49, 11819–11827. doi:10.1039/d0dt02243h

Tremlett, W. D. J., Tong, K. K. H., Steel, T. R., Movassaghi, S., Hanif, M., Jamieson, S. M. F., et al. (2019). Hydroxyquinoline-derived Anticancer Organometallics: Introduction of Amphiphilic PTA as an Ancillary Ligand Increases Their Aqueous Solubility. *J. Inorg. Biochem.* 199, 110768. doi:10.1016/j.jinorgbio.2019.110768

Vasdev, R. A. S., Gaudin, L. F., Preston, D., Jogy, J. P., Giles, G. I., and Crowley, J. D. (2018). Anticancer Activity and Cisplatin Binding Ability of Bis-Quinoline and Bis-Isoquinoline Derived $[Pd_2L_4]^{4+}$ Metallosupramolecular Cages. *Front. Chem.* 6, 563. doi:10.3389/fchem.2018.00563

Vasdev, R., Preston, D., Scottwell, S., Brooks, H., Crowley, J., and Schramm, M. (2016). Oxidatively Locked $[Co_2L_3]^{6+}$ Cylinders Derived from Bis(bidentate) 2-Pyridyl-1,2,3-Triazole "Click" Ligands: Synthesis, Stability, and Antimicrobial Studies. *Molecules* 21, 1548. doi:10.3390/molecules21111548

Vellas, S., Lewis, J., Shankar, M., Sagatova, A., Tyndall, J., Monk, B., et al. (2013). $[Fe_2L_3]^{4+}$ Cylinders Derived from Bis(bidentate) 2-Pyridyl-1,2,3-Triazole "Click" Ligands: Synthesis, Structures and Exploration of Biological Activity. *Molecules* 18, 6383–6407. doi:10.3390/molecules18066383

White, A. P., Robertson, K. N., Cameron, T. S., Liengme, B. V., Leznoff, D. B., Trudel, S., et al. (2007). Synthesis and Characterization of $[M(DMSO)_6][SnCl_6]$ Complexes (M = Fe^{2+}, Co^{2+}, and Ni^{2+}) - an Old Mystery Solved. *Can. J. Chem.* 85, 372–378. doi:10.1139/v07-042

Yang, D., Krbek, L. K. S., Yu, L., Ronson, T. K., Thoburn, J. D., Carpenter, J. P., et al. (2021). Glucose Binding Drives Reconfiguration of a Dynamic Library of Urea-Containing Metal-Organic Assemblies. *Angew. Chem. Int. Ed.* 60, 4485–4490. doi:10.1002/anie.202014568

Yoshizawa, M., Klosterman, J. K., and Fujita, M. (2009). Functional Molecular Flasks: New Properties and Reactions within Discrete, Self-Assembled Hosts. *Angew. Chem. Int. Ed.* 48, 3418–3438. doi:10.1002/anie.200805340

Yu, H., Li, M., Liu, G., Geng, J., Wang, J., Ren, J., et al. (2012). Metallosupramolecular Complex Targeting an α/β Discordant Stretch of Amyloid β Peptide. *Chem. Sci.* 3, 3145–3153. doi:10.1039/c2sc20372c

Zhao, A., Howson, S. E., Zhao, C., Ren, J., Scott, P., Wang, C., et al. (2017). Chiral Metallohelices Enantioselectively Target Hybrid Human Telomeric G-Quadruplex DNA. *Nucleic Acids Res.* 45, 5026–5035. doi:10.1093/nar/gkx244

Zhao, A., Zhao, C., Ren, J., and Qu, X. (2016). Enantioselective Targeting Left-Handed Z-G-Quadruplex. *Chem. Commun.* 52, 1365–1368. doi:10.1039/c5cc08401f

Zhao, C., Song, H., Scott, P., Zhao, A., Tateishi-Karimata, H., Sugimoto, N., et al. (2018). Mirror-Image Dependence: Targeting Enantiomeric G-Quadruplex DNA Using Triplex Metallohelices. *Angew. Chem. Int. Ed.* 57, 15723–15727. doi:10.1002/anie.201809207

Zhao, C., Wu, L., Ren, J., Xu, Y., and Qu, X. (2013). Targeting Human Telomeric Higher-Order DNA: Dimeric G-Quadruplex Units Serve as Preferred Binding Site. *J. Am. Chem. Soc.* 135, 18786–18789. doi:10.1021/ja410723r

Conflict of Interest: The authors declare that the research was conducted in the absence of any commercial or financial relationships that could be construed as a potential conflict of interest.

frontiers in Chemistry

CORRECTION
published: 03 August 2021
doi: 10.3389/fchem.2021.739785

Corrigendum: Cavity-Containing $[Fe_2L_3]^{4+}$ Helicates: An Examination of Host-Guest Chemistry and Cytotoxicity

*Lynn S. Lisboa[1], Mie Riisom[2,3], Roan A. S. Vasdev[1], Stephen M. F. Jamieson[3], L. James Wright[2], Christian G. Hartinger[2] and James D. Crowley[1]**

[1]Department of Chemistry, University of Otago, Dunedin, New Zealand, [2]School of Chemical Sciences, University of Auckland, Auckland, New Zealand, [3]Auckland Cancer Society Research Centre, University of Auckland, Auckland, New Zealand

Keywords: iron(II), helicate, cytotoxicity, host-guest chemistry, metallosupramolecular architectures

OPEN ACCESS

Edited and reviewed by:
Tony D. James,
University of Bath, United Kingdom

****Correspondence:***
James D. Crowley
jcrowley@chemistry.otago.ac.nz

Specialty section:
This article was submitted to Supramolecular Chemistry, a section of the journal Frontiers in Chemistry

Received: *12 July 2021*
Accepted: *15 July 2021*
Published: *03 August 2021*

Citation:
Lisboa LS, Riisom M, Vasdev RAS, Jamieson SMF, Wright LJ, Hartinger CG and Crowley JD (2021) Corrigendum: Cavity-Containing $[Fe_2L_3]^{4+}$ Helicates: An Examination of Host-Guest Chemistry and Cytotoxicity. Front. Chem. 9:739785. doi: 10.3389/fchem.2021.739785

A Corrigendum on

Cavity-Containing $[Fe_2L_3]^{4+}$ Helicates: An Examination of Host-Guest Chemistry and Cytotoxicity

by Lisboa L. S., Riisom M., Vasdev R. A. S., Jamieson S. M. F., Wright L. J., Hartinger C. G. and Crowley J. D. (2021). Front Chem. 9:697684. doi:10.3389/fchem.2021.697684

In the original article, there was a mistake in **Figure 1** as published. The N positions of the pyridines in the ligand structure are incorrect. The corrected **Figure 1** appears below.

The authors apologize for this error and state that this does not change the scientific conclusions of the article in any way. The original article has been updated.

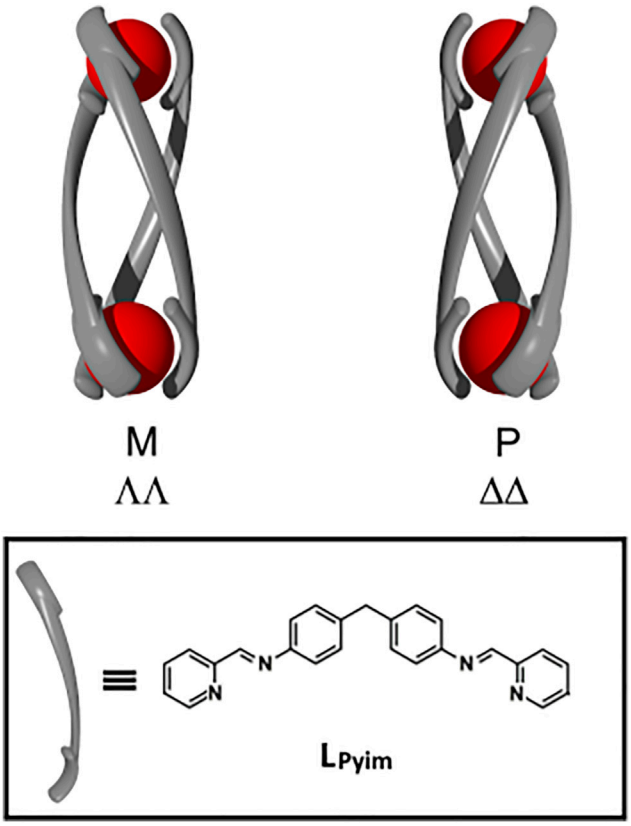

FIGURE 1 | Cartoon representations of the minus (M, ΛΛ), plus (P, ΔΔ) helicate isomers of a generic triple-stranded helicate and the chemical structure of the (1E,1′E)-N,N′-[methylenebis(4,1-phenylene)]bis[1-(pyridin-2-yl)methanimine] ligand ($\mathbf{L_{Pyim}}$) developed by Hannon and co-workers (Hannon et al., 1997).

frontiers in Chemistry

ORIGINAL RESEARCH
published: 07 July 2021
doi: 10.3389/fchem.2021.713305

Solvent-Driven Chirality Switching of a Pillar[4]arene[1]quinone Having a Chiral Amine-Substituted Quinone Subunit

Chunhong Liu, Zhipeng Yu, Jiabin Yao, Jiecheng Ji, Ting Zhao, Wanhua Wu and Cheng Yang**

Key Laboratory of Green Chemistry and Technology of Ministry of Education, College of Chemistry, and Healthy Food Evaluation Research Center, Sichuan University, Chengdu, China

Several new chiral pillar[4]arene[1]quinone derivatives were synthesized by reacting pillar[4]arene[1]quinone (**EtP4Q1**), containing four 1,4-diethoxybenzene units and one benzoquinone unit, with various chiral amines *via* Michael addition. Due to the direct introduction of chiral substituents on the rim of pillar[n]arene and the close location of the chiral center to the rim of **EtP4Q1**, the newly prepared compounds showed unique chiroptical properties without complicated chiral resolution processes, and unprecedented high anisotropy factor of up to −0.018 at the charge transfer absorption band was observed. Intriguingly, the benzene sidearm attached pillar[4]arene[1]quinone derivative **1a** showed solvent- and complexation-driven chirality inversion. This work provides a promising potential for absolute asymmetric synthesis of pillararene-based derivatives.

Keywords: pillar[4]arene[1]quinone, charge-transfer interaction, circular dichroism, anisotropy factors, chirality switching, solvent effects

OPEN ACCESS

Edited by:
Tony D. James,
University of Bath, United Kingdom

Reviewed by:
Xiao-Yu Hu,
Nanjing University of Aeronautics and Astronautics, China
Peter Cragg,
University of Brighton, United Kingdom

****Correspondence:***
Wanhua Wu
wuwanhua@scu.edu.cn
Cheng Yang
yangchengyc@scu.edu.cn

Specialty section:
This article was submitted to Supramolecular Chemistry, a section of the journal Frontiers in Chemistry

Received: *22 May 2021*
Accepted: *14 June 2021*
Published: *07 July 2021*

Citation:
Liu C, Yu Z, Yao J, Ji J, Zhao T, Wu W and Yang C (2021) Solvent-Driven Chirality Switching of a Pillar[4]arene[1]quinone Having a Chiral Amine-Substituted Quinone Subunit. Front. Chem. 9:713305. doi: 10.3389/fchem.2021.713305

INTRODUCTION

Manipulating molecular chirality, being in the core position of contemporary chemical science (Zhang et al., 2014), has been attracting significant attention not only from the point of view of the fundamental science but also the potential applications such as chiral recognition, asymmetry catalysis, and chiral switches (Zhou and Tang, 2005; Goldup, 2016; Gao et al., 2017; Xing and Zhao, 2018; Corra et al., 2019; Yao et al., 2021b). On the other hand, supramolecular chiral photochemistry, which arises from the chiral spatial arrangement of noncovalently involved components in assemblies (Crassous, 2009), has received booming development in recent years due to their close correlation with many natural and artificial systems and a wide range of potential applications (Jung et al., 2001; Nakashima et al., 2001; Borovkov et al., 2003a; Hembury et al., 2008; Yang and Inoue, 2014; Chen et al., 2015; Liu et al., 2015; Wang X. et al., 2020). Compared with molecular chirality, the supramolecular chirality is more attractive in terms of their regulatability by the external conditions such as temperature (Yao et al., 2017; Fan et al., 2019), pH (Kanagaraj et al., 2020; Liang et al., 2020; Hao et al., 2021), redox (Xiao et al., 2020), light (De Poli et al., 2016), chemical additives (Lee et al., 2018), pressure (Yao et al., 2021a), and solvents (Borovkov et al., 2003b; Fan et al., 2019). Pillar[n]arenes (Ogoshi et al., 2008; Xue et al., 2012; Pan et al., 2015; Fan et al., 2016; Jie et al., 2018; Lv et al., 2018; Li G. et al., 2019; Xiao et al., 2019; Ji et al., 2020a; Lou and Yang, 2020; Mi et al., 2020; Liu et al., 2021;

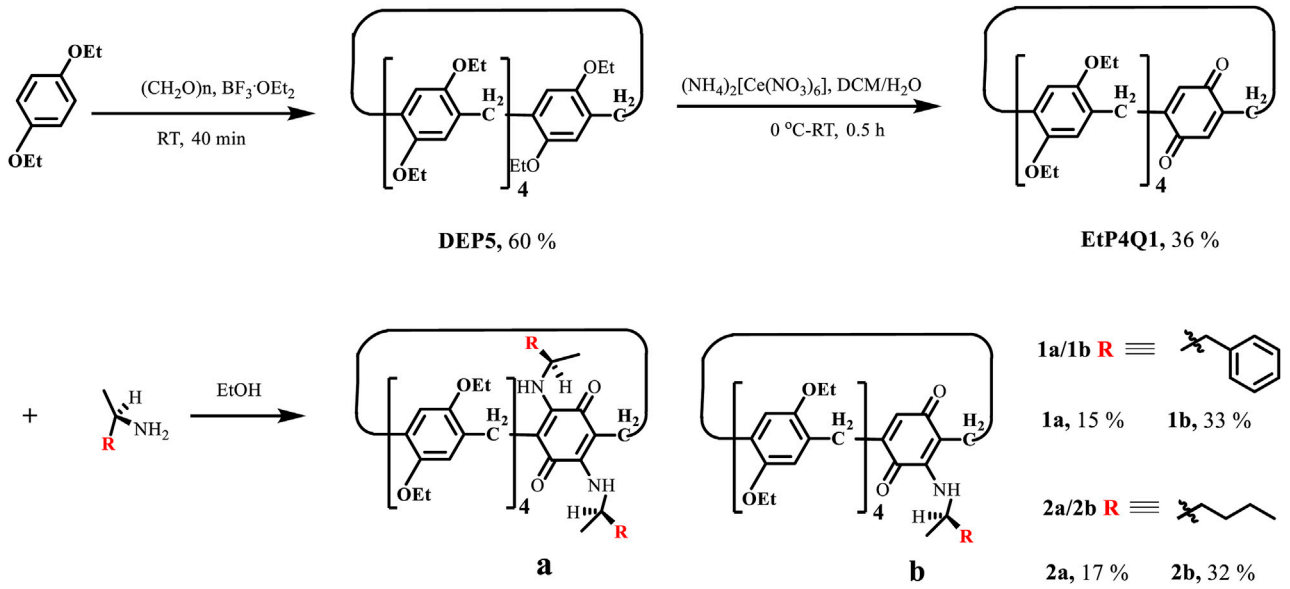

SCHEME 1 | Synthetic routes of chiral amine-bearing pillar[4]arene[1]quinones.

Peng et al., 2021), as a relatively new class of synthetic macrocyclic hosts with some unique properties (Guo et al., (2018); Lai et al., (2019); Liu et al., (2019); Wang et al., (2021), have proved to be an ideal platform to construct unimolecular chirality based on different external stimuli-driven. We have demonstrated that the chirality of pillar[n]arene derivatives could be manipulated by external stimuli, including temperature, redox, light, and pressure (Yao et al., 2017; Xiao et al., 2020; Yao et al., 2021a; Yao et al., 2021b). The synthetic approaches for obtaining chiral pillar[5]arenes include introducing chiral or bulky groups on the openings, fusing a side ring onto one subunit, or threading with an axle to block the interconversion between S_p and R_p conformers (Ogoshi et al., 2011; Chen et al., 2013; Strutt et al., 2014b; Shurpik et al., 2016; Li Q. et al., 2019; Ma et al., 2019; Zhang et al., 2019). However, pillar[5]arenes' planar-chiral S_p and R_p enantiomers need to be separated by HPLC enantio-resolution of the racemic mixture to study their chiroptical properties. Synthesis of chiral pillar[5]arenes without the complicated chiral resolution processes should be more convenient and valuable for studying supramolecular chirality switching. It has been reported that 1,4-benzoquinone undergoes the Michael addition reaction with aliphatic or aromatic amines to selectively afford 2,5-bis(alkyl/arylamino)-1,4-benzoquinones (Almeida Barbosa et al., 2010; Strutt et al., 2014a; Li et al., 2018; Kiruthika et al., 2020; Li et al., 2020). In this work, we report the synthesis of several new chiral pillar[4]arene[1]quinone derivatives and their unique chiroptical properties. We report the synthesis of several new pillar[4]arene[1]quinone derivatives by attaching chiral amines onto the quinone ring of **EtP4Q1**. Homochiral compounds were obtained in moderate to good separate yield without complicated HPLC chiral resolution. These compounds showed unique chiroptical properties with unprecedented high anisotropy g factor of up to −0.018 at the charge transfer absorption band; moreover, the benzene sidearm attached pillar[4]arene[1]quinone derivative **1a** showed solvent- and complexation-driven chirality inversion.

EXPERIMENT

Compounds

A general reaction scheme for the synthesis of chiral pillar[4]arene[1]quinone derivatives is shown in Scheme 1. Diethyl hydroquinone ether–based pillar[5]arene (**DEP5**) was synthesized according to the literature procedure (Ogoshi et al., 2010). Pillar[4]arene[1]quinone (**EtP4Q1**), in which a benzoquinone unit replaces a diethoxybenzene unit in **DEP5**, was synthesized by partial oxidation with ammonium cerium nitrate, following a modified version of the literature procedure (Han et al., 2012). The reactions of the achiral **EtP4Q1** with chiral amines were carried out in ethanol at 75°C in an oil bath for 24 h (Almeida Barbosa et al., 2010; Li et al., 2018). After the solvent was removed under vacuum, the residue was purified by silica gel flash column chromatography using ethyl acetate/petroleum ether as the eluent to give the desired target product (see the supplementary file for detailed experimental procedures and characterizations).

Materials and Instruments

Unless otherwise noted, all reagents and materials were commercially available and used without further purification.

^{1}H NMR was recorded in a $CDCl_3$ solution at room temperature on Bruker AMX-400 (operating at 400 MHz for ^{1}HNMR), and all chemical shifts are reported in ppm with TMS as the internal standard. HRMS data were measured with a Waters Q-TOF Premier instrument. UV-vis spectra were obtained on a JASCO V650 spectrometer at room temperature. Circular dichroism spectra were recorded on a JASCO J-1500 spectrometer, and the obtained data were analyzed using ORIGIN 9.0 software.

RESULTS AND DISCUSSION

Synthesis of 1a/1b and 2a/2b

1,4-Benzoquinones were known to undergo the Michael addition reaction with organic amines to give 2,5-bis(amino)-1,4-benzoquinones (Almeida Barbosa et al., 2010). Huang and coworkers demonstrated that pillar[4]arene[1]quinone could physically adsorb organic amines in the solid-state, which underwent *in situ* Michael addition by elevating the temperature to realize so-called solid–vapor post-synthetic modification (Li et al., 2018). In general, pillar[n]arene derivatives have a pair of planar chiral enantiomeric conformers, which could interconvert through the "oxygen-through-the-annulus" rotation. The attachment of bulky groups on the rims of pillar[n]arene could block the interconversion and lead to a pair of separable enantiomers. The same could be realized by introducing a side ring or threading an axle. Enantiopure pillar[n]arene derivatives showed extremely strong chiroptical properties at the absorption band of hydroquinone ethers due to the inter-ring unit exciton coupling effect. Direct introduction of chiral substituents on the rim of pillar[n]arene could also lead to chiral pillar[n]arene derivatives (Ogoshi et al., 2011; Strutt et al., 2012; Chen et al., 2013; Strutt et al., 2014b; Shurpik et al., 2016; Li Q. et al., 2019; Ma et al., 2019; Zhang et al., 2019). However, the chiral substituents are far away from the aromatic rings in distances and usually show weak chiroptical induction. **EtP4Q1** showed brown charge transfer absorption. The Michael addition reaction allows chiral amines to be introduced onto the quinone ring directly, and we envisioned that the chiral **EtP4Q1** should offer unique chiroptical properties differing from other chiral pillar[5]arene derivatives. **EtP4Q1** was reacted with chiral (R)-(+)-α-methylbenzylamine (**Scheme 1**) in ethanol, which led to two brown products in 15 and 33% yields, respectively, which were demonstrated to be the mono- (**1a**) and di-substituted (**1b**) products, respectively, based on the NMR and HRMS analyses. The same was true in the reaction of (R)-2-aminohexane, which gave the mono- and di-substituted products **2a** and **2b**, respectively, after the silica gel chromatography separation.

UV-Vis Spectral Studies

The UV-vis spectra of chiral amine-substituted pillar[4]arene[1]quinones were measured in chloroform at 25°C. **EtP4Q1** showed a sharp absorption peak at 294 nm and a broad absorption at the visible range (**Figure 1**), assignable to the transitions of hydroquinone ether units and the intramolecular charge transfer, respectively (Mi et al., 2020; Mi et al., 2021). The UV-vis spectra of the mono-substituted pillar[4]arene[1]quinone derivatives **1b** and **2b** exhibited two major transitions, showing a weak broad absorption that tailed to 400–700 nm, which is assignable to a CT transition. Similar to that of **EtP4Q1,** the strong absorption that peaked at ca. 300 nm could be ascribed to the absorption of the hydroquinone units. Interestingly, **1a** and **2a** showed two intensive peaks in the UV range and a broad absorption at 450–700 nm that is bathochromic shifted with a concomitant decrease in intensity compared to those of **1b** and **2b**. The attenuated CT interaction of **1a** and **2a** could be presumably ascribed to the reduced electron withdraw

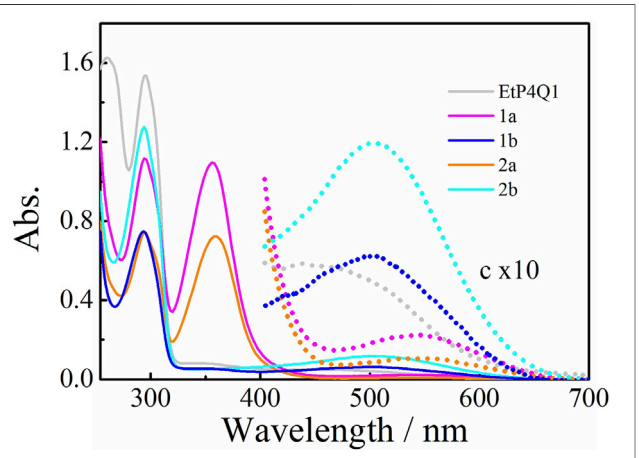

FIGURE 1 | UV-vis absorption spectra of **EtP4Q1**-derived compounds in chloroform solution (50 μM).

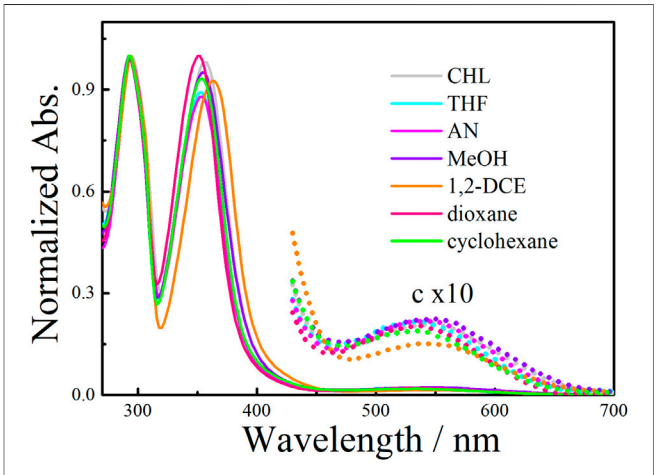

FIGURE 2 | Normalized UV-vis absorption spectra of **1a** compound in various solvents (50 μM).

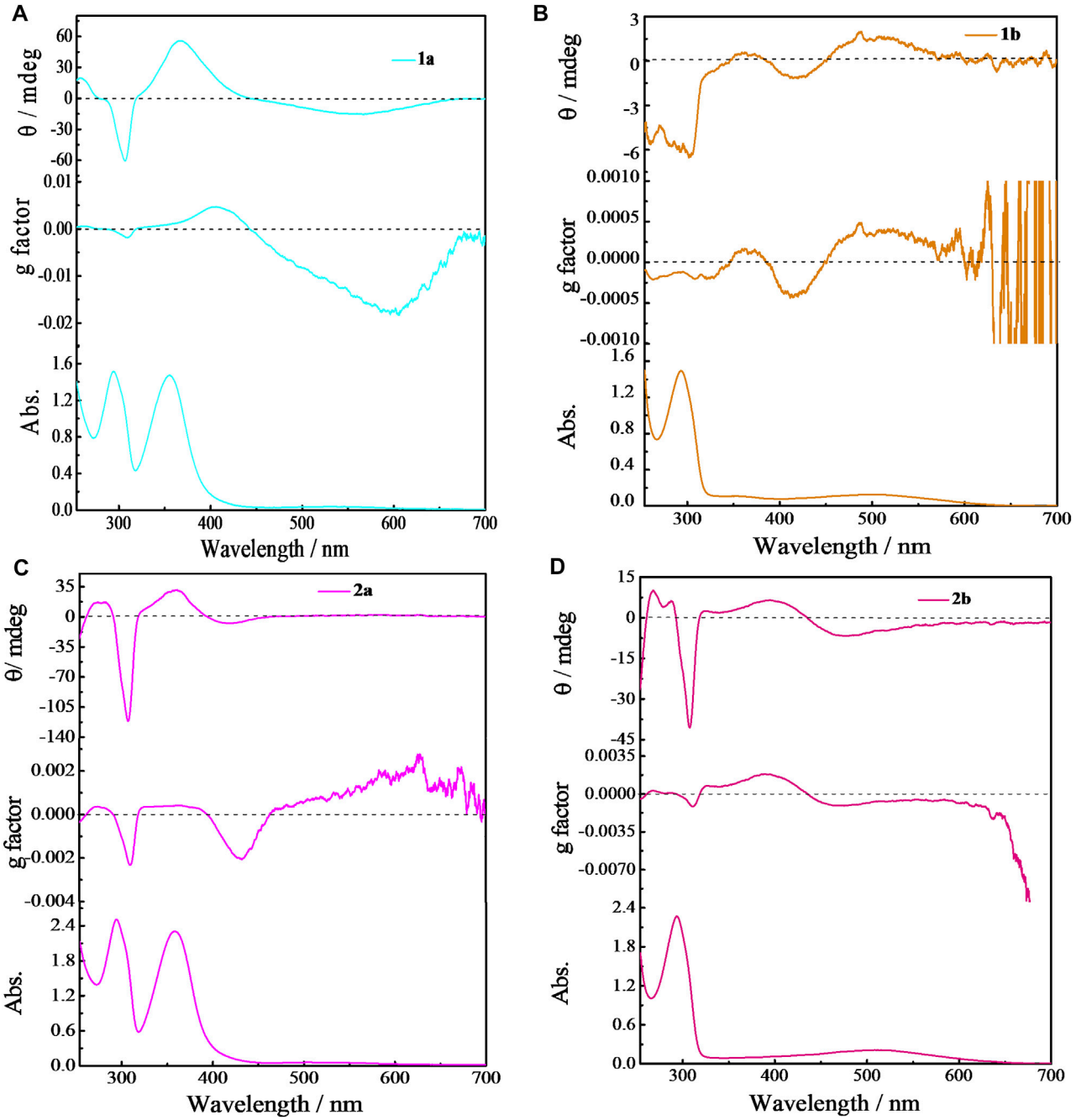

FIGURE 3 | Circular dichroism and UV-vis absorption spectra of **EtP4Q1-**derivated compounds (100 μM) in CHL solution **(A) 1a**; **(B) 1b**; **(C) 2a**; **(D) 2b**.

property of the benzoquinone ring when substituted with two amino substituents, which weakened the intramolecular CT interactions. An independent spectral titration for the intermolecular complexation between **EtP4Q1** and (R)-(+)-α-methylbenzylamine, by increasing the concentration of (R)-(+)-α-methylbenzylamine, was carried out in CHL at 25°C (ESI, **Supplementary Figure S13**). It turned out that the addition of (R)-(+)-α-methylbenzylamine to a solution of **EtP4Q1** did not lead to new absorption in the wavelengths range of 300–400 nm and visible region in the UV-vis spectroscopy, demonstrating that the new absorptions originated from the conjugation of the chiral amine-substituent in the quinone ring.

Weak ground-state intermolecular interactions, including CT, should be significantly affected by environmental factors such as solvent polarity, temperature, and so on (Saito et al., 2004). We

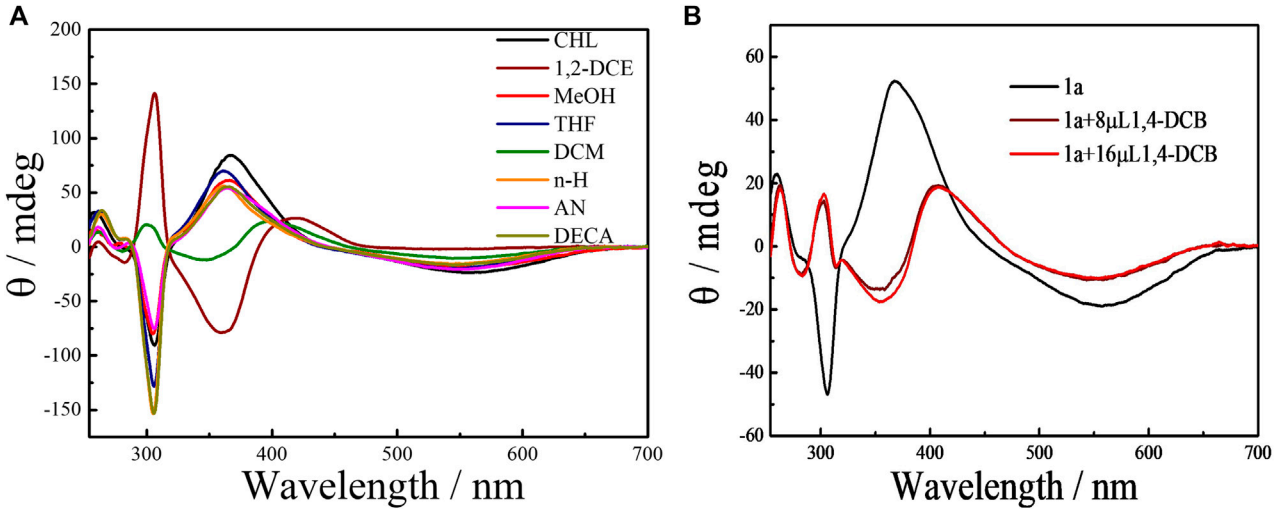

FIGURE 4 | (A) CD spectra of **1a** (50 μM) in various solvents at 25°C. Key: n-H, *n*-hexane; DECA, decalin; DCM, dichloromethane; THF, tetrahydrofuran; 1,2-DCE, 1,2-dichloroethane; CHL, chloroform; AN, acetonitrile and MeOH, methanol. **(B)** CD spectra of **1a** (50 μM) in chloroform solvents by adding 1,4-dicyanobutane (1,4-DCB) at 25°C.

have demonstrated that intermolecular supramolecular interactions can be effectively manipulated by adjusting the environmental effectors, including temperature or solvent (Ji et al., 2020b). As illustrated in **Figure 2**, the solvent-dependent UV-vis absorption spectra of **1a** revealed the CT transition was not restricted to chloroform solution but rather could be observed in various solvents. Moreover, the absorption spectra of the **1a** (50 μM), being measured in chloroform at various temperatures (**Supplementary Figure S14**), showed inconspicuous temperature-dependent behavior of the CT band, confirming that the intramolecular CT dominate in the macrocyclic structure.

Chiroptical Properties of the Macrocyclic Compounds

As mentioned above, pillar[5]arene derivatives possess a pair of enantiomeric conformers, and in general, they adapt per-R_p (R_p, R_p, R_p, R_p, and R_p) or per-S_p (S_p, S_p, S_p, S_p, and S_p) configurations to avoid inter-subunit steric repulsion. We have demonstrated that R_p and S_p conformers gave intensive positive and negative circular dichromism (CD) signals, respectively, at the extrema around 310 nm. The R_p and S_p conformers usually have an equal population (Yao et al., 2017; Xiao et al., 2020). Such conformational equilibrium could be broken by the complexation of a chiral guest to induce CD response, and thus being applied to chiral sensing (Ji et al., 2020a; Chen et al., 2020). In the chiral amine-substituted **EtP4Q1** derivatives, the chiral aliphatic amine or aromatic amine is anchored on the quinone subunit, with the chiral center located close to the rim of **EtP4Q1**, which was expected to significantly influence the chiroptical properties. CD spectra of **1a**/**1b** and **2a**/**2b** were measured at 25°C in chloroform to study the chiroptical properties (**Figure 3**). Negative Cotton effects at around 300 nm were observed for **1a**, **1b**, **2a**, and **2b,** assignable to the π-π* transition of hydroquinone units, which indicated that the hydroquinone units arranged in S_p configurations in the presence of the chiral amine group.

Despite the CD signals at 310 nm, new Cotton effects appeared in the region of 300–400 nm of **1a** and **2a**, which could be ascribed to the transition of 2,5-bis(alkyl/arylamino)-1,4-benzoquinones (Martini and Nachod, 1951; Li et al., 2020). In addition, strong Cotton effects in CT transition in the wavelength region of 400–700 nm were observed (Wang H. J. et al., 2020). In particular, the *g* factor of up to −0.018 was observed with **1a**, which, to our knowledge, is the largest *g* factor ever reported for CT transition (Mori and Inoue, 2005; Mori et al., 2006).

The effect of solvents on the planar chirality of **1a** was investigated. We have demonstrated that negative CD extrema at ca. 310 nm corresponds to S_p configuration of pillar[n]arenes, and vice versa for the R_p configuration(Yao et al., 2017; Xiao et al., 2020). The strong CD spectra observed with these chiral **EtP4Q1** derivatives suggested an unequal population of chiral conformers. We expected that variation of environmental conditions might switch the equilibrium of conformers and thus cause chiroptical change. Indeed, **1a** exhibits negative CD_{ex} in most of the solvents examined, including hexane, acetonitrile, decahydronaphthalene, chloroform, methanol, and THF (**Figure 4A**), suggesting the S_p configuration dominate in these solvents. However, the CD_{ex} at ca. 300 nm was inverted in sign accompanying by a hypochromic shift to give positive CD_{ex} in 1,2-dichloroethane and dichloromethane, indicating inversion of planar chirality to R_p. This result revealed that the relative stability between diastereomeric conformers could be significantly changed by the solvent. The following two aspects were responsible for the chiroptical switching process. The solvation of the chiral amine will cause significant steric interaction between solvent molecules surrounding the chiral amine substituents and hydroquinone ether units to thus critically affect the chiral arrangement of

hydroquinone subunits. Also, DCM and 1,2-DCE were known to complex with pillar[5]arene derivatives, which will push the sidearms of the chiral amine towards the outside of the cavity. Indeed, NMR titration experiments of compound **1a** in $CDCl_3$ upon adding different potions of 1,2-DCE showed that the proton signals of chiral amine significantly shifted downfield and the aromatic protons in pillar[5]arene become broad first and then separated into multiple peaks, when added more than 8% 1,2-DCE (**Supplementary Figure S26**). The chiral center that is closely located at the opening of the macrocyclic ring played an important role in the chiral inversion behavior. Solvent-dependent chiroptical changes were also observed with **1b** (**Supplementary Figure S20**).

The complexation-driven chiral optical switching has also been observed with bicyclic pillar[5]arene derivatives due to the exclusion of the side ring by the complexation of a guest molecule (Yao et al., 2017; Fan et al., 2019; Xiao et al., 2020). We found that stereoinversion with a sign-switching of CD_{ex} from negative to positive was induced by the addition of 1,4-dicyanobutane (1,4-DCB), a strong P[5] cavity binder (Shu et al., 2012), to **1a** in chloroform (**Figure 4B**; **Supplementary Figures S24, S25**).

This is consistent with the chiral inversion phenomenon observed in the solvents of DCM and 1,2-DCE, further suggesting that the benzene ring of the chiral amine is located toward the inside of the cavity. The bulky and rigid benzene ring should cause significant steric repulsion with the complexed 1,4-DCB, when directing inside the cavity to lead to conformational inversion. This conclusion could be supported by the fact that the originally negative CD_{ex} intensity in dichloromethane was further enhanced rather than inverted upon the gradual addition of 1,4-DCB to a solution of **1a** (**Supplementary Figure S23**). However, for **2a** and **2b**, which possess aliphatic sidearms, no solvent-/complexation-driven S_p to R_p chirality switching could be observed (ESI, **Supplementary Figures S21, S22**). We ascribe this to the flexible aliphatic sidearm in **2a**/**2b**, which will not bring significant steric interaction with the complexed guest/solvent molecules.

We have demonstrated that temperature variation could also cause chiroptical switching of bicyclic pillar[n]arenes due to the relatively large entropy changes between the self-included and self-excluded conformations. Variation temperature CD of **1a** was measured in different solvents, which, however, showed only the intensity's variation to a certain extent (ESI, **Supplementary Figures S16–S19**) while the CD sign was never inverted. Similar was true with other chiral **EtP4Q1** derivatives, suggesting a small entropy difference between diastereomeric conformers.

CONCLUSION

In summary, we synthesized a series of new chiral amines functionalized pillar[4]arene[1]quinones, which showed unique chiroptical properties. In particular, **1a** showed strong CD signals at the CT absorption band with an unprecedented high anisotropy *g* factor of up to −0.018. Interestingly, we found that the pillar[4]arene[1]quinone having a benzene sidearm showed solvent- and complexation-driven chirality inversion, while no chirality inversion could be observed with the analogs having aliphatic sidearm. The present results opened a new window for synthesizing pillar[n]arene-based stimuli-responsive chiral molecular devices and provide a promising potential for absolute asymmetric synthesis of pillararene-based derivatives.

DATA AVAILABILITY STATEMENT

The original contributions presented in the study are included in the article/**Supplementary Material**; further inquiries can be directed to the corresponding authors.

AUTHOR CONTRIBUTIONS

CY contributed to the design of the experiment, analysis of the results, and manuscript revision. WW was responsible for advising the project and review the manuscript. ZY advised on data analysis. JY, JJ, TZ, and CL were responsible for experimental studies on synthesizing and characterizing the target compounds and prepared the manuscript. All authors contributed to the manuscript and approved the submitted version.

FUNDING

We acknowledge the support of this work by the National Natural Science Foundation of China (No. 92056116, 21871194, 21971169, 21572142), National Key Research and Development Program of China (No. 2017YFA0505903), Science & Technology Department of Sichuan Province (2019YJ0160, 2019YJ0090, 2017SZ0021), and Fundamental Research Funds for the Central Universities (20826041D4117); compound characterization was obtained with the support of the Comprehensive Training Platform of Specialized Laboratory, College of Chemistry and Prof. Peng Wu of Analytical & Testing Center, Sichuan University, which is greatly appreciated.

SUPPLEMENTARY MATERIAL

The Supplementary Material for this article can be found online at: https://www.frontiersin.org/articles/10.3389/fchem.2021.713305/full#supplementary-material

REFERENCES

Almeida Barbosa, L. C., Alves Pereira, U., Alvares Maltha, C. R., Ricardo Teixeira, R., Moreira Valente, V. M., Oliveira Ferreira, J. R., et al. (2010). Synthesis and Biological Evaluation of 2,5-Bis(alkylamino)-1,4-Benzoquinones. *Molecules* 15, 5629–5643. doi:10.3390/molecules15085629

Borovkov, V. V., Harada, T., Hembury, G. A., Inoue, Y., and Kuroda, R. (2003a). Solid-State Supramolecular Chirogenesis: High Optical Activity and Gradual Development of Zinc Octaethylporphyrin Aggregates. *Angew. Chem. Int. Ed.* 42, 1746–1749. doi:10.1002/anie.200250524

Borovkov, V. V., Hembury, G. A., and Inoue, Y. (2003b). The Origin of Solvent-Controlled Supramolecular Chirality Switching in a Bis(Zinc Porphyrin) System. *Angew. Chem. Int. Ed.* 42, 5310–5314. doi:10.1002/anie.200352493

Chen, L., Si, W., Zhang, L., Tang, G., Li, Z.-T., and Hou, J.-L. (2013). Chiral Selective Transmembrane Transport of Amino Acids through Artificial Channels. *J. Am. Chem. Soc.* 135, 2152–2155. doi:10.1021/ja312704e

Chen, Y., Fu, L., Sun, B., Qian, C., Wang, R., Jiang, J., et al. (2020). Competitive Selection of Conformation Chirality of Water-Soluble Pillar[5]arene Induced by Amino Acid Derivatives. *Org. Lett.* 22, 2266–2270. doi:10.1021/acs.orglett.0c00468

Chen, Z., Wang, Q., Wu, X., Li, Z., and Jiang, Y.-B. (2015). Optical Chirality Sensing Using Macrocycles, Synthetic and Supramolecular Oligomers/polymers, and Nanoparticle Based Sensors. *Chem. Soc. Rev.* 44, 4249–4263. doi:10.1039/c4cs00531g

Corra, S., de Vet, C., Groppi, J., La Rosa, M., Silvi, S., Baroncini, M., et al. (2019). Chemical On/Off Switching of Mechanically Planar Chirality and Chiral Anion Recognition in a [2]Rotaxane Molecular Shuttle. *J. Am. Chem. Soc.* 141, 9129–9133. doi:10.1021/jacs.9b00941

Crassous, J. (2009). Chiral Transfer in Coordination Complexes: Towards Molecular Materials. *Chem. Soc. Rev.* 38, 830–845. doi:10.1039/B806203J

De Poli, M., Zawodny, W., Quinonero, O., Lorch, M., Webb, S. J., and Clayden, J. (2016). Conformational Photoswitching of a Synthetic Peptide Foldamer Bound Within a Phospholipid Bilayer. *Science* 352, 575–580. doi:10.1126/science.aad8352

Fan, C., Wu, W., Chruma, J. J., Zhao, J., and Yang, C. (2016). Enhanced Triplet-Triplet Energy Transfer and Upconversion Fluorescence Through Host-Guest Complexation. *J. Am. Chem. Soc.* 138, 15405–15412. doi:10.1021/jacs.6b07946

Fan, C., Yao, J., Li, G., Guo, C., Wu, W., Su, D., et al. (2019). Precise Manipulation of Temperature-Driven Chirality Switching of Molecular Universal Joints Through Solvent Mixing. *Chem. Eur. J.* 25, 12526–12537. doi:10.1002/chem.201902676

Gao, W., Zhang, Z., Li, P.-F., Tang, Y.-Y., Xiong, R.-G., Yuan, G., et al. (2017). Chiral Molecular Ferroelectrics with Polarized Optical Effect and Electroresistive Switching. *ACS Nano* 11, 11739–11745. doi:10.1021/acsnano.7b07090

Goldup, S. M. (2016). A Chiral Catalyst with a Ring to it. *Nat. Chem* 8, 404–406. doi:10.1038/nchem.2509

Guo, S., Song, Y., He, Y., Hu, X.-Y., and Wang, L. (2018). Highly Efficient Artificial Light-Harvesting Systems Constructed in Aqueous Solution Based on Supramolecular Self-Assembly. *Angew. Chem. Int. Ed.* 57, 3163–3167. doi:10.1002/anie.201800175

Han, C., Zhang, Z., Yu, G., and Huang, F. (2012). Syntheses of a Pillar[4]arene[1]quinone and a Difunctionalized Pillar[5]arene by Partial Oxidation. *Chem. Commun.* 48, 9876–9878. doi:10.1039/C2CC35498E

Hao, T., Yang, Y., Liang, W., Fan, C., Wang, X., Wu, W., et al. (2021). Trace Mild Acid-Catalysed Z → E Isomerization of Norbornene-Fused Stilbene Derivatives: Intelligent Chiral Molecular Photoswitches with Controllable Self-Recovery. *Chem. Sci.* 12, 2614–2622. doi:10.1039/D0SC05213B

Hembury, G. A., Borovkov, V. V., and Inoue, Y. (2008). Chirality-Sensing Supramolecular Systems. *Chem. Rev.* 108, 1–73. doi:10.1021/cr050005k

Ji, J., Li, Y., Xiao, C., Cheng, G., Luo, K., Gong, Q., et al. (2020a). Supramolecular Enantiomeric and Structural Differentiation of Amino Acid Derivatives with Achiral Pillar[5]arene Homologs. *Chem. Commun.* 56, 161–164. doi:10.1039/C9CC08541F

Ji, J., Wu, W., Wei, X., Rao, M., Zhou, D., Cheng, G., et al. (2020b). Synergetic Effects in the Enantiodifferentiating Photocyclodimerization of 2-anthracenecarboxylic Acid Mediated by β-cyclodextrin-pillar[5]arene-hybridized Hosts. *Chem. Commun.* 56, 6197–6200. doi:10.1039/D0CC02055A

Jie, K., Zhou, Y., Li, E., and Huang, F. (2018). Nonporous Adaptive Crystals of Pillararenes. *Acc. Chem. Res.* 51, 2064–2072. doi:10.1021/acs.accounts.8b00255

Jung, J. H., Kobayashi, H., Masuda, M., Shimizu, T., and Shinkai, S. (2001). Helical Ribbon Aggregate Composed of a Crown-Appended Cholesterol Derivative Which Acts as an Amphiphilic Gelator of Organic Solvents and as a Template for Chiral Silica Transcription. *J. Am. Chem. Soc.* 123, 8785–8789. doi:10.1021/ja010508h

Kanagaraj, K., Liang, W., Rao, M., Yao, J., Wu, W., Cheng, G., et al. (2020). pH-Controlled Chirality Inversion in Enantiodifferentiating Photocyclodimerization of 2-Antharacenecarboxylic Acid Mediated by γ-Cyclodextrin Derivatives. *Org. Lett.* 22, 5273–5278. doi:10.1021/acs.orglett.0c01194

Kiruthika, J., Srividhya, S., and Arunachalam, M. (2020). Anion-Responsive Pseudo[3]rotaxane from a Difunctionalized Pillar[4]arene[1]quinone and a Bis-Imidazolium Cation. *Org. Lett.* 22, 7831–7836. doi:10.1021/acs.orglett.0c02710

Lai, H., Zhao, T., Deng, Y., Fan, C., Wu, W., and Yang, C. (2019). Assembly-enhanced Triplet-Triplet Annihilation Upconversion in the Aggregation Formed by Schiff-Base Pt(II) Complex Grafting-Permethyl-β-CD and 9, 10-diphenylanthracence Dimer. *Chin. Chem. Lett.* 30, 1979–1983. doi:10.1016/j.cclet.2019.09.009

Lee, E., Ju, H., Park, I.-H., Jung, J. H., Ikeda, M., Kuwahara, S., et al. (2018). pseudo[1]Catenane-Type Pillar[5]thiacrown Whose Planar Chiral Inversion Is Triggered by Metal Cation and Controlled by Anion. *J. Am. Chem. Soc.* 140, 9669–9677. doi:10.1021/jacs.8b05751

Li, E., Jie, K., Fang, Y., Cai, P., and Huang, F. (2020). Transformation of Nonporous Adaptive Pillar[4]arene[1]quinone Crystals into Fluorescent Crystals Via Multi-step Solid-Vapor Postsynthetic Modification for Fluorescence Turn-On Sensing of Ethylenediamine. *J. Am. Chem. Soc.* 142, 15560–15568. doi:10.1021/jacs.0c07482

Li, E., Jie, K., Zhou, Y., Zhao, R., and Huang, F. (2018). Post-synthetic Modification of Nonporous Adaptive Crystals of Pillar[4]arene[1]quinone by Capturing Vaporized Amines. *J. Am. Chem. Soc.* 140, 15070–15079. doi:10.1021/jacs.8b10192

Li, G., Fan, C., Cheng, G., Wu, W., and Yang, C. (2019). Synthesis, Enantioseparation and Photophysical Properties of Planar-Chiral Pillar[5]arene Derivatives Bearing Fluorophore Fragments. *Beilstein J. Org. Chem.* 15, 1601–1611. doi:10.3762/bjoc.15.164

Li, Q., Li, X., Ning, L., Tan, C.-H., Mu, Y., and Wang, R. (2019). Hyperfast Water Transport through Biomimetic Nanochannels from Peptide-Attached (pR)-Pillar[5]arene. *Small* 15, 1804678. doi:10.1002/smll.201804678

Liang, H., Hua, B., Xu, F., Gan, L.-S., Shao, L., and Huang, F. (2020). Acid/Base-Tunable Unimolecular Chirality Switching of a Pillar[5]azacrown Pseudo[1]Catenane. *J. Am. Chem. Soc.* 142, 19772–19778. doi:10.1021/jacs.0c10570

Liu, C., Yao, J., Xiao, C., Zhao, T., Selvapalam, N., Zhou, C., et al. (2021). Electrochemiluminescent Chiral Discrimination with a Pillar[5]arene Molecular Universal Joint-Coordinated Ruthenium Complex. *Org. Lett.* 23, 3885–3890. doi:10.1021/acs.orglett.1c01016

Liu, M., Zhang, L., and Wang, T. (2015). Supramolecular Chirality in Self-Assembled Systems. *Chem. Rev.* 115, 7304–7397. doi:10.1021/cr500671p

Liu, R., Zhang, Y., Wu, W., Liang, W., Huang, Q., Yu, X., et al. (2019). Temperature-driven Braking of γ-cyclodextrin-curcubit[6]uril-cowheeled [4]rotaxanes. *Chin. Chem. Lett.* 30, 577–581. doi:10.1016/j.cclet.2018.12.002

Lou, X. Y., and Yang, Y. W. (2020). Pillar[N]arene-Based Supramolecular Switches in Solution and on Surfaces. *Adv. Mater.* 32, 2003263. doi:10.1002/adma.202003263

Lv, Y., Xiao, C., and Yang, C. (2018). A Pillar[5]arene-Calix[4]pyrrole Enantioselective Receptor for Mandelate Anion Recognition. *New J. Chem.* 42, 19357–19359. doi:10.1039/C8NJ04802A

Ma, J., Yan, H., Quan, J., Bi, J., Tian, D., and Li, H. (2019). Enantioselective Dynamic Self-Assembly of Histidine Droplets on Pillar[5]arene-Modified Interfaces. *ACS Appl. Mater. Inter.* 11, 1665–1671. doi:10.1021/acsami.8b18202

Martini, C. M., and Nachod, F. C. (1951). Absorption Spectra of Some Substituted Benzoquinones. *J. Am. Chem. Soc.* 73, 2953–2954. doi:10.1021/ja01150a522

Mi, Y., Ma, J., Liang, W., Xiao, C., Wu, W., Zhou, D., et al. (2021). Guest-Binding-Induced Interhetero Hosts Charge Transfer Crystallization: Selective

Coloration of Commonly Used Organic Solvents. *J. Am. Chem. Soc.* 143, 1553–1561. doi:10.1021/jacs.0c11833

Mi, Y., Yao, J., Ma, J., Dai, L., Xiao, C., Wu, W., et al. (2020). Fulleropillar[4]arene: The Synthesis and Complexation Properties. *Org. Lett.* 22, 2118–2123. doi:10.1021/acs.orglett.9b04607

Mori, T., and Inoue, Y. (2005). Circular Dichroism of a Chiral Tethered Donor-Acceptor System: Enhanced Anisotropy Factors in Charge-Transfer Transitions by Dimer Formation and by Confinement. *Angew. Chem. Int. Ed.* 44, 2582–2585. doi:10.1002/anie.200462071

Mori, T., Ko, Y. H., Kim, K., and Inoue, Y. (2006). Circular Dichroism of Intra- and Intermolecular Charge-Transfer Complexes. Enhancement of Anisotropy Factors by Dimer Formation and by Confinement. *J. Org. Chem.* 71, 3232–3247. doi:10.1021/jo0602672

Nakashima, H., Koe, J. R., Torimitsu, K., and Fujiki, M. (2001). Transfer and Amplification of Chiral Molecular Information to Polysilylene Aggregates. *J. Am. Chem. Soc.* 123, 4847–4848. doi:10.1021/ja010119n

Ogoshi, T., Kanai, S., Fujinami, S., Yamagishi, T.-a., and Nakamoto, Y. (2008). para-Bridged Symmetrical Pillar[5]arenes: Their Lewis Acid Catalyzed Synthesis and Host-Guest Property. *J. Am. Chem. Soc.* 130, 5022–5023. doi:10.1021/ja711260m

Ogoshi, T., Kitajima, K., Aoki, T., Fujinami, S., Yamagishi, T.-a., and Nakamoto, Y. (2010). Synthesis and Conformational Characteristics of Alkyl-Substituted Pillar[5]arenes. *J. Org. Chem.* 75, 3268–3273. doi:10.1021/jo100273n

Ogoshi, T., Shiga, R., Yamagishi, T.-a., and Nakamoto, Y. (2011). Planar-Chiral Pillar[5]arene: Chiral Switches Induced by Multiexternal Stimulus of Temperature, Solvents, and Addition of Achiral Guest Molecule. *J. Org. Chem.* 76, 618–622. doi:10.1021/jo1021508

Pan, S., Ni, M., Mu, B., Li, Q., Hu, X.-Y., Lin, C., et al. (2015). Well-Defined Pillararene-Based Azobenzene Liquid Crystalline Photoresponsive Materials and Their Thin Films with Photomodulated Surfaces. *Adv. Funct. Mater.* 25, 3571–3580. doi:10.1002/adfm.201500942

Peng, C., Liang, W., Ji, J., Fan, C., Kanagaraj, K., Wu, W., et al. (2021). Pyrene-tiaraed Pillar[5]arene: Strong Intramolecular Excimer Emission Applicable for Photo-Writing. *Chin. Chem. Lett.* 32, 345–348. doi:10.1016/j.cclet.2020.03.079

Saito, H., Mori, T., Wada, T., and Inoue, Y. (2004). Diastereoselective [2 + 2] Photocycloaddition of Stilbene to Chiral Fumarate. Direct versus Charge-Transfer Excitation. *J. Am. Chem. Soc.* 126, 1900–1906. doi:10.1021/ja0370140

Shu, X., Chen, S., Li, J., Chen, Z., Weng, L., Jia, X., et al. (2012). Highly Effective Binding of Neutral Dinitriles by Simple Pillar[5]arenes. *Chem. Commun.* 48, 2967–2969. doi:10.1039/C2CC00153E

Shurpik, D. N., Padnya, P. L., Evtugyn, V. G., Mukhametzyanov, T. A., Khannanov, A. A., Kutyreva, M. P., et al. (2016). Synthesis and Properties of Chiral Nanoparticles Based on (pS)- and (pR)-Decasubstituted Pillar[5]arenes Containing Secondary Amide Fragments. *RSC Adv.* 6, 9124–9131. doi:10.1039/C5RA25562G

Strutt, N. L., Fairen-Jimenez, D., Iehl, J., Lalonde, M. B., Snurr, R. Q., Farha, O. K., et al. (2012). Incorporation of an A1/A2-Difunctionalized Pillar[5]arene into a Metal-Organic Framework. *J. Am. Chem. Soc.* 134, 17436–17439. doi:10.1021/ja3082523

Strutt, N. L., Zhang, H., Schneebeli, S. T., and Stoddart, J. F. (2014a). Amino-Functionalized Pillar[5]arene. *Chem. Eur. J.* 20, 10996–11004. doi:10.1002/chem.201403235

Strutt, N. L., Zhang, H., and Stoddart, J. F. (2014b). Enantiopure Pillar[5]arene Active Domains within a Homochiral Metal-Organic Framework. *Chem. Commun.* 50, 7455–7458. doi:10.1039/C4CC02559H

Wang, H.-J., Zhang, H.-Y., Zhang, H.-Y., Liu, G., Dai, X., Wu, H., et al. (2020). Guest-induced Supramolecular Chirality Transfer in [2]pseudorotaxanes: Experimental and Computational Study. *Org. Biomol. Chem.* 18, 7649–7655. doi:10.1039/D0OB01347A

Wang, K., Jordan, J. H., Velmurugan, K., Tian, X., Zuo, M., Hu, X. Y., et al. (2021). Role of Functionalized Pillararene Architectures in Supramolecular Catalysis. *Angew. Chem. Int. Ed.* 60, 9205–9214. doi:10.1002/anie.202010150

Wang, X., Jia, F., Yang, L.-P., Zhou, H., and Jiang, W. (2020). Conformationally Adaptive Macrocycles with Flipping Aromatic Sidewalls. *Chem. Soc. Rev.* 49, 4176–4188. doi:10.1039/D0CS00341G

Xiao, C., Liang, W., Wu, W., Kanagaraj, K., Yang, Y., Wen, K., et al. (2019). Resolution and Racemization of a Planar-Chiral A1/A2-Disubstituted Pillar[5]arene. *Symmetry* 11, 773. doi:10.3390/sym11060773

Xiao, C., Wu, W., Liang, W., Zhou, D., Kanagaraj, K., Cheng, G., et al. (2020). Redox-Triggered Chirality Switching and Guest-Capture/Release with a Pillar[6]arene-Based Molecular Universal Joint. *Angew. Chem. Int. Ed.* 59, 8094–8098. doi:10.1002/anie.201916285

Xing, P., and Zhao, Y. (2018). Controlling Supramolecular Chirality in Multicomponent Self-Assembled Systems. *Acc. Chem. Res.* 51, 2324–2334. doi:10.1021/acs.accounts.8b00312

Xue, M., Yang, Y., Chi, X., Zhang, Z., and Huang, F. (2012). Pillararenes, A New Class of Macrocycles for Supramolecular Chemistry. *Acc. Chem. Res.* 45, 1294–1308. doi:10.1021/ar2003418

Yang, C., and Inoue, Y. (2014). Supramolecular Photochirogenesis. *Chem. Soc. Rev.* 43, 4123–4143. doi:10.1039/C3CS60339C

Yao, J., Mizuno, H., Xiao, C., Wu, W., Inoue, Y., Yang, C., et al. (2021a). Pressure-driven, Solvation-Directed Planar Chirality Switching of Cyclophano-Pillar[5]arenes (Molecular Universal Joints). *Chem. Sci.* 12, 4361–4366. doi:10.1039/D0SC06988D

Yao, J., Wu, W., Liang, W., Feng, Y., Zhou, D., Chruma, J. J., et al. (2017). Temperature-Driven Planar Chirality Switching of a Pillar[5]arene-Based Molecular Universal Joint. *Angew. Chem. Int. Ed.* 56, 6869–6873. doi:10.1002/anie.201702542

Yao, J., Wu, W., Xiao, C., Su, D., Zhong, Z., Mori, T., et al. (2021b). Overtemperature-protection Intelligent Molecular Chiroptical Photoswitches. *Nat. Commun.* 12, 2600. doi:10.1038/s41467-021-22880-z

Zhang, J., Wang, Z., Lv, S., Zeng, X., Sun, Y., Li, H., et al. (2019). The Chiral Interfaces Fabricated by D/l-Alanine-Pillar[5]arenes for Selectively Adsorbing ctDNA. *Chem. Commun.* 55, 778–781. doi:10.1039/C8CC09696A

Zhang, L., Qin, L., Wang, X., Cao, H., and Liu, M. (2014). Supramolecular Chirality in Self-Assembled Soft Materials: Regulation of Chiral Nanostructures and Chiral Functions. *Adv. Mater.* 26, 6959–6964. doi:10.1002/adma.201305422

Zhou, J., and Tang, Y. (2005). The Development and Application of Chiral Trisoxazolines in Asymmetric Catalysis and Molecular Recognition. *Chem. Soc. Rev.* 34, 664–676. doi:10.1039/B408712G

Conflict of Interest: The authors declare that the research was conducted in the absence of any commercial or financial relationships that could be construed as a potential conflict of interest.

frontiers in Chemistry

ORIGINAL RESEARCH
published: 21 July 2021
doi: 10.3389/fchem.2021.716294

Role of Host-Guest Interaction in Understanding Polymerisation in Metal-Organic Frameworks

*A.D. Dinga Wonanke, Poppy Bennett, Lewis Caldwell and Matthew A. Addicoat**

Department of Chemistry and Forensics, Nottingham Trent University, Nottingham, United Kingdom

Metal-organic frameworks, MOFs, offer an effective template for polymerisation of polymers with precisely controlled structures within the sub-nanometre scales. However, synthetic difficulties such as monomer infiltration, detailed understanding of polymerisation mechanisms within the MOF nanochannels and the mechanism for removing the MOF template post polymerisation have prevented wide scale implementation of polymerisation in MOFs. This is partly due to the significant lack in understanding of the energetic and atomic-scale intermolecular interactions between the monomers and the MOFs. Consequently in this study, we explore the interaction of varied concentration of styrene, and 3,4-ethylenedioxythiophene (EDOT), at the surface and in the nanochannel of Zn_2(1,4-ndc)$_2$ (dabco), where 1,4-ndc = 1,4-naphthalenedicarboxylate and dabco = 1,4-diazabicyclo[2.2.2]octane. Our results showed that the interactions between monomers are stronger in the nanochannels than at the surfaces of the MOF. Moreover, the MOF-monomer interactions are strongest in the nanochannels and increase with the number of monomers. However, as the number of monomers increases, the monomers turn to bind more strongly at the surface leading to a potential agglomeration of the monomers at the surface.

Keywords: metal-organic frameworks (MOFs), polymerisation, host-guest interaction, DFTB, molecular dynamics

OPEN ACCESS

Edited by:
Tony D. James,
University of Bath, United Kingdom

Reviewed by:
Shenhui Li,
Chinese Academy of Sciences (CAS), China
Hiroyasu Yamaguchi,
Osaka University, Japan
Xin Wu,
The University of Sydney, Australia

****Correspondence:***
Matthew A. Addicoat
matthew.addicoat@ntu.ac.uk

Specialty section:
This article was submitted to Supramolecular Chemistry, a section of the journal Frontiers in Chemistry

Received: *28 May 2021*
Accepted: *05 July 2021*
Published: *21 July 2021*

Citation:
Wonanke ADD, Bennett P, Caldwell L and Addicoat MA (2021) Role of Host-Guest Interaction in Understanding Polymerisation in Metal-Organic Frameworks. Front. Chem. 9:716294. doi: 10.3389/fchem.2021.716294

1 INTRODUCTION

In recent years, the interest and effort in the synthesis, characterisation, functionalisation, modelling, and designing of novel nanoporous materials have gained a massive insurgence (Materazzi et al., 2008). This owes mostly to the fact that the properties of these materials are not only dependent on how atoms are arranged within their crystals, but also on the size and shape of their pores as well as on their specific surface area. For these reasons, nanoporous materials are heavily investigated for application in gas storage, sieving, filtration, extraction, separation, sensors, drug delivery, and electrochemical energy storage and catalysis (Bastani et al., 2013; Ma et al., 2014; Zhang et al., 2014; Forest et al., 2015; Zhang et al., 2015; Wilkerson and Ramesh, 2016; Fu et al., 2017; Rafiee and Shahebrahimi, 2017).

Hitherto, the most rapidly growing and investigated classes of nanoporous materials that hold potentials for an almost limitless range of applications are known as metal-organic frameworks, MOFs (Li et al., 1999; Yaghi et al., 2000; Yaghi et al., 2003; Mueller et al., 2006). MOFs are organic-inorganic hybrid crystalline porous materials that are formed by covalently binding metal ions or clusters, also known as secondary binding units, SBUs, with organic ligands, also known as linkers, in a variety of 2- and 3-dimensional nets or topologies (Furukawa et al., 2013; Butova et al., 2016).

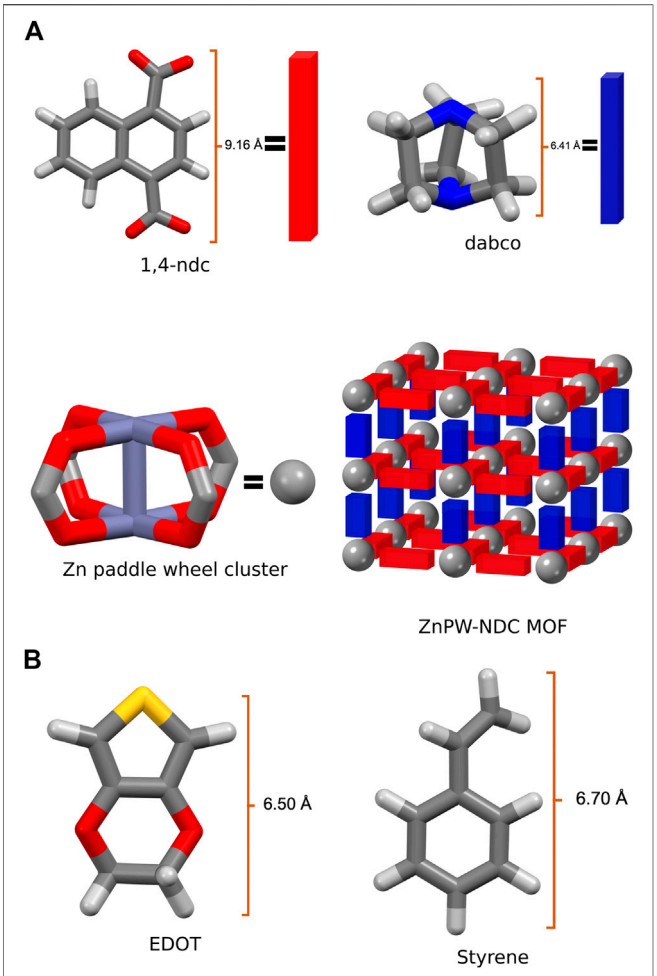

FIGURE 1 | (A) the secondary building units of Zn^2 $(1,4\text{-ndc})^2$ (dabco), represented as a net, where the organic linkers constitute the edges and the metal cluster the nodes, **(B)** Illustration of monomers EDOT and Styrene.

In general, they are materials with typical low mass densities, high internal surface area and large pore volumes. Consequently, they are exploited for several applications including (but not limited to) gas storage, filtration, extraction, separation, sensors, drug delivery, electrochemical energy storage, and catalysis (Furukawa et al., 2013; Ricco et al., 2016; Pettinari et al., 2017).

Moreover, the well-defined porous network and relatively high internal surface area have opened up new avenues for the use of MOFs as a template for various chemical reactions to obtain specific regio- and stereoisomers (Uemura et al., 2005; Liu et al., 2008; Bhakta et al., 2009; Canivet et al., 2011; Distefano et al., 2013; Lee et al., 2015; Chen et al., 2016; Ding et al., 2016; Wang et al., 2017; Mochizuki et al., 2018; Anan et al., 2019; Rivera-Torrente et al., 2019; Schmidt, 2019). Amongst these potential chemical reactions, polymerisation in MOFs has gained significant scientific interest. This is primarily because the highly designable features of MOFs result in nanochannels that can be applied as a tailor-made polymerisation system to obtain highly controlled polymer structures with long-range order. Furthermore, since the MOFs act only as a scaffold for reactions, conventional polymerisation methods can be easily employed, with little or no modification, provided that the reagents and reaction conditions do not destroy the crystal structures of the MOFs (Mochizuki et al., 2018).

So far, polymerisations in MOFs have been used to effectively control polymer molecular weight distribution, stereo-regularity (tacticity), reaction sites, and copolymer sequence (Uemura et al., 2008; Uemura et al., 2009). Consequently, this provides an attractive avenue for not only the precision synthesis of novel polymer materials but also for exploring specific properties of polymer confinement. A comprehensive review describing the state-of-the-art of polymerisation in MOFs was recently published (Schmidt, 2019).

Despite the advantages resulting from polymerisation in MOFs, there is a significant lack in conceptual understanding of how to effectively control these reactions, which consequently restrains their wide-scale application. (Uemura et al., 2009). Firstly, there is still an enormous synthetic challenge on how to effectively infiltrate the monomers in the confinement of the pores before polymerisation. Secondly, there is only very little understanding of the MOF nanochannel polymerisation mechanism, the initiation process and the propagation process. Thirdly, little is known on how the monomer interacts with the MOF framework during polymerisation as well as the mechanism for removing the MOF template (Wang et al., 2017).

The first evidence of polymerisation in MOFs was from the pioneering work of Uemura and co-workers on the radical polymerisation of styrene (Uemura et al., 2005). In this study, the styrene monomer was shown to fully infiltrate the nanochannel by immersing the MOF in the liquid monomer, while excess styrene at the external surface was removed by subjecting the host crystals to reduced pressure. The result from powder X-ray diffraction studies showed that the newly synthesised polymer was fully encapsulated in the nanochannel of the MOF. In a recent study, (Wang et al., 2017), Wang and co-workers performed an oxidative polymerisation of 3,4-ethylenedioxythiophene, EDOT, in a MOF. This time, the authors encountered a significant challenge in fully infiltrating the monomer into the MOF nanochannels and results from this study showed an agglomeration of monomers at the surface of the MOF.

TABLE 1 | UFF-Zenorg binding energies for the most stable MOF⊃monomer composites.

BE (kJ mol^{-1})	Nanochannel		Surface	
No of monomers	**ZnPW⊃EDOT**	**ZnPW⊃styrene**	**MOF⊃EDOT**	**MOF⊃styrene**
1	−121.55	−107.96	−80.28	−114.74
2	−260.49	−228.96	−152.44	−152.99
3	−422.30	−362.63	−198.55	−228.34

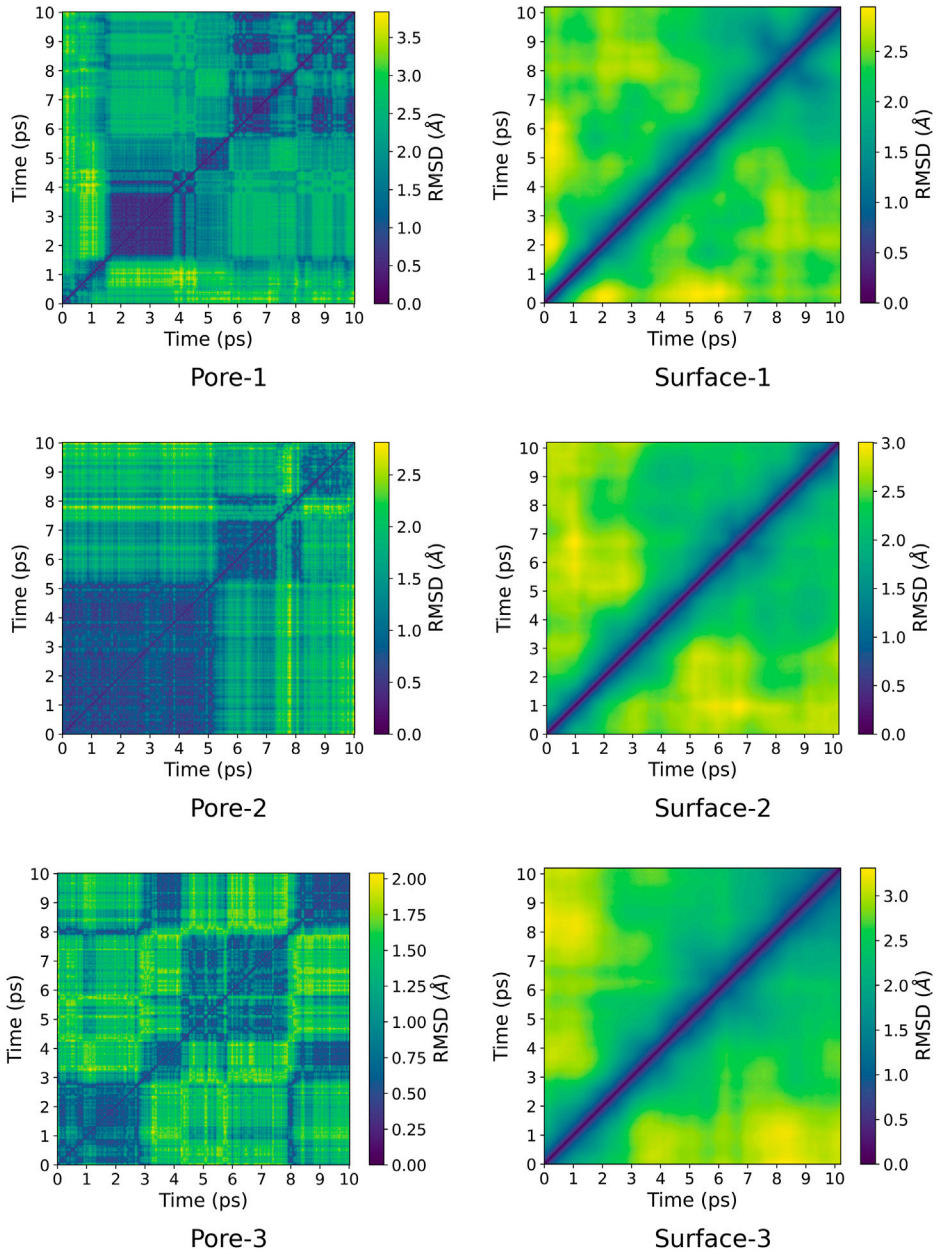

FIGURE 2 | Pairwise RMSD plot for ZnPW⊃EDOT interactions for both nano-channel and surface interaction.The colour gradient corresponds to the RMSD in Å. The labels "Pore" and "Surface" correspond to nano-channel and surface interactions respectively and the numbers after the hyphen correspond to the number of monomer(s) present.

An in-depth understanding of the energetic and atomic-scale intermolecular interactions between the monomers both at the surface and in the nanochannels of the pores would be a significant step towards understanding how to fully control these reactions. Consequently in this study, we explore the interaction of styrene and EDOT, at the surface and in the nanochannel of the MOF, $Zn_2(1,4\text{-ndc})_2$ (dabco), where 1,4-ndc = 1,4-naphthalenedicarboxylate and dabco = 1,4-diazabicyclo [2.2.2]octane. $Zn_2(1,4\text{-ndc})_2$ (dabco), hereafter referred to as ZnPW-NDC MOF, is a MOF possessing a zinc paddlewheel building block on which the naphthalenedicarboxylate linkers are joined to form two-dimensional square grids, which are pillared by the dabco ligands as shown in **Figure 1** (Klein et al., 2012).

2 METHODS

To fully explore the intermolecular interactions between the monomers and the ZnPW-NDC MOF, 100 ZnPW-NDC

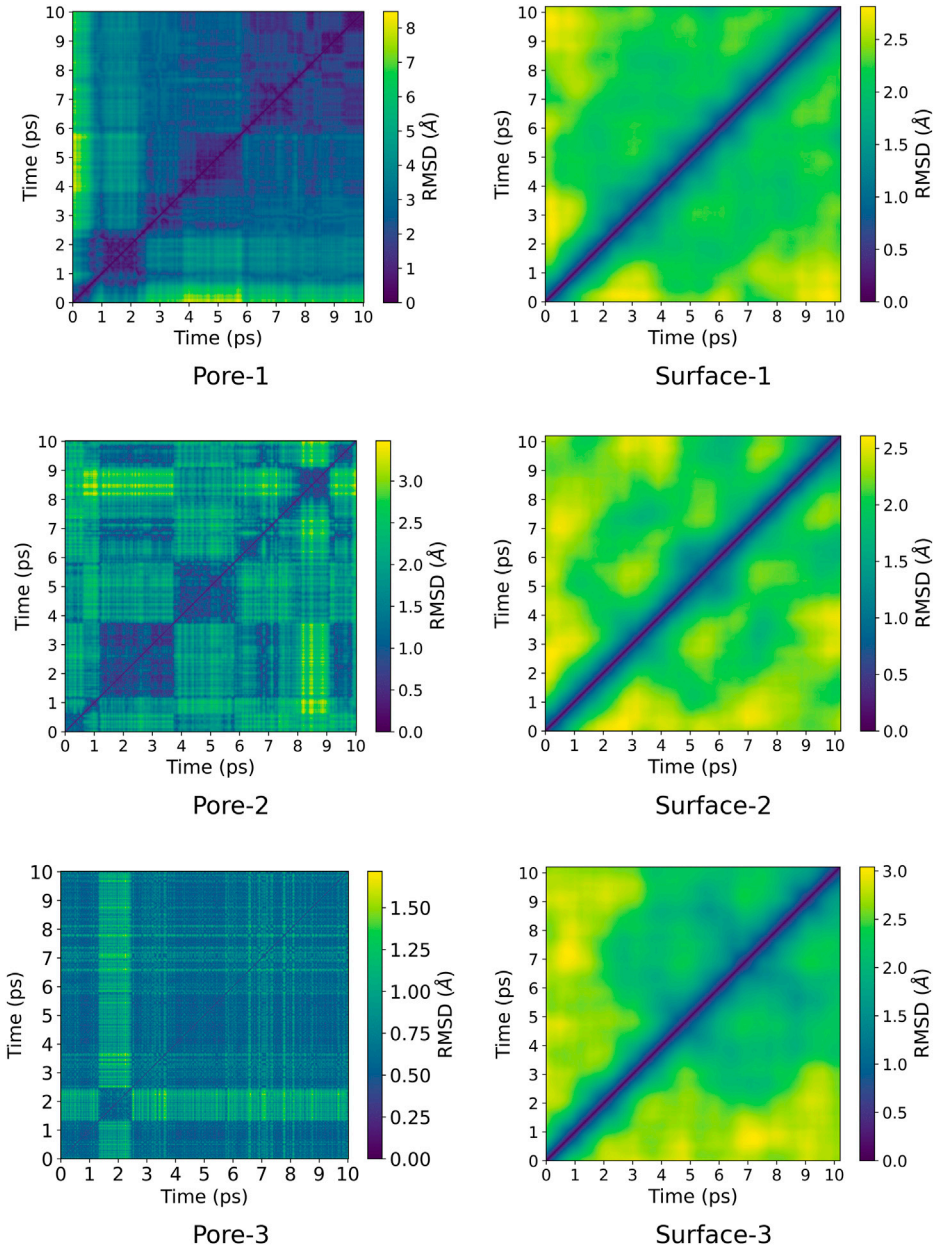

FIGURE 3 | Pairwise RMSD plot for ZnPW⊃styrene interactions for both nano-channel and surface interaction.The colour gradient corresponds to the RMSD in Å. The labels "Pore" and "Surface" correspond to nano-channel and surface interactions respectively and the numbers after the hyphen correspond to the number of monomer(s) present.

MOF⊃monomers complexes were generated for ZnPW-NDC MOF⊃EDOT and ZnPW-NDC MOF⊃styrene complexes using one, two and three monomers both at the interior of the nanochannel and on the surface of the MOF. The ZnPW-NDC MOF lattice was constructed using the Automatic Topological Generator for Framework Structures package, implemented by one of us (Addicoat et al., 2014) The ZnPW-NDC MOF surface was then constructed by building a 3 × 3 × 1 supercell from and converting to a 2D slab by truncating the *c*-axis and capping with water. MOF⊃monomers complexes were then generated using a random structure generator algorithm, Kick (Addicoat et al., 2013), as described in the Electronic Supporting Information, ESI†. Once generated, all the complexes were optimised using Density Functional Tight Binding (DFTB) with znorg parameter set including UFF dispersion correction as implemented in the Amsterdam

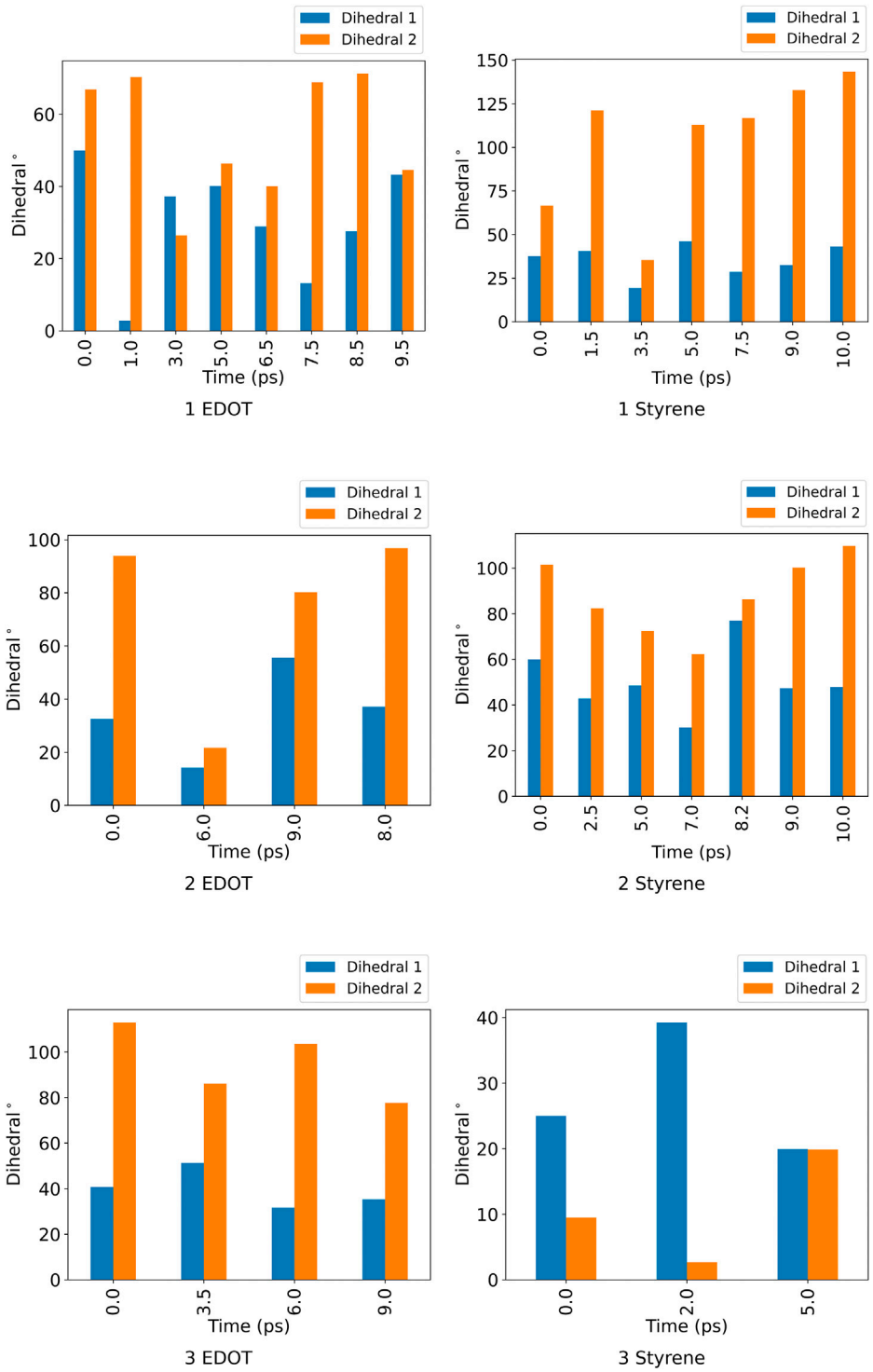

FIGURE 4 | Dihedral angles for the two pairs positionally distinct ndc linker in the unit cell for the distinct conformational states of ZnPW⊃EDOT and ZnPW⊃styrene motifs for nano-channel interaction.

modelling suite, AMS, package version ADF 2019.305 (Hourahine et al., 2020; Moreira et al., 2009; Rappe et al., 1992; teVelde et al., 2001). Once optimised, the lowest energy complexes were selected and used to compute the MOF⊃monomers binding energies, *BE*, using the formula in **Eq. 1**.

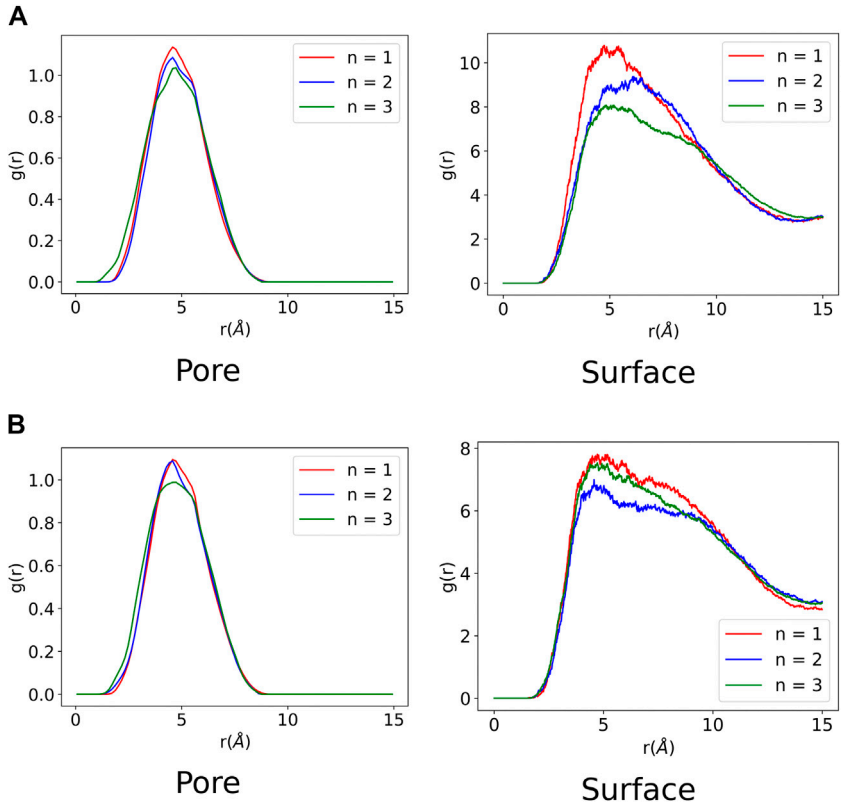

FIGURE 5 | Radial distribution function of ZnPW⊃monomer(s) interactions computed from each molecular dynamic trajectory. *n* corresponds to the number of monomer(s) present in the trajectory. The labels "Pore" and "Surface" correspond to nanochannel and surface interactions respectively. **(A)** Nanochannel and surface ZnPW_EDOT radial distribution function. **(B)** Nanochannel and surface ZnPW_styrene radial distribution function.

$$BE = E_{MOF \supset monomers} - (E_{MOF} + xE_{Monomer}) \quad (1)$$

$E_{MOF \supset monomers}$ is the ground state optimised energy of the MOF⊃monomer complex. E_{MOF} *is the ground state optimised energy of the isolated MOF.* $E_{Monomer}$ is the ground state optimised energy of the monomer and finally, x represents the number of monomers (x = 1, 2 or 3) present in each complex.

A molecular dynamics, MD, simulation was then performed on all the optimal MOF⊃monomer composites in order to gauge the intermolecular interaction between the MOF and the monomer over a given time period. The MD simulations were computed using the same znorg parameter set at 343.1 K, 1 atm in the isothermal-isobaric (NPT) ensemble as implemented in DFTB+ program package (Hourahine et al., 2020). The temperature and pressure in this ensemble were maintained using Nosé-Hoover thermostat and the Berendsen barostat respectively (Berendsen et al., 1984; Martyna et al., 1996). The coupling strength used in thermostat corresponded to the maximum frequency for each composite meanwhile a decay constant of 10 femtoseconds was used for the Berendsen barostat. A time step of 1 femtosecond was used and the trajectory was saved for every time step. A total of 100,200 MD time steps were performed for each of the optimal MOF⊃monomer composites constituting the nanochannels. Meanwhile 10,200 MD time steps were performed for the composites constituting the surface.

All computational data corresponding to detailed energetics, intermolecular interactions and MD trajectories can be freely downloaded from http://doi.org/10.5281/zenodo.4382475.

3 RESULTS AND DISCUSSIONS

3.1 Binding Energy Analysis

The binding energies for the most stable MOF⊃monomer(s) composites are presented in **Table 1**. The magnitude of these binding energies is a direct measure of the strength of intermolecular interactions between the MOF and the monomers. Hence it can be inferred from these results that all the monomers have an obvious attractive interaction with the ZnPW both in the nanochannel and at the surface.

In all cases, the strength of this intermolecular interaction increases with the number of monomers. The interactions are generally observed to be stronger in the nanochannels with ZnPW⊃EDOT showing the strongest interactions which are seen to double as the concentration of monomer increases. In the presence of one monomer, styrene is observed to bind more strongly at the surface, indicating a more favourable surface interaction at lower concentrations, possibly impacting the

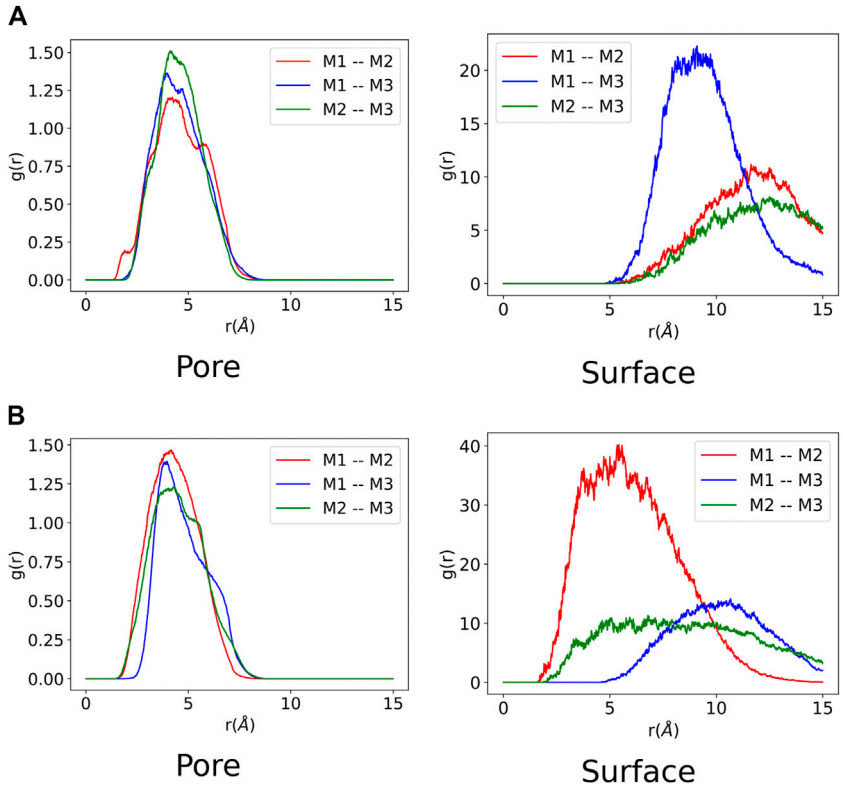

FIGURE 6 | Monomer-monomer radial distribution function from each molecular dynamic trajectory composed of three monomers. Each monomer is labelled M_i (i = 1, 2 or 3). The labels "Pore" and "Surface" correspond to interactions at the nanochannel and surface respectively. **(A)** EDOT-EDOT radial distribution function at nanochannel and surface of ZnPW. **(B)** Styrene-styrene radial distribution function at nanochannel and surface of ZnPW.

incursion of the monomer into the MOF nanochannels by blocking the surface. This significantly large stability resulting from the increase in monomer concentration could be a bottleneck when it comes to extracting the polymer from the MOF. Within the nanochannels, the increase in stability can partly be attributed to strong monomer-monomer interaction, which was further analysed from MD simulations.

3.2 Pairwise Root-Mean-Square Deviation

A pairwise root-mean-square deviation (RMSD) was performed to provide a visual inspection of how each structure changes over time. In the pairwise RMSD, we compute the RMSD of each snapshot in the trajectory with respect to all the other snapshots. The RMSD along the diagonals have values of zero, which correspond to the RMSD of a snapshot with itself. Low RMSD values at the off-diagonal regions correspond to snapshots whose structures are similar to the reference snapshot, while higher values correspond to dissimilar structures. Consequently, occupation of a given state can be observed as blocks of similar RMSDs along the diagonal. The pairwise RMSD for all the MD trajectories are presented in **Figures 2**, **3**, wherein the snapshots are converted into picoseconds, ps and RMSD presented in Ångstrom, Å.

The RMSD for every point in **Figures 2**, **3** were computed using the formula in **Eq. 2** and the python script can freely be downloaded (https://github.com/bafgreat/Pairwise-RMSD).

$$RMSD_{(r,s)} = \sqrt{\frac{1}{N}\sum_{j=1}\left|r_j - s_j\right|^2} \tag{2}$$

Here, r_j and s_j are Cartesian coordinates of atom j in configuration r and s respectively, which have been optimally aligned so that the resulting RMSD should be the minimum distance between both configurations. N is the total number of atoms in each configuration. The pairwise RMSD was calculated for every 10^{th} snapshots in the MD trajectory for the nano-channel interactions, which reduces the total number of snapshots to 10,200, leading to a significant decrease in computational cost. On the other hand, the RMSD was computed for all the snapshots in the surface interaction for which each trajectory was composed of 10,200 snapshots.

The pairwise RMSD for the nano-channels of both ZnPW⊃EDOT and ZnPW⊃styrene presented in **Figures 2**, **3** respectively, shows a series of distinct states that are sampled by the system. Here, regions of similar RMSDs are distinctively represented in blocks, corresponding to distinct conformational states. These states differ by the position of the monomer(s) in the nano-channel, as well as in the orientation of the naphthyl of the ndc linker, which determines the dimension of the pore. The

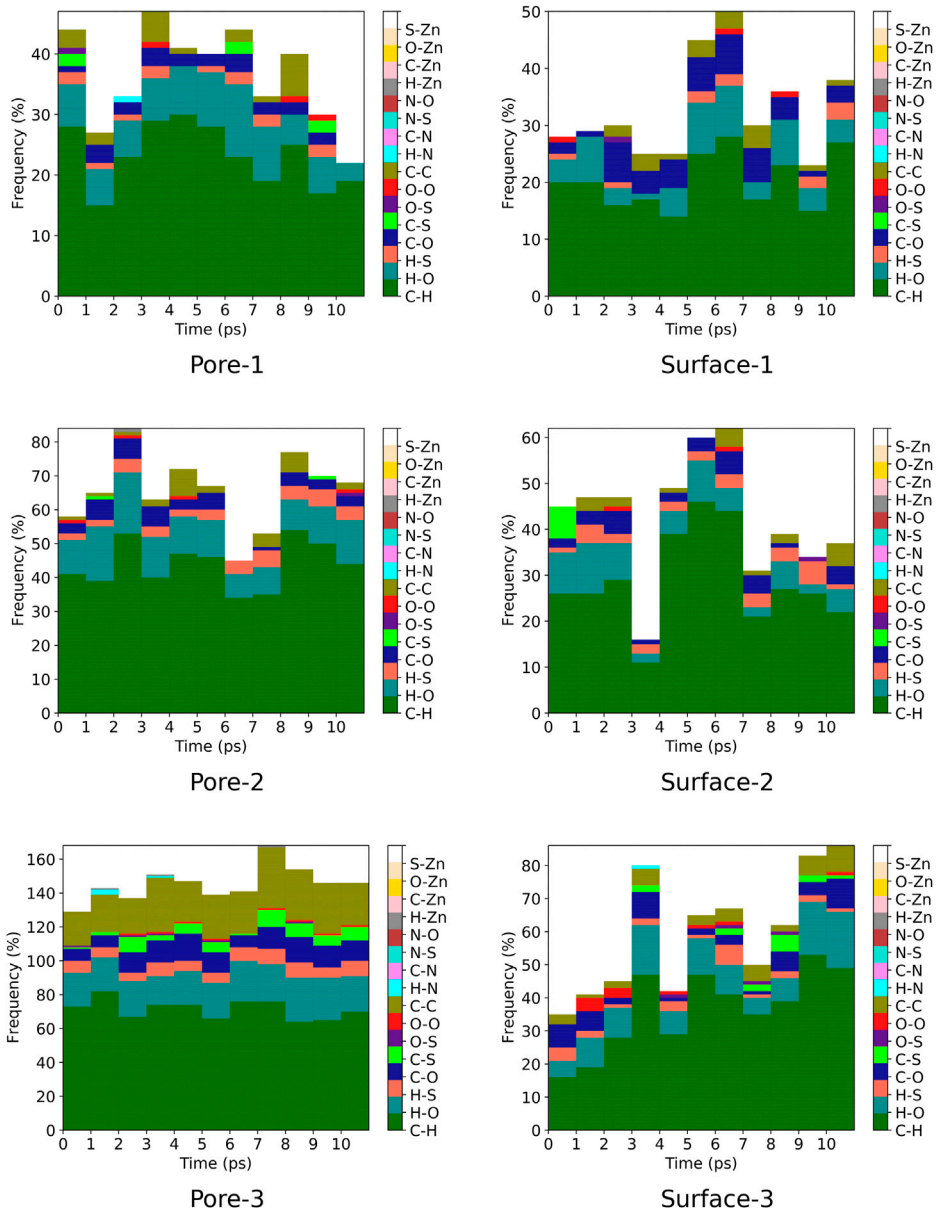

FIGURE 7 | Frequency of ZnPW⊃EDOT intermolecular distances (r < 3.5 Å) for nanochannel and surface interactions. The colour gradient corresponds to specific interatomic interactions and each column correspond to a molecular dynamic trajectory snapshot. Interactions were computed at every 10 ps for systems representing nanochannel interactions and every 1 ps for systems representing surface interactions. The labels "Pore" and "Surface" correspond to nanochannel and surface interactions respectively and the numbers after the hyphen correspond to the number of monomer(s) present.

orientations of these linkers can be determine by the computing their dihedrals with respect to the plane along the lattice coordinate on which they lie as described in the ESI. The dihedral angles for these distinct conformational states is presented in **Figure 4**.

For the ZnPW⊃EDOT system containing two monomers, **Figure 2**, the initial state persists for a longer period before transitioning into the second state. In this state, the dihedral angles formed by one of the ndc linkers are nicely aligned to enable a strong-sandwich π-π intermolecular interaction with one of the EDOT monomers, meanwhile the other monomer interacts favourably with the dabco pillar. Meanwhile, for the ZnPW⊃styerene system containing three monomers, **Figure 3**, the system visits 3 states and remains in the 3rd state for over 7 ps The dihedral angles for both positionally distinct linkers are observed to be below 20°, which results in an open pore system in which all three styrene monomer sit in the centre of the pore enhancing both monomer-monomer interactions as well as MOF-monomer interactions.

At the surface, the transitions from one conformational state to the other are far less distinct. Here, the snapshots show

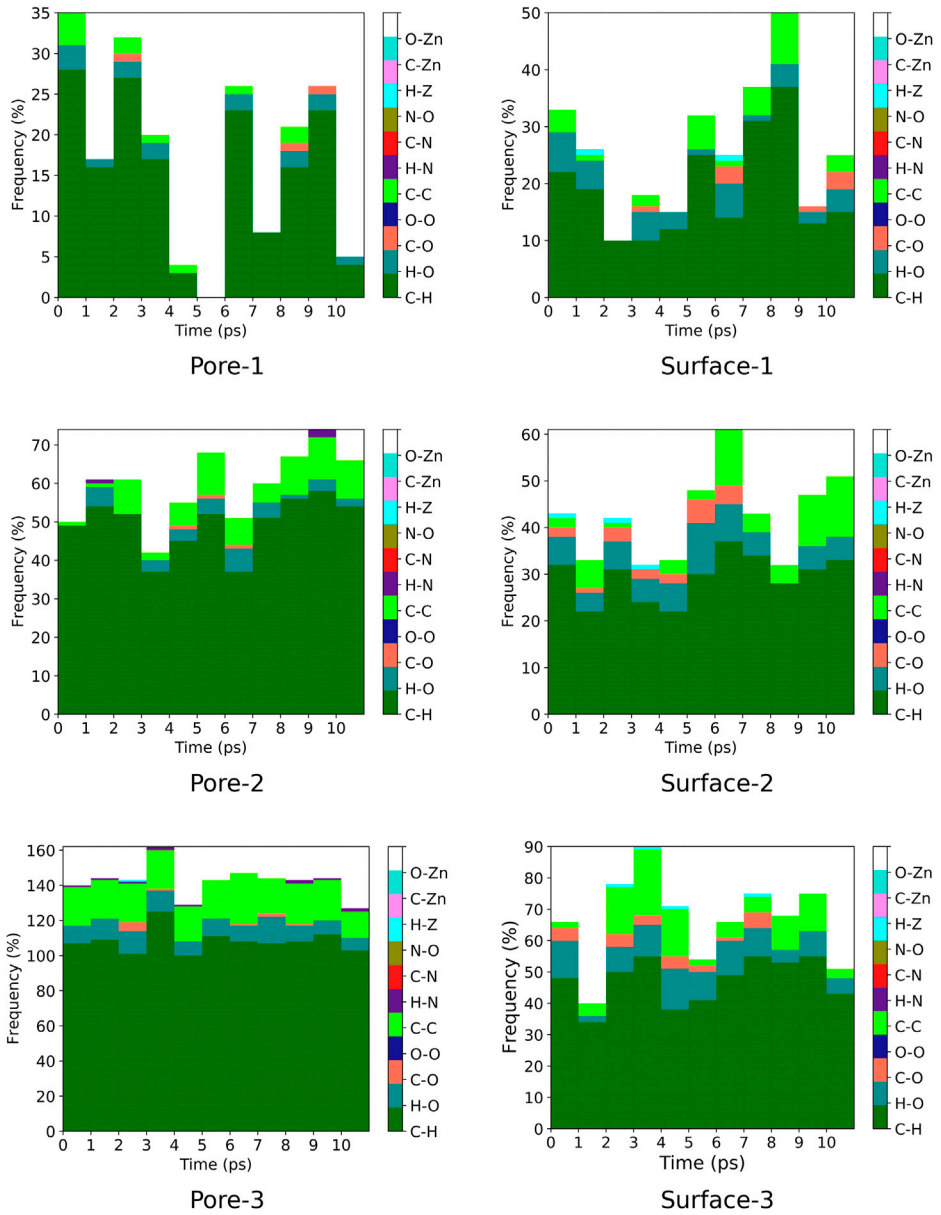

FIGURE 8 | Frequency of ZnPW⊃styrene intermolecular distances (r < 3.5 Å) for nanochannel and surface interactions. The colour gradient corresponds to specific interatomic interactions and each column correspond to a molecular dynamic trajectory snapshot. Interactions were computed at every 10 ps for systems representing nanochannel interactions and every 1 ps for systems representing surface interactions. The labels "Pore" and "Surface" correspond to nanochannel and surface interactions respectively and the numbers after the hyphen correspond to the number of monomer(s) present.

more dissimilarity across the trajectory, indicative of less favourable interactions for which the systems may want to explore for a longer time scale. In the presence of three monomers, there are few regions of similar RMSD at larger time scale.

3.3 Radial Distribution Analysis

A radial distribution function (RDF) was computed for all the MD trajectories to analyse the ZnPW-NDC MOF⊃monomer(s) and monomer–monomer intermolecular interactions. The RDF was computed using MDAnalysis program package (Michaud-Agrawal et al., 2011; Gowers et al., 2016) and an excellent description of the implementation of RDFs from MD trajectories can be found in the paper by Kohlmeyer and co-workers (Levine et al., 2011) In the RDF analysis, the distance between pairs of atoms of the interacting species in each trajectory snapshot are computed and collected into a histogram, which provides the probability distribution for the interacting species to be found at a given distance in space.

The RDF for the ZnPW-NDC MOF⊃monomer(s) and the monomer-monomer intermolecular interactions are presented in **Figures 5**, **6** and respectively.

It can be observed from **Figure 5** that all the monomers have favourable intermolecular interactions with the ZnPW both at the surface and in the nanochannels, which are within the Van der Waals intermolecular range (r < 3.5 Å). However for EDOT, it can be observed from **Figure 5A** that as the number of monomers increases to three, the number of interactions below 2Å increases both at the surface and in the nanochannel, represented by the 3 green peaks. A similar observation is seen for the surface interaction of ZnPW⊃styrene presented in **Figure 5B**. This high propensity for the formation of strong intermolecular interactions at the surfaces of ZnPW when the monomer concentrations increases can be used as a proxy for explaining the experimental difficulties encountered in infiltrating the monomers into the nanochannels (Uemura et al., 2005; Wang et al., 2017). Moreover, the strong interaction (represented by the 3 green peaks in **Figure 5A**) occurring in the nanochannel of ZnPW-NDC MOF⊃EDOT in the presence of three monomers could also explain the relative difficulties encountered during the removal of the ZnPW-NDC MOF from the PEDOT-MOF composite (Wang et al., 2017).

The monomer-monomer interactions for systems containing three monomers are presented in **Figure 6**. It can be observed for both ZnPW-NDC MOF⊃EDOT and ZnPW-NDC MOF⊃styrene that the monomers have a stronger interaction with the ZnPW-NDC MOF in the nanochannels than at the surface. At the surface of ZnPW-NDC MOF⊃EDOT in **Figure 6A**, the monomers are significantly dispersed showing very little evidence of an eventual polymerisation at the surface, which implies that the nanochannels provide an efficient platform that brings the monomer to a sufficiently close distance in order to initiate polymerisation. On the other hand, the styrene monomers show some significant interaction at the surface of the ZnPW as observed in **Figure 6B**.

3.4 Contact Analysis

A contact analysis was computed for MOF⊃monomer(s) intermolecular distances that are below 3.5 Å in each MD trajectory. The contact analysis was computed for every 1 ps for systems representing surface interactions meanwhile for systems representing nanochannel interactions, we computed intermolecular interactions for every 10 ps. The ZnPW-NDC MOF⊃monomer(s) contact analysis are plotted in **Figures 7**, **8** and the data for each of these interactions are found in the ESI†.

For the nanochannel and surface interaction of both monomers with the ZnPW-NDC MOF, the C-H, H-O and C-C are the most common interactions. These correspond to strong hydrogen-bond and hydrophobic interactions occurring between the monomers and the ZnPW. The number of these interactions are observed to increase with the concentration of monomers. In ZnPW-NDC MOF⊃EDOT systems, **Figure 7**, there is also a significant number of H-S and C-S interactions, which are known to be highly polarisable and can consequently increase the (ZnPW-NDC MOF)–EDOT electrostatic interactions (Rohwer et al., 2018).

4 CONCLUSION

In this study, we investigated the intermolecular interactions of two monomers, styrene and EDOT, with ZnPW-NDC MOF metal organic framework. It was observed for both monomers that the ZnPW-NDC MOF⊃monomer(s) intermolecular interactions are stronger in systems with higher monomer concentration for both surface and nanochannel interactions. The monomer–monomer interactions are observed to be strongest in the nanochannels, which is indicative of the nanochannel acting as an effective medium that brings monomers into close proximity therefore potentially optimising the polymerisation process. The ZnPW-NDC MOF⊃EDOT showed strong interactions at the surface of the ZnPW, which has been supported by a previous experimental study (Wang et al., 2017). This study reported an agglomeration of monomers at the surface of the ZnPW resulting in potential difficulties with fully infiltrating the monomer into the nanochannels.

DATA AVAILABILITY STATEMENT

The original contributions presented in the study are included in the article/**Supplementary Material**. All computational data corresponding to detailed energetics, intermolecular interactions and MD trajectories can be freely downloaded from http://doi.org/10.5281/zenodo.4382475. Further inquiries can be directed to the corresponding author.

AUTHOR CONTRIBUTIONS

MAA devised the study. PB and LC ran the calculations. ADDW performed md calculations, did analysis and wrote the manuscript.

FUNDING

MA thanks the EPSRC for a New Investigator award, EP/S015868/1. We also acknowledge HPC resources on THOMAS via membership of the UK's HEC Materials Chemistry Consortium, which is funded by EPSRC (EP/P020194).

SUPPLEMENTARY MATERIAL

The Supplementary Material for this article can be found online at: https://www.frontiersin.org/articles/10.3389/fchem.2021.716294/full#supplementary-material

REFERENCES

Addicoat, M. A., Coupry, D. E., and Heine, T. (2014). AuToGraFS: Automatic Topological Generator for Framework Structures. *J. Phys. Chem. A* 118 (40), 9607–9614. doi:10.1021/jp507643v

Addicoat, M. A., Fukuoka, S., Page, A. J., and Irle, S. (2013). Stochastic Structure Determination for Conformationally Flexible Heterogenous Molecular Clusters: Application to Ionic Liquids. *J. Comput. Chem.* 34 (30), 2591–2600. doi:10.1002/jcc.23420

Anan, S., Mochizuki, Y., Kokado, K., and Sada, K. (2019). Step-growth Copolymerization between an Immobilized Monomer and a mobile Monomer in Metal-Organic Frameworks. *Angew. Chem. Int. Edition* 58 (24), 8018–8023. doi:10.1002/anie.201901308

Bastani, D., Esmaeili, N., and Asadollahi, M. (2013). Polymeric Mixed Matrix Membranes Containing Zeolites as a Filler for Gas Separation Applications: A Review. *J. Ind. Eng. Chem.* 19 (2), 375–393. doi:10.1016/j.jiec.2012.09.019

Berendsen, H. J. C., Postma, J. P. M., van Gunsteren, W. F., DiNola, A., and Haak, J. R. (1984). Molecular Dynamics with Coupling to an External bath. *J. Chem. Phys.* 81 (8), 3684–3690. doi:10.1063/1.448118

Bhakta, R. K., Herberg, J. L., Jacobs, B., Highley, A., Behrens, R., Ockwig, N. W., et al. (2009). Metal-organic Frameworks as Templates for Nanoscale Naalh4. *J. Am. Chem. Soc.* 131 (37), 13198–13199. doi:10.1021/ja904431x

Butova, V. V., Soldatov, M. A., Guda, A. A., Lomachenko, K. A., and Lamberti, C. (2016). Metal-organic Frameworks: Structure, Properties, Methods of Synthesis and Characterization. *Russ. Chem. Rev.* 85, 280–307. doi:10.1070/rcr4554

Canivet, J., Aguado, S., Daniel, C., and Farrusseng, D. (2011). Engineering the Environment of a Catalytic Metal-Organic Framework by Postsynthetic Hydrophobization. *ChemCatChem.* 3 (4), 675–678. doi:10.1002/cctc.201000386

Chen, T., Huo, P., Hou, J.-L., Xu, J., Zhu, Q.-Y., and Dai, J. (2016). Confinement Effects of Metal-Organic Framework on the Formation of Charge-Transfer Tetrathiafulvalene Dimers. *Inorg. Chem.* 55 (24), 12758–12765. doi:10.1021/acs.inorgchem.6b02062

Ding, B., Wang, J., Chang, Z., Xu, G., Hao, X., Shen, L., et al. (2016). Self-sacrificial Template-Directed Synthesis of Metal-Organic Framework-Derived Porous Carbon for Energy-Storage Devices. *ChemElectroChem.* 3 (4), 668–674. doi:10.1002/celc.201500536

Distefano, G., Suzuki, H., Tsujimoto, M., Isoda, S., Bracco, S., Comotti, A., et al. (2013). Highly Ordered Alignment of a Vinyl Polymer by Host-Guest Cross-Polymerization. *Nat. Chem.* 5, 335–341. doi:10.1038/nchem.1576

Forest, C., Chaumont, P., Cassagnau, P., Swoboda, B., and Sonntag, P. (2015). Polymer Nano-Foams for Insulating Applications Prepared from Co2 Foaming. *Prog. Polym. Sci.* 41, 122–145. doi:10.1016/j.progpolymsci.2014.07.001

Fu, Y., Qu, Z., and Zhou, L. (2017). Prediction of the Effective thermal Conductivity of Aerogel Nano-Porous Materials. *Energ. Proced.* 105, 4769–4775. doi:10.1016/j.egypro.2017.03.938

Furukawa, H., Cordova, K. E., O'Keeffe, M., and Yaghi, O. M., (2013), The Chemistry and Applications of Metal-Organic Frameworks, *Science* 341. 1230444.doi:10.1126/science.1230444

Gowers, R. J., Linke, M., Barnoud, J., Tyler, J., Reddy, E., Melo, M. N., et al. (2016). MDAnalysis: A Python Package for the Rapid Analysis of Molecular Dynamics Simulations, in *Proceedings of the 15th Python in Science Conference* (Sebastian Benthall and Scott Rostrup, eds.), pp. 98 – 105.

Hourahine, B., Aradi, B., Blum, V., Bonafé, F., Buccheri, A., Camacho, C., et al. (2020). Dftb+, a Software Package for Efficient Approximate Density Functional Theory Based Atomistic Simulations. *J. Chem. Phys.* 152 (12), 124101. doi:10.1063/1.5143190

Klein, N., Hoffmann, H. C., Cadiau, A., Getzschmann, J., Lohe, M. R., Paasch, S., et al. (2012). "Structural Flexibility and Intrinsic Dynamics in the M2(2,6-Ndc) 2(dabco) (M = Ni, Cu, Co, Zn) Metal–Organic Frameworks. *J. Mater. Chem.* 22, 10303–10312. doi:10.1039/c2jm15601f

Lee, M., Shin, S. M., Jeong, N., and Thallapally, P. K. (2015). Chiral Environment of Catalytic Sites in the Chiral Metal-Organic Frameworks. *Dalton Trans.* 44, 9349–9352. doi:10.1039/c5dt01322d

Levine, B. G., Stone, J. E., and Kohlmeyer, A. (2011). Fast Analysis of Molecular Dynamics Trajectories with Graphics Processing Units-Radial Distribution Function Histogramming. *J. Comput. Phys.* 230 (9), 3556–3569. doi:10.1016/j.jcp.2011.01.048

Li, H., Eddaoudi, M., O'Keeffe, M., and Yaghi, O. M. (1999). Design and Synthesis of an Exceptionally Stable and Highly Porous Metal-Organic Framework. *Nature* 402, 276–279. doi:10.1038/46248

Liu, B., Shioyama, H., Akita, T., and Xu, Q. (2008). Metal-organic Framework as a Template for Porous Carbon Synthesis. *J. Am. Chem. Soc.* 130 (16), 5390–5391. doi:10.1021/ja7106146

Ma, J., Sanchez, J. P., Wu, K., Couples, G. D., and Jiang, Z. (2014). A Pore Network Model for Simulating Non-ideal Gas Flow in Micro- and Nano-Porous Materials. *Fuel* 116, 498–508. doi:10.1016/j.fuel.2013.08.041

Martyna, G. J., Tuckerman, M. E., Tobias, D. J., and Klein, M. L. (1996). Explicit Reversible Integrators for Extended Systems Dynamics. *Mol. Phys.* 87 (5), 1117–1157. doi:10.1080/00268979600100761

Materazzi, S. (2008). "Coordination Compounds and Inorganics," in *Recent Advances, Techniques and Applications*. Editors M. E. Brown and P. K. Gallagher (Elsevier Science B.V.), 439–502. vol. 5 of Handbook of Thermal Analysis and Calorimetry. doi:10.1016/s1573-4374(08)80015-5

Michaud-Agrawal, N., Denning, E. J., Woolf, T. B., and Beckstein, O. (2011). Mdanalysis: A Toolkit for the Analysis of Molecular Dynamics Simulations. *J. Comput. Chem.* 32 (10), 2319–2327. doi:10.1002/jcc.21787

Mochizuki, S., Kitao, T., and Uemura, T. (2018). Controlled Polymerizations Using Metal-Organic Frameworks. *Chem. Commun.* 54, 11843–11856. doi:10.1039/c8cc06415f

Moreira, N. H., Dolgonos, G., Aradi, B., da Rosa, A. L., and Frauenheim, T. (2009). Toward an Accurate Density-Functional Tight-Binding Description of Zinc-Containing Compounds. *J. Chem. Theor. Comput.* 5 (3), 605–614. doi:10.1021/ct800455a

Mueller, U., Schubert, M., Teich, F., Puetter, H., and Schierle-Arndt, K. (2006), Metal-organic Frameworks Prospective Industrial Applications, *J. Mater. Chem.* 16. 626–636.doi:10.1039/b511962f

Pettinari, C., Marchetti, F., Mosca, N., Tosi, G., and Drozdov, A. (2017). Application of Metal-Organic Frameworks. *Polym. Int.* 66 (6), 731–744. doi:10.1002/pi.5315

Rafiee, E., and Shahebrahimi, S. (2017). Organic-inorganic Hybrid Polyionic Liquid Based Polyoxometalate as Nano Porous Material for Selective Oxidation of Sulfides. *J. Mol. Struct.* 1139, 255–263. doi:10.1016/j.molstruc.2017.03.041

Rappe, A. K., Casewit, C. J., Colwell, K. S., Goddard, W. A., and Skiff, W. M. (1992). Uff, a Full Periodic Table Force Field for Molecular Mechanics and Molecular Dynamics Simulations. *J. Am. Chem. Soc.* 114 (25), 10024–10035. doi:10.1021/ja00051a040

Ricco, R., Pfeiffer, C., Sumida, K., Sumby, C. J., Falcaro, P., Furukawa, S., et al. (2016). "Emerging Applications of Metal–Organic Frameworks. *CrystEngComm* 18, 6532–6542. doi:10.1039/c6ce01030j

Rivera-Torrente, M., Pletcher, P. D., Jongkind, M. K., Nikolopoulos, N., and Weckhuysen, B. M. (2019). Ethylene Polymerization over Metal-Organic Framework Crystallites and the Influence of Linkers on Their Fracturing Process. *ACS Catal.* 9 (4), 3059–3069. doi:10.1021/acscatal.9b00150

Rohwer, E. J., Akbarimoosavi, M., Meckel, S. E., Liu, X., Geng, Y., Lawson Daku, L. M., et al. (2018). Dipole Moment and Polarizability of Tunable Intramolecular Charge Transfer States in Heterocyclic-Conjugated Molecular Dyads Determined by Computational and Stark Spectroscopic Study. *The J. Phys. Chem. C* 122 (17), 9346–9355. doi:10.1021/acs.jpcc.8b02268

Schmidt, B. V. K. J. (2019). Metal-organic Frameworks in Polymer Science: polymerization Catalysis, Polymerization Environment, and Hybrid Materials. *Macromolecular Rapid Commun.* 41 (1), 1900333. doi:10.1002/marc.201900333

te Velde, G., Bickelhaupt, F. M., Baerends, E. J., Fonseca Guerra, C., van Gisbergen, S. J. A., Snijders, J. G., et al. (2001). Chemistry with Adf. *J. Comput. Chem.* 22 (9), 931–967. doi:10.1002/jcc.1056

Uemura, T., Kitagawa, K., Horike, S., Kawamura, T., Kitagawa, S., Mizuno, M., et al. (2005). Radical Polymerisation of Styrene in Porous Coordination Polymers. *Royal Soc. Chem.*, 5968–5970. doi:10.1039/b508588h

Uemura, T., Ono, Y., Kitagawa, K., and Kitagawa, S. (2008). Radical Polymerization of Vinyl Monomers in Porous Coordination Polymers: Nanochannel Size Effects on Reactivity, Molecular Weight, and Stereostructure. *Macromolecules* 41 (1), 87–94. doi:10.1021/ma7022217

Uemura, T., Yanai, N., and Kitagawa, S. (2009). Polymerization Reactions in Porous Coordination Polymers. *Chem. Soc. Rev.* 38, 1228–1236. doi:10.1039/b802583p

Wang, T., Farajollahi, M., Henke, S., Zhu, T., Bajpe, S. R., Sun, S., et al. (2017). Functional Conductive Nanomaterials via Polymerisation in Nano-Channels: Pedot in a Mof. *Mater. Horizon.* 4, 64–71. doi:10.1039/c6mh00230g

Wilkerson, J. W., and Ramesh, K. T. (2016). A Closed-form Criterion for Dislocation Emission in Nano-Porous Materials under Arbitrary Thermomechanical Loading. *J. Mech. Phys. Sol.* 86, 94–116. doi:10.1016/j.jmps.2015.10.005

Yaghi, O. M., O'Keeffe, M., and Kanatzidis, M. (2000). Design of Solids from Molecular Building Blocks: Golden Opportunities for Solid State Chemistry. *J. Solid State. Chem.* 152 (1), 1–2. doi:10.1006/jssc.2000.8733

Yaghi, O. M., O'Keeffe, M., Ockwig, N. W., Chae, H. K., Eddaoudi, M., and Kim, J. (2003). Reticular Synthesis and the Design of New Materials. *Nature* 423 (6941), 705–714. doi:10.1038/nature01650

Zhang, H., Fang, W., Li, Z., and Tao, W. (2015). The Influence of Gaseous Heat Conduction to the Effective thermal Conductivity of Nano-Porous Materials. *Int. Commun. Heat Mass Transfer* 68, 158–161. doi:10.1016/j.icheatmasstransfer.2015.08.027

Zhang, H., Gu, W., Li, M. J., Li, Z. Y., Hu, Z. J., and Tao, W. Q. (2014). Experimental Study on the Kinetics of Water Vapor Sorption on the Inner Surface of Silica Nano-Porous Materials. *Int. J. Heat Mass Transfer* 78, 947–959. doi:10.1016/j.ijheatmasstransfer.2014.07.047

Conflict of Interest: The authors declare that the research was conducted in the absence of any commercial or financial relationships that could be construed as a potential conflict of interest.

frontiers in Chemistry

ORIGINAL RESEARCH
published: 02 August 2021
doi: 10.3389/fchem.2021.728845

A Luminescent 1D Silver Polymer Containing [2.2]Paracyclophane Ligands

*Campbell F. R. Mackenzie†, Lucie Delforce†, D. Rota Martir, David B. Cordes, Alexandra M. Z. Slawin and Eli Zysman-Colman**

Organic Semiconductor Centre, EaStCHEM School of Chemistry, University of St Andrews, Fife, United Kingdom

[2.2]Paracyclophane scaffolds have seen limited use as building blocks in supramolecular chemistry. Here, we report the synthesis and characterization of a 1D coordination polymer consisting of silver(I) ions bound to a [2.2]paracyclophane scaffold functionalized with two 4-pyridyl units. The structure of the polymer has been determined from single crystal X-ray diffraction analysis and reveals two different silver coordination motifs that alternate along the 1D coordination polymer. The coordination polymer exhibits strong blue and sky-blue fluorescence in solution and in the crystalline solid state, respectively.

Keywords: coordination polymer, cyclophane, supramolecular chemistry, silver(I), paracyclophane

OPEN ACCESS

Edited by:
Tangxin Xiao,
Changzhou University, China

Reviewed by:
Subhamay Pramanik,
University of Kansas, United States
Christopher Pigge,
The University of Iowa, United States
Luiz Fernando Cappa De Oliveira,
Juiz de Fora Federal University, Brazil

****Correspondence:***
Eli Zysman-Colman
eli.zysman-colman@st-andrews.ac.uk

†These authors have contributed equally to this work

Specialty section:
This article was submitted to Supramolecular Chemistry, a section of the journal Frontiers in Chemistry

Received: *22 June 2021*
Accepted: *12 July 2021*
Published: *02 August 2021*

Citation:
Mackenzie CFR, Delforce L, Rota Martir D, Cordes DB, Slawin AMZ and Zysman-Colman E (2021) A Luminescent 1D Silver Polymer Containing [2.2] Paracyclophane Ligands. Front. Chem. 9:728845. doi: 10.3389/fchem.2021.728845

INTRODUCTION

Coordination polymers are polymeric arrays of monomeric units that are held together through metal coordination (Yang et al., 2015). These materials continue to attract attention due to their use in a wide range of applications from medicine (Medici et al., 2016), to catalysis (Zeng et al., 2016), sensors (Yi et al., 2016) and luminescent materials (Yersin et al., 2017) (To et al., 2020). Among the metals used to synthesize coordination polymers, silver is of particular interest due to the range of geometries and coordination modes available (Young and Hanton, 2008). Silver has been demonstrated to form coordination polymers with a range of morphologies, 1D, 2D and 3D coordination networks have been demonstrated for a range of ligands (Carlucci et al., 1995) (Chen et al., 2006) (Roy et al., 2016).

Luminescent coordination polymers containing silver(I) were first documented in 1999 (Tong et al., 1999) with the report of a self-assembled 3D coordination polymer of silver(I) with bis-phenol Schiff base ligands that showed bright blue emission in both the solid state and in solution. Since then, many luminescent silver coordination polymers have been reported. Macrocycles and 2D structures made of Ag(I) and pyrimidine-based thioether ligands, reported by Han and coworkers (Han et al., 2005), also show bright luminescence. Liu and coworkers (Liu et al., 2005) reported 2D networks with metallocyclophane motifs with high electric conductivity due to columnar aromatic stacking motifs formed through both intra- and intermolecular π−π interactions. They also report a 2D zigzag sheet structure, in which silver triflate forms tubelike double chains with 4,4′-bis (2,5-dimethylstyryl) biphenyl molecules acting as links between the chains to form the sheets. Both of those compounds exhibit luminescence in the solid state and show excitation and emission maxima are shifted to longer wavelength as compared to those of the corresponding metal-free ligands. The same observation was made by Huo and coworkers (Huo et al., 2016) who reported a series of luminescent Ag(I) coordination polymers with different coordination modes tuned via different multidentate bis(1,2,3-triazole) ligands and anions. This anion-responsive behavior was also detected by Fan and coworkers (Fan et al., 2014) in 3D porous luminescent triazol-type Ag(I) framework with

green luminescence emission. Co-crystallization of Ag(I) complexes with bipyridine and benzimidazole was reported by Cai and coworkers (Cai et al., 2011) to yield 1D infinite coordination polymer chains with both intraligand emission and ligand-to-metal charge transfer contribution. We reported the first example of a phosphorescent Ag(I) coordination polymer that incorporated iridium (III) metalloligands (Rota Martir et al., 2018).

The two benzene rings of the [2.2]paracyclophane (pCp) are disposed cofacially (Bahrin et al., 2017, 2), which give rise to through-space (π–π *trans*-annular) and through-bond [σ(bridge)–π(annular)] electronic interactions, affecting the chemical, optical, and electronic properties of the molecule (Kahnt et al., 2007; Elacqua and MacGillivray, 2010). It has been shown that positioning organic functional groups on the pCp core ring shifts its luminescence properties (Braun et al., 2017; Anhäuser et al., 2019; Rota Martir et al., 2019). Exploiting the electronic coupling present between the two benzene decks of the pCP, the first examples of pCp compounds emitting via a thermally activated delayed fluorescence mechanism were recently reported by Spuling, Sharma and co-workers (Spuling et al., 2018). There are few examples of the pCp scaffold used in metallosupramolecular self-assembly (Meyer-Eppler et al., 2014; Gon et al., 2017; Anhäuser et al., 2019; Rota Martir et al., 2019). A $[Pd_3(pCpd4py)_6](BF_4)_6$ 3D-photoactive cage assembly incorporating a pyridyl-substituted pCp scaffold and Pd has been reported (Rota Martir et al., 2019), this macrocycle is emissive in both the solid state and solution, with emission red-shifted relative to the ligand.

Herein we report the synthesis and photoluminescence properties of a remarkable 1D coordination polymer containing silver(I) ions in two different coordination environments. The coordination polymer Ag-pCp was obtained from the reaction of Ag(I) ions and a [2.2] paracyclophane functionalized at the 7 and 15-positions with 4-pyridyl moieties (pCpd4py).

METHODS

Synthesis

The ligand pCpd4py was prepared according to a previously published method (Rota Martir et al., 2019). All other chemicals and solvents were obtained from commercial suppliers and used as received, solvents used for photophysical measurements were of spectroscopic grade.

Synthesis of Ag-pCp polymer. In a small vial, pCpd4py (4.0 mg, 0.01 mmol, 1 equiv.) was dissolved in 1 ml of dichloromethane. To this vial a solution of $AgPF_6$ (10 mg, 0.04 mmol, 3.6 equiv.) in 1 ml of acetonitrile was carefully layered on top. The vial was sealed and left at room temperature, crystals began forming after 3 days and the reaction was complete after 10 days. The colorless crystals were collected to give the product (5.0 mg, 52% yield). The product was identified by single crystal X-ray diffraction, with the formula determined to be $[Ag_3(pCpd4py)_4(NCCH_3)_6(CH_2Cl_2)_2]$ (CCDC: 2089070).

Photophysics

Absorption spectra were recorded at room temperature on a Shimdazu-1800 spectrophotometer in 1 cm quartz cuvettes. For emission studies, degassed solutions were prepared via three freeze-pump-thaw cycles and spectra were taken using a home-made Schlenk quartz cuvette. Crystalline samples were finely ground and mounted in a quartz sample holder for solid-state measurements. Steady-state emission, excitation spectra and time-resolved emission spectra were recorded at 298 K using an Edinburgh Instruments F980 fluorimeter. Samples were excited at 378 nm using a pulsed diode laser for time-resolved measurements.

RESULTS AND DISCUSSION

Coordination of silver ions to the 4-pyridyl groups of pCpd4py proceeded readily, with the coordination polymer crystallizing from solution cleanly in moderate yield.

The X-ray crystal structure of the coordination polymer is shown in **Figure 1**. The asymmetric unit of the structure comprises one and a half silver(I) ions, two pCp4py ligands, one and a half PF_6^- anions, one molecule of dichloromethane solvent and three molecules of acetonitrile solvent. This remarkable structure consists of a 1D coordination polymer in which there are two different coordination environments for the silver(I) ions. One silver ion (Ag1) is in a linear, 2-coordinate environment, while the second silver ion (Ag2) is in a trigonal planar 3-coordinate environment.

The linear coordination environment around Ag1 has two strongly bound nitrogen atoms from the pCpd4py ligand. Ag1 is located at an inversion center, this results in a perfect 180° N-Ag1-N bond angle and identical Ag1-N distances of 2.141(4) Å. A linear N-Ag-N bond has been observed in some Ag-coordination polymers, for example in *rac*-IrAg (Rota Martir et al., 2018); however, in many cases the linear coordination is distorted by the presence of anions and solvent molecules (Chen et al., 2006). In the extended coordination sphere, there are two weakly bound acetonitrile molecules, with longer Ag to N distances of 2.833(10) Å. The weakly coordinated acetonitrile molecules are nearly perpendicular to the Ag-N_{py} bonds, with a N_{py}-Ag1-N_{MeCN} angle of 87.6(3) The Ag1-N distance in Ag-pCp is similar to the 2.141 and 2.156 Å observed in *rac*-IrAg (Rota Martir et al., 2018) and also similar to the Ag-N distances of between 2.123 and 2.133 Å seen in a series of linear two-coordinate $[Ag(pyridine)_2]^+$ structures. (Chen et al., 2007).

The coordination environment around Ag2 is a nearly perfect trigonal planar environment, with Ag2-N bond lengths of 2.224(4), 2.246(5) and 2.268(4) Å and N-Ag2-N angles between 112.85(16) and 124.31(17), with the Ag(I) ion displaced 0.099 Å out of the mean-plane of the nitrogen atoms. This is similar to the coordination environment seen in a pair of $[Ag(isonicotinamide)_3]^+$ crystals where Ag-N bond lengths ranged between 2.213 and 2.321 Å, N-Ag-N bond angles were *ca.* 105, 120 and 135°, and the Ag(I) ion was displaced 0.007 or 0.017 Å out of the mean-plane of the nitrogen atoms (B. Aakeröy et al., 1998). A three-coordinate geometry for silver is the third most common seen, behind four-

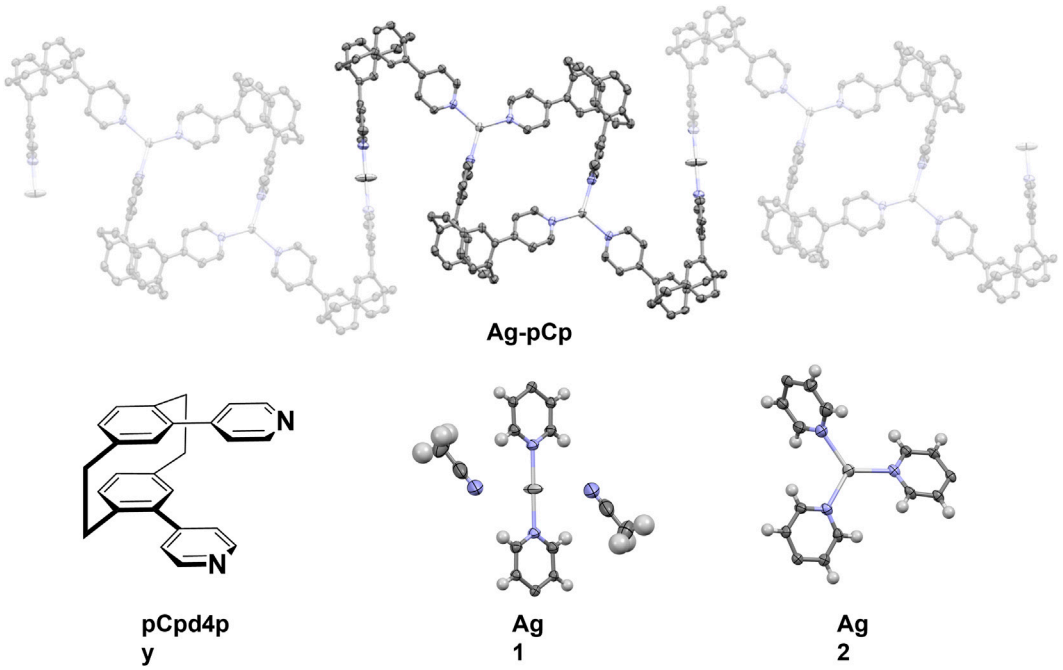

FIGURE 1 | (Top) Representation of the X-ray crystal structure of Ag-pCp, hydrogen atoms, solvent molecules and anions are omitted for clarity. (Bottom, L-R) Diagram of ligand pCpd4py, two different coordination environments for the silver atoms (thermal ellipsoid plot, 50% probability ellipsoids).

and two-coordinate (Young and Hanton, 2008), in many of these examples the coordination environment is distorted from the ideal trigonal planar, trigonal pyramidal or T-shaped geometries by the use of bidentate ligands or the presence of weak interactions with solvent molecules or anions (Durini et al., 2017). The angled orientation of the coordinating pyridyl groups makes each Ag2 center a chiral molecular propeller, although from the symmetry of the space group, centers of both handedness are present and individual polymer chains are achiral.

The phenyl rings of the pCp4py ligands show a distortion from planarity similar to that seen in related pCp compounds (angle across the *para*-substitution axis 15.6–16.2°). (Rota Martir et al., 2019). Despite this, the dihedral angle between mean planes of the phenyl groups still shows them to be parallel (1.8° for both ligands). Each ligand shows two rather different dihedral angles between the phenyl and its pyridyl substituent, although these match reasonably well between the two ligands (31.6 and 49.2° for one, 36.9 and 51.7° for the other). In turn, this leads to similar angles between pyridyl rings for each of the two ligands (75.4 and 83.2°). This matches the conformation seen in other pyridyl-cyclophanes. (Rota Martir et al., 2019).

Each polymer chain is built from alternating $[Ag_2(pCpd4py)_2]$ 32-membered metallamacrocycles (which include just the trigonal planar Ag2) and Z-shaped linkers, comprising two ligands bound linearly to Ag1. This results in a flat, tape-like coordination polymer (**Figure 1**), with chains propagating along the [0 1 −1] diagonal axis, and a polymer repeat-distance of 21.42 Å. Adjacent polymer chains are offset such that the edge of one tape overlies that of the next, with the pCp of the Z-shape above the trigonal planar Ag2 center. Despite this positioning, no π···π interactions are found in the structure, the shortest distance between centroids being 4.33 Å. However, this positioning of adjacent chains does allow for the formation of CH···π interactions chains, involving a methylene hydrogen of one pCpd4py and the π-system of a pyridine ring of the other, at a C-H···centroid distance of 2.70 Å [C···centroid separation of 3.528(6) Å]. These interactions occur in pairs across an inversion center, and link adjacent chains into two-dimensional sheets in the (1 1 1) plane (**Figure 2**). No direct intermolecular interactions occur between adjacent sheets. There are no close contacts between the silver(I) atoms, in contrast to many low-coordinate silver complexes. (Chen et al., 2007).

Both anions and solvent molecules form weak C-H···A interactions, although only the PF_6^- anions and one of the molecules of acetonitrile interact directly with the polymer chains, other interactions being between anion and solvent or solvent and solvent. None of the anions or solvent molecules bridge directly between chains. The C-H···N distances occur at 2.47 and 2.61 Å [C···N separations of 3.371(15) and 3.24(2) Å] and the C-H···F distances range from 2.40 to 2.45 Å [corresponding C···F separations of 3.150(9) to 3.400(14) Å]. One PF_6^- interacts solely with one polymer chain, while the other interacts with a chain and multiple solvent molecules. These weak interactions give rise to discrete T-shaped motifs comprising one dichloromethane, one PF_6^- and three acetonitriles (**Figure 2**). Two polymer chains in the same sheet are weakly linked via the PF_6^- and one acetonitrile, while this sheet can in turn be linked to a chain in another sheet via the weak Ag···NCMe interactions.

Ag-pCp is luminescent, exhibiting sky-blue emission (λ_{PL} = 497 nm) in the crystalline solid state and deep-blue emission in DCM solution (λ_{PL} = 419 nm), **Figure 3**.

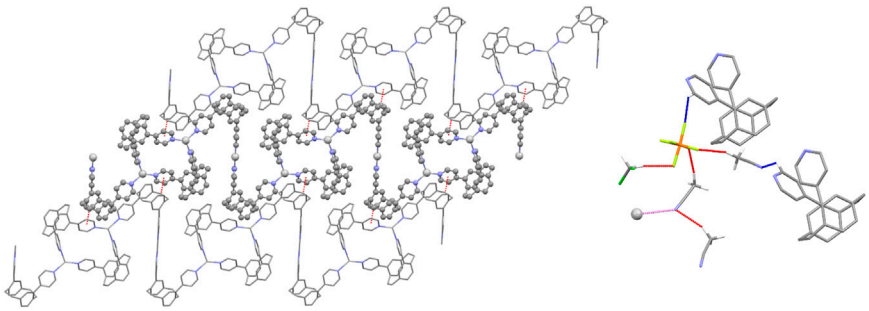

FIGURE 2 | Representations of the intermolecular interactions in the solid-state structure of Ag-pCp. (Left) View of a two-dimensional sheet in the (1 1 1) plane formed by C-H·π interactions (shown red) linking adjacent chains. The central chain is highlighted for clarity. (Right) View of the weakly interacting T-shaped motif (interactions shown red) formed by solvent and anion. Links from the motif to polymer chains are shown for both C-H···A (shown blue) and Ag···N (shown pink) interactions.

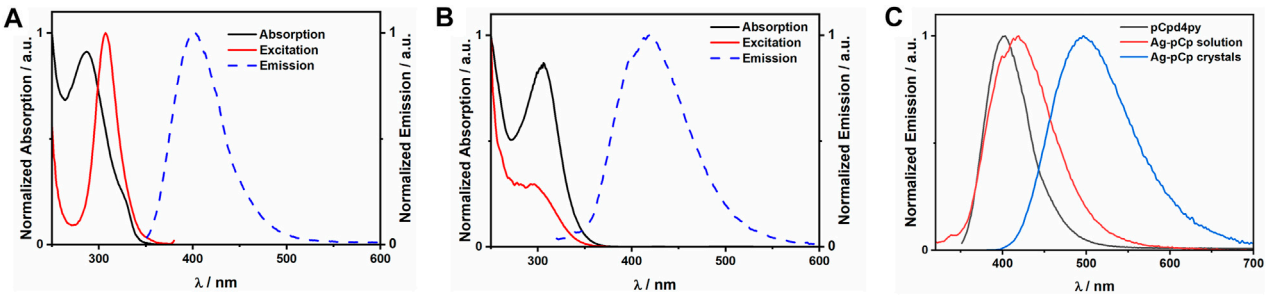

FIGURE 3 | Plots of the normalized absorption, excitation and emission spectra for **(A)** pCpd4py in acetonitrile, **(B)** Ag-pCp in dichloromethane. **(C)** Comparison of the emission spectra for the ligand and Ag-pCp in solution and crystalline states.

Coordination polymers are liable to exist as shorter oligomers in solution, although in a non-coordinating solvent like DCM, Ag-pCp is expected to retain its structural motifs in the oligomeric fragments. The solution-state emission is only slightly red-shifted from the emission of the ligand (λ_{PL} = 403 nm), suggesting that the emission is fluorescence from a ligand centered (^{1}LC) singlet excited state, with the red-shift due to the stabilization of the LUMO and the singlet excited state upon coordination of the Lewis acidic silver(I) ions to the pyridyl group of the ligand. This same red-shift in emission upon coordination of a metal ion to pCpd4py was seen for $[Pd_3(pCpd4py)_6](BF_4)_6$. (Rota Martir et al., 2019). There is a similar red-shift observed in the absorption spectrum of a DCM solution of Ag-pCp (λa_{bs} = 306 nm) in comparison to the free ligand (λ_{abs} = 287 nm). The emission lifetime of pCpd4py and the DCM solution of Ag-pCp are very similar (pCpd4py: τ_{PL} = 5.42 ns, Ag-pCp: τP_L = 5.27 ns), while crystalline Ag-pCp has a longer emission lifetime of 19 ns.

The electronic properties of both the ligand and subunits of the polymer were investigated by DFT and TD-DFT calculations to provide further insight into the nature of the emission properties and the corresponding energy levels of the excited states of the compounds. Details of the calculations performed are provided in the Supplementary Material, while plots of the Kohn-Sham orbitals are shown in **Figure 4**. The optimized structure of the ligand showed a large gap of 4.50 eV between the HOMO and LUMO, which is also reflected in the high excited state energy of 3.77 eV for S_1. There is no spatial separation between the HOMO and LUMO, leading to a large singlet-triplet energy gap, ΔE_{ST}, of 0.89 eV.

We next investigated Ag-pCp. The polymer was broken down into two different chromophoric units that were studied separately. The first unit contained a single two-coordinate silver center with the two coordinating pCpd4py ligands (matching the environment of Ag1). The second unit contained two three-coordinate silver centers, with two pCpd4py ligands bridging the Ag ions and forming a metallamacrocycle, and two additional ligands completing the coordination sphere of each Ag center (matching Ag2). The optimized geometry for each silver environment is similar to the crystallographically determined structures. The optimized Ag1 structure has a linear, two-coordinate environment around the silver ion, with the two pyridine groups being co-planar. The Ag2 structure retains the trigonal planar coordination environment observed experimentally, although the environment is slightly distorted, with py-Ag-py bond angles ranging from 94 to 140° and the Ag-N_{py} distances ranging from 2.238 to 2.395 Å with the silver ions displaced up to 0.229Å from the mean-plane of the nitrogen atoms.

The coordination of the silver ions to the ligand in each of these units resulted in a strong stabilization of more than 50 meV on the LUMO of the compounds, with little change observed in the HOMO energy. The HOMO remaining localized on a single ligand, while the LUMO is distributed across multiple ligands. In all cases there is no metal contribution to the orbitals (**Figure 3**).

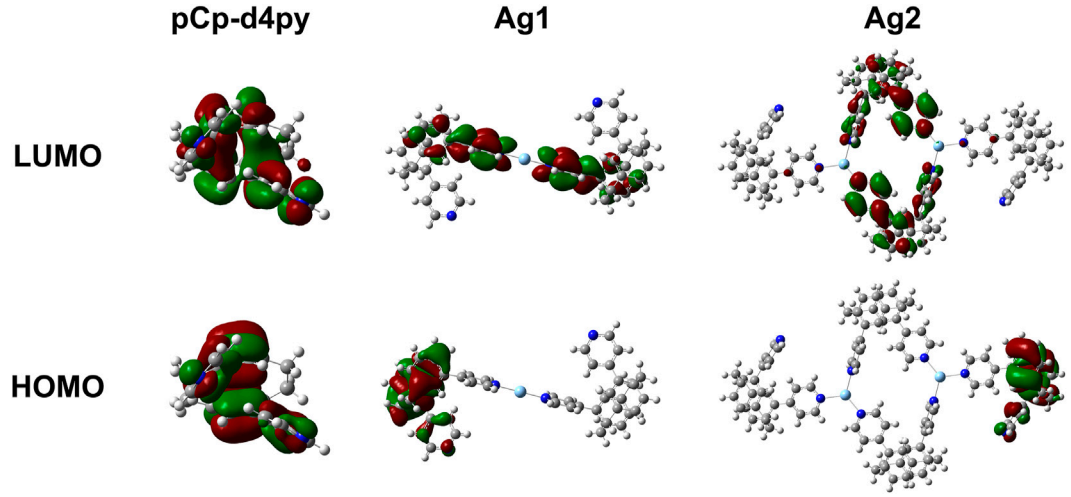

FIGURE 4 | Plots of the molecular orbitals (top–LUMO, bottom–HOMO) for pCpd4py and the two different Ag-containing model units from Ag-pCp.

The smaller Ag1-type unit shows a significant (50 meV) red-shift in the excited state energy of S_1, while the larger Ag2-type unit shows a more moderate 20 meV red-shift of the emissive excited state. The calculated red-shift for the Ag2-containing fragment is close to the 11 meV red-shift observed between the solution state emission of the ligand in MeCN and that of the polymer in DCM. This suggests that the Ag2-type group is a good computational model for the whole polymer in solution.

CONCLUSION

We have prepared a new luminescent 1D silver(I) coordination polymer Ag-pCp. The polymer has a very interesting structure, containing both linear 2-coordinate and trigonal planar 3-coordinate silver atoms in the polymer chain. Ag-pCp is blue fluorescent in both the crystalline state and in DCM solution.

DATA AVAILABILITY STATEMENT

The datasets presented in this study can be found in online repositories. The names of the repository/repositories and accession number(s) can be found below: https://doi.org/10.17630/9e0d4b83-171a-4805-aef8-a9fbac035c1f.

AUTHOR CONTRIBUTIONS

CM performed the calculations and co-authored the manuscript, LD performed the synthesis and assisted in preparing the manuscript, DM performed the emission measurements, DC and AS performed the X-ray crystallography studies, EZ managed the project and co-authored the manuscript.

FUNDING

CM and EZ-C wish to thank the Engineering and Physical Sciences Research Council (EP/P014082/1, EP/M02105X/1 and EP/R035164/1).

SUPPLEMENTARY MATERIAL

The Supplementary Material for this article can be found online at: https://www.frontiersin.org/articles/10.3389/fchem.2021.728845/full#supplementary-material

REFERENCES

Aakeröy, C. B., Beatty, A. M., and Helfrich, B. A. (1998). Two-fold Interpenetration of 3-D Nets Assembled via Three-Co-Ordinate Silver(I) Ions and Amide-Amide Hydrogen Bonds. *J. Chem. Soc. Dalton Trans.*, 1943–1946. doi:10.1039/A802520G

Anhäuser, J., Puttreddy, R., Lorenz, Y., Schneider, A., Engeser, M., Rissanen, K., et al. (2019). Chiral Self-Sorting Behaviour of [2.2]paracyclophane-Based Bis(pyridine) Ligands. *Org. Chem. Front.* 6, 1226–1235. doi:10.1039/C9QO00155G

Bahrin, L. G., Sarbu, L. G., Jones, P. G., Birsa, L. M., and Hopf, H. (2017). [2.2] Paracyclophane-bis(triazole) Systems: Synthesis and Photochemical Behavior. *Chem. Eur. J. Eur. J.* 23, 12338–12345. doi:10.1002/chem.201701593

Braun, C., Nieger, M., and Bräse, S. (2017). Unprecedented One-Pot Reaction towards Chiral, Non-racemic Copper(I) Complexes of [2.2]Paracyclophane-Based P,N -Ligands. *Chem. Eur. J.* 23, 16452–16455. doi:10.1002/chem.201704115

Cai, S.-L., Zheng, S.-R., Tan, J.-B., Pan, M., Fan, J., and Zhang, W.-G. (2011). An Unprecedented Supramolecular Network with Channels Filled by 1D Coordination Polymer Chains: Cocrystallization of Ag(i)-4,4′-Bipyridine and Ag(i)-Benzimidazole Complexes. *CrystEngComm* 13, 6345–6348. doi:10.1039/C1CE05535F

Carlucci, L., Ciani, G., Proserpio, D. M., and Sironi, A. (1995). 1-, 2-, and 3-Dimensional Polymeric Frames in the Coordination Chemistry of AgBF4 with Pyrazine. The First Example of Three Interpenetrating 3-Dimensional Triconnected Nets. *J. Am. Chem. Soc.* 117, 4562–4569. doi:10.1021/ja00121a014

Chen, C.-L., Kang, B.-S., and Su, C.-Y. (2006). Recent Advances in Supramolecular Design and Assembly of Silver(i) Coordination Polymers. *Aust. J. Chem.* 59, 3–18. doi:10.1071/ch05225

Chen, C. Y., Zeng, J. Y., and Lee, H. M. (2007). Argentophilic Interaction and Anionic Control of Supramolecular Structures in Simple Silver Pyridine Complexes. *Inorg. Chim. Acta* 360, 21–30. doi:10.1016/j.ica.2006.06.013

Durini, S., Ardizzoia, G. A., Therrien, B., and Brenna, S. (2017). Tuning the Fluorescence Emission in Mononuclear Heteroleptic Trigonal Silver(i) Complexes. *New J. Chem.* 41, 3006–3014. doi:10.1039/C6NJ04058F

Elacqua, E., and MacGillivray, L. R. (2010). From the Decks to the Bridges: Optoelectronics in [2.2]paracyclophane Chemistry. *Eur. J. Org. Chem.* 2010, 6883–6894. doi:10.1002/ejoc.201000930

Fan, Z., Wang, Y. Y., Xu, Y. Y., Su, X. M., Wu, X. X., Huo, J. Z., et al. (2014). Synthesis and Characterization of a Novel 3D Porous Luminescent Ag(I) Framework with a Multidentate Triazole Ligand. *Inorg. Chim. Acta* 410, 178–182. doi:10.1016/j.ica.2013.11.002

Gon, M., Morisaki, Y., and Chujo, Y. (2017). A Silver(I)-induced Higher-Ordered Structure Based on Planar Chiral Tetrasubstituted [2.2]paracyclophane. *Chem. Commun.* 53, 8304–8307. doi:10.1039/C7CC03615A

Han, L., Wu, B., Xu, Y., Wu, M., Gong, Y., Lou, B., et al. (2005). Assembly of Luminescent Ag(I) Coordination Architectures Adjusted by Modification of Pyrimidine-Based Thioether Ligands. *Inorg. Chim. Acta* 358, 2005–2013. doi:10.1016/j.ica.2004.12.023

Huo, J. Z., Su, X. M., Wu, X. X., Liu, Y. Y., and Ding, B. (2016). Hydrothermal Synthesis and Characterization of a Series of Luminescent Ag(I) Coordination Polymers with Two New Multidentate Bis-(1,2,3-Triazole) Ligands: Structural Diversity, Polymorphism and Photoluminescent Sensing. *Cryst. Eng. Comm.* 18, 6640–6652. doi:10.1039/C6CE01275B

Kahnt, A., Guldi, D. M., de la Escosura, A., Martínez-Díaz, M. V., and Torres, T. (2007). [2.2]Paracyclophane: a Pseudoconjugated Spacer for Long-Lived Electron Transfer in Phthalocyanine-C60dyads. *J. Mater. Chem.* 18, 77–82. doi:10.1039/B712751K

Liu, S. Q., Kuroda-Sowa, T., Konaka, H., Suenaga, Y., Maekawa, M., Mizutani, T., et al. (2005). Silver(I) Coordination Polymers of Fluorescent Oligo(phenylenevinylene) with π–π Stackings: Luminescence and Conductivity. *Inorg. Chem.* 44, 1031–1036. doi:10.1021/ic0400585

Medici, S., Peana, M., Crisponi, G., Nurchi, V. M., Lachowicz, J. I., Remelli, M., et al. (2016). Silver Coordination Compounds: A New Horizon in Medicine. *Coord. Chem. Rev.* 327-328, 349–359. doi:10.1016/j.ccr.2016.05.015

Meyer-Eppler, G., Topić, F., Schnakenburg, G., Rissanen, K., and Lützen, A. (2014). Chiral Self-Sorting Oftrans-Chelating Chiral Ligands upon Formation of PdIIComplexes. *Eur. J. Inorg. Chem.* 2014, 2495–2501. doi:10.1002/ejic.201402057

Rota Martir, D., Delforce, L., Cordes, D. B., Slawin, A. M. Z., Warriner, S. L., Jacquemin, D., et al. (2019). A Pd3L6 Supramolecular Cage Incorporating Photoactive [2.2]paracyclophane Units. *Inorg. Chem. Front.* 7, 232–238. doi:10.1039/C9QI01147A

Rota Martir, D., Rajamalli, P., Cordes, D. B., Slawin, A. M. Z., and Zysman-Colman, E. (2018). Marigold Flower-like Assemblies of Phosphorescent Iridium-Silver Coordination Polymers. *Macromol. Rapid Commun.* 39, 1800501. doi:10.1002/marc.201800501

Roy, S., Titi, H. M., Tripuramallu, B. K., Bhunia, N., Verma, R., and Goldberg, I. (2016). Silver Coordination Polymers Based on Newly Designed Bis(cyanobenzyl)bipiperidine Ligand: Synthesis, Anion Exchange, Guest Inclusion, Electrochemical, and Photoluminescence Properties. *Cryst. Growth Des.* 16, 2814–2825. doi:10.1021/acs.cgd.6b00151

Spuling, E., Sharma, N., Samuel, I. D. W., Zysman-Colman, E., and Bräse, S. (2018). (Deep) Blue Through-Space Conjugated TADF Emitters Based on [2.2] paracyclophanes. *Chem. Commun.* 54, 9278–9281. doi:10.1039/C8CC04594A

To, W.-P., Cheng, G., Tong, G. S. M., Zhou, D., and Che, C.-M. (2020). Recent Advances in Metal-TADF Emitters and Their Application in Organic Light-Emitting Diodes. *Front. Chem.* 8, 653. doi:10.3389/fchem.2020.00653

Tong, M.-L., Chen, X.-M., Ye, B.-H., and Ji, L.-N. (1999).Self-Assembled Three-Dimensional Coordination Polymers with Unusual Ligand-Unsupported Ag–Ag Bonds: Syntheses, Structures, and Luminescent Properties. *Angew. Chem. Int. Ed.* 38, 2237–2240. doi:10.1002/(SICI)1521-3773(19990802)38:15<2237::AID-ANIE2237>3.010.1002/(sici)1521-3773(19990802)38:15<2237::aid-anie2237>3.0.co;2-9

Yang, L., Tan, X., Wang, Z., and Zhang, X. (2015). Supramolecular Polymers: Historical Development, Preparation, Characterization, and Functions. *Chem. Rev.* 115, 7196–7239. doi:10.1021/cr500633b

Yersin, H., Czerwieniec, R., Shafikov, M. Z., and Suleymanova, A. F. (2017). TADF Material Design: Photophysical Background and Case Studies Focusing on CuI and AgI Complexes. *ChemPhysChem* 18, 3508–3535. doi:10.1002/cphc.201700872

Yi, F.-Y., Chen, D., Wu, M.-K., Han, L., and Jiang, H.-L. (2016). Chemical Sensors Based on Metal-Organic Frameworks. *ChemPlusChem* 81, 675–690. doi:10.1002/cplu.201600137

Young, A. G., and Hanton, L. R. (2008). Square Planar Silver(I) Complexes: A Rare but Increasingly Observed Stereochemistry for Silver(I). *Coord. Chem. Rev.* 252, 1346–1386. doi:10.1016/j.ccr.2007.07.017

Zeng, L., Guo, X., He, C., and Duan, C. (2016). Metal-Organic Frameworks: Versatile Materials for Heterogeneous Photocatalysis. *ACS Catal.* 6, 7935–7947. doi:10.1021/acscatal.6b02228

Conflict of Interest: The authors declare that the research was conducted in the absence of any commercial or financial relationships that could be construed as a potential conflict of interest.

Publisher's Note: All claims expressed in this article are solely those of the authors and do not necessarily represent those of their affiliated organizations, or those of the publisher, the editors and the reviewers. Any product that may be evaluated in this article, or claim that may be made by its manufacturer, is not guaranteed or endorsed by the publisher.

frontiers in Chemistry

ORIGINAL RESEARCH
published: 18 August 2021
doi: 10.3389/fchem.2021.729125

Heteroacene-Based Amphiphile as a Molecular Scaffold for Bioimaging Probes

*Tharindu A. Ranathunge[1], Mahesh Loku Yaddehige[1], Jordan H. Varma[1], Cameron Smith[1], Jay Nguyen[2], Iyanuoluwani Owolabi[2], Wojciech Kolodziejczyk[3], Nathan I. Hammer[1], Glake Hill[3], Alex Flynt[2] and Davita L. Watkins[1]**

[1]Department of Chemistry and Biochemistry, University of Mississippi University, Oxford, MS, United States, [2]Cellular and Molecular Biology, The University of Southern Mississippi, Hattiesburg, MS, United States, [3]Interdisciplinary Center for Nanotoxicity, Department of Chemistry, Physics and Atmospheric Sciences, Jackson State University, Jackson, MS, United States

The challenges faced with current fluorescence imaging agents have motivated us to study two nanostructures based on a hydrophobic dye, 6*H*-pyrrolo[3,2-*b*:4,5-*b*']bis [1,4] benzothiazine (TRPZ). TRPZ is a heteroacene with a rigid, pi-conjugated structure, multiple reactive sites, and unique spectroscopic properties. Here we coupled TRPZ to a tert-butyl carbamate (BOC) protected 2,2-bis(hydroxymethyl)propanoic acid (bisMPA) dendron via azide-alkyne Huisgen cycloaddition. Deprotection of the protected amine groups on the dendron afforded a cationic terminated amphiphile, **TRPZ-bisMPA**. **TRPZ-bisMPA** was nanoprecipitated into water to obtain nanoparticles (NPs) with a hydrodynamic radius that was <150 nm. For comparison, **TRPZ-PG** was encapsulated in pluronic-F127 (Mw = 12 kD), a polymer surfactant to afford NPs almost twice as large as those formed by **TRPZ-bisMPA**. Size and stability studies confirm the suitability of the **TRPZ-bisMPA NPs** for biomedical applications. The photophysical properties of the **TRPZ-bisMPA NPs** show a quantum yield of 49%, a Stokes shift of 201 nm (0.72 eV) and a lifetime of 6.3 ns in water. Further evidence was provided by cell viability and cellular uptake studies confirming the low cytotoxicity of **TRPZ-bisMPA NPs** and their potential in bioimaging.

Keywords: bioimaging, Stokes-shift, heteroacenes, amphiphile, nanoparticles

OPEN ACCESS

Edited by:
Ronald K. Castellano, University of Florida, United States

Reviewed by:
Matthew Brandon Baker, Maastricht University, Netherlands
Emily Pentzer, Texas A&M University, United States

****Correspondence:***
Davita L. Watkins
dwatkins@olemiss.edu

Specialty section:
This article was submitted to Supramolecular Chemistry, a section of the journal Frontiers in Chemistry

Received: *22 June 2021*
Accepted: *03 August 2021*
Published: *18 August 2021*

Citation:
Ranathunge TA, Yaddehige ML, Varma JH, Smith C, Nguyen J, Owolabi I, Kolodziejczyk W, Hammer NI, Hill G, Flynt A and Watkins DL (2021) Heteroacene-Based Amphiphile as a Molecular Scaffold for Bioimaging Probes. Front. Chem. 9:729125. doi: 10.3389/fchem.2021.729125

INTRODUCTION

Bioimaging techniques are crucial to understanding biological processes of living systems. Among many imaging techniques, fluorescence imaging (visible to near-infrared, >400 nm) is a powerful, noninvasive method for diagnostics. It can provide excellent spatiotemporal resolution that affords the investigation of biological systems in real-time (Haustein and Schwille, 2007). In light of the aforementioned advantages, some application-based drawbacks remain in regards to the most common imaging agents and dyes (James and Gambhir, 2012). These include inadequate stability, low water solubility, and poor biocompatibility (Choi and Frangioni, 2010; Khan et al., 2019).

Inorganic hybrids such as single-wall carbon nanotubes (SWCNTs) (Jena et al., 2020) and inorganic quantum dots (QDs) (Gil et al., 2021) currently show the most promise, possessing high stability; however, these materials exhibit poor metabolism and high toxicity (Gil et al., 2021). Seeking solely organic or carbon-based alternatives, fluorescent dyes, e.g., rhodamine, (Grimm et al.,

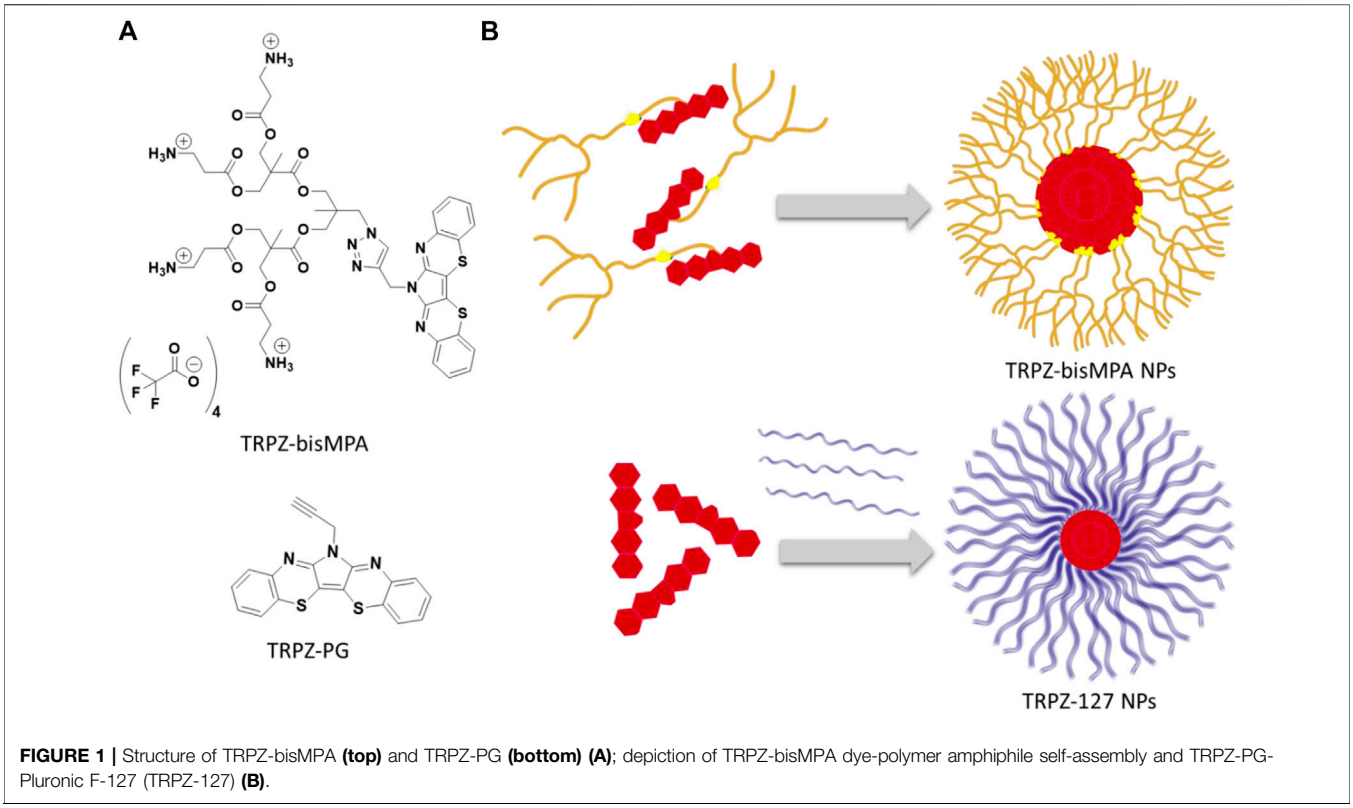

FIGURE 1 | Structure of TRPZ-bisMPA **(top)** and TRPZ-PG **(bottom) (A)**; depiction of TRPZ-bisMPA dye-polymer amphiphile self-assembly and TRPZ-PG-Pluronic F-127 (TRPZ-127) **(B)**.

2020), fluorescein, (Ando et al., 2019), oxazine, (Vogelsang et al., 2009), have been widely adopted. However, they too exhibit unfavorable properties, specifically small Stokes shifts, which typically results in self-quenching and images with poor signal-to-noise ratios. With considerable interest in bioimaging applications, focused strategies have been in place to garner highly soluble emissive materials with low toxicity and large Stokes shifts for accurate and high-resolution images.

Current research efforts in bioimaging have taken a more supramolecular approach in which nanoparticles (NPs) are beginning to dominate (Mourdikoudis et al., 2018; Zhang et al., 2019; Zhang et al., 2020). These strategies have afforded biocompatible, water-soluble efficient probes where hydrophobic fluorophores undergo a structural organization that contributes to favorable photophysical properties. In this study, we designed and synthesized a heteroacene amphiphile based on 6*H*-pyrrolo [3,2-*b*:4,5-*b*']bis[1,4]benzothiazine (TRPZ). The structures of interest are shown in **Figure 1**, where the hydrophobic framework of TRPZ has been modified to form a self-assembling species capable of forming stable NPs for bioimaging applications.

TRPZ is similar to pentacene and pyrene in that it possesses a conjugated structure and unique spectroscopic properties. Its structure readily forms pi-aggregates/excimers at high concentrations due to the stacking interactions of the pi-conjugated backbone resulting in a red-shift of the fluorescence and a bright green-yellow emission. Additionally, it possesses multiple reactive sites with the central pyrrole nitrogen atom offering a diverse library of derivatives with potentially unique functionalities.

Here we propargylated the central nitrogen on TRPZ (**TRPZ-PG**) and coupled it to a dendritic bisMPA alanine possessing protected amine termini via copper(I)-catalyzed azide-alkyne cycloaddition (CuAAC). Deprotection of tert-butyl carbamates (BOC) protected amine groups with trifluoroacetic acid (TFA) afforded a cationic terminated **TRPZ-bisMPA** amphiphile. In aqueous media, **TRPZ-bisMPA** is capable of self-assembling into nanoparticles (NPs) where TRPZ makes up the core and bisMPA is the corona or exterior. In parallel, **TRPZ-PG** was encapsulated in pluronic-F127 (Mw = 12 kD), a polymer surfactant, to make a second NP system, **TRPZ-127 NPs**. We report the size and photophysical properties of the two resulting NP systems. Based on these results, **TRPZ-bisMPA** was then assessed via biological studies to demonstrate TRPZ as a promising platform for designing new versatile bioimaging probes.

MATERIALS AND METHODS

Reagents and solvents were purchased from Sigma-Aldrich and used without further purification unless otherwise specified. All synthetic procedures were carried out under nitrogen atmosphere using standard Schlenk line techniques unless otherwise stated. Additional synthetic details and general procedures are given in the electronic supporting information (SI).

Synthesis of A-MPA-4-ala

Synthesis of (2,2,5-trimethyl-1,3-dioxan-5-yl)methanol (2): The 2-(hydroxymethyl)-2-methylpropane-1,3-diol (10.10 g, 80.1 mmol) was stirred in 50 ml of acetone, 2,2-dimethoxypropane (DMP) (13.1 g, 126 mmol) and PTSA (0.79 g, 4.14 mmol) were added under room temperature. After the completion of the addition, the reaction mixture was stirred for 4 h. Then it was filtered through an amberlyst column, and the solvent was evaporated, and the residue was put under 60°C and full vacuum for 2 h. Then it was put under vacuum overnight to give (2) as a colorless liquid with 96% yield. ^{1}H NMR (500 MHz, $CDCl_3$) δ 3.67 [m, (d, s overlap J = 11.8 Hz, 2H; s, 2H)], 3.60 (d, J = 11.8 Hz, 2H), 2.55 (s, 1H), 1.44 (s, 3H), 1.40 (s, 3H), 0.83 (s, 3H).

Synthesis of (2,2,5-trimethyl-1,3-dioxan-5-yl)methyl 4-methylbenzenesulfonate (3): Compound (2) (10.9 g, 68.0 mmol) was dissolved in 34 ml of pyridine, and it was added dropwise to the stirred solution of p-toluenesulfonyl chloride (35.7 g, 187 mmol) in 48 ml of pyridine at 0°C under nitrogen. After the complete addition, the reaction mixture was stirred 48 h at room temperature. Then the reaction mixture was added dropwise to 100 ml of 40% ammonium chloride solution at 0°C. After complete addition, it was allowed to stir at room temperature for 2 h. Then it was filtered and washed with DI water until the pyridine smell was gone. Then the residue was dissolved in 25 ml of DCM and extracted with half saturated ammonium chloride and saturated NaCl solution. Yellow DCM solution was dried with anhydrous sodium sulfate. Then the solvent was evaporated, and the residue was placed under full vacuum for 12 h to give (3) as a yellow solid with 89% yield. ^{1}H NMR (500 MHz, $CDCl_3$) δ 7.86–7.79 (m, 2H), 7.38 (d, J = 7.6 Hz, 2H), 4.11 (s, 2H), 3.58 (s, 4H), 2.47 (s, 3H), 1.39 (d, J = 4.8 Hz, 3H), 1.25 (d, J = 4.7 Hz, 3H), 0.84 (s, 3H).

Synthesis of 5-(azidomethyl)-2,2,5-trimethyl-1,3-dioxane (4): Compound (3) (14.6 g, 46.4 mmol), NaN_3 (12.1 g, 186 mmol), water (10 ml), and DMF (80 ml) were stirred at 110°C for 48 h under reflux. The mixture was poured into 150 ml water and extracted four times with Et_2O (4 × 200 ml). The organic phase was dried over anhydrous $MgSO_4$, and the solvent was removed under reduced pressure. The residue was purified by column chromatography with silica gel (100 g) and ethyl acetate/n-hexane (1:4) to give 7.48 g of a colorless liquid with an 87% yield. ^{1}H NMR (500 MHz, $CDCl_3$) δ 3.58 (d, J = 2.8 Hz, 4H), 3.51 (s, 2H), 1.40 (d, J = 13.8 Hz, 6H), 0.81 (d, J = 1.1 Hz, 3H).

Synthesis of 2-(azidomethyl)-2-methylpropane-1,3-diol (5): Compound (4) (7.05 g, 40.3 mmol) was dissolved in 35 ml of methanol. 7.00 g of a Dowex, acid resin was added, and the reaction mixture was stirred for 12 h at 50°C. When the reaction was complete, the Dowex was filtered off in a vacuum filter under a low vacuum and carefully washed with methanol. The methanol was evaporated to give 5.41 g of white crystals with a 93% yield. ^{1}H NMR (400 MHz, $CDCl_3$) δ 3.73–3.58 (m, 4H), 3.56–3.43 (m, 2H), 2.19 (s, 2H), 0.89 (d, J = 2.0 Hz, 3H).

Synthesis of A-MPA-4-AC (6): 2,2,5-trimethyl-1,3-dioxane-5-carboxylic acid was prepared using similar method mentioned in compound (2) synthesis. 2,2,5-trimethyl-1,3-dioxane-5-carboxylic acid (6.48 g, 37.2 mmol), 1,1′-carbonyldiimidazole (CDI) (9.05 g, 55.8 mmol) were dissolved in 30 ml of ethyl acetate and it was stirred 1 h at 50°C. CsF (0.75 g, 4.93 mmol), Compound (5) (1.80 g, 12.4 mmol) were dissolved in 10 ml of ethyl acetate separately, and it was slowly added to the reaction mixture under nitrogen at 50°C. It was stirred for 12 h. When the reaction was complete 200 ml DI water was added and allowed to stir for 2 h at room temperature. Then it was extracted with 1 M HCl (200 ml × 3), 1 M $NaHSO_4$ (200 ml × 3), 10% Na_2CO_3, saturated NaCl (200 ml), and it was dried under anhydrous $MgSO_4$. Ethyl acetate was evaporated to give 5.22 g of colorless oil liquid with a 92% yield. ^{1}H NMR (500 MHz, $CDCl_3$) δ 4.21 (d, J = 11.7 Hz, 4H), 4.13–4.09 (m, 4H), 3.68 (d, J = 11.7 Hz, 4H), 3.42–3.39 (m, 2H), 1.43 (d, J = 32.2 Hz, 12H), 1.18 (d, J = 1.6 Hz, 6H), 1.08 (d, J = 1.5 Hz, 3H).

Synthesis of A-MPA-4-OH (7): Compound (6) (5.00 g, 10.9 mmol) was dissolved in 20 ml of methanol. 5.00 g of a Dowex, acid resin was added, and the reaction mixture was stirred for 12 h at 50°C. When the reaction was complete the Dowex, acid resin was filtered off in a vacuum filter under a low vacuum and carefully washed with methanol. The methanol was evaporated to give 3.96 g of colorless liquid with a 96% yield. ^{1}H NMR (300 MHz, $CDCl_3$) δ 4.09 (s, 4H), 3.88 (d, J = 11.2 Hz, 4H), 3.78–3.67 (m, 4H), 3.43 (s, 4H), 3.38 (s, 2H), 1.12–1.09 (m, 6H), 1.09–1.07 (m, 3H).

Synthesis of A-MPA-4-ala (8): *N*-boc-alanine (3.70 g, 19.6 mmol), 1,1′-carbonyldiimidazole (CDI) (3.49 g, 21.5 mmol) were dissolved in 30 ml of dry ethyl acetate, and it was stirred for 1 h at 50°C. CsF (0.43 g, 2.81 mmol), compound (7) (1.23 g, 3.26 mmol) were dissolved in 5 ml of dry ethyl acetate and it was slowly added to the reaction mixture under nitrogen at 50°C. It was stirred for 12 h. When the reaction was complete 250 ml DI water was added and allowed to stir for 2 h at room temperature. Then it was extracted with 1 M HCl (200 ml × 3), 1 M $NaHSO_4$ (200 ml × 3), 10% Na_2CO_3, saturated NaCl (200 ml), and it was dried under anhydrous $MgSO_4$. Ethyl acetate was evaporated to give 3.15 g with a 91% yield. ^{1}H NMR (400 MHz, $CDCl_3$) δ 5.19 (s, 4H), 4.31–4.19 (m, 8H), 4.02 (d, *J* = 2.4 Hz, 4H), 3.38 (q, *J* = 6.2 Hz, 8H), 3.33 (s, 2H), 2.55 (t, *J* = 5.9 Hz, 8H), 1.27 (s, 6H), 1.02 (s, 3H).

Synthesis Route of TRPZ-bisMPA

Synthesis of 3,4-dichloro-1-(prop-2-yn-1-yl)-1H-pyrrole-2,5-dione (9): A total of 0.40 g of dichloromaleimide (2.40 mmol) and 2-ethylhexylbromide (0.48 ml, 2.9 mmol) and DMF (10 ml) in a 2-neck round bottom flask under nitrogen. The mixture was vigorously stirred at 140°C for 24 h. After that, the solution was quenched with 0.1 M HCl and extracted with diethyl ether. The organic layer was dried over Na_2SO_4 and concentrated under reduced pressure, and purification by silica gel column chromatography (30% DCM/Hexane) resulted in a cream-colored powder of *N*-(propargyl) dichloromaleimide (0.554 g, 90%). ^{1}H NMR (400 MHz, $CDCl_3$) δ 4.31–4.30(d), 2.23(s).

Synthesis of TRPZ-Propagyl (10): A mixture of 2-aminothiophenol (0.386 g, 2.8 mmol) and *N*-(propargyl) dichloromaleimide (0.30 g, 1.4 mmol) was dissolved in 24 ml of acetic acid. The reaction mixture was refluxed under a nitrogen atmosphere for 24 h. After being cooled to room

temperature, the mixture was quenched with brine and extracted with ethyl acetate. The organic layer was separated, dried over anhydrous Na_2SO_4, and concentrated under reduced pressure. The product was purified via flash column chromatography (30% chloroform/hexane) and obtained as orange solid (0.18 g, 50%). ^{1}H NMR (400 MHz, chloroform-*d*) ^{1}H NMR (400 MHz, $CDCl_3$) δ 7.72 (d, J = 8.0 Hz, 2H), 7.34–7.26 (m, 4H), 7.18 (ddd, J = 8.3, 7.2, 1.4 Hz, 2H), 5.20 (s, 2H), 2.29 (t, J = 2.5 Hz, 1H). ^{13}C NMR (75 MHz, $CDCl_3$) δ 148.79, 136.97, 130.48, 128.26, 127.11, 126.57, 111.17, 77.23, 73.36, 33.08. ^{1}H–^{1}H correlation spectroscopy (COSY) spectrum is provided in the SI. HRMS (ESI/Q-TOF) m/z: $[M + H]^+$ Calcd for $C_{19}H_{11}N_3S_2$ 345.0394; Found 345.0365 with an isotope pattern similar to the predicted pattern.

Synthesis of TRPZ-bisMPA-amine-BOC (11): This procedure was modified from previously reported procedures (Ihre et al., 1998). To the stirred solution of A-MPA-4-ala (0.60 g, 0.56 mmol), TRPZ-propagyl (0.29 g, 0.84 mmol) in 8 ml of DMF, CuBr (322 mg, 2.21 mmol) was added under nitrogen flushing. After complete addition, *N,N,N′,N″,N″*-pentamethyldiethylenetriamine (PMDETA) (388 mg, 2.30 mmol) was added and allowed to stir under nitrogen at 55°C for 48 h. The reaction mixture was precipitated to 200 ml diethyl ether. After settling, the diethyl ether layer was decanted, and the remaining product was air-dried. This precipitation, decanting, and the air-drying process was repeated twice more. The crude product was dissolved in 100 ml of DCM. It was extracted with 0.1 M EDTA solution. It was further purified using size exclusion chromatography (Sephadex LH-20) to give 0.59 g of TRPZ-bisMPA-amine-Boc with 74% yield. ^{1}H NMR (400 MHz, DMSO-d_6) δ 8.03 (s, 1H), 7.51 (d, *J* = 7.9 Hz, 2H), 7.44 (d, *J* = 8.0 Hz, 2H), 7.32 (t, *J* = 7.6 Hz, 2H), 7.22 (t, *J* = 7.6 Hz, 2H), 6.77 (s, 4H), 5.32 (s, 2H), 4.41 (s, 2H), 4.16 (d, *J* = 11.9 Hz, 8H), 3.94 (s, 4H), 3.12 (d, *J* = 6.4 Hz, 8H), 2.41 (t, *J* = 7.4 Hz, 8H), 1.34 (s, 36H), 1.17 (d, *J* = 20.4 Hz, 6H), 0.84 (s, 3H). HRMS (ESI/Q-TOF) m/z: [M + H]+ Calcd for $C_{66}H_{90}N_{10}O_{20}S_2$ 1407.5852; Found 1407.5813 with an isotope pattern similar to the predicted pattern.

Synthesis of TRPZ-bisMPA (12): TRPZ-bisMPA-amine-Boc was dissolved in 5 ml of chloroform and 2 ml of trifluoroacetic acid (TFA) was slowly added and stirred for 45 min. The reaction mixture was air-dried and dissolved in 10 ml of chloroform. It was added dropwise to 500 ml of diethyl ether and stirred for 2 h. It was filtered, and the precipitation procedure was repeated three times. Finally, the resulting solid was put under the vacuum for 24 h to give 0.39 g of the pure product with 93% yield. The formation of the **TRPZ-bisMPA** was confirmed via the disappearance of BOC groups (1.34 ppm). ^{1}H NMR (400 MHz, DMSO-d_6) δ 8.07 (s, 1H), 7.53 (d, *J* = 7.8 Hz, 2H), 7.44 (d, *J* = 7.8 Hz, 2H), 7.33 (t, *J* = 7.7 Hz, 2H), 7.24 (t, *J* = 7.6 Hz, 2H), 5.33 (s, 2H), 4.42 (s, 2H), 4.22 (d, *J* = 11.5 Hz, 8H), 3.94 (s, 4H), 3.01 (q, *J* = 6.2 Hz, 8H), 2.64 (d, *J* = 7.1 Hz, 8H), 1.17 (s, 6H), 0.85 (s, 3H).

Preparation and Characterization of Nanoparticles

For the nanoprecipitation method (Chandrasiri et al., 2020), 100 μL tetrahydrofuran (THF) was used as the organic solvent to dissolve 2 mg of **TRPZ-bisMPA** separate glass vial. The solution was added dropwise to a separate vial of Milli-Q water at pH 7.0 (2 ml) while gently stirring to obtain a 1 mg/ml final concentration. THF was allowed to evaporate under a stream of nitrogen. NP solutions were allowed to equilibrate for 12 h before further study.

TRPZ-127 NPs was prepared and modified according to the previously reported procedure (Wu et al., 2017). First, **TRPZ-PG** (2 mg) was dissolved under rapid sonication in THF (2 ml). Then, a THF solution (1 ml) containing **TRPZ-PG** (1 mg/ml) and Pluronic F-127 (5 mg/ml) was used to prepare **TRPZ-127 NPs** by rapidly injecting the solution into deionized water (1 ml) under continuous sonication using a bath sonicator. After sonication for an additional 1 min, THF was evaporated under a nitrogen atmosphere.

Aggregate sizes and ζ-potentials measurements were carried out on a Malvern Instrument Zetasizer Nano ZS using a He–Ne laser with a 633 nm wavelength, a detector angle of 173° at 25°C. The size measurements were performed in triplicate for each sample at 0.5 mg/ml concentration to ensure consistency. The morphological study of the aggregates formed from the NPs was carried out by TEM using a JEOL 1230 TEM operated at 100 kV to collect the TEM images using a Gatan Orius 831 bottom mounted CCD camera.

Absorption and Photoluminescence Assessment

The absorption measurements were done on a Varian Cary-5000 spectrometer (Dorval, QC, Canada). While the fluorescence studies were performed on Horiba Quantamaster fluorimeter with a xenon lamp and PMT detector using glass cuvettes. Fluorescence quantum yields were measured with samples of low sample concentration (10^{-5} M) and excited close to their maximum absorption. The spectroscopic energy gap (E_g^{opt}) was calculated from the onset of absorbance (Li et al., 2012).

Cell Viability, Treatment and Imaging

Human embryonic kidney (HEK293) cells were used for the assay. HEK cells were grown under standard conditions (37°C, 5% CO_2, DMEM media with 10% FBS). Nanoparticles were added to tissue culture media and allowed 24 h incubation period in cytotoxicity studies. Cytotoxicity of the nanoparticles was evaluated with a CyQUANT LDH Cytotoxicity Assay Kit (Invitrogen) using a microplate reader (BioTek Synergy H1). Following manufacturer protocols, both negative and positive controls are used in the assay. Experimental values are transformed based on two values: zero-cytotoxicity value (background) and 100% cytotoxicity value (cells treated with lysis buffer based on manufacturer protocol). Each experiment is represented by relative values based on the control values. Imaging of particle distribution in cells was done 30 min after the addition of 10 μg/ml NPs to culture media. TRPZ fluorescence in HEK cells was observed with a Leica Stellaris STED confocal microscope using both conventional and STED modes.

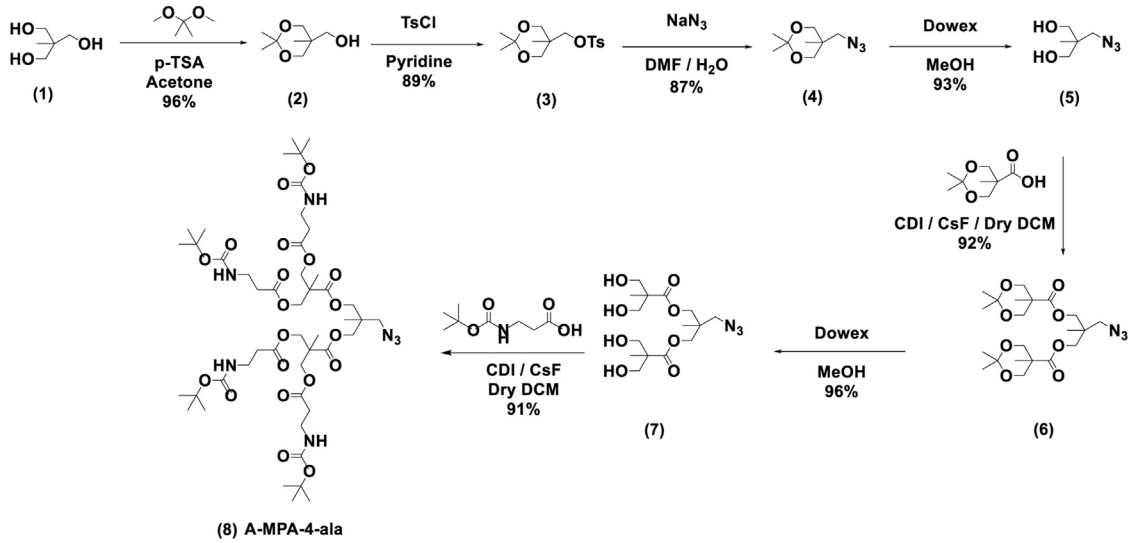

SCHEME 1 | Synthesis of dendron segment, A-MPA-4-ala; the synthesis was modified accordingly using previously reported procedures (Yaddehige et al., 2020).

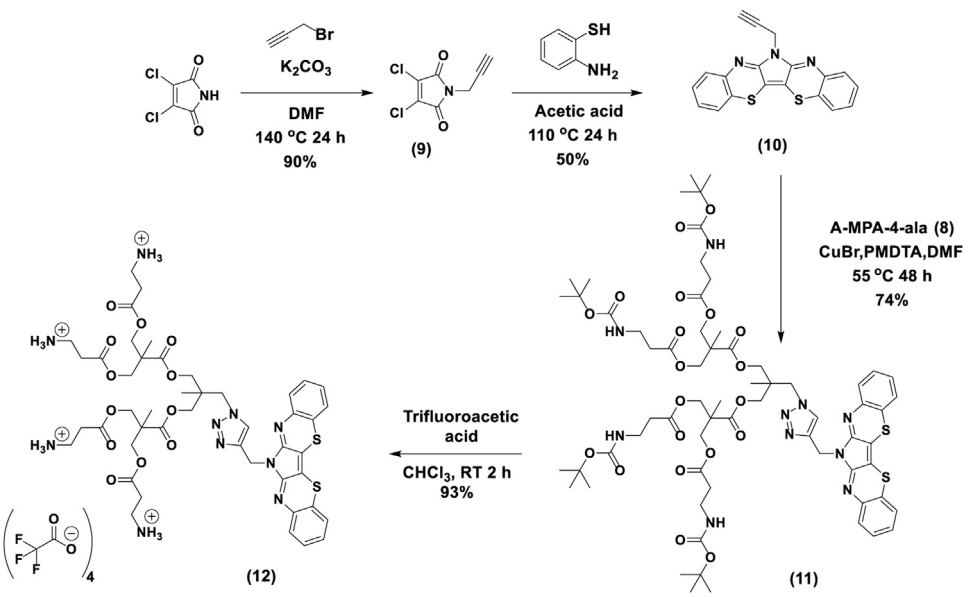

SCHEME 2 | Synthesis route for TRPZ-bisMPA.

RESULTS AND DISCUSSION

Design and Synthesis

TRPZ, first discovered by Dimroth and Reicheneder (1969), possesses a simple yet fascinating molecular structure. Its pi-framework and redox properties have made it beneficial in the field of organic electronics. TRPZ, being planar in structure, can undergo efficient crystalline packing via intermolecular sulfur–sulfur interactions and hydrogen bonding between pyrrole hydrogens and thiazine nitrogens (Hong et al., 2008; Hong et al., 2009). The molecule has multiple reactive sites which can be functionalized to increase its solubility and be further developed using electron-withdrawing and electron-donating groups to afford donor-acceptor oligomers with exceptional optical properties.

Based on its unique properties, we aimed to expand the application of this unique emissive building block towards bioimaging. However, due to its hydrophobic nature, we sought to modify TRPZ via N-substitution of the central pyrrole to produce a self-assembling amphiphile. To induce

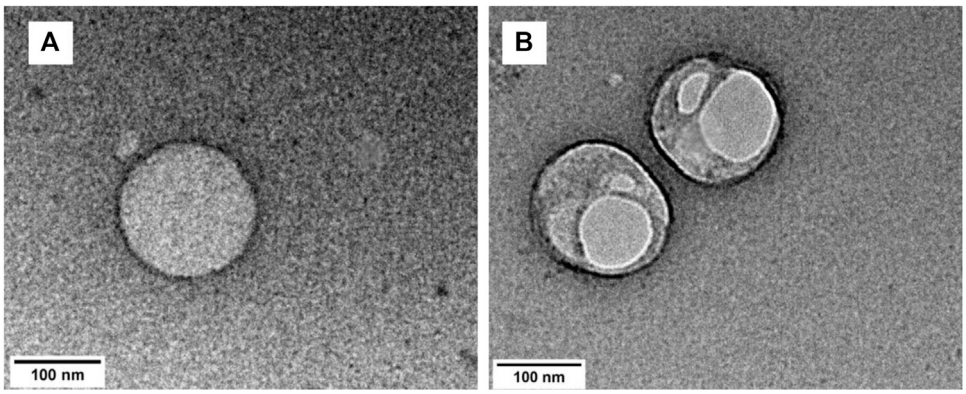

FIGURE 2 | TEM image of a TRPZ-bisMPA NPs **(A)** and TEM image of a TRPZ-127 NPs **(B)** in Milli-Q water from nanoprecipitation method. Additional images are provided in the SI.

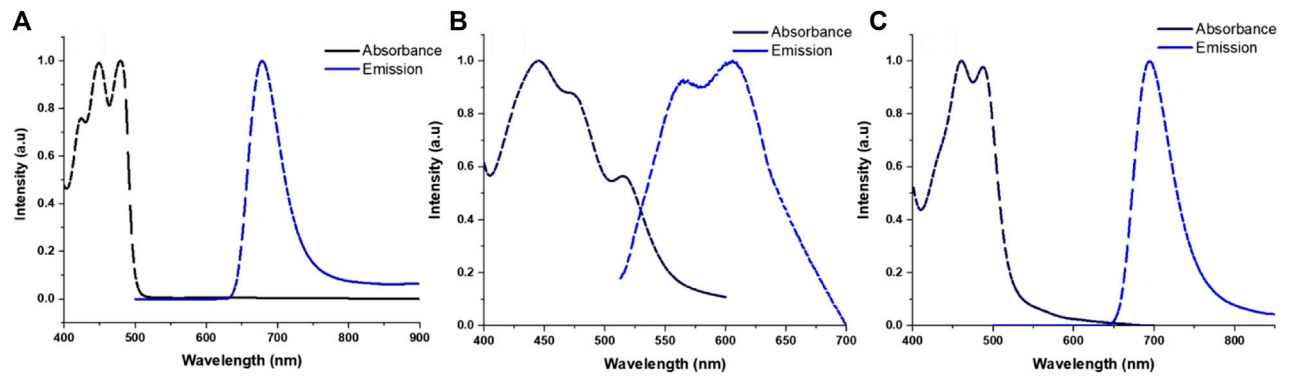

FIGURE 3 | Normalized absorbance and emission profiles for TRPZ-PG **(A)** in THF, TRPZ-127 NPs **(B)** and TRPZ-bisMPA NPs **(C)** in Milli-Q water.

amphiphilicity and promote self-assembly, bisMPA was selected as the dendritic segment. A hydrophilic moiety, its synthetic accessibility allows esterification under mild reaction conditions and provides a level of biodegradability and biocompatibility (Feliu et al., 2012). Additionally, it was capped with alanine to afford a cationic surface to increase colloidal stability, cellular uptake and better its water solubility (Gessner et al., 2002; Lipfert et al., 2014; Dragoman et al., 2017). This amphiphilic property is expected to make TRPZ capable of forming NPs independently, **TRPZ-bisMPA NPs**.

The resulting NP morphology is anticipated to be that of a micelle structure in which the dendron extends towards the hydrophilic water surface protecting the hydrophobic TRPZ portion within the core. The positively charged terminal ends of the amphiphile would effectively stabilize the NPs via electrostatic interactions.

In parallel, we compared NPs formed from **TRPZ-bisMPA** with conventional nanostructures in which a surfactant polymer is employed to encapsulate hydrophobic dyes. We encapsulated **TRPZ-PG** into a water-soluble polymer surfactant (Pluronic F-127), **TRPZ-127 NPs**. Although frequently employed, the encapsulation strategy has significant drawbacks (e.g., poor loading) that limit its application. Often the nature of the molecule being encapsulated has varying physiochemical properties that contrast to the solubilizing block of the amphiphilic polymer being employed. This, of course, leads to lower encapsulation efficiencies and can destabilize the resulting nanostructure (Jeong et al., 2020). By assessing the two NP systems, **TRPZ-bisMPA NPs** and **TRPZ-127 NPs**, we aim to explore the former as a versatile molecular bioimaging probe suitable for numerous biomedical applications.

The synthesis of the dendron segment, A-MPA-4-ala (8), is shown in **Scheme 1**, which consists of a seven-step synthetic route. In the first step, the 1,3-diol moiety of bisMPA (1) was protected to afford compound 2 by reaction of bisMPA with 2,2-dimethoxypropane and a catalytic amount of p-toluenesulfonic acid (TsOH) in dry acetone. In order to make the hydroxyl group a better leaving group, compound 2 was reacted with p-toluenesulfonyl chloride (TsCl) in pyridine to obtain compound 3. The next step, the azido group, was substituted using sodium azide (NaN_3) and DMF to obtain compound 4. The

TABLE 1 | Optical properties of the TR-PZ systems dye in THF[a] and NPs in water[b].

TR-PZ systems	λ_{abs}^{max} (nm)	E_g^{opt} (eV)	λ_{ems}^{max} (nm)	Stokes shift (nm, eV)	Φ (%)	τ (ns)
TRPZ-PG[a]	447, 478	2.46	678	200 (0.76)	79	5.3
TRPZ-127 NPs[b]	452, 480, 515	2.48	563, 606	126 (0.54) 83 (0.38)	<0.5	t_1 = 0.8 (66.9%),t_2 = 5.7 (33.1%)
TRPZ-bisMPA NPs[b]	460, 494	2.52	695	201 (0.72)	49	6.3

following step was carried out to deprotect dimethoxy moiety using an anion exchange resin-Dowex to obtain compound 5. Before proceeding to the next step, 2,2,5-trimethyl-1,3-dioxane-5-carboxylic acid was synthesized using a similar method to compound 2. Then, 2,2,5-trimethyl-1,3-dioxane-5-carboxylic acid was employed in a Malkoch esterification (García-Gallego et al., 2015) with compound 5, using 1,1′-carbonyldiimidazole (CDI) to activate the carbonyl group and cesium fluoride (CsF) as a catalyst to obtain compound 6. Dowex deprotection was done in the next step to obtain compound 7. The final step was esterification between beta-alanine and compound 7 to obtain A-MPA-4-ala.

The synthesis of **TRPZ-bisMPA** (12) consists of four synthetic steps (**Scheme 2**). First, dichloromaleimide was propargylated at the nitrogen position to obtain compound 9. **TRPZ-PG** was synthesized *via* a condensation method between 2-aminothiophenol and *N*-(propargyl) dichloromaleimide (compound 10). Then **TRPZ-PG** (10) and A-MPA-4-ala (8) were reacted using click-chemistry to obtain TRPZ-bisMPA-amine-Boc (compound 11). Finally, acid was used for deprotection of the tert-butyl carbamates (BOC) protected amine groups to afford a cationic terminated **TRPZ-bisMPA** amphiphile (compound 12).

Self-Assembly and Nanoparticle Formation

The particle formation for **TRPZ-bisMPA** was done by nanoprecipitation. The hydrodynamic diameter was analyzed via dynamic light scattering (DLS) (**Supplementary Figure S8A**). **Supplementary Table S1** summarizes the sizes and surface charges for the NPs formed. Nanoprecipitation affords NPs with a spherical morphology possessing a hydrodynamic diameter of 129.9 nm (±20). The polydispersity (PDI) for **TRPZ-bisMPA NPs** indicated high uniformity with values around 0.2. **Figure 2A** shows transmission electron microscopy (TEM) images for **TRPZ-bisMPA NPs**. TEM images support DLS data and provide direct evidence of NP formation with a diameter of 155.1 nm (±16).

For comparison, **TRPZ-PG** was encapsulated with Pluronic F-127 (Mw = 12.6 kDa). It is not readily soluble in water unless incorporated within a water-soluble surfactant. Pluronic F-127 is known to self-assembly independently with sizes that are much smaller than those observed in this study (<50 nm) (Domínguez-Delgado et al., 2016). The DLS data indicates a larger NPs assembly than that of **TRPZ-bisMPA NPs. TRPZ-127 NPs** exhibit a hydrodynamic diameter of 323.5 nm (±97 nm) (**Supplementary Figure S8B**) and PDI of 0.19. TEM images of **TRPZ-127 NPs** show spherical assemblies with average diameters of 181.5 nm (±66) (**Figure 2B**). The encapsulation efficiency (EE%) of 38.5% and dye loading efficiency (DL%) of 7.1% are tabulated in the SI.

Surface properties of the NPs *via* ζ-potential values aid in supporting the sizes obtained from DLS and TEM. The ζ-potential, which depends on the surface charge, is essential for the stability of NPs in suspension. Additionally, it is a critical factor in regards to the function and toxicity of NPs specifically for biological application. TRPZ-bisMPA NPs exhibit ζ-potentials of 17.2 mV. The positive charge results from the outer surface consisting of cationic amines. In contrast, TRPZ-127 NPs show -0.5 mV of average surface charge, which is close to neutral due to the lack of charge on the polymer surfactant used. The positive surface charge on TRPZ-bisMPA NPs corresponds to small and more stable aggregates (Kumar and Dixit, 2017).

Photophysical Properties

The normalized absorption and emission spectra of TRPZ and its NPs are shown in **Figure 3** with additional photophysical data tabulated in **Table 1**. In a comparison of **TRPZ-PG** fluorophore with the two NP suspensions, **TRPZ-PG** shows two major absorbance peaks at 447 and 478 nm in THF (**Figure 3A**). The band at 447 nm can be assigned to the pi to pi* electronic transition of the phenyl rings. Bands at 478 nm are assigned to the n to pi* transitions. The calculated optical band gap of the **TRPZ-PG** is 2.46 eV (onset: 504 nm). The emission maximum of the fluorophore is at 678 nm with a Stokes shift of 0.76 eV (200 nm). Note that the propargyl group does not contribute to the observed photophysical properties via pi orbital overlap.

For the NPs, noticeable broadening and red-shifting (2–16 nm) in the spectra suggest enhanced intermolecular interactions due to aggregation in the NP core. **TRPZ-127 NPs** display three absorbance peaks at 452 nm, 480 nm, and 515 nm in water, as shown in normalized absorbance spectra (**Figure 3B**). Compared to both **TRPZ-PG** and **TRPZ-bisMPA NPs**, a peak shoulder at 515 nm is observed, presumably due to a differing aggregation pattern within the particle. **TRPZ-127 NPs** possess a weak emission and is blue-shifted towards 563 and 606 nm relative to **TRPZ-PG**.

Interestingly there is a contrast in optical properties between the amphiphile and encapsulated **TRPZ**. **TRPZ-bisMPA NPs** show absorbance peaks at 460 and 494 nm in water (**Figure 3C**). Upon excitation, **TRPZ-bisMPA NPs** exhibit a strong neon green fluorescence with an emission band centered at 695 nm and a Stokes shift of 0.72 eV (201 nm). The optical profile for **TRPZ-bisMPA NPs** resembles that of "free" **TRPZ-PG** in THF, with a

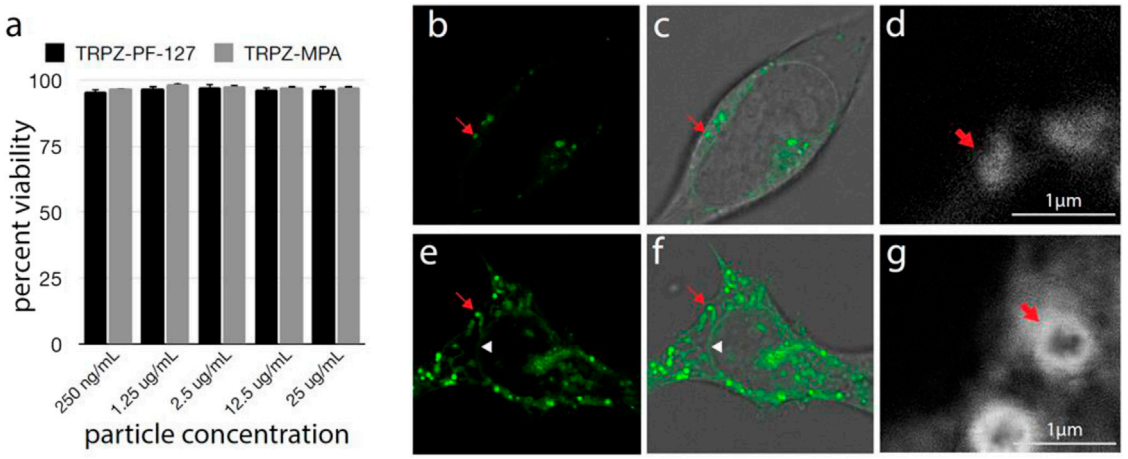

FIGURE 4 | Cell viability and uptake of TRPZ nanoparticles **(A)** Percent cell viability after treatment with TRPZ-bisMPA NPs and TRPZ-127 NPs. Concentrations tested listed below. No significant difference was seen between any condition as determined by Tukey ANOVA **(B–G)**. Fluorescence microscopy of TRPZ-bisMPA NPs **(B–D)** and TRPZ-127 NPs **(E–G)** localization after cell loading. Images were acquired by conventional confocal microscopy **(B,E)** or STED **(D,G)**. Brightfield images were overlaid with fluorescence imaging **(C,F)**. Red arrow indicates a labeled lysosome. White triangle in TRPZ-127 NPs images shows nuclear membrane. Enlargement located in the SI.

20 nm red shift for the latter. This behavior is presumably due to an aggregation behavior that is reminiscent of a monomeric form (e.g., "free" or non-aggregated **TRPZ-PG** form) of the dye with extended electron delocalization. The weaker emission of **TRPZ127 NPs** relative to **TRPZ-bisMPA NPs** is supported by a negative solvatochromism observed for **TRPZ-PG** (**Supplementary Figure S13**). These results suggest that **TRPZ-PG** possesses a nonpolar excited state and can form high-energy aggregates (e.g., H-aggregates) that are not dominant with the amphiphilic derivative.

The Stokes shifts observed for the molecules and NP suspension are quite significant. Large Stokes shifts are important when overcoming spectral overlapping to retain good signal-to-noise ratios for bioimaging applications. Additionally, a large Stokes shift can be indicative of a number of photophysical causes such as intramolecular charge transfer (ICT), (Yang et al., 2013), low reorganization energy, (Chen et al., 2019), and exciplex formation (Horváth et al., 2015). Among the aforementioned reasons, the Stokes shifts observed for TRPZ and its NPs are presumably due to the emission facilitated by the proaromatic pyrrole trapped in the quinoidal structure (Wu et al., 2010; Brogdon et al., 2016). Computational calculations for **TRPZ-bisMPA** support this notion where HOMO orbitals showed proaromatic molecular orbitals (MOs) and an aromatic excited state (LUMO) predominately at the pyrrole ring (**Supplementary Figure S10**). Electron localization function (ELF) and localized-orbital locator (LOL) analysis and profiles (**Supplementary Figure S11**) were employed to further support our hypothesis regarding proaromaticity. ELF has been widely used to evaluate electron localization while LOL offers insight on localized bonding features (Schmider and Becke, 2000; Tsirelson and Stash, 2002). Using the ELF-pi analysis, the aromatic rings display high electron delocalization where they are clearly separated from those with localized bonding. As expected, the ELF-pi values and analysis of bond orbitals confirm aromaticity. Additionally, localization functions show aromaticity following excitation which is a signature of proaromaticity (Cocq et al., 2015).

Along with a large Stokes shift, **TRPZ-bisMPA NPs** possess a high quantum yield (Φ) in water, Φ = 49%. Typically, the Φ for conventional bioimaging dyes are much lower in water due to unfavorable solvent-solute interactions, which induce non-radiative pathways and quench emission (Lakowicz, 2006; Hong et al., 2016). In this case, self-assembly of the amphiphile reduces dye-water interactions and aids to maintain the optical properties of a monomeric form of the dye (e.g., **TRPZ-PG**) (Zhegalova et al., 2014). **TRPZ-127 NPs** show weaker emission and lower Φ of 0.5% in water, most likely due to a variation in the aggregation patterns of TRPZ and the formation of H-aggregates inside the NP. **TRPZ-PG** fluorophore displays a decent Φ in organic solvents (Φ = 79% in THF). However, due to its poor solubility, comparison in aqueous media was not achievable.

Experimental lifetime plots are shown in SI (**Supplementary Figures S14–S16**). Fluorescent lifetime (τ) expresses the time allocated by a fluorophore in the excited state before relaxing to the ground state. Additionally, fluorescence lifetime measurements are highly sensitive to the surrounding environment (Boreham et al., 2016). **TRPZ-PG** in THF shows a signal exponential component of 5.3 ns and **TRPZ-bisMPA NPs** exhibits a lifetime of 6.3 ns. In contrast, **TRPZ-127 NPs** shows a dual exponential lifetime: t_1 of 0.8 ns and t_2 of 5.7 ns. The two exponentials are due to both the aggregated and monomeric (e.g., non-aggregated) form being present inside the NP. When compared with **TRPZ-PG** and the absence of a lower (t_1) value, the lifetime of 0.8 ns can be assigned to high-energy aggregates, which in this case is the dominant form (66.9%).

Cellular Viability, Uptake, and Imaging

The impact of the NPs on cell viability was tested by LDH assay (**Figure 4A**). Even at very high concentrations, a negligible effect was seen on cell viability. Analysis by Tukey ANOVA found no significant difference between conditions. *In vivo* testing will be needed to further assess the effect of the NPs on physiology; however, these results suggest our NPs will be well-tolerated in biological environments.

Confocal microscopy found that both **TRPZ-bisMPA NPs** and **TRPZ-127 NPs** accumulate most significantly in endosomes (**Figures 4B–G**). The cationic surface charge of **TRPZ-bisMPA NPs** leads to apparent cellular uptake via electrostatic interactions with anionic cell membranes. Similar results have been observed with other dendrimer-based NPs modified with anime groups (Morris et al., 2017; Ray et al., 2018; Ingle et al., 2020). Likely owing to the polar groups on the MPA dendron, TRPZ fluorescence is observed throughout the interior of the lysosome (**Figure 4D**).

TRPZ-127 NPs show not only accumulation in the lysosome but also labeling of various cellular membranes, including nuclear membranes (**Figures 4E,F**). Staining of the nuclear membrane indicates that TRPZ fluorescence has spread throughout the endomembrane system, trafficking all the way to the endoplasmic reticulum (ER). Stimulated emission depletion microscopy (STED) images of **TRPZ-127 NPs** and **TRPZ-bisMPA NPs** aid in comparing cellular uptake where fluorescence labeling is localized to the membrane of the organelle and not the interior, as observed with **TRPZ-bisMPA NPs** (**Figures 4D,G**; **Supplementary Figure S17**). It appears that **TRPZ-127** is much more aggressively loading into cells; however, this is not the case. We speculate that the encapsulated dye may have escaped its NPs and, due to its hydrophobic nature, became embedded into membrane interiors. The unloaded dye being hydrophobic actively segregates into cells while **TRPZ-bisMPA NPs** remain intact and localized in the lysosome.

CONCLUSION

In summary, a comparative analysis of two NP systems was conducted. Evaluation via spectroscopic, light scattering and microscopic techniques confirm colloidal stability and provided insight on photophysical properties of the molecular scaffold as a potential bioimaging agent. Cell viability studies indicate low cytotoxicity of the materials and their suitability for biological application. However, cellular distribution of TRPZ originating from the two sets of NPs suggests a fundamentally different interaction with cells. Such results suggest that a variation in formulation could be used for different fundamental applications. Overall the approach described here opens up avenues towards developing fluorescent NPs from a simple yet appealing scaffold to afford materials with tuneable properties for bioimaging applications.

DATA AVAILABILITY STATEMENT

The original contributions presented in the study are included in the article/**Supplementary Material**, further inquiries can be directed to the corresponding author.

AUTHOR CONTRIBUTIONS

TR, MY, JV, and DW developed the project and conceived the experiments. TR, MY, and JV synthesized the target molecules, formulated the NPs and conducted baseline colloidal studies. TR, CS, and NH performed the characterizations of optical properties and interpreted the photophysical results. WK and GH contributed the theoretical simulations. JN, IO, and AF conducted cytotoxicity and cellular uptake studies. TR, MY, and DW wrote the manuscript. All authors contributed to the scientific discussion.

ACKNOWLEDGMENTS

The authors would like to thank Mississippi INBRE (P20GM103476) and National Science Foundation (CBET MRI 2019023 and OIA 1757220) for providing the funding for this study.

SUPPLEMENTARY MATERIAL

The Supplementary Material for this article can be found online at: https://www.frontiersin.org/articles/10.3389/fchem.2021.729125/full#supplementary-material

REFERENCES

Ando, N., Soutome, H., and Yamaguchi, S. (2019). Near-infrared Fluorescein Dyes Containing a Tricoordinate boron Atom. *Chem. Sci.* 10 (33), 7816–7821. doi:10.1039/C9SC02314C

Boreham, A., Brodwolf, R., Walker, K., Haag, R., and Alexiev, U. (2016). Time-Resolved Fluorescence Spectroscopy and Fluorescence Lifetime Imaging Microscopy for Characterization of Dendritic Polymer Nanoparticles and Applications in Nanomedicine. *Molecules* 22 (1), 17. doi:10.3390/molecules22010017

Brogdon, P., Giordano, F., Puneky, G. A., Dass, A., Zakeeruddin, S. M., Nazeeruddin, M. K., et al. (2016). A Computational and Experimental Study of Thieno[3,4-B]thiophene as a Proaromatic π-Bridge in Dye-Sensitized Solar Cells. *Chem. Eur. J.* 22 (2), 694–703. doi:10.1002/chem.201503187

Chandrasiri, I., Abebe, D. G., Loku Yaddehige, M., Williams, J. S. D., Zia, M. F., Dorris, A., et al. (2020). Self-Assembling PCL-PAMAM Linear Dendritic Block Copolymers (LDBCs) for Bioimaging and Phototherapeutic Applications. *ACS Appl. Bio Mater.* 3 (9), 5664–5677. doi:10.1021/acsabm.0c00432

Chen, W.-C., Chou, P.-T., and Cheng, Y.-C. (2019). Low Internal Reorganization Energy of the Metal-Metal-To-Ligand Charge Transfer Emission in Dimeric Pt(II) Complexes. *J. Phys. Chem. C* 123 (16), 10225–10236. doi:10.1021/acs.jpcc.9b00224

Choi, H. S., and Frangioni, J. V. (2010). Nanoparticles for Biomedical Imaging: Fundamentals of Clinical Translation. *Mol. Imaging* 9 (6), 291–310. doi:10.2310/7290.2010.00031

Cocq, K., Lepetit, C., Maraval, V., and Chauvin, R. (2015). "Carbo-aromaticity" and Novel Carbo-Aromatic Compounds. *Chem. Soc. Rev.* 44 (18), 6535–6559. doi:10.1039/C5CS00244C

Dimroth, P., and Reicheneder, F. (1969). Novel Pigments from Dichloromaleimides. *Angew. Chem. Int. Ed. Engl.* 8 (10), 751–752. doi:10.1002/anie.196907512

Domínguez-Delgado, C. L., Fuentes-Prado, E., Escobar-Chávez, J. J., Vidal-Romero, G., Rodríguez-Cruz, I. M., and Díaz-Torres, R. (2016). "Chitosan and PluronicF-127: Pharmaceutical Applications," in *Encyclopedia of Biomedical Polymers and Polymeric Biomaterials* (New York, NY, USA: Taylor & Francis), 1513–1535. doi:10.1081/e-ebpp-120050057

Dragoman, R. M., Grogg, M., Bodnarchuk, M. I., Tiefenboeck, P., Hilvert, D., Dirin, D. N., et al. (2017). Surface-Engineered Cationic Nanocrystals Stable in Biological Buffers and High Ionic Strength Solutions. *Chem. Mater.* 29 (21), 9416–9428. doi:10.1021/acs.chemmater.7b03504

Feliu, N., Walter, M. V., Montañez, M. I., Kunzmann, A., Hult, A., Nyström, A., et al. (2012). Stability and Biocompatibility of a Library of Polyester Dendrimers in Comparison to Polyamidoamine Dendrimers. *Biomaterials* 33 (7), 1970–1981. doi:10.1016/j.biomaterials.2011.11.054

García-Gallego, S., Hult, D., Olsson, J. V., and Malkoch, M. (2015). Fluoride-Promoted Esterification with Imidazolide-Activated Compounds: A Modular and Sustainable Approach to Dendrimers. *Angew. Chem. Int. Ed.* 54 (8), 2416–2419. doi:10.1002/anie.201411370

Gessner, A., Lieske, A., Paulke, B. R., and Müller, R. H. (2002). Influence of Surface Charge Density on Protein Adsorption on Polymeric Nanoparticles: Analysis by Two-Dimensional Electrophoresis. *Eur. J. Pharma. Biopharm.* 54 (2), 165–170. doi:10.1016/S0939-6411(02)00081-4

Gil, H. M., Price, T. W., Chelani, K., Bouillard, J.-S. G., Calaminus, S. D. J., and Stasiuk, G. J. (2021). NIR-quantum Dots in Biomedical Imaging and Their Future. *iScience* 24 (3), 102189. doi:10.1016/j.isci.2021.102189

Grimm, J. B., Tkachuk, A. N., Xie, L., Choi, H., Mohar, B., Falco, N., et al. (2020). A General Method to Optimize and Functionalize Red-Shifted Rhodamine Dyes. *Nat. Methods* 17 (8), 815–821. doi:10.1038/s41592-020-0909-6

Haustein, E., and Schwille, P. (2007). Trends in Fluorescence Imaging and Related Techniques to Unravel Biological Information. *HFSP J.* 1 (3), 169–180. doi:10.2976/1.2778852

Hong, W., Wei, Z., Xi, H., Xu, W., Hu, W., Wang, Q., et al. (2008). 6H-Pyrrolo[3,2-b:4,5-b′]bis[1,4]benzothiazines: Facilely Synthesized Semiconductors for Organic Field-Effect Transistors. *J. Mater. Chem.* 18 (40), 4814–4820. doi:10.1039/B809486A

Hong, W., Wei, Z., Xu, W., Wang, Q., and Zhu, D. (2009). Synthesis and Properties of Heteroacenes Containing Pyrrole and Thiazine Rings as Promising N-type Organic Semiconductor Candidates. *Chin. J. Chem.* 27 (4), 846–849. doi:10.1002/cjoc.200990141

Hong, N. Y., Kim, H. R., Lee, H. M., Sohn, D. K., and Kim, K. G. (2016). Fluorescent Property of Indocyanine green (ICG) Rubber Ring Using LED and Laser Light Sources. *Biomed. Opt. Express* 7 (5), 1637–1644. doi:10.1364/boe.7.001637

Horváth, P., Šebej, P., Šolomek, T., and Klán, P. (2015). Small-Molecule Fluorophores with Large Stokes Shifts: 9-Iminopyronin Analogues as Clickable Tags. *J. Org. Chem.* 80 (3), 1299–1311. doi:10.1021/jo502213t

Ihre, H., Hult, A., Fréchet, J. M. J., and Gitsov, I. (1998). Double-Stage Convergent Approach for the Synthesis of Functionalized Dendritic Aliphatic Polyesters Based on 2,2-Bis(hydroxymethyl)propionic Acid. *Macromolecules* 31 (13), 4061–4068. doi:10.1021/ma9718762

Ingle, N. P., Hexum, J. K., and Reineke, T. M. (2020). Polyplexes Are Endocytosed by and Trafficked within Filopodia. *Biomacromolecules* 21 (4), 1379–1392. doi:10.1021/acs.biomac.9b01610

James, M. L., and Gambhir, S. S. (2012). A Molecular Imaging Primer: Modalities, Imaging Agents, and Applications. *Physiol. Rev.* 92 (2), 897–965. doi:10.1152/physrev.00049.2010

Jena, P. V., Cupo, C., and Heller, D. A. (2020). "Near Infrared Spectral Imaging of Carbon Nanotubes for Biomedicine," in *Near Infrared-Emitting Nanoparticles for Biomedical Applications*. Editors A. Benayas, E. Hemmer, G. Hong, and D. Jaque (Cham: Springer International Publishing)), 103–132. doi:10.1007/978-3-030-32036-2_6

Jeong, C., Noh, I., Rejinold, N. S., Kim, J., Jon, S., and Kim, Y.-C. (2020). Self-Assembled Supramolecular Bilayer Nanoparticles Composed of Near-Infrared Dye as a Theranostic Nanoplatform to Encapsulate Hydrophilic Drugs Effectively. *ACS Biomater. Sci. Eng.* 6 (1), 474–484. doi:10.1021/acsbiomaterials.9b01587

Khan, I., Saeed, K., and Khan, I. (2019). Nanoparticles: Properties, Applications and Toxicities. *Arabian J. Chem.* 12 (7), 908–931. doi:10.1016/j.arabjc.2017.05.011

Kumar, A., and Dixit, C. K. (2017). "Methods for Characterization of Nanoparticles," in *Advances in Nanomedicine for the Delivery of Therapeutic Nucleic Acids*. Editors S. Nimesh, R. Chandra, and N. Gupta (Cambridge, MA: Woodhead Publishing), 43–58. doi:10.1016/b978-0-08-100557-6.00003-1

Lakowicz, J. R. (2006). "Solvent and Environmental Effects," in *Principles of Fluorescence Spectroscopy* Editors J. R. Lakowicz (Boston, MA: Springer US), 205–235.

Li, S., Lu, X., Xue, Y., Lei, J., Zheng, T., and Wang, C. (2012). Fabrication of Polypyrrole/graphene Oxide Composite Nanosheets and Their Applications for Cr(VI) Removal in Aqueous Solution. *PloS One* 7 (8), e43328. doi:10.1371/journal.pone.0043328

Lipfert, J., Doniach, S., Das, R., and Herschlag, D. (2014). Understanding Nucleic Acid-Ion Interactions. *Annu. Rev. Biochem.* 83 (1), 813–841. doi:10.1146/annurev-biochem-060409-092720

Morris, C. J., Aljayyoussi, G., Mansour, O., Griffiths, P., and Gumbleton, M. (2017). Endocytic Uptake, Transport and Macromolecular Interactions of Anionic PAMAM Dendrimers within Lung Tissue. *Pharm. Res.* 34 (12), 2517–2531. doi:10.1007/s11095-017-2190-7

Mourdikoudis, S., Pallares, R. M., and Thanh, N. T. K. (2018). Characterization Techniques for Nanoparticles: Comparison and Complementarity upon Studying Nanoparticle Properties. *Nanoscale* 10 (27), 12871–12934. doi:10.1039/C8NR02278J

Ray, S., Li, Z., Hsu, C.-H., Hwang, L.-P., Lin, Y.-C., Chou, P.-T., et al. (2018). Dendrimer- and Copolymer-Based Nanoparticles for Magnetic Resonance Cancer Theranostics. *Theranostics* 8 (22), 6322–6349. doi:10.7150/thno.27828

Schmider, H. L., and Becke, A. D. (2000). Chemical Content of the Kinetic Energy Density. *J. Mol. Struct. THEOCHEM* 527 (1), 51–61. doi:10.1016/S0166-1280(00)00477-2

Tsirelson, V., and Stash, A. (2002). Determination of the Electron Localization Function from Electron Density. *Chem. Phys. Lett.* 351 (1), 142–148. doi:10.1016/S0009-2614(01)01361-6

Vogelsang, J., Cordes, T., Forthmann, C., Steinhauer, C., and Tinnefeld, P. (2009). Controlling the Fluorescence of Ordinary Oxazine Dyes for Single-Molecule Switching and Superresolution Microscopy. *Proc. Natl. Acad. Sci.* 106 (20), 8107–8112. doi:10.1073/pnas.0811875106

Wu, Y.-L., Bureš, F., Jarowski, P. D., Schweizer, W. B., Boudon, C., Gisselbrecht, J.-P., et al. (2010). Proaromaticity: Organic Charge-Transfer Chromophores with Small HOMO-LUMO Gaps. *Chem. Eur. J.* 16 (31), 9592–9605. doi:10.1002/chem.201001051

Wu, Y., Wang, K., Huang, S., Yang, C., and Wang, M. (2017). Near-Infrared Light-Responsive Semiconductor Polymer Composite Hydrogels: Spatial/Temporal-Controlled Release via a Photothermal "Sponge" Effect. *ACS Appl. Mater. Inter.* 9 (15), 13602–13610. doi:10.1021/acsami.7b01016

Yaddehige, M. L., Chandrasiri, I., Barker, A., Kotha, A. K., Dal Williams, J. S., Simms, B., et al. (2020). Structural and Surface Properties of Polyamidoamine (PAMAM) - Fatty Acid-based Nanoaggregates Derived from Self-assembling Janus Dendrimers. *ChemNanoMat* 6 (12), 1833–1842. doi:10.1002/cnma.202000498

Yang, G., Li, S., Wang, S., Hu, R., Feng, J., Li, Y., et al. (2013). Novel Fluorescent Probes Based on Intramolecular Charge- and Proton-Transfer Compounds. *Pure Appl. Chem.* 85 (7), 1465–1478. doi:10.1351/PAC-CON-13-02-06

Zhang, X., Gong, C., Akakuru, O. U., Su, Z., Wu, A., and Wei, G. (2019). The Design and Biomedical Applications of Self-Assembled Two-Dimensional Organic Biomaterials. *Chem. Soc. Rev.* 48 (23), 5564–5595. doi:10.1039/C8CS01003J

Zhang, Y., Fang, F., Li, L., and Zhang, J. (2020). Self-Assembled Organic Nanomaterials for Drug Delivery, Bioimaging, and Cancer Therapy. *ACS Biomater. Sci. Eng.* 6 (9), 4816–4833. doi:10.1021/acsbiomaterials.0c00883

Zhegalova, N. G., He, S., Zhou, H., Kim, D. M., and Berezin, M. Y. (2014). Minimization of Self-Quenching Fluorescence on Dyes Conjugated to Biomolecules with Multiple Labeling Sites via Asymmetrically Charged NIR Fluorophores. *Contrast Media Mol. Imaging* 9 (5), 355–362. doi:10.1002/cmmi.1585

Conflict of Interest: The authors declare that the research was conducted in the absence of any commercial or financial relationships that could be construed as a potential conflict of interest.

Publisher's Note: All claims expressed in this article are solely those of the authors and do not necessarily represent those of their affiliated organizations, or those of the publisher, the editors and the reviewers. Any product that may be evaluated in this article, or claim that may be made by its manufacturer, is not guaranteed or endorsed by the publisher.

frontiers in Chemistry

ORIGINAL RESEARCH
published: 21 December 2021
doi: 10.3389/fchem.2021.816069

Carboxylato-Pillar[6]arene-Based Fluorescent Indicator Displacement Assays for Caffeine Sensing

Qunpeng Duan, Yibo Xing and Kainan Guo*

School of Chemical and Printing-dyeing Engineering, Henan University of Engineering, Zhengzhou, China

In the present work, we have developed a new indicator displacement system based on pillararene for anionic water-soluble carboxylato pillar [6] arene (WP6) and aromatic fluorescent dye safranine T (ST). A large fluorescence enhancement and colour change of ST were observed after complexation with electron-rich cavity in WP6 because of host-guest twisted intramolecular charge-transfer interactions. The constructed pillararene-indicator displacement system can be applied for caffeine selective detection in water.

OPEN ACCESS

Edited by:
Tangxin Xiao,
Changzhou University, China

Reviewed by:
Xuan Wu,
Chinese Academy of Sciences(CAS), China
Jianzhuang Chen,
East China University of Science and Technology, China

***Correspondence:**
Qunpeng Duan
qpduan@haue.edu.cn

Specialty section:
This article was submitted to Supramolecular Chemistry, a section of the journal Frontiers in Chemistry

Received: *16 November 2021*
Accepted: *02 December 2021*
Published: *21 December 2021*

Citation:
Duan Q, Xing Y and Guo K (2021) Carboxylato-Pillar[6]arene-Based Fluorescent Indicator Displacement Assays for Caffeine Sensing. Front. Chem. 9:816069. doi: 10.3389/fchem.2021.816069

Keywords: pillararene, host-guest complex, fluorescent, indicator displacement assay, caffeine sensing

INTRODUCTION

Fluorescent indicator displacement assays (F-IDAs) are typically used to convert synthetic receptors into optical sensors in supramolecular chemistry. In F-IDAs, the competitive binding principle is used: after binding a fluorescent indicator to the receptor, when a competing analyte is introduced into the indicator–receptor pair, the indicator is discharged from the receptor to induce a fluorescence change (Wiskur, et al., 2001;Nguyen and Anslyn, 2006). Macrocyclic hosts typically provide ideal receptors for use because of their particular composition and excellent functions. The macrocyclic hosts, such as cyclodextrins (Crini, 2014; Pal, et al., 2015), calixarenes (Koh, et al., 1996; Hennig, et al., 2007; Guo and Liu, 2014; Zheng, et al., 2018), cucurbiturils (Florea and Nau, 2011; Praetorius, et al., 2008; Barrow, et al., 2015; Sonzini, et al., 2017) and pillararenes (Wang P, et al., 2014; Bojtár, et al., 2015; Bojtár, et al., 2016; Hua, et al., 2016; Bojtár, et al., 2017; Hua, et al., 2018; Xiao, et al., 2018, Xiao, et al., 2019a; Xiao, et al., 2019b), combined with various dyes have been applied as receptors in F-IDAs for specific and selective sensing in drugs, biomolecules, or other organic compounds.

This study established an FID assay with a water-soluble pillararene for caffeine detection. Caffeine is the most widely consumed psychostimulant drug worldwide. Appropriate caffeine intake may enhance alertness, attention, and nerve cell activity and decrease the possibility of type 2 diabetes. However, excessive intake of caffeine may possibly cause a headache, high blood pressure, irregular small muscle movement, and allergy, especially in teenagers and pregnant women (Nehlig, et al., 1992; Rapuri, et al., 2001; Smith, 2002; Lovallo et al., 2005). Caffeine detection can be realised with costly and complex methods, such as HPLC-MS and immunoassay (Wu, et al., 2000; Oberleitner, et al., 2014). Therefore, caffeine detection remains inconvenient for public usage. Thus, we realised novel host–guest recognition between water-soluble pillararene (WP6) and safranine T (ST) and revealed the operation of this host–guest recognition motif as an FID assay in caffeine detection (**Scheme 1**). The assay seems selective for theophylline and theobromine.

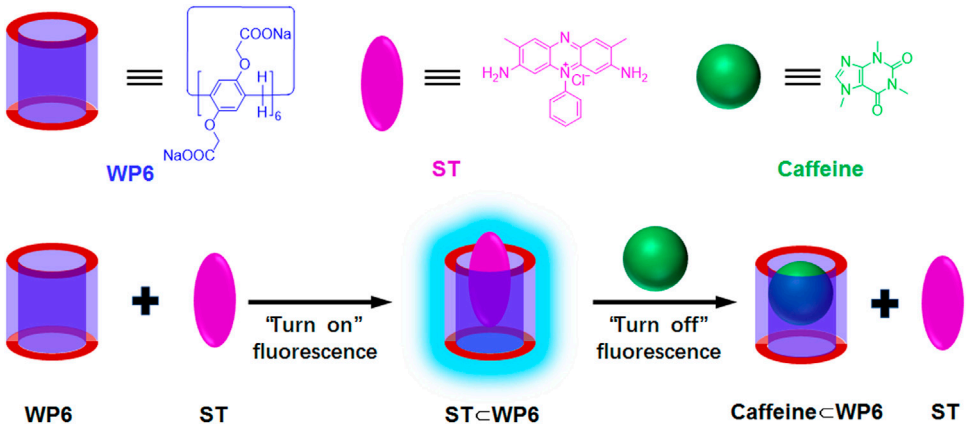

SCHEME 1 | Chemical structures and cartoon presentations of WP6, ST and caffeine and illustration of the turn-off fluorescence detection of caffeine through indicator displacement process.

MATERIALS AND METHODS

The reagents used were marketable and applied directly without further purification. WP6 (Yu et al., 2012) was synthesized by following the known procedures. Nuclear magnetic resonance (NMR) spectra were obtained using the Bruker Avance III HD 400 spectrometer with the deuterated solvent as the lock and the residual solvent as the internal reference. Fluorescence spectra were obtained by using the Agilent Cary Eclipse fluorescence spectrophotometer. To prevent the dilution effect during titration, WP6 stock solutions were produced using the same ST solution. The measurement was repeated three times for each experiment. Displacement assay for theophylline and theobromine was performed at pH 7.2 with WP6 at varying concentrations of theophylline and theobromine, respectively. All the experiments were conducted at room temperature (298 K).

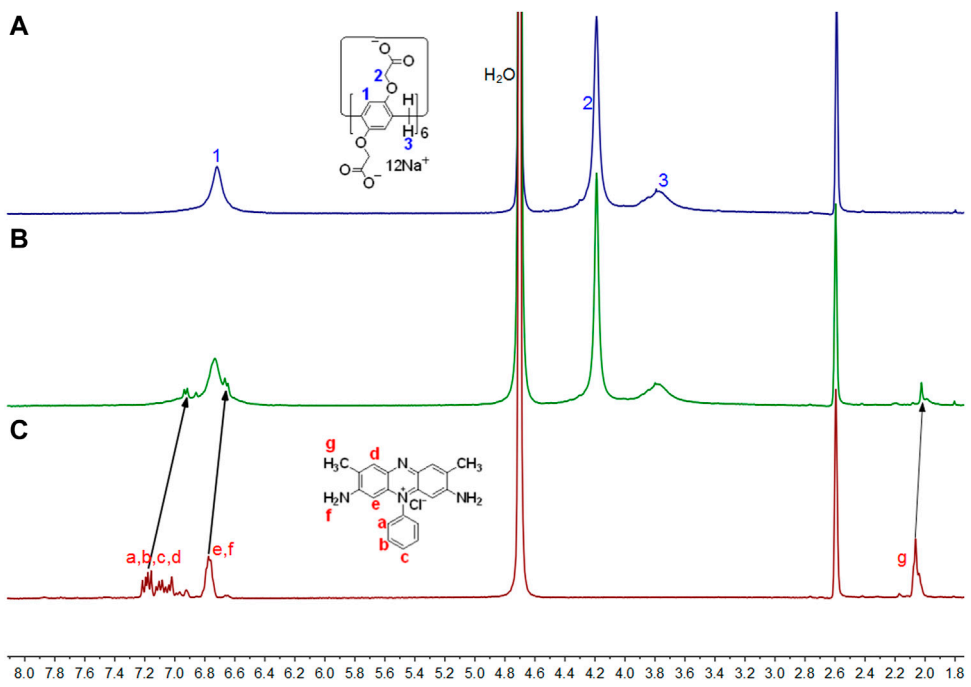

FIGURE 1 | Partial ^{1}H NMR spectra (400 MHz, D_2O:DMSO-d_6 = 1:1, 298 K) for **(A)** 3 mM WP6, **(B)** 3 mM WP6 and 10 mM ST, **(C)** 10 mM ST.

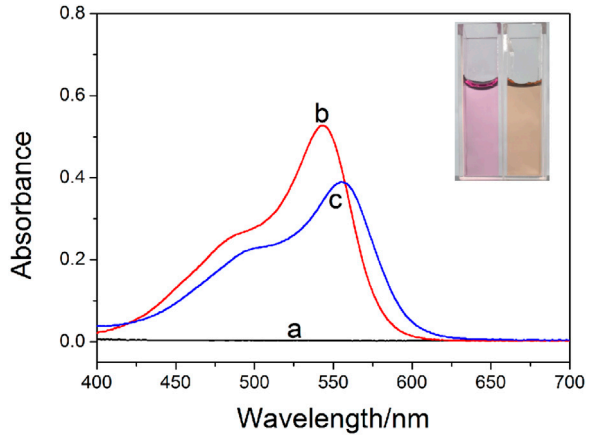

FIGURE 2 | UV-vis spectra for **(A)** WP6, **(B)** ST, and **(C)** ST in the presence of 50 equiv. of WP6 (1×10^{-3} M) in PBS (pH = 7.2). The inserted photo displays the colour changes related to ST with the addition of WP6.

RESULTS AND DISCUSSION

Complexation of ST With WP6

To study the host–guest complexation between WP6 and ST, ^{1}H NMR spectroscopy was first performed. Given that the complex solubility of neat D_2O did not occur at the mM scale, DMSO-d_6 cosolvent was supplemented. According to **Figure 1**, ST aromatic protons in the complex shifted upfield to varying degrees. This result revealed that ST was encapsulated by WP6 cavity and protons on ST were shielded by the electron-rich cyclic structure when the inclusion complex formed (Wang Y. et al., 2014). The characteristic signal broadening of the protons on ST was observed because of the shielding effects of the aromatic host (Li et al., 2010). Furthermore, protons on WP6 revealed minor chemical shifts resulting from host–guest interactions between WP6 and ST.

The formation of host–guest complex between WP6 and ST was further confirmed through UV-vis absorption spectroscopy. (**Figure 2**). A broad absorption band above 555 nm, corresponding to the charge-transfer interaction between electron-rich WP6 and electron-deficient ST, was observed. Furthermore, after adding WP6 to ST, a red shift appeared, which indicated that a representative charge-transfer complex was formed (Wang Y et al., 2014). The fluorescence titration of ST with WP6 was performed under ambient temperature in water. According to. **Figure 3A**, an enhancement in fluorescence and a red shift in the emission spectra were observed with the progressive supplement of WP6, which indicated that a strong supramolecular complex was formed. These changes may arise from the formation of twisted intramolecular charge transfer (TICT) state when ST occupied the WP6 cavity in the aqueous buffer. Under the TICT state, the phenyl or phenazinyl group is assumed to rotate around bonds that connect them to the central single bond. The twisting movement is subjected to restriction of the encapsulated **ST** guest, leading to enhanced fluorescence (Grabowski et al., 2003; Bojtár, et al., 2015).

The association constant (K_a) and the optical spectroscopic data of ST and corresponding WP6 complex are listed in **Table 1**, which presents a comparison with the data of ST complexes with β-cyclodextrin, ST⊂β-CD (Zhang et al., 2005), disulphide bridged β–cyclodextrin, ST⊂SS-β-CD (Yang et al., 2017), and γ-cyclodextrin, ST⊂γ-CD (Wang et al., 2012). An association constant of $K_a = (1.50 \pm 0.06) \times 10^4\ M^{-1}$ was obtained using a nonlinear fitting to the fluorescence spectra, measured by titration experiments. The stoichiometry of 1:1 for the complexes was tested with the molar ratio approach, based on the fluorescence data related to WP6-ST mixtures.

The optimal association constant revealed system applicability to FID. The spectroscopic data for complex ST⊂WP6 were similar to the spectroscopic data for the complex of the dye containing

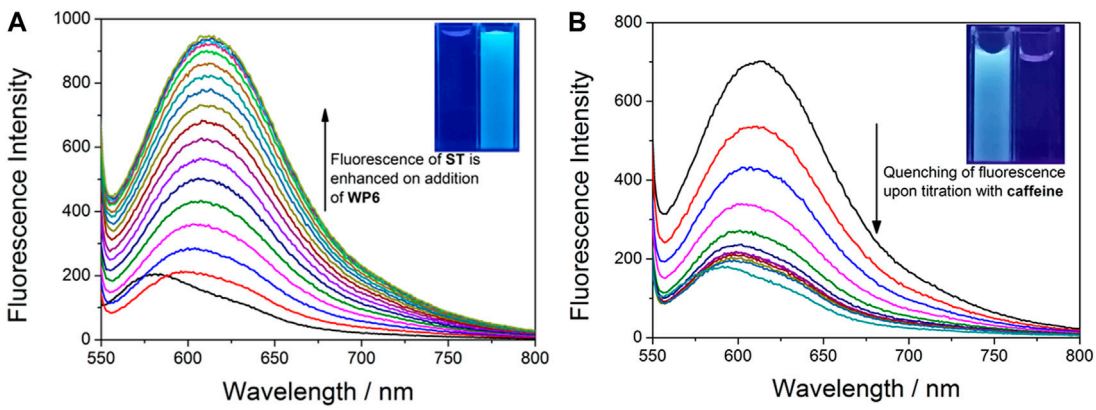

FIGURE 3 | (A) Changes of the fluorescence intensity in ST (0.02 mM) upon the titration of WP6 (0–25 equiv.) in PBS (λ_{ex} = 523 nm, λ_{em} = 584 nm, pH = 7.2). The inserted photo exhibits an enhancement in fluorescence in water under excitation at 365 nm via the UV lamp at 298 K. **(B)** Fluorescence titration for the competitive displacement of ST (0.02 mM) from WP6 (0.3 mM) using caffeine (0–150 equiv.) in PBS at pH 7.2 (λ_{ex} = 523 nm, λ_{em} = 584 nm). The inserted photo exhibits the corresponding fluorescence quenching in water under excitation at 365 nm via the UV lamp at 298 K.

TABLE 1 | Association constants (K_a) and optical spectroscopic data for the complexes of **ST** with **WP6** and other macrocycles.

	K_a	λabs (nm)	λem (nm)	References
ST	—	523	577	This work
ST⊂β-CD	160 M^{-1}	525	573	Zhang et al., 2005
ST⊂SS-β-CD	4.7 × 10^3 M^{-1}	525	576	Yang et al., 2017
ST⊂γ-CD	7.41 × 10^3 M^{-1}	411	579	Wang et al., 2012
ST⊂WP6	(1.50 ± 0.06) × 10^4 M^{-1}	555	584	This work

SS-β-CD, ST⊂β-CD (Yang et al., 2017), which proved the similarity of polarity of these two macrocycles. However, because of the weak interactions, the association constant with the uncharged cyclodextrin was lowered by an order of magnitude.

Complexation of Caffeine, Theophylline, and Theobromine With WP6

Next, for evaluating analyte complexation, ^{1}H NMR spectra were obtained for caffeine, theophylline, and theobromine. **Supplementary Figure S1** reveals that all the proton signals of caffeine shifted upfield at various extents, which indicated that caffeine was threaded into the host cavity. Furthermore, according to the 2D NOESY spectrum (**Supplementary Figure S4**), NOE correlation signals were obtained between protons H_{a-d} of caffeine and proton H_1 on WP6, verifying WP6's assignment for the caffeine threaded structure. Signals from the NMR spectra for theophylline and theobromine exhibited similar changes after adding WP6 (**Supplementary Figures S2, S3**).

Next, fluorescence titrations were performed at 298 K in PBS at pH 7.2 for estimating the binding behaviours of WP6 with caffeine, theophylline, and theobromine in a quantitative manner. Job plots (**Supplementary Figure S8**) drawn using fluorescence titration data suggest WP6 and the three guests in a 1:1 host–guest complex of the aqueous solution, respectively.

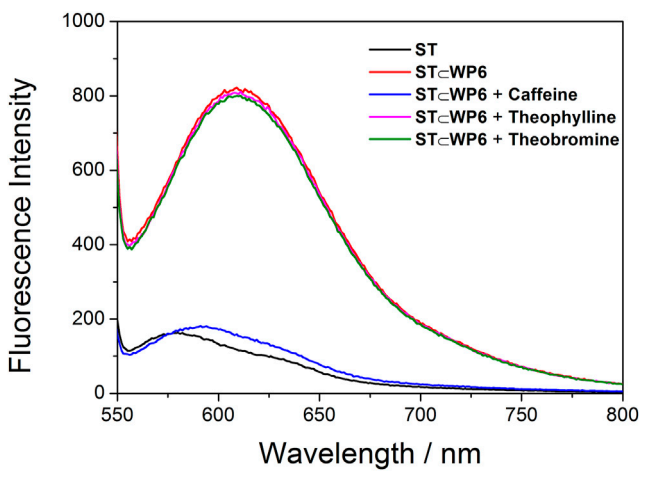

FIGURE 4 | Fluorescence spectra for ST (0.02 mM) + WP6 (0.35 mM) with caffeine (2 mM), theophylline (2 mM), and theobromine (2 mM), respectively.

Based on the nonlinear curve-fitting approach (**Supplementary Figures S10, S11**), the measured association constants (K_a) were (2.51 ± 0.24) × 10^4 M^{-1}, (9.30 ± 0.04) × 10^3 M^{-1}, and (9.14 ± 0.08) × 10^3 M^{-1} for caffeine, theophylline, and theobromine, respectively. The K_a value for the binding of caffeine is approximately an order of magnitude greater than the binding of theophylline and theobromine.

Fluorescent Indicator Displacement

Next, the indicator displacement process was used to measure the nonfluorescent host–indicator complex to detect caffeine. **Figure 3B** displays the typical process of displacement titration. When caffeine was gradually added into a mixed PBS solution with ST and WP6, fluorescence intensity quenching was apparent. The result proved that the added caffeine was able to rival with ST to push the indicator from the WP6 cavity. The following optical changes could be attributed to the formation of the caffeine⊂WP6 complex, which exhibited higher stability compared with ST⊂WP6. Furthermore, the 'turn-off' fluorescence changes resulting from caffeine addition could be observed by naked eyes by using a simple UV lamp (**Figure 3B**). The results indicate that the applicability of the ST⊂WP6 complex to an F-IDA for sensing anticancer drug caffeine.

The ST⊂WP6 system as a caffeine sensor exhibited higher selectivity than theophylline and theobromine. Theophylline and theobromine at the same concentration (2 mM) were added to the solution of the ST⊂WP6 complex, respectively. **Figure 4** displays changes of the fluorescence ratio I/I0 in the ST⊂WP6 complex on the addition of theophylline and theobromine, respectively. Negligible fluorescence changes were observed following the addition of theophylline and theobromine. Under the used conditions, theophylline and theobromine induced limited interference in the caffeine selective responses, suggesting the prominent selectivity of the method for caffeine. This selectivity can be attributed to the difference in binding constants between the host WP6 and the guests.

CONCLUSION

In conclusion, a new host–indicator composed of an electron-deficient dye ST and anionic water-soluble pillar[6] arene WP6 was developed. After the ST⊂WP6 complex was formed, the twisted intramolecular charge-transfer-induced fluorescence enhancement and solution colour changes were apparent. Furthermore, this supramolecular system was successfully applied as a fluorescent indicator displacement assay to detect

caffeine. Large signal modulation and a selective response towards caffeine against theophylline and theobromine were observed.

DATA AVAILABILITY STATEMENT

The original contributions presented in the study are included in the article/**Supplementary Material**, further inquiries can be directed to the corresponding author.

AUTHOR CONTRIBUTIONS

QD designed the work. YX and KG made contributions to the experiments and collective data. The paper was written by QD. All authors extensively discussed the results, reviewed the manuscript, and approved the final version of the manuscript to be submitted.

FUNDING

This work was supported by the Research and Cultivation Foundation of Henan University of Engineering (PYXM202009).

SUPPLEMENTARY MATERIAL

The Supplementary Material for this article can be found online at: https://www.frontiersin.org/articles/10.3389/fchem.2021.816069/full#supplementary-material

REFERENCES

Barrow, S. J., Kasera, S., Rowland, M. J., Del Barrio, J., and Scherman, O. A. (2015). Cucurbituril-Based Molecular Recognition. *Chem. Rev.* 115, 12320–12406. doi:10.1021/acs.chemrev.5b00341

Bojtár, M., Kozma, J., Szakács, Z., Hessz, D., Kubinyi, M., and Bitter, I. (2017). Pillararene-Based Fluorescent Indicator Displacement Assay for the Selective Recognition of ATP. *Sensors Actuators B: Chem.* 248, 305–310. doi:10.1016/j.snb.2017.03.163

Bojtár, M., Paudics, A., Hessz, D., Kubinyi, M., and Bitter, I. (2016). Amino Acid Recognition by Fine Tuning the Association Constants: Tailored Naphthalimides in Pillar[5]arene-Based Indicator Displacement Assays. *RSC Adv.* 6, 86269–86275. doi:10.1039/C6RA15003A

Bojtár, M., Szakács, Z., Hessz, D., Kubinyi, M., and Bitter, I. (2015). Optical Spectroscopic Studies on the Complexation of Stilbazolium Dyes with a Water Soluble Pillar[5]arene. *RSC Adv.* 5, 26504–26508. doi:10.1039/C4RA14809F

Crini, G. (2014). Review: A History of Cyclodextrins. *Chem. Rev.* 114, 10940–10975. doi:10.1021/cr500081p

Florea, M., and Nau, W. M. (2011). Strong Binding of Hydrocarbons to Cucurbituril Probed by Fluorescent Dye Displacement: A Supramolecular Gas-Sensing Ensemble. *Angew. Chem. Int. Ed.* 50, 9338–9342. doi:10.1002/anie.201104119

Grabowski, Z. R., Rotkiewicz, K., and Rettig, W. (2003). Structural Changes Accompanying Intramolecular Electron Transfer: Focus on Twisted Intramolecular Charge-Transfer States and Structures. *Chem. Rev.* 103 (10), 3899–4032. doi:10.1021/cr940745l

Guo, D.-S., and Liu, Y. (2014). Supramolecular Chemistry of P-Sulfonatocalix[n]arenes and its Biological Applications. *Acc. Chem. Res.* 47, 1925–1934. doi:10.1021/ar500009g

Hennig, A., Bakirci, H., and Nau, W. M. (2007). Label-Free Continuous Enzyme Assays with Macrocycle-Fluorescent Dye Complexes. *Nat. Methods* 4, 629–632. doi:10.1038/nmeth1064

Hua, B., Shao, L., Yu, G., and Huang, F. (2016). Fluorescence Indicator Displacement Detection Based on Pillar[5]arene-Assisted Dye Deprotonation. *Chem. Commun.* 52, 10016–10019. doi:10.1039/C6CC04919B

Hua, B., Shao, L., Zhang, Z., Sun, J., and Yang, J. (2018). Pillar[6]arene/acridine orange Host-Guest Complexes as Colorimetric and Fluorescence Sensors for Choline Compounds and Further Application in Monitoring Enzymatic Reactions. *Sensors Actuators B: Chem.* 255, 1430–1435. doi:10.1016/j.snb.2017.08.141

Koh, K. N., Araki, K., Ikeda, A., Otsuka, H., and Shinkai, S. (1996). Reinvestigation of Calixarene-Based Artificial-Signaling Acetylcholine Receptors Useful in Neutral Aqueous (Water/Methanol) Solution. *J. Am. Chem. Soc.* 118 (4), 755–758. doi:10.1021/ja951488k

Li, C., Zhao, L., Li, J., Ding, X., Chen, S., Zhang, Q., et al. (2010). Self-assembly of [2]Pseudorotaxanes Based on Pillar[5]arene and Bis(imidazolium) Cations. *Chem. Commun.* 46, 9016–9018. doi:10.1039/C0CC03575K

Lovallo, W. R., Whitsett, T. L., al'Absi, M., Sung, B. H., Vincent, A. S., and Wilson, M. F. (2005). Caffeine Stimulation of Cortisol Secretion across the Waking Hours in Relation to Caffeine Intake Levels. *Psychosom Med.* 67, 734–739. doi:10.1097/01.psy.0000181270.20036.06

Nehlig, A., Daval, J.-L., and Debry, G. (1992). Caffeine and the Central Nervous System: Mechanisms of Action, Biochemical, Metabolic and Psychostimulant Effects. *Brain Res. Rev.* 17, 139–170. doi:10.1016/0165-0173(92)90012-B

Nguyen, B. T., and Anslyn, E. V. (2006). Indicator-Displacement Assays. *Coordination Chemistry Rev.* 250, 3118–3127. doi:10.1016/j.ccr.2006.04.009

Oberleitner, L., Grandke, J., Mallwitz, F., Resch-Genger, U., Garbe, L.-A., and Schneider, R. J. (2014). Fluorescence Polarization Immunoassays for the Quantification of Caffeine in Beverages. *J. Agric. Food Chem.* 62, 2337–2343. doi:10.1021/jf4053226

Pal, K., Mallick, S., and Koner, A. L. (2015). Complexation Induced Fluorescence and Acid-Base Properties of Dapoxyl Dye with γ-cyclodextrin: a Drug-Binding Application Using Displacement Assays. *Phys. Chem. Chem. Phys.* 17, 16015–16022. doi:10.1039/C5CP01696G

Praetorius, A., Bailey, D. M., Schwarzlose, T., and Nau, W. M. (2008). Design of a Fluorescent Dye for Indicator Displacement from Cucurbiturils: A Macrocycle-Responsive Fluorescent Switch Operating through a pKa Shift. *Org. Lett.* 10, 4089–4092. doi:10.1021/ol8016275

Rapuri, P. B., Gallagher, J. C., Kinyamu, H. K., and Ryschon, K. L. (2001). Caffeine Intake Increases the Rate of Bone Loss in Elderly Women and Interacts with Vitamin D Receptor Genotypes. *Am. J. Clin. Nutr.* 74, 694–700. doi:10.1093/ajcn/74.5.694

Smith, A. (2002). Effects of Caffeine on Human Behavior. *Food Chem. Toxicology* 40, 1243–1255. doi:10.1016/S0278-6915(02)00096-0

Sonzini, S., McCune, J. A., Ravn, P., Scherman, O. A., and van der Walle, C. F. (2017). A Simple Supramolecular Assay for Drug Detection in Urine. *Chem. Commun.* 53, 8842–8845. doi:10.1039/C7CC04081D

Wang, P., Yao, Y., and Xue, M. (2014). A Novel Fluorescent Probe for Detecting Paraquat and Cyanide in Water Based on Pillar[5]arene/10-Methylacridinium Iodide Molecular Recognition. *Chem. Commun.* 50, 5064–5067. doi:10.1039/C4CC01403K

Wang, X., Xu, D., Adresi, Y., and Wang, X. (2012). Studies on Interaction of Safranine T with Herring Sperm DNA in γ−Cyclodextrin. *Turk J. Bioch* 37 (2), 175–180. doi:10.5505/tjb.2012.22931

Wang, Y., Xu, J.-F., Chen, Y.-Z., Niu, L.-Y., Wu, L.-Z., Tung, C.-H., et al. (2014). Photoresponsive Supramolecular Self-Assembly of Monofunctionalized Pillar[5]arene Based on Stiff Stilbene. *Chem. Commun.* 50, 7001–7003. doi:10.1039/C4CC02760D

Wiskur, S. L., Ait-Haddou, H., Lavigne, J. J., and Anslyn, E. V. (2001). Teaching Old Indicators New Tricks. *Acc. Chem. Res.* 34, 963–972. doi:10.1021/ar9600796

Wu, J., Xie, W., and Pawliszyn, J. (2000). Automated In-Tube Solid Phase Microextraction Coupled with HPLC-ES-MS for the Determination of Catechins and Caffeine in Tea. *Analyst* 125, 2216–2222. doi:10.1039/B006211L

Xiao, T., Qi, L., Zhong, W., Lin, C., Wang, R., and Wang, L. (2019b). Stimuli-Responsive Nanocarriers Constructed from Pillar[n]arene-Based Supra-amphiphiles. *Mater. Chem. Front.* 3, 1973–1993. doi:10.1039/C9QM00428A

Xiao, T., Xu, L., Zhong, W., Zhou, L., Sun, X.-Q., Hu, X.-Y., et al. (2018). Advanced Functional Materials Constructed from Pillar[n]arenes. *Isr. J. Chem.* 58, 1219–1229. doi:10.1002/ijch.201800026

Xiao, T., Zhou, L., Xu, L., Zhong, W., Zhao, W., Sun, X.-Q., et al. (2019a). Dynamic Materials Fabricated from Water Soluble Pillar[n]arenes Bearing Triethylene Oxide Groups. *Chinese Chem. Letters* 30, 271–276. doi:10.1016/j.cclet.2018.05.039

Yang, L., Zhao, H., Li, Y., Zhang, Y., Ye, H., Zhao, G., et al. (2017). Insights into the Recognition of Dimethomorph by Disulfide Bridged β-cyclodextrin and its High Selective Fluorescence Sensing Based on Indicator Displacement Assayfide Bridged β–Cyclodextrin and its High Selective Fluorescence Sensing Based on Indicator Displacement Assay. *Biosensors Bioelectronics* 87, 737–744. doi:10.1016/j.bios.2016.09.044

Yu, G., Xue, M., Zhang, Z., Li, J., Han, C., and Huang, F. (2012). A Water-Soluble Pillar[6]arene: Synthesis, Host-Guest Chemistry, and its Application in Dispersion of Multiwalled Carbon Nanotubes in Water. *J. Am. Chem. Soc.* 134, 13248–13251. doi:10.1021/ja306399f

Zhang, G., Pang, Y., Shuang, S., Dong, C., Choi, M. M. F., and Liu, D. (2005). Spectroscopic Studies on the Interaction of Safranine T with DNA in β-cyclodextrin and Carboxymethyl-β-Cyclodextrin. *J.Photochem.Photobiol., A.* 169, 153–158. doi:10.1016/j.jphotochem.2004.06.016

Zheng, Z., Geng, W.-C., Gao, J., Wang, Y.-Y., Sun, H., and Guo, D.-S. (2018). Ultrasensitive and Specific Fluorescence Detection of a Cancer Biomarkervianamolar Binding to a Guanidinium-Modified Calixarene. *Chem. Sci.* 9, 2087–2091. doi:10.1039/C7SC04989G

Conflict of Interest: The authors declare that the research was conducted in the absence of any commercial or financial relationships that could be construed as a potential conflict of interest.

Publisher's Note: All claims expressed in this article are solely those of the authors and do not necessarily represent those of their affiliated organizations, or those of the publisher, the editors and the reviewers. Any product that may be evaluated in this article, or claim that may be made by its manufacturer, is not guaranteed or endorsed by the publisher.

frontiers in Chemistry

ORIGINAL RESEARCH
published: 31 January 2022
doi: 10.3389/fchem.2021.804893

Seeding Chiral Ensembles of Prolinated Porphyrin Derivatives on Glass Surface: Simple and Rapid Access to Chiral Porphyrin Films

*Gabriele Magna[1], Tanja Traini[1], Mario Luigi Naitana[1], Gianlorenzo Bussetti[2], Fabio Domenici[1], Gaio Paradossi[1], Mariano Venanzi[1], Corrado Di Natale[3], Roberto Paolesse[1], Donato Monti[4] and Manuela Stefanelli[1]**

[1]Department of Chemical Science and Technologies, University of Rome Tor Vergata, Roma, Italy, [2]Department of Physics, Politecnico di Milano, Milan, Italy, [3]Department of Electronic Engineering, University of Rome Tor Vergata, Roma, Italy, [4]Department of Chemistry, Università La Sapienza, Roma, Italy

An easy and fast method to achieve chiral porphyrin films on glass is herein reported. The on-surface formation of organized supramolecular architectures with distinctive and remarkable chiroptical features strictly depends on the macrocycles used, the solvent chosen for the casting deposition, and most importantly, on the roughness of the glass slide. Dynamic light scattering studies performed on 10^{-4}–10^{-6} M porphyrin solutions revealed the presence of small porphyrin aggregates, whose size and number increase depending on the initial concentration. Once transferred on surface, these protoaggregates act as nucleation seeds for the following, self-assembling into larger structures upon solvent evaporation, with a process driven by a fine balance between intermolecular and molecule–substrate interactions. The described method represents a straightforward way to fabricate porphyrin-based chiral surfaces onto a transparent and economic substrate in few minutes. The results obtained can be particularly promising for the development of sensors based on stereoselective optical active films, targeting the detection of chiral analytes of practical relevance, such as the so-called emerging pollutants released in the environment from agrochemical, food, and pharmaceutical manufacturing.

Keywords: porphyrins, drop-casting, solvent effect, glass surface, self-aggregation, dynamic light scattering, supramolecular chirality

OPEN ACCESS

Edited by:
Chao Deng,
Soochow University, China

Reviewed by:
Maria Castriciano,
University of Messina, Italy
Roberto Purrello,
University of Catania, Italy

****Correspondence:***
Manuela Stefanelli
manuela.stefanelli@uniroma2.it

Specialty section:
This article was submitted to Supramolecular Chemistry, a section of the journal Frontiers in Chemistry

Received: *29 October 2021*
Accepted: *14 December 2021*
Published: *31 January 2022*

Citation:
Magna G, Traini T, Naitana ML, Bussetti G, Domenici F, Paradossi G, Venanzi M, Di Natale C, Paolesse R, Monti D and Stefanelli M (2022) Seeding Chiral Ensembles of Prolinated Porphyrin Derivatives on Glass Surface: Simple and Rapid Access to Chiral Porphyrin Films. Front. Chem. 9:804893. doi: 10.3389/fchem.2021.804893

INTRODUCTION

The understanding of chirality at solid surfaces is of ever-growing importance, and an increasing number of studies have been reported over the years to shed light on the fundamentals and practices in achieving chiral surfaces with definite enantioselectivity (Gellman, 2010; Zaera, 2017; Albano et al., 2020; Xu et al., 2021). As a matter of fact, chirality can be observed or provided to achiral surfaces taking advantage of several options spanning from the addition of chiral modifiers (Zaera, 2008), the adsorbing of chiral molecules at ultra-high vacuum (Costa et al., 2015), or from liquid phase (Huang et al., 2003), or even by self-assembly of achiral molecules that form chiral domains thanks to the surface dimensional constraints (Tao and Bernasek, 2005). Specifically for the transfer of chiral molecules from solution to surface, the final chiroptical features are strictly dependent on a

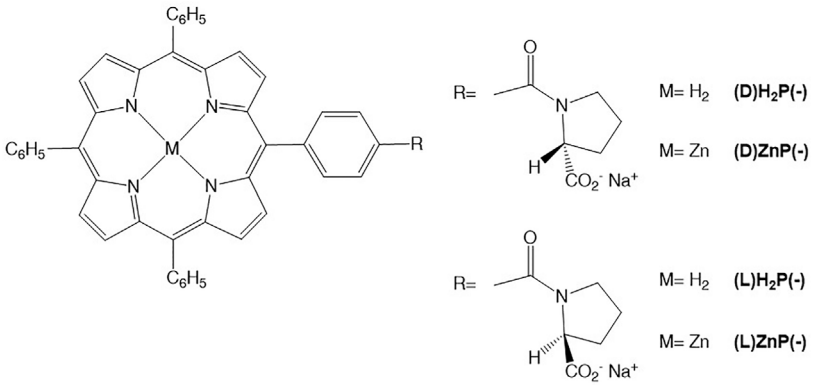

SCHEME 1 | Porphyrin derivatives used in these studies.

combination of different forces controlling the supramolecular organization in solution as well as the interaction/adsorption with the specific substrate. Over the course of our research, we found that various amphiphilic porphyrin derivatives bearing a stereogenic information on the peripheral molecular positions form chiral mesoscopic structures of tunable size in different hydro–organic media, depending on the interplaying of structural motifs and solvent bulk properties (i.e., type and relative ratio of the hydro–organic mixture used, ionic strength, and monomer concentration) (Monti et al., 2010; Caroleo et al., 2019; Stefanelli et al., 2020a). Within this set of tetrapyrroles, cationic derivatives functionalized with a peripheral (L)-proline moiety have been also exploited for the preparation of chiral films to be applied for sensor development. Two strategies have been basically reported: 1) the steering of the self-aggregation of chiral porphyrin monomers in ethanol/water mixture of proper composition to give in 1–2 days chiral assemblies that spontaneously layer on glass substrate dipped into the solution (Monti et al., 2011); 2) the use of Langmuir–Blodgett technique to assemble the porphyrin molecules onto a glass surface in chiral multilayers through air/water interfacial organization (Colozza et al., 2019). Films based on the anionic counterpart (L)ZnP(-) (**Scheme 1**) anchored to ZnO nanoparticles have been also chirally organized on quartz microbalance surfaces and used for the stereoselective recognition of limonene enantiomer vapors (M. Stefanelli et al., 2019). The need of realizing cost-effective and easy to handle sensor platforms prompted us to access the chiral films on common solid supports by simple operation of all the stages, starting with material preparation to film deposition. Additionally, the achievement of a convenient signal for the detection is highly desirable. With this aim in mind, we have carried out the studies herein reported, concerning the development of a straightforward method to fabricate optically active films on glass by drop-casting of (L) or (D)-prolinated porphyrin building blocks dissolved in suitable organic solvents (**Scheme 1**). The choice of glass as substrate for film deposition is mainly due to its optical transparency that makes the layer chirality assessment possible by circular dichroism (CD) spectroscopy on one side, along with the detection of the eventual interaction with a target analyte by means of an easily recordable optical signal change (i.e., absorption, fluorescence, and CD spectral variations upon analyte detection). We can anticipate that the chiroptical properties of the produced films are deeply influenced by the porphyrin molecular structure (i.e., the configuration of the appended proline and the presence or not of a coordinated metal ion into the core), the solvent used for the deposition, and last but not the least, the roughness of the glass substrate. These findings highlight the complex interplaying of supramolecular interactions occurring when chirality is transferred from the solution to the solid state. The easiness and the versatility of the described protocol make it a viable approach in fabricating chiral films based on porphyrins for stereoselective sensor applications.

RESULTS AND DISCUSSION

Evaluation of the Solvent Effect on the Chirality of the Film

The challenging stage for the drop-casting production of chiral solid films is surely the identification of the proper solvent to use for the stock solution. As reported in the literature, the nature of the solvent used is extremely relevant to define the structures that the layers adopt and the overall chirality (Iavicoli et al., 2009; Chen et al., 2019), since both derive from a combination of the interaction strength of the molecules with the surface and their solubility (Zaera 2009; Mali and De Feyter, 2013). Moreover, solvent parameters like viscosity, surface tension, and vapor pressure strictly impact the film adhesion to the substrate and the evaporation rate, producing layers featuring different structural motifs and homogeneity (Resedean et al., 2020).

We carried out our investigations on the Zn porphyrin enantiomers [(D)- and (L)ZnP(-), **Scheme 1**], whose

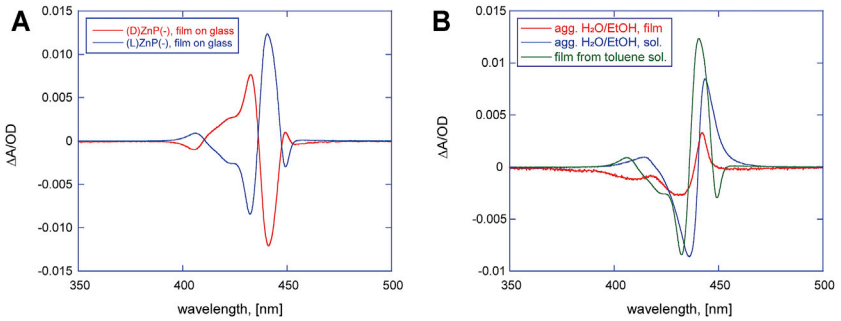

FIGURE 1 | (A) Circular dichroism (CD) spectra of (D)- (red trace) and (L)ZnP(-) (blue trace) casted films on glass from 10^{-4} M toluene solutions. **(B)** (L)ZnP(-) chiral aggregates obtained in different conditions: aggregates grown from EtOH/H_2O (25:75, v/v) at 5 μM concentration (blue trace) and the corresponding film on glass (red trace); chiral films on glass from 10^{-4} M toluene solution (green trace).

aggregation behavior in hydroalcoholic solution was recently studied in depth (Stefanelli et al., 2020a; Savioli et al., 2020). We have selected three solvents of different polarity, coordination abilities, and adhesion properties in which the porphyrin derivatives are soluble, namely, ethanol (EtOH), tetrahydrofuran (THF), and toluene. Films were deposited by drop-casting 10 μl from 10^{-4} M stock solutions of each porphyrin derivative on glass slides, followed by solvent evaporation (see the *Experimental* section for the detailed procedures). The layered materials were optically characterized by UV-vis and CD spectroscopies. For all the films tested, UV-vis spectra showed broad Soret bands, with peaks lying in the 435–440 nm range, red shifted if compared with the corresponding porphyrin solution (420–424 nm range), indicating that macrocycles are aggregated in J-type structures at solid state (see **Supplementary Figure S1**).

The assessment of the chiroptical features of the solid films have been carried out by CD spectroscopy and evidenced a remarkable influence of the solvent on the chirality at solid state.

As far as the films of (D)- or (L)ZnP(-) from THF and EtOH are concerned, negligible dichroic bands, barely observable in the 350- to 500-nm spectral range (data not shown) have been recorded, indicating an ineffective reading out of the chiral information during the self-assembly process occurring onto the glass surface in these solvents. Completely different results were obtained for the drop-casting of toluene solutions, which conversely produced layers with extensive supramolecular chirality. As shown in **Figure 1A**, the CD spectrum for films of (D)ZnP(-) is characterized by two sets of excitonically coupled bands at about 441, 433, and 407 nm, indicating electronic coupling between layered macrocycles that arranged in a (+) clockwise (CW) mutual conformation, as excitonic theory states (Berova et al., 2000) (**Figure 1A**, red trace). For the other enantiomer, a specular CD profile is obtained, featuring three bisignate negative bands with the same crossover points found for the (D) counterpart**,** pointing out a (−) anticlockwise (ACW) mutual orientation of porphyrin macrocycles (**Figure 1A**, blue trace). CD readouts (theta, expressed in mdeg), have been converted in ΔA/OD, where OD is the optical density of the sample and ΔA the difference measured in the sample absorbance between the left and right polarization of light. For this normalization purpose, both CD and optical density of films have been evaluated by performing absorbance measurements with Jasco J-1500 without moving the glass slide in order to measure these two quantities on the exact same spot. Remarkably, we found out that the normalized CD values are unexpectedly reproducible over different areas of the spot, even more so by considering that simple drop-casting method for the coating is used. This robustness results in an almost flawless specularity of CD signals obtained for films produced by toluene solutions of the two enantiomers of ZnP(-) (see **Figure 1A**). These spectral features were obtained independently on the batch used for deposition with the same sign and intensities, to prove a good reproducibility of the deposition method. All these findings combined definitely pointed out that the final chirality of the films is driven by the specific peripheral stereochemical information of the single unit and transferred from molecular to aggregate level upon self-assembly process.

The dependence of the chiroptical features in terms of pattern and intensity on the macrocycle concentration was also investigated. **Supplementary Figure S2** (Supplementary Material) shows that the CD signal magnitude of (D)ZnP(-) films on glass slides increases at higher bulk solution concentrations without any perceptible changes in the chiral features. The calculated ratios between the maximum of the CD signals and recorded OD (see the *Experimental* section for details) shows that this parameter is substantially constant in the investigated range of concentrations (0.013, in the 0.5–1 × 10^{-4} M). Similar results have been obtained for the deposition of the (L) porphyrin enantiomer in the same conditions.

Comparing the spectral features of the (L)ZnP(-) film from toluene (**Figure 1B**, green trace) with the ones obtained for aggregates grown in EtOH/H_2O (25:75 v/v) solutions (**Figure 1B**, blue trace), and one deposited at solid state (**Figure 1B**, red trace), a certain resemblance can be observed, even if the ones obtained for films casted by toluene show a higher degree of complexity, detectable with the emerging dichroic band at 449 nm.

The close similarity between these systems allows us to invoke a like aggregation mode between porphyrin platforms during the

TABLE 1 | Dynamic light scattering (DLS) analysis of (L)ZnP(-) and the achiral ZnpCTPP in different solvents and concentrations.

Entry	Sample	Solvent	[M]	Aggregate	
				d_h [nm] ± σ	PDI
1	**(L)ZnP**	Toluene	10^{-4}	290 ± 20	0.05
2	**(L)ZnP**	Toluene	10^{-5}	160 ± 60	0.2
3	**(L)ZnP**	Toluene	10^{-6}	50 ± 30	0.4
4	**(L)ZnP**	Ethanol	10^{-4}	No aggregates	
5	**ZnpCTPP**	Toluene	10^{-4}	No aggregates	

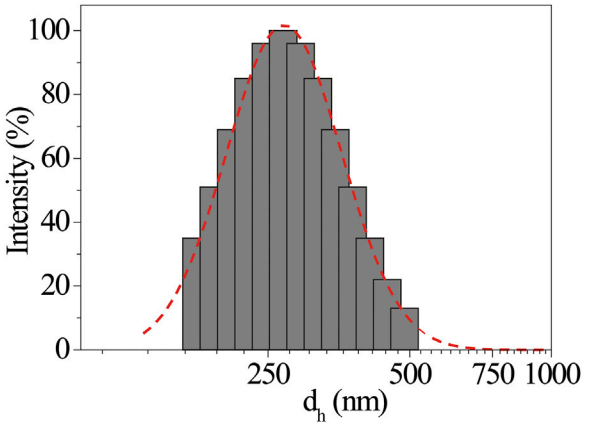

FIGURE 2 | Representative dynamic light scattering (DLS) intensity size distribution of (L)ZnP(-) 10^{-4} M toluene solution, where the presence of self assemblies is detected. Gaussian fit in dotted line.

film formation, involving the coordination of the proline carboxylate to the Zn^{2+} ion (Stefanelli et al., 2020b). It must be said that the aggregation conditions are rather different in the two cases. Indeed, in EtOH/H_2O, the aggregation is boosted by hydrophobic effect, which can be surely excluded here in driving film formation. On the other hand, the chirality transfer during the self-assembly process on glass and the resulting nanostructured supramolecular chirality should be the result of several concomitant factors as, for example, the evaporation kinetic (Hattori et al., 2017). Moreover, it is abundantly reported that porphyrin aggregation often is based on the "sergeants-and-soldiers" principle, where a small set of specific aggregates acts as chiral seeds to catalyze the following aggregation process (Mammana et al., 2007). Based on these considerations, we decided to perform DLS studies to assess the eventual presence of protoaggregated species in the (L)ZnP(-) 10^{-4} M toluene bulk solutions (**Table 1**, entry 1). As shown in **Figure 2**, the sample presents aggregates with low polydispersity size distribution, centered at d_h~290 nm. Additionally, this distribution resulted to be influenced by porphyrin concentration. According to the comparative DLS analysis shown in **Table 1**, lowering the concentration down to 10^{-5} M is reflected in a lowering of the average size together with a significant increase in the size polydispersity (**Table 1**, entry 2). At 10^{-6} M, very small aggregates (~50 nm size) were slightly detectable after high acquisition time (**Table 1**, entry 3). Experiment on long-term evolution of the size distribution would be desirable to understand whether such differences can be related to a change in the aggregation kinetics with porphyrin concentration. It is important to mention that toluene solutions of (D)ZnP(-) enantiomer were also checked under the same experimental conditions, showing no significant variation in the behavior of the size distribution, above reported for the (L)- counterpart.

On the other hand, the involvement of Zn coordination on the chirality transfer from solutions to solid films is also suggested by the fact that films obtained from EtOH and THF are CD silent: In both cases, the remarkable coordination abilities toward Zn metal ions with respect to toluene make these solvents strong competitors for the aminoacidic residue. As a consequence, individual porphyrin macrocycles are well solvated, and the development of oligomeric structures is scarcely probable or driven to the formation of nucleation seeds below a critical threshold (**Table 1**, entry 4).

Additionally, ZnpCTPP is here utilized as a nonchiral probe since it also possesses a coordinated Zn(II) ion and a carboxylate group that should be able to drive the formation of ordered supramolecular assemblies. However, DLS studies disclose the absence of detectable aggregates in toluene at high concentration (**Table 1**, entry 5), proving the importance of the proline-appended group on the early aggregation stage. Furthermore, in case of films from nonchiral porphyrins, chiroptical signals should still emerge when symmetry-breaking effect of the surface, or stochastic formation of nucleation seeds with right- or left-handed orientation occur during the deposition (Chen et al., 2006). In this case, these events can be clearly ruled out by the fact that the CD signal of film from ZnpCTPP toluene solution on glass are silent.

To further investigate the network of interactions between solvent and porphyrins involved in both the aggregation process and in the effective chirality transfer to the solid state, we studied the drop-casted films of the corresponding free bases [(L)- and (D)H_2P(-), **Scheme 1**] from THF and EtOH (toluene was excluded since these macrocycles are scarcely soluble in this solvent). Once again, films from THF did not feature any dichroic bands (data not shown). On the contrary, CD spectra of the spotted 10^{-4} M solutions of both enantiomers in EtOH displayed mirrored bisignated bands, although poorly reproducible in terms of intensity, sign, and spectral pattern depending on the batch solutions (data not shown). We have ascribed this evidence to the formation of small nucleation seeds of random overall symmetry, due to the lack of specific driving force such as the metal–ion coordination. The same behavior has been in fact observed upon aggregation of these species in hydroalcoholic solution (Stefanelli et al., 2020b) that results in the formation of supramolecular structures with very low g-factor.

DLS measurements support this hypothesis, since at the same concentration, (L)H_2P(-) ethanol solutions showed a low tendency to form aggregates (which were rarely detectable at

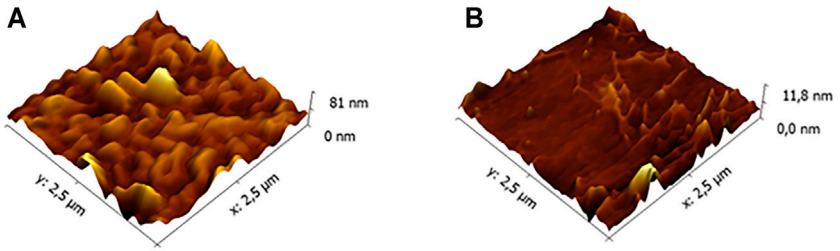

FIGURE 3 | Atomic force microscopy (AFM) morphologies of **(A)** a commercial and **(B)** low-roughness glasses.

sizes in the range of 50–150 nm), suggesting a good solvation capacity of ethanol.

Evaluation of the Influence of the Glass Substrate on Films

It is well known that several surface properties like wettability/nature and roughness are crucial for the film formation, affecting important mechanical as well as optical features, particularly at micro/nano scale. In our studies, we have investigated the influence of the glass surface on the chiroptical properties of the formed films by drop-casting toluene (L)/(D)ZnP(-) porphyrin solutions on glass slides of different source (i.e., commercial and of low roughness). A first difference among the films formed onto these two substrates was pointed out by the corresponding UV-vis spectra (**Supplementary Figure S3**), which showed a Soret band more red shifted and narrower for the layers casted on the ultraflat slide, indicative of a higher specificity in forming J-aggregated structures on such a substrate. Concurrently, CD measurements showed chiroptical features exclusively in the case of this film, pointing out a remarkable influence of the substrate roughness on the final porphyrin arrangement onto the surface in a chiral fashion.

This interesting result led us to investigate more in depth the film morphology, and the results will be reported in a separate paper focused on this issue. Herein, we anticipate that the morphological investigation has highlighted a significant difference between the commercial glass and the low-roughness one. AFM images reported in the **Figure 3** clearly show that the commercial glass (**Figure 3A**) is characterized by many hills and valleys with an overall height difference of about 75 nm. Conversely, the low-roughness glasses (**Figure 3B**) possess wide terraces, where the surface roughness is below 6 nm. Only in confined areas, we have observed some scratches that increase the overall roughness up to 10 nm. These evident differences between the two glass types can give a rationale of the observed porphyrin film chirality discussed above. Indeed, we can surmise that the porphyrin deposition onto a flat surface can facilitate the chiral organization of the macrocycles during the solvent evaporation. Conversely, the irregular commercial glass surface does not offer an optimal platform for a uniform film growth, which results in lack of stereospecificity.

Herein, we can conclude that the film chiral arrangement onto surface is due to a fine interplay of effects, i.e., the nature of the solvent, the concentration of the porphyrin monomer, and the nature of the deposition surface.

At the end of these investigations, we also evaluated some important film properties for applicative purposes, namely, the stability over time and temperature assessed by CD spectroscopy (**Supplementary Figures S4A, B**, respectively). We observed that the (L)/(D) porphyrin films casted by from toluene solution undergo a small rearrangement during 24–36 h and then remain stable until 72 h after the casting. At the end of this time, *ca.* 25% of the CD signal is lost and is kept constant for further 7 days. The organic layers are found more sensitive to heating, preserving their optical properties when exposed to temperature up to 50°C, and deteriorating for higher temperatures. In addition, AFM investigation gave a direct visualization of the film morphological evolution as a function of time. **Figure 4** summarizes and compares the (D)ZnP(-) porphyrin film after about 100 h from the sample preparation. At the beginning, the morphology shows domains characterized by dendritic structures (**Figure 4A**), in good agreement with analogous systems reported in literature (Iavicoli et al., 2009). The film is not stable in ambient conditions, but undergoes a new assembling where the overall film roughness is slightly reduced (**Figure 4B**). It is reasonable that some solvent residuals, embedded inside the film after the deposition, are removed (e.g., evaporation) with a longer time interval, and a remarkable change in the porphyrin aggregates is produced.

Conclusion and future perspectives

These studies report a convenient way to achieve chiral films by the efficient transfer of chirality from porphyrin molecular systems to film on glass by selecting a proper solvent for drop-casting process. The results obtained point out the crucial role played by nucleation seeds (small chiral porphyrin oligoaggregates), which are formed in solution. We found, in fact, that the use of oxygen donor solvents (EtOH and THF) well solvate the macrocycles either as free bases and zinc complexes, so hampering the effective supramolecular organization of the forming film in a chiral fashion. In analogy with our previous studies, the formation of chiral assemblies based on (L)/(D) prolinated porphyrins is guided by the coordination of the aminoacidic moiety to the zinc ion. For this reason, the use of toluene as solvent proves to be a

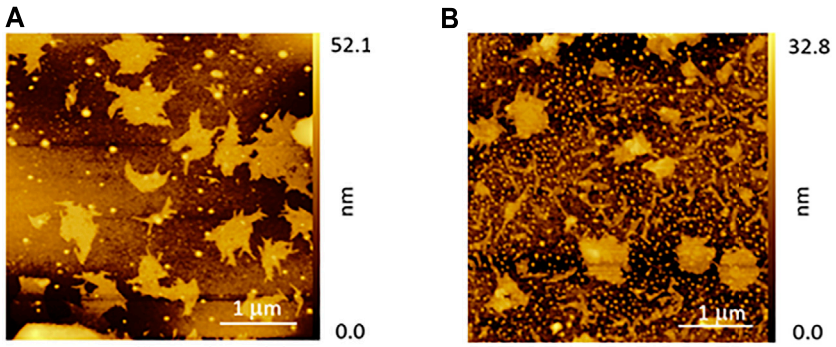

FIGURE 4 | AFM morphologies of the (D)ZnP(-) film as a function of time: **(A)** as deposited and **(B)** after about 100 h with the sample taken in ambient conditions.

good choice. Indeed, besides the noncoordinating character, toluene possesses also the highest surface tension (28.4, 26.4, and 22.1 mN/m for toluene, THF, and EtOH, respectively) and the lowest vapor pressure (29, 200, and 59 hPa at 20°C for toluene, THF, and EtOH, respectively), which favor the film adhesion to the substrate and prevent either the fast evaporation of solvent and excessive drying pattern formation, both essential conditions for a stereospecific growth of porphyrin aggregates during the self-assembly process. CD spectra evidence for films of both (L)- and (D) ZnP(-) have different patterns with respect to those observed in the case of the aggregation in solution. These results indicate the occurrence of specific interactions between the growing structures and the glass, whose roughness necessarily has to be around 1 nm for the effective chiral arrangement of macrocycles onto the surface. These findings would be of importance for the easy development of cost-effective molecular films to be potentially used in fields where chiral materials are highly desired, as asymmetric catalysis (Simonneaux et al., 2006; Mallat et al., 2007) and chiral sensors (Sannicolò et al., 2014; Shang et al., 2017; Stefanelli et al., 2019). In this regard, we can anticipate that the as-deposited films are fluorescent and highly stable when immersed in water solutions even for a prolonged period. Therefore, these features warrant for their use in optical chiral sensing measurements, which are currently ongoing in our laboratories and whose results will be reported in due course.

EXPERIMENTAL SECTION

General

Porphyrin derivatives investigated in these studies have been prepared as previously reported by our group (Stefanelli et al., 2020b) by using reagents and solvents of commercial sources (Sigma Aldrich, ChemImpex, TCI) in the highest degree of purity without further purifications. The casted films were analyzed by UV-vis spectroscopy using, according to the experimental needs, either a Varian Cary 100 or a JASCO J-1500, equipped with a thermostated cell holder set at 298 K, and purged with ultra-pure nitrogen gas. CD spectroscopic measurements were carried out by Jasco J-1500 equipped as just mentioned. The evaluation of the film optical density (OD) was performed consecutively by only changing the operative mode of J-1500 spectrophotometer without moving the sample, in order to irradiate the same spot of the porphyrin film in both absorbance and CD measurements. Different traces at different stock concentrations were taken, referenced against untreated blank glass slide. Linear dichroism contribution (LD) has been found to be <0.0004 DOD units in all the cases examined. Also, to rule out the strong contributions of birefringence effects, both front and back of the slide were measured without evidencing significative changes in the CD profiles.

Porphyrin Film Preparation

The porphyrin solutions to be casted on glass slides were prepared as follows: 10^{-4} M solutions of macrocycles in 4 ml of the chosen solvent (ethanol, tetrahydrofuran, or toluene) were kept under sonication for 2 min (Fisher Scientific FB15047 apparatus). The solution was then filtered first through a 0.45-µm and then a 0.22-µm FilterBio® syringe filters, sonicated again, and left to stand for 1 h before casting. Concentrations were confirmed by UV-vis spectroscopy. The porphyrin solution should be used within 2 weeks from preparation, to ensure optimal and reproducible results.

Microscope glass slides (SuperFrost®, Menzel) cut into 76 mm × 26 mm and ultra-flat quartz-coated glass substrate (Ossila, 25 mm × 25 mm) pieces were used for deposition as received. Porphyrin solution (10 µl) was layered on the glass slide surface by drop-casting method. The drop was left to dry at standard laboratory conditions, until complete solvent evaporation. The time of evaporation and dimension of spots strictly depend on the solvent used. Glass pieces can be reused after removing the organic layers by extensive washing with a suitable organic solvent (usually chloroform or dichloromethane). Afterward, the slide is treated with acetone and gently dried utilizing a flow of pure nitrogen.

Dynamic Light Scattering Studies

Size distribution by dynamic light scattering (DLS) was performed with Hamamatsu HC120 photometer (Brookhaven, NY, United States), equipped with a BI-200SM goniometer, a BI-9000 AT photocorrelator allowing

to detect a particle size dynamic range from 5 to 5,000 nm, a solid-state laser (Suwtech Inc., SHA, CN) with a wavelength of 532 nm powered by a power supply LDC-2500 (Suwtech Inc.), and a phototube (Hamamatsu Photonics K.K., JP). The solvents used for the sample dissolution were prefiltered with a 0.22-μm hydrophobic filter (FilterBio®). Eight hours after the sample preparation, a volume of 500 μl of stock solution was transferred into a quartz cuvette and maintained at a temperature of 25° C using an external F30-C thermostat (Julabo GmbH, DE), circulating water in a coil placed in the vat containing the refractive index matching liquid. Acquisition time was set to 6 min. The size of chiral porphyrin assemblies was estimated by the hydrodynamic diameter (d_h) distributions according to the Stokes–Einstein equation. The autocorrelation functions were analyzed using the CONTIN algorithm of the Dynamic Light Scattering Software ver. 3.18 provided by Brookhaven Instruments. A Gaussian fitting procedure was applied to the intensity distribution of d_h using the OriginPro 8.1 software for extrapolating average d_h values ± standard deviation from three independent measurements. Polydispersity index (PDI) was calculated from cumulant analysis of the measured intensity autocorrelation function.

Atomic Force Microscopy Measurements

A commercial Keysight 5500 atomic force microscopy (AFM) equipment was employed for the sample topographic analysis. Images were collected in noncontact mode to prevent possible damages of the porphyrin aggregates during contact measures. Silicon NanoSensors tip were used with a resonance frequency in air of about 300 kHz. The apex radius is about 20 nm. After the acquisition, images were analyzed by the free Gwyddion software.

DATA AVAILABILITY STATEMENT

The original contributions presented in the study are included in the article/**Supplementary Material**. Further inquiries can be directed to the corresponding author.

AUTHOR CONTRIBUTIONS

DM, GM, and MS contributed to the conception and design of the study. MN synthesized the title porphyrins. TT prepared the porphyrin samples and performed the drop-casting on glass. MV and GM performed the circular dichroism measurements. GB performed the AFM studies. FD and GP performed the DLS measurements. MS, GM, RP, CD, and DM wrote the manuscript. MS and RP were responsible for the financial support to the work. All authors contributed to the discussion and interpretation of the results and to the manuscript revision, and read and approved the submitted version.

FUNDING

This research was funded by the H2020-FETOPEN, 828779, INITIO project and by the University of Rome Tor Vergata, Italy, ASPIRE project-E84I20000220005.

SUPPLEMENTARY MATERIAL

The Supplementary Material for this article can be found online at: https://www.frontiersin.org/articles/10.3389/fchem.2021.804893/full#supplementary-material

REFERENCES

Albano, G., Pescitelli, G., and Di Bari, L. (2020). Chiroptical Properties in Thin Films of π-Conjugated Systems. *Chem. Rev.* 120, 10145–10243. doi:10.1021/acs.chemrev.0c00195

Berova, N., Nakanishi, K., and Woody, R. W. (2000). *Circular Dichroism: Principles and Applications*. 2nd Edn. Weinheim: Wiley-WCH.

Caroleo, F., Stefanelli, M., Magna, G., Venanzi, M., Paolesse, R., Sennato, S., et al. (2019). Kinetic and Spectroscopic Studies on the Chiral Self-Aggregation of Amphiphilic Zinc and Copper (L)-prolinate-tetraarylporphyrin Derivatives in Different Aqueous media. *Org. Biomol. Chem.* 17, 1113–1120. doi:10.1039/C8OB02689K

Chen, P., Ma, X., Duan, P., and Liu, M. (2006). Chirality Amplification of Porphyrin Assemblies Exclusively Constructed from Achiral Porphyrin Derivatives. *ChemPhysChem* 7, 2419–2423. doi:10.1002/cphc.200600402

Chen, K., Jiao, T., Li, J., Han, D., Wang, R., Tian, G., et al. (2019). Chiral Nanostructured Composite Films via Solvent-Tuned Self-Assembly and Their Enantioselective Performances. *Langmuir* 35, 3337–3345. doi:10.1021/acs.langmuir.9b00014

Colozza, N., Stefanelli, M., Venanzi, M., Paolesse, R., and Monti, D. (2019). Fabrication of Langmuir-Blodgett Chiral Films from Cationic (L)-Proline-Porphyrin Derivatives. *J. Porphyrins Phthalocyanines* 23, 462–468. doi:10.1142/S1088424619500305

Costa, D., Pradier, C.-M., Tielens, F., and Savio, L. (2015). Adsorption and Self-Assembly of Bio-Organic Molecules at Model Surfaces: A Route towards Increased Complexity. *Surf. Sci. Rep.* 70, 449–553. doi:10.1016/j.surfrep.2015.10.002

Gellman, A. J. (2010). Chiral Surfaces: Accomplishments and Challenges. *ACS Nano* 4, 5–10. doi:10.1021/nn901885n

Hattori, S., Vandendriessche, S., Koeckelberghs, G., Verbiest, T., and Ishii, K. (2017). Evaporation Rate-Based Selection of Supramolecular Chirality. *Chem. Commun.* 53, 3066–3069. doi:10.1039/C6CC09842H

Huang, J., Egan, V. M., Guo, H., Yoon, J.-Y., Briseno, A. L., Rauda, I. E., et al. (2003). Enantioselective Discrimination of D- and L-Phenylalanine by Chiral Polyaniline Thin Films. *Adv. Mater.* 15, 1158–1161. doi:10.1002/adma.200304835

Iavicoli, P., Simón-Sorbed, M., and Amabilino, D. B. (2009). Surface Aggregate Morphology of Chiral Porphyrins as a Function of Constitution and Amphiphilic Nature. *New J. Chem.* 33, 358–365. doi:10.1039/b815177f

Mali, K. S., and De Feyter, S. (2013). Principles of Molecular Assemblies Leading to Molecular Nanostructures. *Phil. Trans. R. Soc. A.* 371, 20120304. doi:10.1098/rsta.2012.0304

Mallat, T., Orglmeister, E., and Baiker, A. (2007). Asymmetric Catalysis at Chiral Metal Surfaces. *Chem. Rev.* 107, 4863–4890. doi:10.1021/cr0683663

Mammana, A., D'Urso, A., Lauceri, R., and Purrello, R. (2007). Switching off and on the Supramolecular Chiral Memory in Porphyrin Assemblies. *J. Am. Chem. Soc.* 129, 8062–8063. doi:10.1021/ja071447b

Monti, D., De Rossi, M., Sorrenti, A., Laguzzi, G., Gatto, E., Stefanelli, M., et al. (2010). Supramolecular Chirality in Solvent-Promoted Aggregation of Amphiphilic Porphyrin Derivatives: Kinetic Studies and Comparison between Solution Behavior and Solid-State Morphology by AFM Topography. *Chem. - A Eur. J.* 16, 860–870. doi:10.1002/chem.200901964

Monti, D., Stefanelli, M., Raggio, M., Colozza, N., Venanzi, M., Lettieri, R., et al. (2011). Solid State Deposition of Chiral Amphiphilic Porphyrin Derivatives on

Glass Surface. *J. Porphyrins Phthalocyanines* 15, 1209–1219. doi:10.1142/S1088424611004117

Răsădean, D.-M., Gianga, T.-M., Jávorfi, T., Hussain, R., Siligardi, G., and Pantoş, G. D. (2020). Mapping the Chiroptical Properties of Local Domains in Thin Films of Chiral Silicon Phthalocyanines by CD Imaging. *Molecules* 25, 6048. doi:10.3390/molecules25246048

Sannicolò, F., Arnaboldi, S., Benincori, T., Bonometti, V., Cirilli, R., Dunsch, L., et al. (2014). Potential-Driven Chirality Manifestations and Impressive Enantioselectivity by Inherently Chiral Electroactive Organic Films. *Angew. Chem.* 126, 2661–2665. doi:10.1002/ange.201309585

Savioli, M., Stefanelli, M., Magna, G., Zurlo, F., Caso, M. F., Cimino, R., et al. (2020). Tunable Supramolecular Chirogenesis in the Self-Assembling of Amphiphilic Porphyrin Triggered by Chiral Amines. *Ijms* 21, 8557. doi:10.3390/ijms21228557

Shang, X., Song, I., Ohtsu, H., Lee, Y. H., Zhao, T., Kojima, T., et al. (2017). Supramolecular Nanostructures of Chiral Perylene Diimides with Amplified Chirality for High-Performance Chiroptical Sensing. *Adv. Mater.* 29, 1605828. doi:10.1002/adma.201605828

Simonneaux, G., Lemaux, P., Ferrand, Y., and Raultberthelot, J. (2006). Asymmetric Heterogeneous Catalysis by Metalloporphyrins. *Coord. Chem. Rev.* 250, 2212–2221. doi:10.1016/j.ccr.2006.01.014

Stefanelli, M., Magna, G., Zurlo, F., Caso, F. M., Di Bartolomeo, E., Antonaroli, S., et al. (2019). Chiral Selectivity of Porphyrin-ZnO Nanoparticle Conjugates. *ACS Appl. Mater. Inter.* 11, 12077–12087. doi:10.1021/acsami.8b22749

Stefanelli, M., Mandoj, F., Magna, G., Lettieri, R., Venanzi, M., Paolesse, R., et al. (2020a). The Self-Aggregation of Porphyrins with Multiple Chiral Centers in Organic/Aqueous Media: The Case of Sugar- and Steroid-Porphyrin Conjugates. *Molecules* 25, 4544. doi:10.3390/molecules25194544

Stefanelli, M., Savioli, M., Zurlo, F., Magna, G., Belviso, S., Marsico, G., et al. (2020b). Porphyrins through the Looking Glass: Spectroscopic and Mechanistic Insights in Supramolecular Chirogenesis of New Self-Assembled Porphyrin Derivatives. *Front. Chem.* 8, 587842. doi:10.3389/fchem.2020.587842

Tao, F., and Bernasek, S. L. (2005). Chirality in Supramolecular Self-Assembled Monolayers of Achiral Molecules on Graphite: Formation of Enantiomorphous Domains from Arachidic Anhydride. *J. Phys. Chem. B* 109, 6233–6238. doi:10.1021/jp0452397

Xu, Y., Duan, J.-J., Yi, Z.-Y., Zhang, K.-X., Chen, T., and Wang, D. (2021). Chirality of Molecular Nanostructures on Surfaces via Molecular Assembly and Reaction: Manifestation and Control. *Surf. Sci. Rep.* 76, 100531. doi:10.1016/j.surfrep.2021.100531

Zaera, F. (2008). Chiral Modification of Solid Surfaces: a Molecular View. *J. Phys. Chem. C* 112, 16196–16203. doi:10.1021/jp804588v

Zaera, F. (2009). Regio-, Stereo-, and Enantioselectivity in Hydrocarbon Conversion on Metal Surfaces. *Acc. Chem. Res.* 42, 1152–1160. doi:10.1021/ar900049m

Zaera, F. (2017). Chirality in Adsorption on Solid Surfaces. *Chem. Soc. Rev.* 46, 7374–7398. doi:10.1039/C7CS00367F

Conflict of Interest: The authors declare that the research was conducted in the absence of any commercial or financial relationships that could be construed as a potential conflict of interest.

Publisher's Note: All claims expressed in this article are solely those of the authors and do not necessarily represent those of their affiliated organizations, or those of the publisher, the editors, and the reviewers. Any product that may be evaluated in this article, or claim that may be made by its manufacturer, is not guaranteed or endorsed by the publisher.

Advantages of publishing in Frontiers

OPEN ACCESS
Articles are free to read for greatest visibility and readership

FAST PUBLICATION
Around 90 days from submission to decision

HIGH QUALITY PEER-REVIEW
Rigorous, collaborative, and constructive peer-review

TRANSPARENT PEER-REVIEW
Editors and reviewers acknowledged by name on published articles

Frontiers
Avenue du Tribunal-Fédéral 34
1005 Lausanne | Switzerland

Visit us: www.frontiersin.org
Contact us: frontiersin.org/about/contact

REPRODUCIBILITY OF RESEARCH
Support open data and methods to enhance research reproducibility

DIGITAL PUBLISHING
Articles designed for optimal readership across devices

FOLLOW US
@frontiersin

IMPACT METRICS
Advanced article metrics track visibility across digital media

EXTENSIVE PROMOTION
Marketing and promotion of impactful research

LOOP RESEARCH NETWORK
Our network increases your article's readership